## ERRATA

| Page | Line | For.... | Read..... |
|---|---|---|---|
| 41 | 29 | the subscripts | and the subscripts |
| 46 | 10 | Rand(1965)who introduced | Rand(1965) introduced |
| 46 | 30 | energy dissipation | energy dissipator |
| 64 | 22 | erogidc | ergodic |
| 66 | 15 | satic | static |
| 72 | 8 | unbaised | unbiased |
| 73 | 5 | In array | An array |
| 73 | 18 | digitsed | digitised |
| 78 | 10 | autocorrleation | autocorrelation |
| 83 | 1 | Frequenty | Frequently |
| 96 | 11 | $F[y(t)]=\frac{Y}{2}\int_{-\infty}^{+\infty}[.....]dt$ | $F[y(t)]=\frac{Y}{2}\int_{-\infty}^{+\infty}[.....]dt$ |
| 97 | 14 | $\frac{AT}{2}\int_{-\infty}^{+\infty}.....$ | $\frac{YT}{2}\int_{-\infty}^{+\infty}.....$ |
| 99 | 12 | $c(t)=\sum_{n=-\infty}^{\infty}(t-n\Lambda t)=\nabla(t,\Lambda t)$ | $c(t)=\sum_{n=-\infty}^{\infty}\delta(t-n\Delta t)=\nabla(t,\Delta t)$ |
| 119 | 3 | $\int_{-\infty}^{+\infty}y^2dy$ | $\int_{-0.5}^{+0.5}y^2dy$ |
| 122 | 5 | $\{[\Sigma_{t=1}^{N}(x_t-\bar{x})^2][\frac{1}{N}\Sigma_{t=1}^{N}(y_t-\bar{y})]\}^{\frac{1}{2}}$ | $\{[\frac{1}{N}\Sigma_{t=1}^{N}(x_t-\bar{x})^2][\frac{1}{N}\Sigma_{t=1}^{N}(y_t-\bar{y})]\}^{\frac{1}{2}}$ |
| 125 | 14 | Considering a plane jet | Consider a plane jet |
| 127 | 26 | U, V and W | where U, V and W |
| 127 | 27 | co-ordinate direction | co-ordinate directions |
| 132 | 19 | $\frac{1}{2}\int_0\frac{\partial}{\partial x}(\rho U^2)dy$ | $\frac{1}{2}\int_0^{\infty}\frac{\partial}{\partial x}(\rho U^2)dy$ |
| 138 | 1 | Myer et al. (1963) | Myers et al. (1963) |
| 138 | Fig.D.3 | Meyers et al. (1963) | Myers et al. (1963) |
| 140 | 7 | (Mayer et al. 1963) | (Myers et al. 1963) |
| 140 | 10 | Mayer et al. (1963) | Myers at al. (1963) |
| 147 | 17 | human erros | human errors |
| 169 | 22 | for v ans w | for v and w |
| 178 | 2 | differential hs the form | differential has the form |
| 181 | 33 | is the coefficient of kinematic | is the kinematic |
| 184 | 11 | pressrue | pressure |
| 190 | 28 | wir | wire |
| 198 | 6 | $\Delta t=0.05$ sec | $\Delta t=0.005$ sec |
| 205 | 4 | Section 6.5.1 | Section E.6.5.1 |
| 209 | 3 | horizonatal | horizontal |
| 213 | 18 | Figs. F.7,F.13 and F.14 | Figs. F.7,F.14 and F.15 |
| 216 | 4 | sharpe parameter | shape parameter |
| 221 | 30 | of the coefficients | of the coefficients of |
| 224 | 4 | veloctily | velocity |
| 225 | 19 | comparaison | comparison |
| 231 | 7 | experiencied | experienced |
| 245 | 8 | infered | inferred |
| 282 | 11 | independnent | independent |
| 291 | 19 | Trans. Engng. Instn. Canada | Trans. Engng. Inst. Canada |

IMPERIAL COLLEGE OF SCIENCE AND TECHNOLOGY

DEPARTMENT OF CIVIL ENGINEERING

# FAST WATER STREAMS DEFLECTED BY TRANSVERSE WALLS

by

A.R. BOKAIAN, *Dip. Civ. Eng., D.E.A., M.Sc., D.I.C.*

Thesis submitted to the University of London
for the Degree of Doctor of Philosopy in
the Faculty of Engineering

January 1980

*to my parents and my brother*

## SYNOPSIS

Experimental work has been carried out to investigate the phenomena associated with a water jet of finite dimensions issuing from an overflow spillway when it is deflected by a smooth vertical transverse wall which is perpendicular to the initial flow direction. The state of development of the supercritical flow at the toe of the spillway was quasi-potential in all tests. Three distinct regions of flow were identified. In region I, which began at the toe of the spillway, the water depth remained approximately constant apart from a region adjacent to the outlet where a degree of lateral discharge was observed. In region II, a hydraulic jump with a lateral discharge was observed. In region III, the flow separated from the bed and impinged violently on the wall and became entirely parallel to it, resulting in a complex wave pattern at the wall.

Wall and bed pressures, flow directions, velocities and the wave heights were measured by using tapping points, a yawmeter, a pitot-static tube and wave recording probes respectively. Redirection of the flow along the channel centre line in both regions I and II was found to be negligible. In region I, the velocity profiles could be approximated by a power law curve whereas in region II, the mean flow characteristics were studied in a form relevant to a two-dimensional wall jet. The mean velocity of the forward flow was found to be self-similar when a velocity scale and a length scale were used. The streamwise development of these scales showed some departures from those observed in classical wall jets due to the adverse pressure gradient. A procedure was developed to predict the surface profile. The waves at the retaining wall had a pseudo-periodic behaviour with significant frequencies of less than 3 Hz. A mathematical relationship was developed to design the wall height by a probabilistic approach.

ACKNOWLEDGEMENTS

The writer wishes to express his sincere gratitude to the late Professor J.R.D. Francis for his guidance, continuous encouragement and unfailing support throughout most of the period of this research. The writer is particularly indebted to Professor P. Ackers whose advice and helpful comments have contributed considerably. The efforts and kind assistance of Mr. A. Scott-Moncrieff are gratefully acknowledged.

The conduct of this research work required the skilled and sympathetic help of most of the academic and the technical staff in the Hydraulics Section and Laboratory and their help is very much appreciated. The writer is particularly indebted to Mr. G. Thomas for his advice on the design of various instruments and his assistance with the presentation of the graphs and tables in this thesis. The credit for photographs belongs to Miss. J. Gurr and her assistant Mr. F. Milson, the Departmental Photgraphers.

The friendship of Hydraulics and Hydrology research students was warmly appreciated and their varied social and geographic roots broadened my outlook on life. Discussions with my colleagues, Mr. S.J. Robinson, Mr. J. Stefanakos and Mr. P.M. Johnston at various stages of this work are very much appreciated. Thanks are also extended to Miss J. Barritt and Miss J. Rout for their unfailing patience and care in typing this thesis.

Special mention is awarded to my wife Susan, for her constant inspiration throughout the period of this research as her understanding and encouragement will always be a goal for me to emulate.

CONTENTS


| | | Page |
|---|---|---|
| SYNOPSIS | | 3 |
| ACKNOWLEDGEMENTS | | 4 |
| CONTENTS | | 5 |
| GLOSSARY OF SYMBOLS | | 11 |
| MAJOR ABBREVIATIONS | | 25 |
| CHAPTER A | INTRODUCTION | 27 |
| CHAPTER B | BACKGROUND | 33 |
| B.1 | GENERAL | 34 |
| B.2 | DIMENSIONAL ANALYSIS AND SIMILARITY | 35 |
| B.3 | THE ENERGY AND MOMENTUM COEFFICIENTS | 36 |
| B.3.1 | Energy Coefficient | 36 |
| B.3.2 | Momentum Coefficient | 38 |
| B.4 | FROUDE NUMBER | 39 |
| B.5 | HYDRAULIC JUMPS | 40 |
| B.5.1 | Classical Hydraulic Jump | 40 |
| B.5.1.1 | Position Sensitivity of a Classical Hydraulic Jump | 42 |
| B.5.1.2 | Energy Loss in a Classical Hydraulic Jump | 43 |
| B.5.1.3 | Classification of Classical Hydraulic Jumps | 44 |
| B.5.2 | Forced Hydraulic Jumps | 44 |
| B.5.3 | Submerged Hydraulic Jump | 46 |
| B.5.4 | Spatial Hydraulic Jump | 47 |
| CHAPTER C | THEORETICAL ANALYSIS OF RANDOM WAVES | 48 |
| C.1 | GENERAL | 49 |
| C.2 | BASIC DESCRIPTIONS OF PHYSICAL DATA | 50 |
| C.2.1 | Classifications of Deterministic Data | 52 |
| C.2.1.1 | Sinusoidal Periodic Data | 53 |
| C.2.1.2 | Complex Periodic Data | 54 |
| C.2.1.3 | Almost-Periodic Data | 55 |
| C.2.1.4 | Transient Non-periodic Data | 56 |
| C.2.2 | Classifications of Random (Stochastic or Probabilistic) Data | 58 |

C.2.2.1 Sample Mean 60
C.2.2.2 Sample Autocorrelation 60
C.2.2.3 Ensemble Mean 60
C.2.2.4 Ensemble Autocorrelation 62
C.2.2.5 Stationary Random Processes 62
C.2.2.6 Ergodic Random Processes 63
C.2.2.7 Non-stationary Random Processes 64
C.2.2.8 Self-stationary Random Processes 64
C.3 BASIC DESCRIPTIVE PROPERTIES OF RANDOM DATA 66
C.3.1 Mean Square Values (Mean Values and Variances) 66
C.3.2 Probability Density Functions 66
C.3.2.1 Illustrations 68
C.3.2.2 Applications 71
C.3.3 Sampling Theory 71
C.3.3.1 Unbiased Estimates 71
C.3.3.2 Consistent Estimates 72
C.3.4 Digitising of Continuous Data 72
C.3.4.1 Raw Data 73
C.3.4.2 Ordered Array (Ranked Array) 73
C.3.5 Calculation of the Mean Value 73
C.3.6 Calculation of the Standard Deviation 73
C.3.7 Coefficient of Dispersion 73
C.3.8 Skewness 74
C.3.9 Kurtosis 75
C.3.10 Percentile 76
C.3.10.1 Percentile for a Digitised Time History Record 77
C.3.11 Autocorrelation Functions 77
C.3.12 Autocovariance Functions 79
C.3.13 Autocorrelation Coefficients 79
C.3.13.1 Correlograms 80
C.3.13.1.1 Illustrations 80
C.3.13.1.2 Applications 80
C.3.14 Power Spectral Density Functions 82
C.3.14.1 Normal Power Spectral Density Functions 83
C.3.14.2 Illustrations of Some Power Spectral Density Functions 83
C.3.14.3 Application of Power Spectral Density Functions to Water Waves 85

C.3.14.3.1 Average Power of the Process 85

C.3.14.3.2 Sinusoidal Waves 86

C.3.14.3.3 Almost Periodic Waves 87

C.3.14.3.4 Ergodic Random Waves 87

C.3.14.4 Importance of Energy Density Functions 88

C.4 SPECTRAL ANALYSIS USING FOURIER TRANSFORM TECHNIQUES 90

C.4.1 Representation of a Periodic Function by a Fourier Series 90

C.4.2 The Fourier Integral and Transform 90

C.4.2.1 Convolution Integral 92

C.4.2.2 Fourier Transform of Products of Two Functions 92

C.4.3 Application of Fourier Transforms in Spectral Analysis 92

C.4.4 Windows 93

C.4.5 Fourier Transform of a Sine Wave 93

C.4.5.1 The Infinite Continuous Record 96

C.4.5.2 The Finite Continuous Record 97

C.4.5.3 The Finite Record with Discrete Values Only 99

C.4.6 Leakage 101

C.4.6.1 Hanning Window 102

C.5 POWER SPECTRUM OF DIGITISED DATA 105

C.5.1 Fourier Series Representation (Harmonic Analysis) 105

C.5.1.1 Parseval's Theorem 108

C.5.2 Transformation of Data to Zero Mean Value 108

C.5.3 Fourier Line Spectrum-Raw Periodogram 109

C.5.4 Hanning Window for a Digitised Time Series 110

C.5.5 Properties of the Raw Periodogram 111

C.5.6 Smoothing 112

C.5.6.1 Properties of the Smoothed Periodogram 112

C.5.6.2 Recommendation for the Value of m 113

C.5.6.3 Confidence Limits for the Smoothed Periodogram 114

C.5.7 3 Point Smoothing 114

C.5.8 Aliasing 114

C.5.8.1 Theorem 115

C.5.9 Fast Fourier Transform 116
C.5.10 Recommendation for Sampling Rate and Length of the Record 117
C.6 QUANTIZATION ERROR 118
C.7 JOINT PROPERTIES OF RANDOM DATA 120
C.7.1 Cross-Correlation Functions 120
C.7.2 Estimation of the Cross-Correlation Functions 121
C.7.3 Cross-Correlogram 122
C.7.3.1 Applications 123

CHAPTER D WALL JETS 124

D.1 PLANE TURBULENT WALL JETS 125
D.1.1 Equation of Motion 126
D.1.2 Similarity Analysis of Equations of Motion 129
D.1.3 Integral Momentum Equation 132
D.1.4 Dimensional Considerations 134
D.1.5 Experimental Results 135
D.2 PLANE TURBULENT FREE JET AND WALL JET 141
D.2.1 The Free Jet 142
D.2.2 The Wall Jet 143

CHAPTER E EXPERIMENTAL SET-UP AND MEASURING TECHNIQUES 145

E.1 GENERAL 146
E.2 TOLERANCE ON MEASUREMENT 147
E.2.1 Uncertainty 147
E.2.1.1 Categories of Uncertainties 147
E.2.2 Repeatability 149
E.2.3 Combination of Uncertainties 150
E.2.4 Accuracy 150
E.2.5 Method of Least Squares 150
E.3 THE LABORATORY ARRANGEMENT 151
E.3.1 General Layout 151
E.3.2 Supply and Disposal of Water 151
E.3.3 Control of Flow to the Chute 151
E.3.4 Water Flow Rate Measurements 154
E.3.4.1 Calibration of the Spillway Crest 156
E.4 MEASUREMENT OF MEAN FLOW PROPERTIES 159
E.4.1 The Effect of Fluctuations 159
E.5 MANOMETERS 161

E.5.1 Calibration of Manometers 161
E.5.2 Lag in Leads 161
E.5.3 System Response 161
E.5.4 Manometer Boards 163
E.6 MEAN VELOCITY FIELD MEASUREMENTS 167
E.6.1 Design of the Pitot-Static Tube 167
E.6.2 The Effect of Misalignment 168
E.6.3 Theoretical Investigation of the Turbulent Effect on Flow Measurement by Pitot-Static Tube 169
E.6.4 The Turbulence Effect on Flow Measurement by Pitot-Static Tube 170
E.6.5 The Calibration Factor for the Pitot-Static Tube 172
E.6.5.1 Calibration of the Pitot-Static Tube 172
E.6.6 Correction of Turbulent Flow Pitot-Static Tube Measurements 174
E.6.7 Pitot-Static Tubes in Pressure Gradient Flows 178
E.7 DETERMINATION OF THE MEAN FLOW DIRECTION 181
E.7.1 Design of the Pressure-Type Yawmeter 182
E.7.2 Woolen Tufts 183
E.8 MEASUREMENT OF THE MEAN WALL PRESSURE 184
E.9 MEASUREMENT OF THE MEAN BED PRESSURE 189
E.10 THE MEASUREMENT AND ANALYSIS OF WAVE HEIGHT 190
E.10.1 Calibration of the Wave Recorder Probes 192
E.10.2 The Analyser 193
E.10.3 Selection of Paper Speed and Digitisation Interval 197
E.10.4 Number of Data Points and Length of Recording Paper 198
E.10.5 Calibration Lines of the Wave Recording Probes 199
E.10.6 Estimation of Uncertainty in Wave Height Measurement 201
E.10.7 Estimation of Uncertainty in Frequency 203
E.11 EXPERIMENTAL PROGRAMME 204
E.11.1 Critical Point for the Flow Over the Spillway 209

CHAPTER F EXPERIMENTAL RESULTS AND DISCUSSION 211

F.1 FLOW DIRECTION 212
F.2 FLOW CHARACTERISTICS OF REGION I 214
F.2.1 Theory of the Boundary Layer 214
F.2.1.1 Parameters of Turbulent Boundary Layers 214

F.2.1.2 Von Karman Momentum Equation 215

F.2.2 Velocity Profiles in Region I 217

F.2.2.1 Power Law Applied to the Velocity Profiles in Region I 222

F.2.3 Nominal Boundary Layer Thickness at the Toe of the Spillway 225

F.3 FLOW CHARACTERISTICS OF REGIONS II AND III 227

F.3.1 Bed Pressure Field in Regions II and III 227

F.3.2 Pressure Field 228

F.3.3 Velocity Distributions in Region II 230

F.3.3.1 Universal Similarity Curves of the Velocity Distributions in the Forward Flow of Region II 231

F.3.3.2 Variation of the Velocity Scale and the Length Scale 238

F.3.3.3 Prediction of the Surface and Energy Profiles 239

F.3.4 Governing Equations of Motion in the Forward Flow of Region II and the Mathematical Condition for Separation 243

F.3.4.1 Mathematical Condition for Separation 244

F.3.5 Pressure Distribution on the Retaining Wall 246

F.4 WAVES AT THE RETAINING WALL 250

F.4.1 Analysis of the Waves in Amplitude Domain 254

F.4.1.1 Universal Similarity Curve for the Distribution of the Wave Height at the Middle of the Retaining Wall 261

F.4.1.2 Coefficients of Dispersion of the Wave Heights 264

F.4.2 Analysis of the Wave Heights in Time Domain 265

F.4.3 Analysis of the Wave Heights in Frequency Domain 269

F.5 SUMMARY OF CONCLUSIONS AND SUGGESTIONS FOR FUTURE RESEARCH 274

F.5.1 Summary of Conclusions 274

F.5.2 Recommendations for Future Research 276

APPENDICES 277

APPENDIX I THE DIRAC DELATA FUNCTION 278

APPENDIX II THE CHI-SQUARED DISTRIBUTION 280

APPENDIX III THE LINEAR REGRESSIONS 282

REFERENCES 286

# GLOSSARY OF SYMBOLS

The notation used is not unique; the same symbol may be used to denote more than one quantity or variable, but the context will make it clear which applies in a particular section of the thesis. As far as practicable, a common notation has been used throughout, but if a special usage is confined to one chapter or appendix, this is indicated in the following listing:

| Symbol | Definition |
|---|---|
| A | cross-sectional area of flow.<br>area under the pulse, Eq. (C.89).<br>a constant, Fig. C.6. |
| A(t) | deterministic multiplication factor. |
| $A_1, A_2$ | constants. |
| a | amplitude of a sine wave, Eq. (C.62).<br>regression constant, Eq. (III.4b).<br>a constant. |
| *a* | gate opening, Fig. E.7. |
| *a* | group of experiments, Section E.11. |
| a' | an arbitary constant, Eq. (C.102). |
| a(t) | a differentiable function of t. |
| $a, \ldots, a_{N/2}$ | coefficients, Eqs. (C.116). |
| $a, \ldots, a_n$ | coefficients in Fourier series. |
| $a_c$ | depth of flow at the vena contracta, Fig. E.7. |
| B | a fluctuating characteristic of a turbulent flow. |
| b | an arbitary constant.<br>regression coefficient, Eqs. (III.4a) and (III.11) |
| *b* | channel width.<br>impingement width. |
| *b* | group of experiments, Section E.11. |
| b(t) | a differentiable function of t. |

| | |
|---|---|
| $b_o,\ldots,b_{N/2}$ | coefficients, Eqs. (C.116). |
| $b_o,\ldots,b_n$ | coefficients in Fourier series. |
| $C_d$ | coefficient of dispersion, Eq. (F.41).<br>overall discharge coefficient, Eq. (E.8). |
| $C_f$ | coefficient of boundary shear stress, Eq. (F.5). |
| C(f) | Fourier Transform of Dirac Comb. |
| c | calibration constant, Eq. (E.25).<br>a constant. |
| $C_1, C_2, C_3$ | constants. |
| c(t) | Dirac comb along time axis. |
| $c_d$ | discharge coefficient, Eq. (E.6a). |
| $c_f$ | skin-friction coefficient, Eq. (D.40c). |
| $c_f'$ | skin-friction coefficient, Eq. (D.52). |
| $c_v$ | correction coefficient, Eq. (E.7). |
| D | external diameter of the pitot-static tube. |
| d | depth of flow in an open channel, Eq. (B.2).<br>thickness of the plane jet (or the slot height), Fig. D.1. |
| $d_1$ | depth of flow before the hydraulic jump, Fig. B.2. |
| $d_2$ | depth of flow after the hydraulic jump, Fig. B.2. |
| $d_m, d_{m1}, d_{m2}$ | depths of the supercritical water flow at the toe of the spillway along the channel centre line, Figs. E.21 and E.22. |
| $d_t$ | tailwater depth. |
| $d_w$ | mean momentum depth. |
| e | the exponential. |
| $e$ | total head of a cross - sectional area of flow (specific energy). |
| $e_o$ | specific energy at the toe of the spillway. |
| $e_1, e_2$ | specific energies of flow before and after the hydraulic jump respectively, Fig. B.2. |

| | |
|---|---|
| $e_k$ | kinetic energy flux of a cross-sectional area of flow per unit time, Eq. (B.8). |
| $e_L$ | energy loss, Eq. (B.17b). |
| $e_t$ | total energy, Eq. (B.9). |
| $e_w$ | average total wave energy per unit surface area, Eq. (C.64). |
| exp | the exponential. |
| $F(R_{probe})$ | a function of probe Reynolds number, Eq. (E.17). |
| $F_1, F_2, F_3$ | components of the body force in the x,y,z - directions respectively. |
| $F(t)$ | a function of parameter t. |
| Fr | Froude number. |
| $Fr_1$ | Froude number of the flow preceding the hydraulic jump, Eq. (B.15). |
| $f, f_o$ | frequencies. |
| $f(t_o)$ | function of $t_o$, Eq. (I.2). |
| $f(t)$ | function of variable t, Eqs. (C.69) and (C.77b). |
| $f_1(t), f_2(t)$ | functions of variable t, Eq. (C.79). |
| $f(\beta)$ | function of $\beta$, Eq. (E.23). |
| $f(\eta)$ | function of $\eta$, Eqs. (D.12a) and (F.18a). |
| $f(\chi^2)$ | function of the random variable $\chi^2$, Eq. (II.1). |
| $f_1$ | fundemental frequency. |
| $f_1, f_2, \ldots f_\infty$ | frequencies, Eq. (C.12). |
| $f_1(M_j, \rho, x, \nu)$ | function of $M_j, \rho, x$ and $\nu$, Eq. (D.37a). |
| $f_2(M_j, \rho, x, \nu)$ | function of $M_j, \rho, x$ and $\nu$, Eq. (D.37b). |
| $f_3(M_j, \rho, x, \nu)$ | function of $M_j, \rho, x$ and $\nu$, Eq. (D.37c). |
| $f_1', \ldots, f_\ell'$ | frequencies, Eq. (C.133). |
| $f_{max}$ | maximum frequency. |
| $f_N$ | Nyquist frequency. |
| $f_p$ | frequency of the pth harmonic of the Fourier series. |

| | |
|---|---|
| $G(f)$ | power spectral density function defined for non-negative frequencies only. |
| $\hat{G}(f)$ | estimated power spectral density function. |
| $G_c(f)$ | power spectrum of a continuous time series. |
| $G_d(f)$ | power spectrum of a discrete time series. |
| $g$ | population skewness coefficient, Eq. (C.35). acceleration due to gravity. |
| $\hat{g}$ | estimated skewness coefficient, Eq. (C.36). |
| $g(f)$ | function of f, Eqs. (C.14) and (C.77a). |
| $g_1(f), g_2(f)$ | functions of variable f, Eq. (C.79). |
| $g_1(R_j), g_2(R_j), g_3(R_j)$ | functions of the nozzle Reynolds number, Eqs. (D.38a), (D.38b) and (D.38c). |
| $g(t)$ | a function of variable t. |
| $g(\xi)$ | a function of variable $\xi$, Eq. (C.78). |
| $g(\eta)$ | function of $\eta$, Eq. (D.14). |
| $H$ | water level over the spillway crest. |
| $H(\omega_n)$ | function of $\omega_n$, Eq. (C.74b). |
| $H_1$ | water depth, Fig. E.7. total upstream energy head over the spillway crest, Eq. (E.6.a). |
| $H_1(\omega)$ | function of $\omega$, Eq. (C.76b). |
| $H_2$ | height of the spillway crest above the channel bed. |
| $H_n$ | nth complex Fourier series coefficient. |
| $h$ | height of the water surface above the datum, Fig. IV.1. static reading, Eq. (E.18b). |
| $h_1$ | pitot reading, Eq. (E18b). |
| $h$ | water depth. |
| $I$ | input (or the reading). |
| $\hat{I}(f)$ | raw periodogram defined for non-negative frequencies only. |
| $I_r$ | interquartile range, Eq. (C.41). |

| | |
|---|---|
| $i$ | $\sqrt{-1}$. |
| | a counter. |
| $i$ | fluctuating part of the input I with respect to its average $\bar{I}$. |
| $J(u)$ | function of u, Eq.(C.84). |
| $J_1(f)$ | function of f, Eq.(C.112). |
| $j$ | a counter. |
| $K$ | calibration factor. |
| $K_1, K_2$ | constants, Eq.(E.19). |
| $k$ | shape factor, Eq.(F.4). |
| | a variable less than unity, Fig.(C.17). |
| | calibration factor, Eq. (E.25). |
| | a counter. |
| $L$ | length of the weir crest. |
| $L_j$ | length of the hydraulic jump, Fig.B.2. |
| $L_j$ | longitudinal distance between the toe of the forced hydraulic jump and the retaining wall. |
| $\ell$ | an integer, Eq.(C.133). |
| | impingement length. |
| $M$ | integral magnitude, Eq.(C.72). |
| | an integer, Eqs.(C.127) and (C.128). |
| $M_j$ | jet momentum flux at the nozzle, Eq.(D.37). |
| $m$ | pressure force plus the momentum of a cross-sectional area of flow per unit width. |
| $m_o$ | pressure force plus the momentum per unit width of the flow at the toe of the spillway. |
| $m$ | an integer. |
| | a counter. |
| $m^*$ | an integer, Eq.(C.132). |
| $m_r$ | rth central moment. |
| $m_y$ | median. |
| $N$ | number of data points or sample size, Eq.(C.32). |
| $N$ | integer number, Fig. C.10 |

| | |
|---|---|
| n | sample size, Eqs. (C.31). |
| | total number of measurements. |
| | a counter. |
| | an integer. |
| *n* | number of sample functions in an ensemble, Fig. (C.9). |
| | number of parameters in Buckingham π theorem. |
| | co-ordinate direction, Fig. (IV.1). |
| | an exponent. |
| P | probability of exceedance of the wave height above the retaining wall. |
| | bed pressure, Fig.(F.11). |
| | pressure at any point, Eq.(D.1). |
| | pressure outside of the jet, Eq.(D.9a). |
| $P_\infty$ | pressure outside of the jet, Eq. (D.7). |
| $\overline{P}$ | average power of a process,Eq.(C.52). |
| P(y) | probability distribution function (cumulative probability distribution function),Eq.(C.27). |
| p | pressure measured by static orifice. |
| | data point in millivolts, Eq. (E.25). |
| | an exponent, Eq.(D.13a). |
| | static pressure. |
| | a counter. |
| p(y) | probability density function of the variable y. |
| $p_o$ | water depth $y_o$ expressed in millivolts. |
| $p_1$ | pressure measured by pitot orifice. |
| *p1,p2,p3* | positions of the retaining wall with respect to the chute. |
| Q | discharge. |
| *Q* | discharge, Eq. (D.53). |
| q | discharge per unit width. |
| | an exponent, (Eq.D.13b). |
| *R* | repeatability. |
| $R_j$ | nozzle Reynolds number, Eq.(D.39). |

| | |
|---|---|
| $R_p$ | amplitude of the pth harmonic, Eq. (C.118a). |
| | Reynolds number based on the length along the flat plate. |
| $R_{probe}$ | probe Reynolds number. |
| $R_\delta$ | Reynolds number based on the length along the spillway. |
| $R_j$ | Reynolds number of the water jet at the toe of the spilllway. |
| $R_y(t_1,\tau)$ | ensemble autocorrelation, Eqs.(C.18). |
| $R_y(\tau)$ | autocorrelation function. |
| $R_{y_1}(t,\tau),\ldots,R_{y_n}(t,\tau)$ | sample autocorrelations. |
| $R_{xy}(\tau)$ | cross-correlation function between random variables x(t) and y(t). |
| $\hat{R}_{xy}(\tau)$ | estimated cross-correlation function between random variables x(t) and y(t). |
| r | Pearson product - moment correlation coefficient. |
| | a counter. |
| $n$ | radius of curvature, Eqs. (IV.2) |
| | number of basic quantities in Buckingham $\pi$ theorem. |
| | pipe radius, Eq.(F.6). |
| $r_\tau$ | estimated autocorrelation coefficient. |
| $n_m$ | uncertainity, Eq. (E.4). |
| S | output (or the quantity being measured). |
| s | sample standard deviation. |
| $\delta$ | fluctuating part of the output S with respect to its average $\bar{S}$. |
| | a counter, Eq. (C.140). |
| | an exponent, Eq. (D.32). |
| | co-ordinate direction. |
| $s_x$ | standard deviation of a set of n values of the independent variable x. |

| | |
|---|---|
| $s_y$ | standard deviation of a set of n values of the dependent variable y. |
| $s_y$ | standard deviation of a set of n measurements of a quantity $y$. |
| $s_{\bar{y}}$ | standard deviation of the mean $\bar{y}$. |
| $s'_y$ | relative standard deviation of a set of n measurements of a quantity $y$. |
| $s^2$ | sample variance. |
| T | period in which the process repeats itself (wavelength), Eq. (C.4). |
| | observation time (length of the record or period of sampling). |
| | averaging time. |
| | width of data window, |
| $T_o$ | total time, Fig. C.10. |
| t | time variable. |
| | a distance, Fig. E.21. |
| | a variable. |
| $t$ | an exponent, Eq. (D.46). |
| $t_o$ | a variable, Eqs. (I.1). |
| $t_1$ | starting time. |
| $t_1, t_2, t_3, t_4$ | time variables. |
| t1, t2 | distances, Fig. E.22. |
| $t_c$ | value of the mathematical Student $t$ function, Table E.1. |
| $t_k$ | (100k) th percentile. |
| $t_{\alpha,n}$ | value of the mathematical Student $t$ function, Eq. (III.8d). |
| U | turbulent time mean velocity in the x co-ordinate direction. |
| | velocity at vena contracta, Eq.(E.18a). |
| | velocity of the undisturbed stream, Eq.(E.17). |
| | velocity at a distance y above the bed or the flat plate. |

| | |
|---|---|
| $U_o$ | uniform velocity at the nozzle, Fig. D.1. |
| $U_1$ | mean velocity, Section E.6.5.1. |
| $U_\infty$ | velocity of the approaching flow to the flat plate, Fig. F.3. |
| $U_*$ | shear velocity. |
| $U_m$ | average flow velocity. |
| $U_y$ | velocity at a distance $y$ from the pipe wall, Eq. (F.6). |
| $U^*$ | local main stream velocity component in the direction parallel to the plate. |
| $U_{m1}, U_{m2}$ | average velocities before and after the hydraulic jump, Eq.(B.14). |
| $U_{mab}$ | mean velocity in section ab, Eq.(IV.1). |
| $U_{max}$ | maximum velocity at any section or velocity scale. |
| u | turbulent fluctuating velocity in the x co-ordinate direction. |
| | a variable. |
| $u_o$ | paper speed. |
| $\vec{V}$ | instantaneous velocity vector. |
| V | turbulent time mean velocity in the y co-ordinate direction. |
| $\vec{v}$ | turbulent velocity vector. |
| v | turbulent fluctuating velocity in the y co-ordinate direction. |
| $v_1, \ldots, v_N$ | ranked array of a digitised sample record. |
| $v_1, \ldots, v_n$ | variables, Eq.(E.5). |
| W | turbulent time mean velocity in the z co-ordinate direction. |
| W(f) | data window Fourier Transform multiplier. |
| $W_1(f)$ | function of f, Eq.(C.108). |
| w | turbulent fluctuating velocity in the z co-ordinate direction. |
| | wave height, Eq.(E.31). |

| | |
|---|---|
| $w_r$ | Hanning window weighting function. |
| $w(t)$ | data-window function in time domain. |
| $w_1,\ldots w_n$ | uncertainty intervals, Eq.(E.5). |
| $w_h$ | retaining wall height. |
| $w_{h_o}$ | combined uncertainty introduced by the non-linearity of the potentiometers, resolution limitation and operational error. |
| $w_w$ | total uncertainty in wave height measurement, Eq.(E.31). |
| $w_{y_o}$ | total uncertainty from the reading by the point gauge and from the application of the least squares method associated with the water depth $y_o$ in the calibration well. |
| $w_\psi$ | uncertainty in the function $\psi$. |
| X | a variable. |
| x | longitudinal distance from the retaining wall in the upstream direction. |
| | co-ordinate direction (co-ordinate position). |
| | a variable. |
| $x_o$ | length of the potential core, Fig.D.1. |
| $x_1,\ldots,x_N$ | N values assumed by the variable x. |
| $x_1,\ldots,x_n$ | independent variables, Eqs. (III.1). |
| $\bar{x}$ | arithmetic mean of a set of n values of the independent variable x. |
| | longitudinal distance from the efflux section, Fig.D.1. |
| $x_j$ | longitudinal distance from the toe of the forced hydraulic jump in a downstream direction along the channel centre line. |
| $x_p$ | co-ordinate position, Fig. F.3. |
| $x_\delta$ | straight line length begining from an arbitrary point on the spillway crest, Fig. F.8. |
| Y | amplitude of sinusoidal function y(t), Eqs. (C.2) and (C.85). |

| | |
|---|---|
| $Y, Y_1$ | amplitudes of cosine waves, Eqs. (C.85) and (C.97). |
| $Y_o, .., Y_n$ | coefficients in Fourier series. |
| $Y$ | vertical distance above the channel bed or the flat plate.<br>axis in the direction of the height of the nozzle.<br>co-ordinate direction (co-ordinate position). |
| $y$ | distance from the pipe wall, Eq.(F.6).<br>vertical height above datum, Eq. (IV.2).<br>a quantity subject to measurement, Section E.2.1.1. |
| $\bar{Y}$ | sample mean.<br>arithmetic mean of a set of n values of the dependent variable y. |
| $\overline{y}$ | arithmetic mean of the n measurements of the variable $y$. |
| $y(t), \tilde{y}(t)$ | continuous time dependent variables. |
| $y_o(t)$ | time series of zero mean (fluctuating in water surface elevation about a zero mean), Eq.(C.59). |
| $y_1(t), y_2(t)$ | period functions with period T. |
| $y_1(t), \ldots, y_n(t)$ | sample functions. |
| $y_1(t)_1, y_2(t)_2, y_3(t)_3, y_4(t)_4$ | continuous time dependent variables, Fig.C.1. |
| $y_o$ | water depth in the calibration well, Eq.(E.26e). |
| $y_1, y_2$ | constants, Eq.(C.28). |
| $y_1, \ldots, y_N$ | discrete time series of size N. |
| $y_1, \ldots, y_n$ | dependent variables, Eq.(III.1b).<br>water levels in the calibration well. |
| $y_1, \ldots, y_n$ | measured quantities, Eq.(E.1). |
| $z$ | co-ordinate direction (co-ordinate position). |
| $\alpha$ | energy coefficient.<br>$100(1-\alpha)$ is the confidence interval. |
| $\beta$ | momentum coefficient.<br>a dimensionless coefficient, Eq. (E.22). |
| $\beta_1, \beta_2$ | momentum coefficients of flow before and after the hydraulic jump respectively, Eq. (B.14). |

| | |
|---|---|
| $\gamma$ | population kurtosis coefficient, Eq. (C.37). |
| $\hat{\gamma}$ | estimated kurtosis coefficient, Eq. (C.38). |
| $\gamma(\tau)$ | autocovariance function. |
| $\Delta d$ | depth interval in velocity measurements. |
| $\Delta h$ | difference in surface elevation, Figs.E.9 and IV.2. |
| $\Delta t$ | sampling interval (increment of time). |
| $\Delta t_1, \ldots, \Delta t_N$ | time increments, Fig.C.10. |
| $\Delta x$ | longitudinal distance between the static and the pitot orifices, Fig.E.9. |
| $\Delta X$ | digitisation interval. |
| $\delta$ | boundary layer thickness. |
| $\delta_1$ | length scale. |
| $\delta_2$ | depth of forward flow. |
| $\delta_d$ | displacement thickness. |
| $\delta_m$ | momentum thickness. |
| $\delta U$ | total deviation from the mean velocity $U_m$ Eq. (B.4). |
| $\varepsilon$ | small positive time increment, Fig.I.1. |
| $\eta$ | dimensionless co-ordinate, Eqs.(D.12b) and (F.18b). |
| | a dimensionless coefficient, Eq.(B.7b). |
| $\eta_1$ | dimensionless co-ordinate, Table D.2 and Fig. F.17. |
| $\xi$ | a variable. |
| $\theta$ | angle between the spillway face and the horizontal. |
| | phase angle. |
| | a variable. |
| $\theta(f)$ | function of frequency. |
| $\theta_o$ | initial phase angle with respect to time origin (phase angle). |

| | |
|---|---|
| $\theta_1,\ldots.\theta_n$ | phase angles. |
| $\theta_1,\ldots,\theta_n$ | phase angles. |
| $\mu$ | dynamic viscosity.<br>population mean value. |
| $\hat{\mu}$ | estimated mean value. |
| $\mu_y(t_1)$ | ensemble mean of the dependent variable y at time $t_1$, Eq. (C.17). |
| $\mu_{y_1},\ldots\ldots,\mu_{y_n}$ | sample means, Eq. (C.15). |
| $\nu$ | coefficient of kinematic viscosity.<br>number of degrees of freedom. |
| $\pi$ | constant equal to 3.1416.... . |
| $\rho$ | mass density of fluid. |
| $\hat{\rho}_{xy}(\tau)$ | estimated cross-correlation coefficient between random variables x(t) and y(t). |
| $\rho_\tau$ | population autocorrelation coefficient. |
| $\Sigma$ | summation sign. |
| $\sigma$ | population standard deviation. |
| $\sigma^2$ | population variance. |
| $\tau$ | time lag (time displacement).<br>total shear stress. |
| $\tau_o$ | boundary shear stress (or wall shear stress). |
| $\tau_t$ | turbulent shear stress. |
| $\phi$ | redirection angle. |
| $\phi_p$ | phase of pth harmonic, Eq. (C.118b). |
| $\phi(x,t)$ | a continuous function of x and t. |
| $\psi$ | root mean square value.<br>a function, Eq. (E.5). |
| $\psi^2$ | mean square value. |
| $\omega,\omega_o$ | angular frequencies. |

| | |
|---|---|
| $\omega_N$ | Nyquist angular frequency. |
| $\omega_n$ | angular frequency, Eq.(C.73a). |
| $\Omega$ | dummy variable. |
| $\mathscr{F}$ | a dimensionless variable defined in Eq.(F.38). |
| $\partial$ | partial derivative. |
| $\int$ | integral. |

SUBSCRIPTS

| | |
|---|---|
| 1 | section before the hydraulic jump.<br>section close to the channel outlet. |
| 2 | section after the hydraulic jump.<br>channel centre line section. |
| 3 | section close to the side wall. |
| c | denotes emphasis on continuity. |
| d | denotes emphasis on discrete function. |
| i | subscript in tensor notation, Eq.(D.1)<br>unless otherwise defined in text. |
| j | subscript in tensor notation, Eq.(D.1)<br>unless otherwise defined in text. |
| k | subscript in tensor notation, Eq.(D.1)<br>unless otherwise defined in text. |
| m | average over cross section unless otherwise<br>defined in text. |
| max | maximum. |
| min | minimum. |
| $\overline{(\ )}$ | mean time average of ( ). |

## MAJOR ABBREVIATIONS

| Symbol | Definition |
|---|---|
| ac.f. | autocorrelation function. |
| acv.f. | autocovariance function. |
| c.c.f. | cross correlation function. |
| d.f. | degrees of freedom. |
| d.f.d. | degrees of freedom of deviations about the regression. |
| d.f.r. | degrees of freedom attributable to the regression. |
| d.f.t. | total degrees of freedom. |
| e.d.f. | energy density function. |
| erf( ) | error function of ( ). |
| E[ ] | expected value of [ ]. |
| F.F.T. | Fast Fourier Transform. |
| F[ ] | Fourier Transform of [ ]. |
| L.D.A. | Laser Doppler Anemometer. |
| l.s.m. | least squares method. |
| m.s.d. | mean square of deviations about the regression. |
| m.s.r. | mean square attributable to the regression. |
| Prob [ ] | probability that [ ]. |
| p.d. | probability distribution. |
| p.d.f. | probability density function. |
| r.h.s. | right - hand - side. |
| r.v. | random variable. |
| r.m.s. | root mean square value. |
| sec | second. |
| s.d.[ ] | standard deviation of [ ]. |
| s.e.(a) | standard error of the regression constant. |
| s.e.(b) | standard error of the regression coefficient. |
| $s.e._p(y)$ | standard error of the predicted value for a given x. |
| s.s.d. | sum of squares of deviations about the regression. |
| s.s.r. | sum of squares attributable to the regression. |
| s.s.t. | total sum of squares. |
| Var [ ] | variance of [ ]. |

| | |
|---|---|
| $\Gamma(\nu/2)$ | Gamma function with argument $\nu/2$. |
| $\Delta$ | increment. |
| $\delta(\ )$ | Dirac delta function of ( ). |
| $\chi^2_\nu$ | a chi-squared random variable with $\nu$ degrees of freedom. |
| $\nabla(t,\Delta t)$ | Dirac comb with spacing equal to $\Delta t$. |
| $(\ )'$ | the first derivative of ( ) unless otherwise defined in text. |
| $(\ )''$ | the second derivative of ( ) unless otherwise defined in text. |
| $(\ )^{(m)}$ | the mth derivative of ( ). |
| $\lvert(\ )\rvert$ | absolute value of ( ). |
| $\{\ \}$ | an ensemble of sample functions unless otherwise defined in text. |
| $\hat{(\ )}$ | estimate of ( ). |
| $\tilde{(\ )}$ | denotes emphasis on continuity. |

# CHAPTER A

# INTRODUCTION

The phenomena associated with a fast water stream deflected by a transverse wall are of considerable practical interest and occur in a number of engineering situations. Water jets issuing from hydraulic structures such as spillways or sluice gates which are deflected over a short distance by a transverse barrier are examples of such situations. This thesis describes an experimental and analytical study of the effect on a plane turbulent water jet of finite dimensions when it is deflected by a plane smooth vertical transverse wall which is perpendicular to the initial flow direction. Since the normal impingement of water jets on smooth walls is the simplest configuration, its study should be of importance in understanding of more complicated situations.

The work which instigated the present research was undertaken at Imperial College in 1976 by Chiari when he was trying to obtain an insight into the pool-ladder stilling pond scheme. In the early experiments, only the gross characteristics of the problem were studied with very little attention being given to the detailed flow processes. A better understanding of these gross characteristics should result in a more rational and economical design procedure for this type of hydraulic phenomenon.

Plates I,II and III show a supercritical water flow issuing from an overflow spillway onto a smooth horizontal channel of the same width, with the flow being deflected by a plane smooth vertical transverse wall which is perpendicular to the flow direction. Observation of the flow indicated that as the water came down from the spillway, the free surface converged steadily until it attained a minimum depth at a section situated close to the toe of the spillway. At this section the free surface became horizontal. From this section to the retaining wall, three reasonably distinct regions of flow could be identified. In region I, the water depth remained approximately constant with the exception of a region adjacent to the outlet where a degree of lateral discharge was observed. In region II a hydraulic jump with a lateral discharge was observed. In region III the flow impinged violently on the retaining wall and became absolutely parallel to the wall, resulting in a complex wave pattern adjacent to the retaining wall. It is appropriate therefore to refer to region III as the 'impingement region'. In regions I and II, in a section parallel to the retaining wall,the water surface profile decreased considerably near the channel outlet due to the lateral discharge.

PLATE I A SUPERCRITICAL WATER FLOW DEFLECTED BY A TRANSVERSE BARRIER

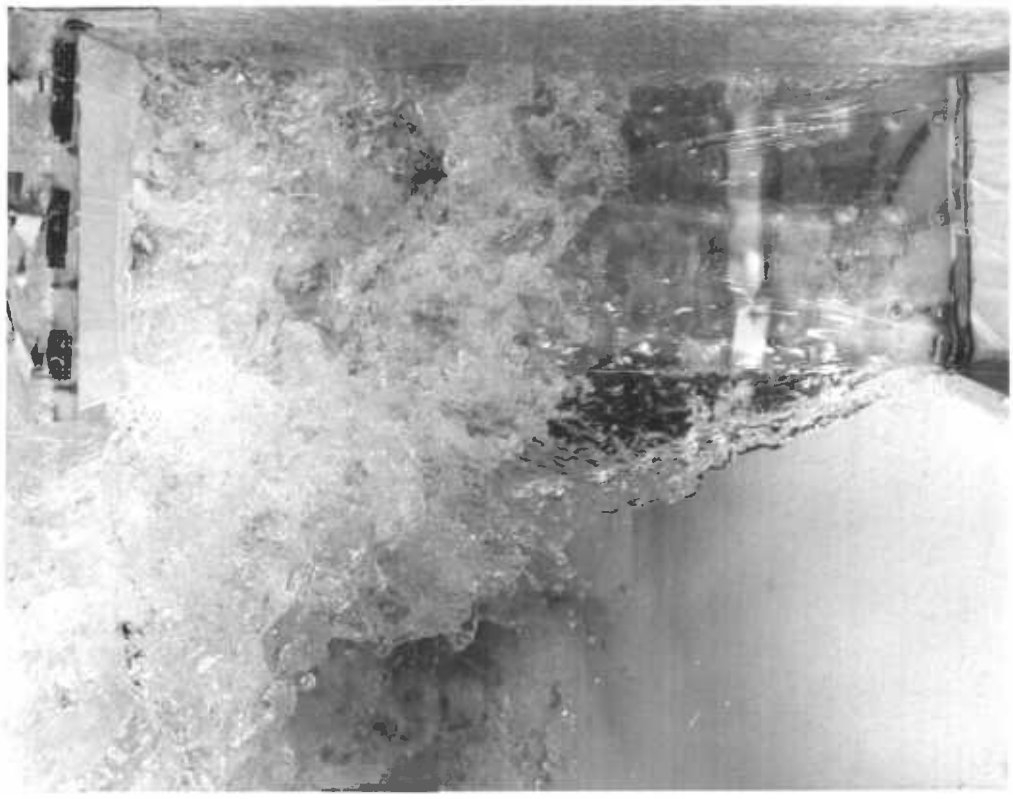

PLATE II PLAN VIEW

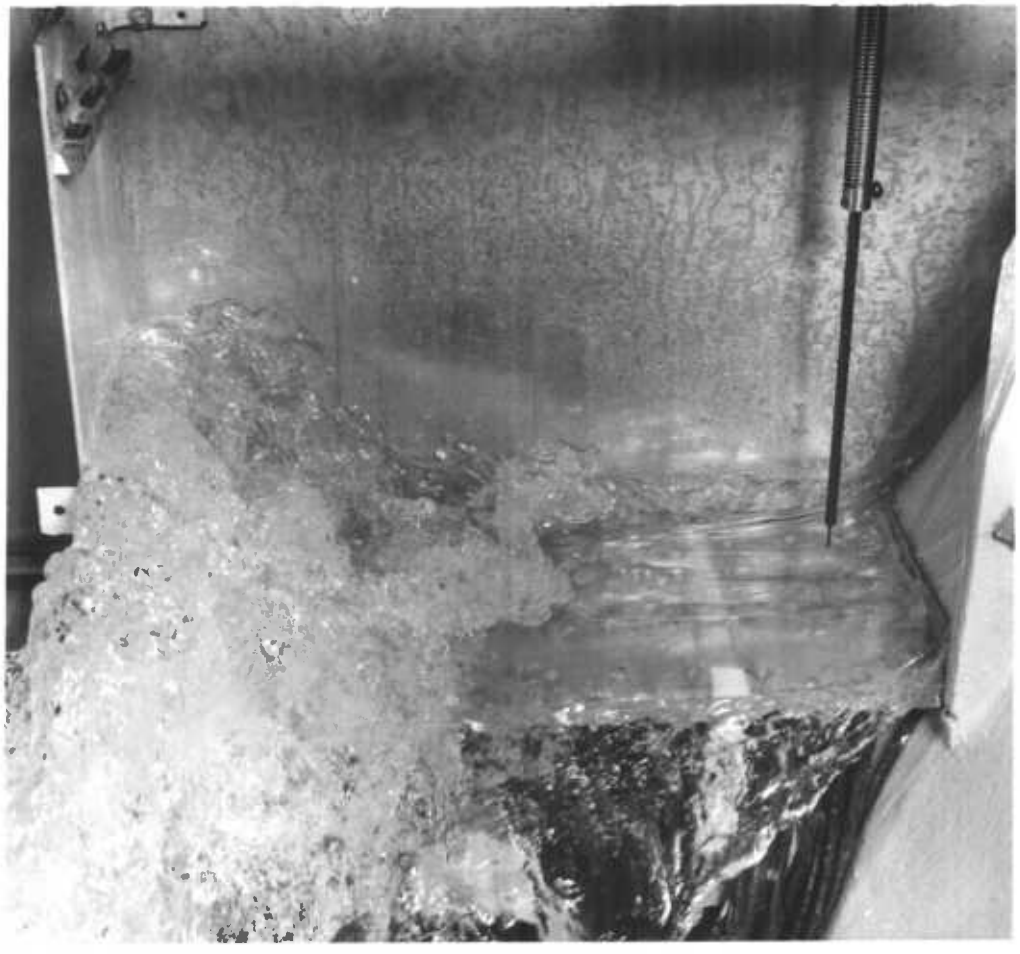

PLATE III SIDE VIEW

A FAST WATER STREAM DEFLECTED BY A TRANSVERSE WALL

The fast water stream in region I which contained a large amount of kinetic energy was complicated by the development of secondary flows and the presence of cross waves. However, there was very little redirection of the supercritical flow along the channel centre line in this region. In region II, the water surface began to rise abruptly from the toe of the hydraulic jump, which oscillated about a mean position. Since this hydraulic jump was formed due to the presence of a barrier, it is appropriate to refer to it as a 'forced' hydraulic jump. The distinctive feature of region II was the presence of a violent roller in the upper part of the flow; this roller started at the toe of the hydraulic jump and ended before it reached the retaining wall. Due to the surface breaking, a considerable amount of air was entrained in the forced hydraulic jump. The velocity of the flow in region II varied considerably in both magnitude and direction, and even underwent full reversal in the roller. The flow in the roller of the forced hydraulic jump, which is opposed to the main stream, is known as the backward flow or return flow. The behaviour of the roller, however, was found to be very complicated. The roller influenced the production of turbulent energy from the mean flow and also its dissipation. The forward flow in region II underwent a deflection from the channel centre line larger than that in region I. Finally, the forward flow of region II became separated from the bed, impinged violently on the retaining wall and became parallel to it. Due to the impingement, most of the remaining kinetic energy of the flow was converted into potential energy. The violent impingement of the flow on the retaining wall generated waves which were irregular both in height and period at the retaining wall.

Observation of the flow indicated that with the retaining wall at a fixed position with respect to the spillway, an increase in the discharge of the incoming flow from the spillway caused the wave height at the retaining wall and the jump length (the distance between the toe of the jump and the retaining wall) in any section parallel to the channel centre line to increase. It was observed that if the discharge was high enough, the toe of the hydraulic jump would reach the toe of the spillway. Furthermore, it was found that with a constant discharge of incoming flow, the wave heights at the retaining wall and the jump length were not changed appreciably by changing the position of the retaining wall with respect to the spillway.

Due to the existence of three different regions of flow with different characteristics, the presence of a free surface, the turbulent nature and non-uniform flow condition, the behaviour of the flow was not suitable for a completely theoretical analysis. In view of this, experimental methods had to be used to investigate the problem on a reduced scale model; model studies being a cheap and relatively reliable way of solving what might otherwise be intractable problems.

The main objective of studying regions I and II was to determine the velocity and pressure fields. Investigation of the velocity field, especially in region II, was of considerable importance, since it was thought that high velocity jet might travel along the bed without much retardation to considerable distances, thereby causing scour.Flow exploration in these two regions was restricted to the turbulent mean motion of the phenomenon. The waves associated with the impingement of the flow on the retaining wall were of a fluctuating nature. The difficulties caused by the waves were mainly due to their excessive height. The overtopping of water on the retaining wall could jeopardize the structure. On the other hand a very conservative wall height could increase the cost of the work. It was the object of this research to investigate the behaviour of the waves at the retaining wall through their periods and heights by obtaining their complete time history records. Due to the separation of the flow, the strong curvature of the streamlines and the existence of complex waves in the impingement region, the pressure at the wall was non-hydrostatic. A further insight into the flow characteristics in the impingement region was gained by studying the pressure distribution on the retaining wall.

# CHAPTER B

# BACKGROUND

## B.1 GENERAL

The rapid transition from supercritical flow to subcritical flow is known as a hydraulic jump and has great significance in many branches of science and technology. The hydraulic jump which is an area of considerable energy dissipation is an important field of study for civil, chemical and mechanical engineers as well as for those working in fluid mechanics. For this reason the existing literature on different types of hydraulic jump is large and continues to grow rapidly every year. In order that review of literature on different kinds of hydraulic jump would not become too large, it was felt necessary to select from this array of publications those which most closely applied to the particular area of study in question. However, before discussing any literature, some basic principles of dimensional analysis and similarity must be defined.

## B.2 DIMENSIONAL ANALYSIS AND SIMILARITY

The theory of dimensional analysis has two major fields of application, firstly the tidying up of arguments involving a large number of physical parameters, and the development of criteria governing dynamic similarity between two flow situations which are geometrically similar but of different size. A necessary condition for employing dimensional analysis is that the variables involved in the physical phenomenon should be known; the relationships between the variables only are being sought. By a dimensional analysis procedure, the phenomenon may be formulated as a relation between a set of dimensionless groups of the variables.

The basis of the theory is the 'Buckingham $\pi$ theorem', which is given here without proof. It states the 'the number of independent dimensionless groups that may be employed to describe a phenomenon known to involve, $n$, variables is equal to the number $(n-h)$, where, $h$, is usually the number of basic dimensions needed to express the variables dimensionally'. Dimensional analysis must be used cautiously in the pseudo-science of engineering fluid mechanics, where the main object is to produce formulae accurate enough for quantitative engineering design. Such formulae can be broadly classified as being (Blench, 1969):

(a) Borrowed from rigorous hydrodynamics and true for fluids and conditions idealised from reality and is sometimes quite unrealistic.

(b) Obtained by a speculative hypothesis as to the mechanism of a partially understood process, and then by applying more or less rigorous dynamics to the speculative premises. The results are only as good as the speculations made and may be misleading, sometimes containing dynamical impossibilities.

(c) Obtained by the fitting of mathematical curves to plotted data without any bias towards a particular speculative hypothesis. This approach is unlikely, except in simple cases, to deal with all factors physically relevant to even the observed situation; the experimenter or observer may even be ignorant of the existence of some factors.

## B.3 THE ENERGY AND MOMENTUM COEFFICIENTS

Ie open channels, due to the presence of a free water surface and the friction along the solid boundary, the velocities in the channel are not uniformly distributed over the channel cross-section. In fact

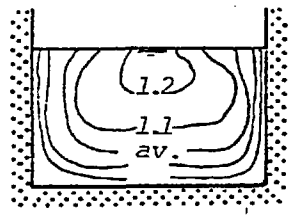


Fig. B.1 Curves of equal velocity in a channel section

viscous effects make the velocities lower near to the solid boundaries than at a distance from them. The *average flow velocity* can be calculated from the following relationship

$$U_m = \frac{Q}{A} \tag{B.1}$$

where Q is the discharge and A is the cross-sectional area of the channel and subscript m represents the average over the cross-section.

### B.3.1 Energy Coefficient

Due to the non-uniform velocity distribution (Fig. B.1), the true mean velocity head across the channel section, $(U^2)_m/2g$, where g is acceleration due to gravity, will not necessarily be equal to $U_m^2/2g$. The value of the total head of a cross-sectional area of flow (specific energy) is therefore given by

$$e = d + \alpha\frac{U_m^2}{2g} \tag{B.2}$$

where d is the water depth and $\alpha$ is the *correction coefficient* to be applied to the velocity head as calculated from the mean velocity. The coefficient $\alpha$ which is also known as the *Coriolis coefficient, energy coefficient* or *velocity distribution coefficient* can be mathematically expressed in the following form

$$\alpha = \frac{1}{QU_m^2}\int_A U^3 dA = \frac{1}{AU_m^3}\int_A U^3 dA \tag{B.3}$$

However, in this context, it should be noted that $U_m$ is not a directly measurable quantity but a derived one (Eq. B.1).

Just as in solid mechanics, any area $A = \int_A dA$ has first and second moments in x and y co-ordinates defined as $\int_A x\,dA$ and $\int_A x^2 dA$, so there is in fluid mechanics a first moment defining the mean velocity $U_m = (1/A)\int_A U dA$, with higher moments $\int_A U^2 dA$ and $\int_A U^3 dA$ depending on the velocity distribution across the section A. The velocity at any point is $U = U_m + \delta U$ where $\delta U$ is the total deviation from the mean velocity $U_m$. Equation (B.3) expands to

$$AU_m^3\alpha = \int_A U_m^3 dA + 3\int_A U_m^2 \delta U dA + 3\int_A U_m (\delta U)^2 dA + \int_A (\delta U)^3 dA \qquad (B.4)$$

By definition of a mean value, $\int_A \delta U dA = 0$, leading to

$$AU_m^3\alpha = U_m^3 \int_A dA + 3U_m \int_A (\delta U)^2 dA + \int_A (\delta U)^3 dA \qquad (B.5)$$

or

$$\alpha = 1 + \frac{3}{AU_m^2}\int_A (\delta U)^2 dA + \frac{1}{AU_m^3}\int_A (\delta U)^3 dA \qquad (B.6)$$

If $\delta U$ is small, $\int_A (\delta U)^3 dA$ is negligible compared to $\int_A (\delta U)^2 dA$ and Eq. (B.6) may be written as

$$\alpha \simeq 1 + \frac{3}{AU_m^2}\int_A (\delta U)^2 dA = 1 + 3\eta \qquad (a)$$

where

$$\eta = \frac{1}{AU_m^2}\int_A (\delta U)^2 dA \qquad (b)$$

(B.7)

If the velocity distribution across section A is uniform, $\delta U = 0$, and $\alpha = 1$. If $\delta U \neq 0$, then $\eta > 0$ and from Eq. (B.7a), $\alpha > 1$. The velocity distribution coefficient, $\alpha$, always exceeds unity. It should be remembered that $e$ is the *average energy line level* for the whole flow. The *kinetic energy flux* past a channel section per unit time is expressed as

$$e_k = \alpha\rho g Q U_m^2/2g \qquad (B.8)$$

where $\rho g$ is the specific weight of fluid. The total energy can be written as

$$e_t = \rho g Q\,(\alpha U_m^2/2g + d) \qquad (B.9)$$

An examination of current hydraulics text books where open channel flow is detailed shows that there are large variations in the suggested values for $\alpha$ and $\beta$. For straight prismatic channels with steady turbulent flow $\alpha$- values approximately range between 1.03 and 1.10 and seldom exceed 1.15, and it is doubtful whether the precision attainable with channel calculations warrants their inclusion, particularly as the experimental data on values of $\alpha$ are rather sparse and not always consistent (Henderson, 1966). Low values of $\alpha$ apply to wide deep streams and high values to small sections (Selin, 1969). For complex cross-sections, or close to constrictions such as bridge piers and weirs, the values of $\alpha$ may be much higher. In some cases the velocity head makes up only a minor part of the total energy head and $\alpha = 1$ can then be used for practical purposes.

### B.3.2 Momentum Coefficient (Boussinesq Coefficient)

The *momentum coefficient* $\beta$ represents the effect of the non-uniform velocity distribution at a cross-section on the momentum flux of the flow. The rate of transfer of momentum through an element of area dA is equal to $\rho U dQ$; hence by an argument similar to that preceding it can be deduced that the momentum correction coefficient is

$$\beta = \frac{\int_A U_m^2 dA}{U_m^2 A} = \frac{\int_A U_m^2 dA}{U_m Q} \qquad (B.10)$$

The mean value of the pressure force plus the momentum of a cross-sectional area (Fig. B.1) of flow per unit width is therefore given by

$$m = \tfrac{1}{2}\rho g d^2 + \rho \beta Q U_m \qquad (B.11)$$

The coefficients $\alpha$ and $\beta$ are never less than 1; they are both equal to unity when the velocity is uniform across the section, and the further the velocity departs from uniform the larger the coefficients become. The form of Eqs. (B.3) and (B.10) makes it clear that $\alpha$ is more sensitive to velocity variation than $\beta$, so that for a given channel section, $\alpha > \beta$.

## B.4 FROUDE NUMBER

In open channel flow the ratio of a typical velocity head to a typical linear dimension of the flow is a measure of the extent to which gravitational action influences the flow phenomenon - the larger its magnitude then the smaller the relative effect of gravity, and vice versa. A *flow parameter* of this type often used is called the 'Froude number', and the simplest and the most pertinent of its several alternative forms is the following (Harrison, 1965 and White, Perkins, Harrison and Ackers, 1978)

$$Fr = \frac{U_m}{\sqrt{gd/\alpha}} \tag{B.12}$$

Eq. (B.12) could be written as

$$Fr = \sqrt{2(\alpha U_m^2/2g)/d} \tag{B.13}$$

indicating that the Froude number is the square root of twice the ratio of velocity head to depth.

## B.5 HYDRAULIC JUMPS

The hydraulic jump is one of the most interesting phenomena occurring in the field of hydraulic engineering. It has been a matter of interest and research for almost five centuries since it was first described by Leonardo da Vinci (Rouse and Ince, 1957). In general a hydraulic jump constitutes the rapid transition from supercritical to subcritical flow.

In civil engineering practice, it is common to form a jump downstream of a hydraulic structure, such as a spillway or sluice gate where velocities are high and it is necessary to dissipate some of the kinetic energy of the flow. The turbulent characteristics of the jump can be used either to mix chemicals or to aerate the water used in city water supplies or recovered in sewage plant treatment. The hydraulic jump is not only an effective means of reducing the mean flow energy, but also a very efficient mechanism for restoring uniform conditions to the flow. The characteristics of the hydraulic jump (*conjugate depth ratio* and *energy dissipation*), its geometry (*length* and *shape* of the surface roller), and location have been the subject of much experimental work.

### B.5.1 Classical Hydraulic Jump

The hydraulic jump formed in a smooth, wide, and horizontal rectangular channel is known as the *classical jump*. In the classical jump the water surface begins to rise quite abruptly at the beginning, or *toe*, of the jump, which oscillates about a mean position, and continues to rise up until it reaches a section beyond which it is essentially level. This section denotes the end of the jump. Chow (1959) gives a very good summary of the results of some of the most important investigations. Rouse, Siao and Nagaratnam (1959) investigated the turbulence characteristics of the hydraulic jump in an air-flow model using a hot-wire anemometer. They found that, except for Froude numbers well below 2, the hydraulic jump presents a 'breaking front' (the *roller*) which is responsible for air entrainment in the jump and formation of turbulence and hence the dissipation of energy. At the juncture between the oncoming stream and the return flow of the roller of the jump there is a pronounced velocity gradient, and the resulting

shear gives rise to a rapid generation of turbulence (Flores, 1954 and Rouse et al., 1959). For Froude numbers below 2 an 'undular hydraulic jump' occurs,characterised by a succession of water surface undulations (a train of unbroken standing waves) involving a negligible loss of energy in the jump (Chow, 1959 and Rouse et al., 1959).

The classical jump, in spite of its complex appearance which can be accompanied by violent turbulence, eddying, surface undulations, and air entrainment with consequential head loss, may be successfully analysed by application of the impulse-momentum principle. The analysis of a two-dimensional classical hydraulic jump in a horizontal smooth channel is usually achieved by making the assumption that all boundary friction losses are negligible and that the turbulent velocity fluctuations at the beginning and end are negligible. Also it is assumed that the pressure distributions immediately before and after the jump are hydrostatic. With these assumptions and by the application of the one-dimensional momentum principle in conjunction with the continuity equation, it may be written that

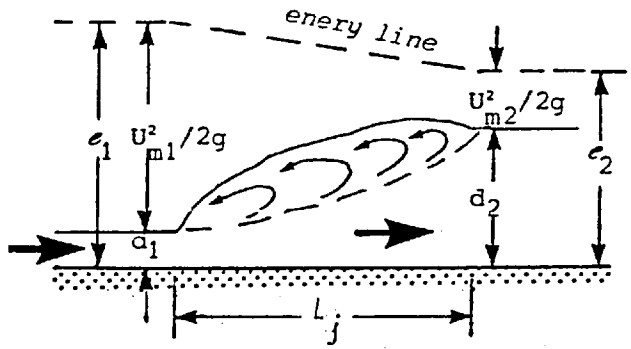


Fig. B.2 Definition sketch of hydraulic jump

$$\rho g d_1^2/2 - \rho g d_2^2/2 = \rho q(\beta_2 U_{m2} - \beta_1 U_{m1}) \qquad (B.14)$$

where

$d_1$ = depth of flow before the jump
$d_2$ = depth of flow after the jump
$\rho$ = mass density
$g$ = acceleration due to gravity
$q$ = discharge per unit width
$\beta_1$ = momentum coefficient of flow before the jump
$\beta_2$ = momentum coefficient of flow after the jump
$U_{m1}$ = velocity of flow before the jump
$U_{m2}$ = velocity of flow after the jump

the subscripts 1 and 2 refer to the sections before and after the jump

respectively (Fig. B.2). However, if the velocity distribution at the toe of the jump is assumed to be similar to that at the end, a single value of $\beta$ can be used for both sections. In this case, if the Froude number of the flow preceding the jump (supercritical Froude number) is defined as

$$Fr_1 = U_{m1}/\sqrt{gd_1} \qquad (B.15)$$

Eq. (B.14) can be written in the following form

$$d_2/d_1 = \tfrac{1}{2}[(1 + 8\beta Fr_1^2)^{\frac{1}{2}} - 1] \qquad (B.16)$$

The two depths $d_1$ and $d_2$ are known as *conjugate depths*. When the velocity distribution is assumed to be uniform i.e. $\beta = 1$, Eq. (B.16) reduces to the form given in the standard hydraulic text books and is known as the *Belanger momentum equation*.

Since the hydraulic jump is a steady phenomenon (of course, in the mean), the flow outside the roller must supply energy to the roller at precisely the same rate at which the energy in the roller is decaying. It is assumed that the roller accounts for all the loss of energy in the jump, and this is approximately the case (Rouse et al., 1959), the rate at which energy is decaying in the roller must be precisely the difference in energy fluxes of the upstream and downstream flows. Several definitions of the *jump length* have been proposed; two of the most commonly used are, the distance from the toe of the jump to the end of the roller, and the distance from the toe of the jump to the point where the tail-water depth is reached.

### B.5.1.1 Position Sensitivity of a Classical Hydraulic Jump

The location of the hydraulic jump is known to be sensitive to changes in tailwater elevation. This fact diminishes from the value of the jump as an energy dissipator. Early significant research into this problem was undertaken by Bradley and Peterka (1957) who investigated the effect of a tailwater change on the position of the toe in the stilling basins designed by using the standard US Bureau of Reclamation specifications. Wilson (1965) defined a property of the flow through a hydraulic jump and called it the 'position sensitivity'. It was defined as the rate of displacement of the toe of the jump along the channel with respect to changes in tailwater elevation.

On the basis of this definition further work has been carried out by Wilson (1967) and subsequently by Wilson and Turner (1972) to show how the sensitivity is dependent upon the Froude number, boundary roughness and the channel bed slope. It has been established that the jump becomes less sensitive to tailwater change if the Froude number is increased and if the channel bed slope is increased. For obvious practical reasons, a low value of jump sensitivity is desirable. In order to achieve this state, the Froude number should be as large as is possible.

### B.5.1.2 Energy Loss in a Classical Hydraulic Jump

The loss of energy in a jump is equal to the difference in the specific energies before and after the jump. If the energy coefficient, $\alpha$, and the momentum coefficient, $\beta$, are assumed to be unity, the theoretical loss in the hydraulic jump, $e_L$, given by (Fig. B.2)

$$\frac{e_L}{e_1} = \frac{1}{8}\,\frac{[(1+8Fr_1^2)^{\frac{1}{2}}-3]^3}{(2+Fr_1^2)[(1+8Fr_1^2)^{\frac{1}{2}}-1]} \quad \text{(a)}$$

$$e_L = \frac{(d_2-d_1)^3}{4d_1d_2} \quad \text{(b)} \qquad \text{(B.17)}$$

in which $e_1$ is the specific energy of the flow before the jump. Equation (B.17a), which is the ratio of the energy dissipated in the jump to the total energy at the beginning of the jump, is known as the 'efficiency' of the hydraulic jump. The depth ratio $d_2/d_1$, is considered to be a measure of the 'strength' of the jump (Henderson, 1966); by Eq. (B.17a), $Fr_1^2$ is also a measure of this property. The cubic term in Eq. (B.17b) shows that the energy loss increases very sharply as the strength of the jump increases. From Eq. (B.17a) it can be found that for a supercritical number $Fr_1$ of 20 the energy loss is $0.86\,e_1$.

The velocity distribution downstream of a hydraulic jump is generally quite non-uniform and the high velocity filaments are concentrated near the bed of the channel. As such, the energy and the momentum coefficients are far from unity and hence the actual energy loss is smaller than the theoretical energy loss $e_L$ expressed by Eq. (B.17b) (Hartung and Csallner, 1967). Garg and Sharma (1971) have shown that the energy loss for a jump having Fr less than 4 was significantly smaller than the theoretical value obtained from Eq. (B.17b). They found that the percentage deviation increased with a decrease in the Froude number.

### B.5.1.3 Classification of Classical Hydraulic Jumps

For a supercritical stream discharging from a slot, if a 'normal hydraulic jump' (also known as the *free hydraulic jump*) is to be formed at the efflux section where the depth is $d_1$ and the Froude number is $Fr_1$, (the energy coefficient $\alpha$ and the momentum coefficient $\beta$ are assumed to be unity at the efflux section), the tailwater depth $d_t$ should be equal to the subcritical sequent depth $d_2$ given by Eq. (B.16). If $d_t$ is less than $d_2$, the jump is swept downstream and is known as a 'repelled jump'. If, however, $d_t$ is greater than $d_2$, the jump becomes submerged or drowned. This is known as a 'submerged hydraulic jump', or *drowned jump* or simply the *submerged jump*.

### B.5.2 Forced Hydraulic Jumps

The control of a hydraulic jump so that supercritical flow does not occur outside the limits of a stilling basin and thereby scour the natural channel floor is extremely important. Effective control of a hydraulic jump may be achieved by a *submerged cross-jet* (Kao, 1971), a gradual (Arbhabhirama and Abella, 1971) or an abrupt expansion in the channel cross-section (Rajaratnam and Subramanya, 1968).

An efficient method of controlling the formation of a jump is to use either two-dimensional baffles known as 'sills' (baffle walls)

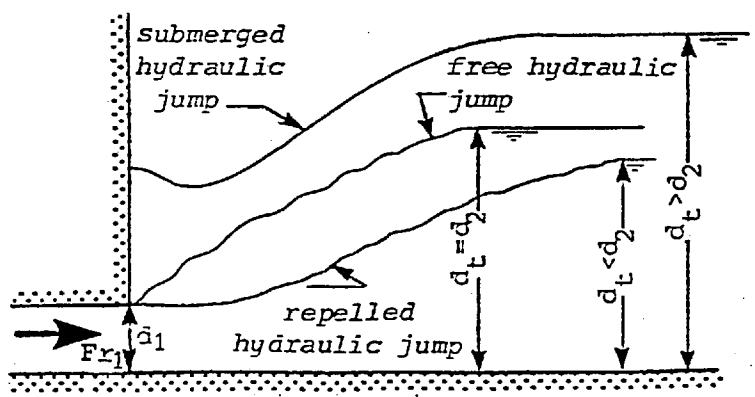


Fig. B.3 Free, repelled and submerged jumps

or three-dimensional baffles (baffle blocks, baffle piers , also known as friction blocks) on the apron or simply by depressing or abrupt rising of the apron itself (with or without a subcritical tailwater). Such a jump which is forcibly formed is defined as the *forced hydraulic jump*. The forced hydraulic jump, which is a basic design element of the well-known hydraulic jump-type stilling basins has characteristics quite different from those of a classical free hydraulic jump.

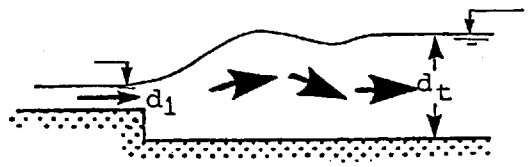


(a) *Jump formation at abrupt drop*

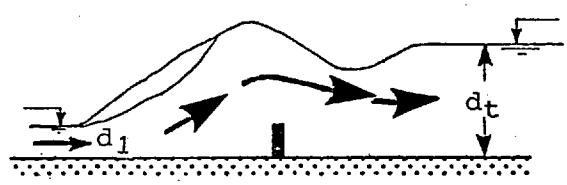


(b) *Jump formation at baffle wall*

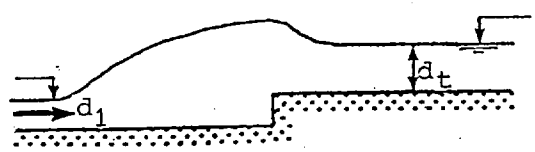


(c) *Jump formation at an abrupt rise*

Fig. B.4

The control of hydraulic jump by sills is useful if the downstream depth is smaller than the sequent depth for a normal jump. If the downstream depth is larger than the sequent depth for a normal jump, a drop in the channel floor must be used in order to ensure that a jump occurs. It is generally known that an abrupt drop in the bed of a rectangular channel stabilizes a hydraulic jump in the vicinity of the drop for a wide range of the tailwater depth (Rajaratnam and Ortiz, 1977).

A large amount of experimental information exists on forced hydraulic jumps, but the first attempt to study them appears to have been made by Forster and Skrinde (1950). They studied the forced jump created by a sharp-crested baffle wall and also that created by an abrupt rise in the floor of the channel. Interesting experiments (Weaver, 1950) have shown that the force exerted on a baffle wall in the jump decreases as the wall is moved away from the toe, reaching a minimal value when it is near the end of the roller; it then increases to assume a constant value for any further movement of the baffle. This study was followed by those of Harleman (1955) and Bradley and Peterka (1957). Rand (1965) who introduced an interesting method of analysis with a view to generalizing the stilling basin design. Rouse, Bhoota and Hsu (1951) and later Moore and Morgan (1959) studied the formation of a jump at an abrupt drop. Careful studies were also made by McCorquodal and Regts (1968). The next attempts were made by Rajaratnam (1964) and subsequently by Rajaratnam and Murahari (1971) who expressed the force exerted on the baffle piers or blocks by application of the well-known drag equation. By introducing this drag equation into the momentum equation, they established a general method of analysis for a number of cases. Supercritical flow over a square section sill without any tailwater was investigated experimentally by Karki (1976) and very recently Tyagi, Prande and Mittal (1978) reported interesting results from experiments on baffle walls in a hydraulic jump.

### B.5.3 Submerged Hydraulic Jump

If the tail-water depth is greater than the subcritical sequent depth $d_2$ given by the Eq. (B.16), then the tailwater advances over the jump, and a submerged jump is formed. Submerged jumps occur most commonly below barrages, weirs, canal head sluices and, in some cases when the tail-water depths are very large, below spillways and river outlets. It has not been conclusively established whether it is more desirable to have the submerged jump as an energy dissipation. It is generally believed that as the submergence increases the high velocity stream or jet may not mix as intensively as in the case of the free hydraulic jump and, as such, the energy dissipation might be comparatively less (Rajaratnam and Rao,

1963). Furthermore, it is feared that the high velocity jet may travel along the bed, without much retardation over considerable distances, thereby causing scour (Rajaratnam, 1965). Therefore, the submerged jump should not ordinarily be preferred to the free jump for energy dissipation purposes. Liu (1949) and Henry (1950) studied extensively the backward flow in the case of a submerged hydraulic jump. Submerged jumps below spillways were studied extensively by Stepanov (1958).

### B.5.4 Spatial Hydraulic Jump

A hydraulic jump occurs under spatial conditions when a supercritical stream, confined by parallel boundaries, encounters a wider and deeper tail-water level. Examples of spatial jumps occur when the water flow is only part of the weir crest or is only through one of the many adjoining gate openings. At the outlet of a culvert or bottom outlet of a dam leading to wider water, the characteristic side rollers (Fig. B.5)

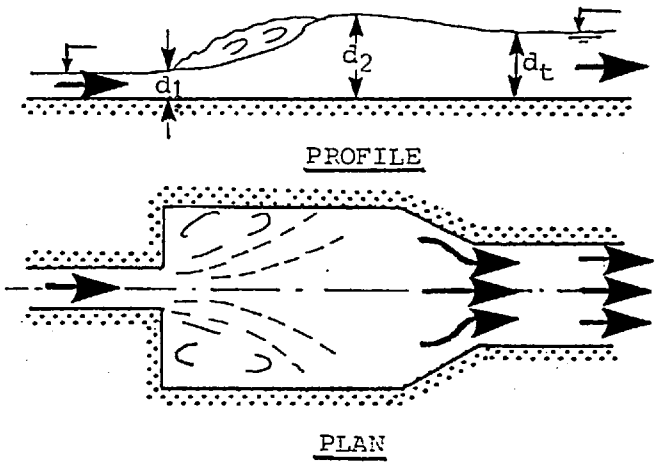


Fig. B.5 Hydraulic jump in an expansion

are visible and require a three-dimensional consideration. Also when the given tail-water depth is so small that a classical hydraulic jump, even aided by appartenances, is no longer able to form, then a good way of guaranteeing the necessary energy dissipation is by means of a spatial hydraulic jump. Such jumps, which are strongly influenced by the formation of side eddies, were studied by Unny (1961) and Herbrand (1973). Both of these researchers found that a jump in the region of a lateral expansion requires a shallower stilling basin that the classical hydraulic jump with the same inflow conditions.

# CHAPTER C

# THEORETICAL ANALYSIS OF RANDOM WAVES

## C.1 GENERAL

Spectral analysis is basically a very useful and convenient tool which aids the design of structures which are subjected to time dependent stochastic loads such as those exerted by wind-generated water surface waves, or random waves existing near a retaining wall which has been discussed earlier. It is very important to be able to predict accurately wave conditions in order to achieve a successful retaining wall design.

From the work done before 1939 by scientists such as Munk and Sverdrup (1947), the well-known *significant wave method* was developed. This method is still used by many practical engineers at the moment and consists of describing a complex wave pattern using simple terms such as *significant wave height* and *wave period*. However this procedure was soon found to be unsatisfactory. The description of complex wave conditions by two parameters and the extrapolation of simplified wave model test results to field situations was gradually disfavoured and the need for new and more sophisticated approaches was felt.

By the early 1960's, a movement to look at waves in more detail was underway. Studies such as those by Blackman and Tuckey (1958), Funke (1960), Kinsman (1965) and Wiegel (1964) established new techniques to deal with complex waves of random nature by looking at the structure of the waves e.g. wave energy spectrum etc.

The variation in water surface elevation at three different positions along a retaining wall was recorded simultaneously. The time series records were analysed using the new techniques of *Fast Fourier Transform* and *smoothing* rather than the costly traditional methods such as the one based on autocovariance method. Appropriate recommendations and guides are given for duration of wave sampling, wave sampling rate and digitisation procedure of the wave record. The relationships as they are presented in this chapter and in the implemented computer programme are given a general form and can be used not only for waves adjacent to the retaining wall in this research but also for analysis of any similar random data.

F.F.T. permits the calculation of the Fourier Transform of a long series of data in a reasonably short computing time. In addition to a review of Fourier Transforms, a number of detailed points arising out of the application of F.F.T. are discussed in this chapter. However, before deriving the theory, some basic properties of the data must be considered.

## C.2 BASIC DESCRIPTIONS OF PHYSICAL DATA

Any observed data representing a physical phenomenon can be broadly classified as being either *deterministic* or *nondeterministic*. Deterministic data is that data that can be described by an explicit mathematical relationship. There are many physical phenomena in practice which generate data that can be represented reasonably accurately by explicit mathematical relationships. For example, the motion of a satellite which is in orbit about the Earth, the temperature of water as heat is applied, the motion of a rigid body which is suspended from a fixed foundation by a linear spring, are all basically deterministic. However, there are many other physical phenomena which produce data that is not deterministic. For example, the height of waves in a confused sea represents data which cannot be described by an explicit mathematical relationship. There is no way of predicting an exact value at some future instant of time. This data is *random (stochastic)* in character and must be described in terms of probability statements and statistical averages rather than by explicit equations.

The classification of physical data as being either deterministic or random is debatable in many cases. For example, it may be argued that there is no physical data in actual practice that can be truly deterministic since there is always a possibility that some unforeseen event in the future might influence the phenomenon producing data in a manner which was not originally considered. Conversely, it may be argued that there is no physical data encountered in practice that is truly random since exact mathematical descriptions may be possible if there was sufficient knowledge of the basic mechanisms of the phenomenon producing the data. In practical terms, the decision as to whether or not physical data is deterministic or random is usually based upon the ability to reproduce the data by controlled experiments. If an experiment producing specific data of interest can be repeated many times and with identical results (within the limits of experimental error), then the data can generally be considered deterministic. If an experiment cannot be designed which will produce identical results when the experiment is repeated, then the data must usually be considered random in nature.

It is easy to see that the deterministic process may be considered an offshoot of stochastic processes. This can be explained most easily by a diagram, Fig. C.1. All four processes may be considered stochastic, but the degree of randomness in $y_1(t_1)$ far outweighs the deterministic element of the process, whereas in $y_4(t_4)$ the degree of randomness (random element) of the process is zero, $y_4(t_4)$ is therefore deterministic.

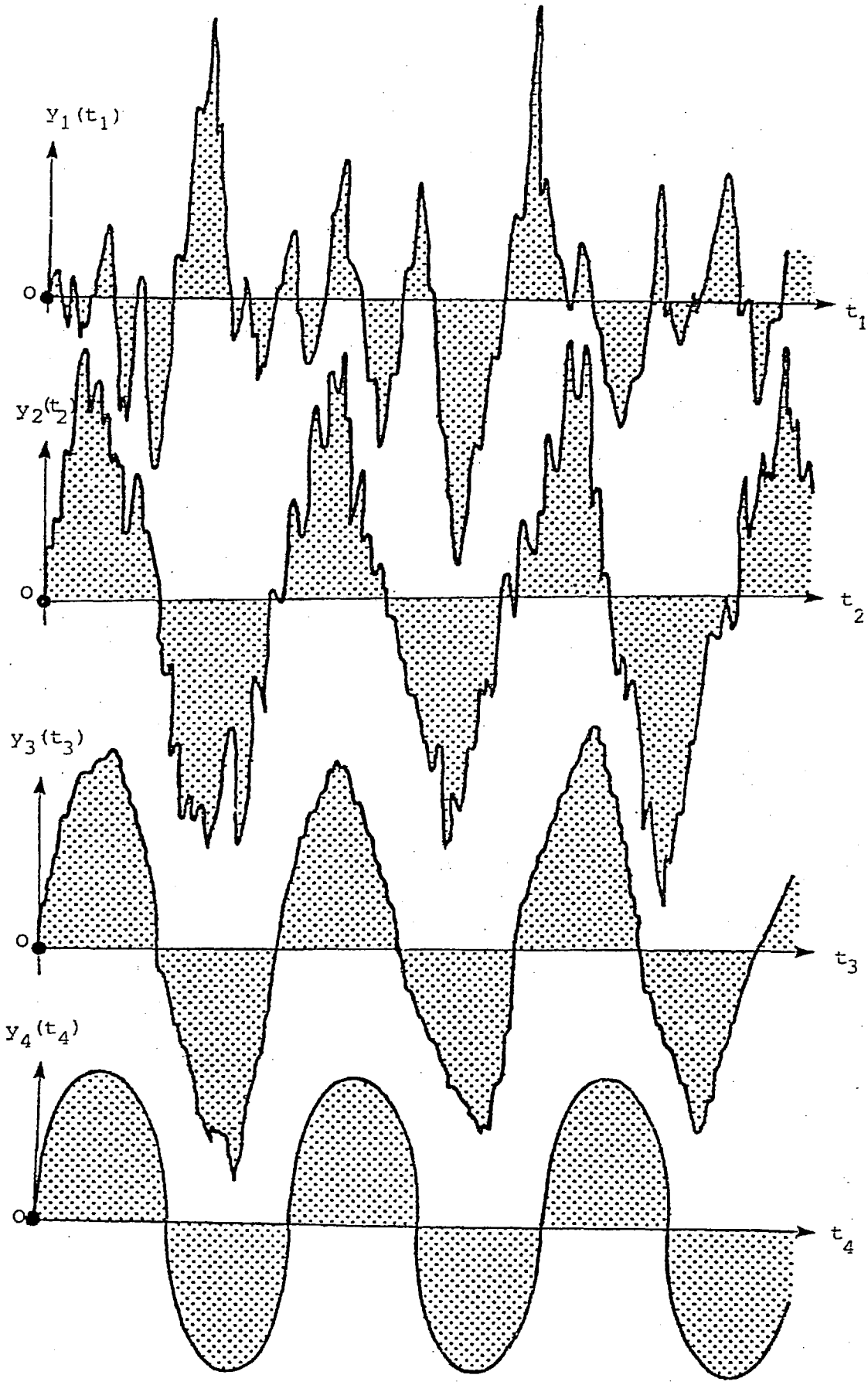


Fig.C.1 Stochastic processes*

* The above illustration could be assumed as 4 simultaneous time history records taken from a process

A great deal of argument has taken place about the nomenclature in stochastic processes. In this thesis the terms *stochastic, random* and *probabilistic* will mean the same (mathematically correct). Therefore a stochastic (random or probabilistic) process will be considered to be a process which has both deterministic and random (stochastic or probabilistic) elements. The two limiting cases, will be called *completely random* and *deterministic*.

### C.2.1 Classifications of Deterministic Data

Data representing deterministic processes can be categorized as being either *periodic* or *non-periodic*. Periodic means that there is a number T, called the *period* of the function such that

$$y(t) = y(t + T) \tag{C.1}$$

for all t. The function between t and (t+T) can be of any shape. If two functions $y_1(t)$ and $y_2(t)$, both have a period T, then the function $ay_1(t) + by_2(t)$ (a and b are constants) is also periodic with T. Periodic data can be further categorized as being either *sinusoidal* or *non-sinusoidal (complex periodic)*. Non-periodic data can be further categorized as being either 'almost-periodic' or *transient*. These various classifications for deterministic data are schematically illustrated in Fig. C.2. Of course, any combination of these forms may also occur. For the purposes of this review, each of these types of deterministic data along with physical examples will be briefly discussed.

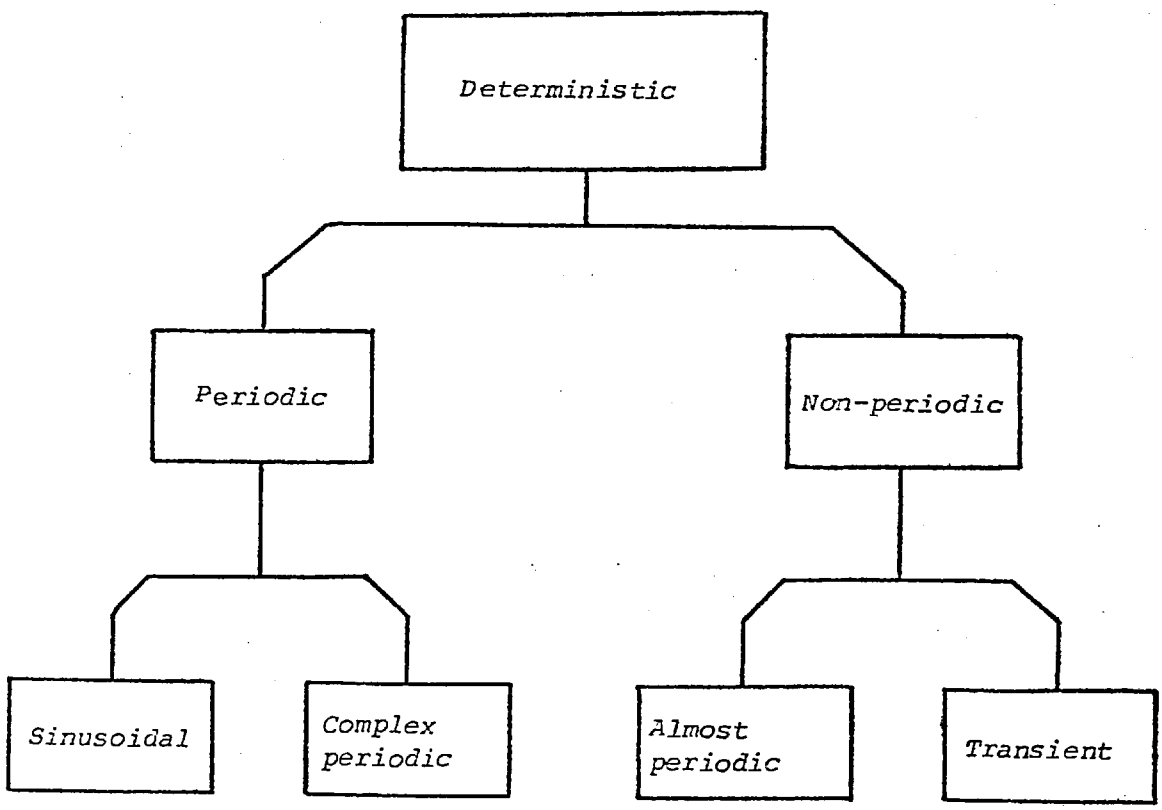


Fig. C.2 Classifications for deterministic data

### C.2.1.1 Sinusoidal Periodic Data

Sinusoidal data is that type of periodic data which can be defined mathematically by a time-varying function of the form

$$y(t) = Y\sin(\omega_o t + \theta_o) \qquad (C.2)$$

where

$y(t)$ = instantaneous value of the dependent variable at time t

$Y$ = amplitude

$\omega_o$ = *angular frequency*

$t$ = independent variable

$\theta_o$ = initial phase angle with respect to time origin.

The sinusoidal time history described by Eq. (C.2) is usually referred to as a 'sine wave'. Equation (C.2) with a suitable choice of time origin may be rewritten as

$$y(t) = Y\sin(\omega_o t) \qquad (C.3)$$

Equation (C.3) can be described by a time history plot or by an amplitude-frequency plot as illustrated in Fig. C.3.

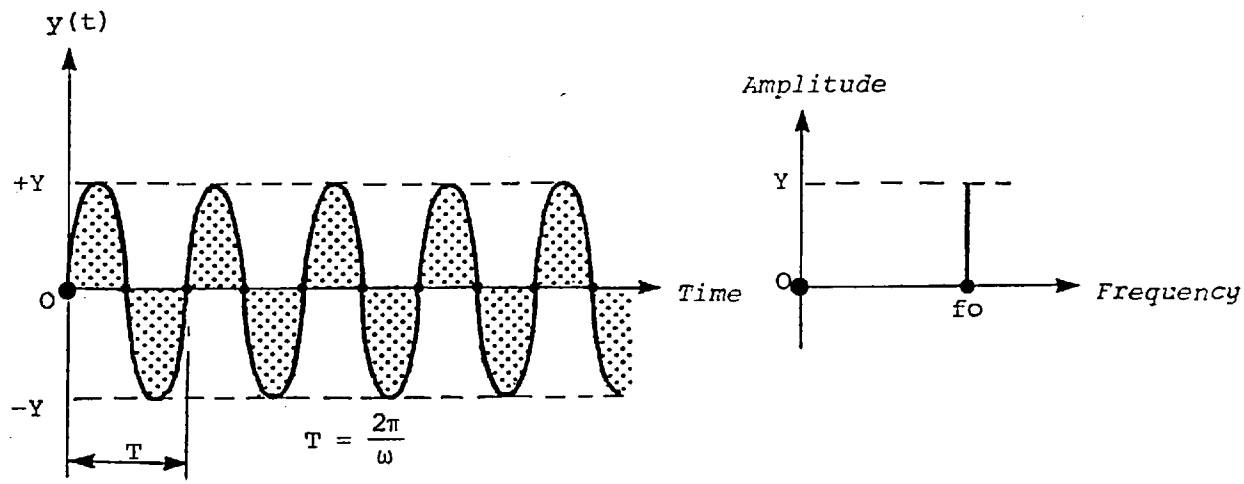


Fig. C.3 Time history and amplitude-frequency diagram for a sinusoidal data

The time interval required for one complete fluctuation in a cycle of sinusoidal data is called the period T or *wavelength*. The frequency $f_o$, defined as $f_o = \omega_o/2\pi$ and period T are related by $T = 1/f_o$, since

$$\left.\begin{aligned} y(t) &= Y\sin[2\pi f_o(t+T)] = Y\sin[2\pi f_o(t+\tfrac{1}{f_o})] \\ y(t) &= Y\sin(2\pi f_o t) \end{aligned}\right\} (C.4)$$

Purely sinusoidal motion is very difficult to find in nature. Examples that are close to sinusoidal motion are a weigth vibrating on a spring and a wave generator driven by an eccentric crank.

### C.2.1.2 Complex Periodic Data

Complex data is that type of periodic data which can be defined mathematically by a time-varying function whose waveform repeats itself at regular intervals such that

$$y(t) = y(t \pm nT) \qquad n = 1,2,3, \ldots \qquad \left.\right\} \text{(C.5)}$$

where T is the period in which the pattern repeats itself. The number of cycles per unit time is called the *fundamental frequency* $f_1$; a special case for complex periodic data is clearly sinusoidal data where $f_1 = f_o$.

The mathematical expression describing complex periodic phenomena is

$$y(t) = Y_o + Y_1 \sin(2\pi f_1 t + \theta_1) + Y_2 \sin(4\pi f_1 t + \theta_2) + \ldots \qquad \text{(C.6)}$$

or

$$y(t) = Y_o + \sum_{n=1}^{\infty} Y_n \sin(2\pi n f_1 t + \theta_n) \qquad \text{(C.7)}$$

Except in a few cases, complex periodic data may be expanded into a *Fourier series* according to the following formula

$$y(t) = \frac{a_o}{2} + \sum_{n=1}^{\infty} [a_n \cos(2\pi n f_1 t) + b_n \sin(2\pi n f_1 t)] \qquad \text{(C.8)}$$

where $f_1 = \frac{1}{T}$

$$a_n = \frac{2}{T} \int_o^T y(t) \cos(2\pi n f_1 t)\, dt \qquad n = 0,1,2, \ldots \qquad \left.\right\} \text{(C.9)}$$

$$b_n = \frac{2}{T} \int_o^T y(t) \sin(2\pi n f_1 t)\, dt \qquad n = 1,2,3, \ldots \qquad \left.\right\} \text{(C.10)}$$

From Eq. (C.7) it may be seen that

$$Y_o = \frac{a_o}{2} \qquad Y_n = (a_n^2 + b_n^2)^{\frac{1}{2}} \qquad \theta_n = \tan^{-1} \frac{b_n}{a_n} \qquad \text{(C.11)}$$

In words, Eq. (C.7) states that complex periodic data consists of a static component, $Y_o$, and an infinite number of sinusoidal components, called *harmonics*, which have amplitudes $Y_n$ and phases $\theta_n$. The frequencies of the harmonic components are all integral multiples of $f_1$.

When analyzing periodic data in practice, the phase angles $\theta_n$ are often ignored. The spectrum is called 'discrete' since the amplitudes are present only at discrete corresponding values of frequency.

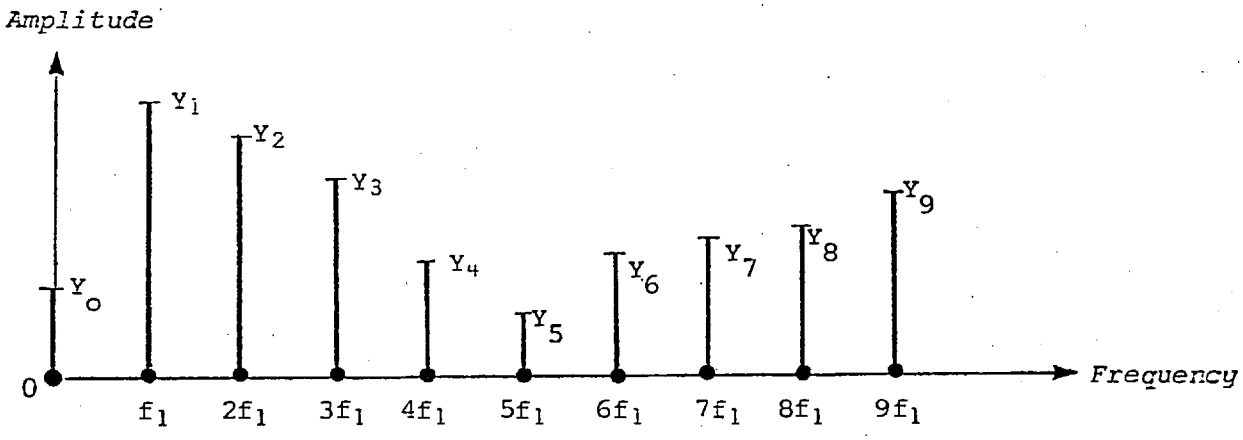


Fig. C.4 Amplitude-frequency diagram for a complex periodic data

Physical phenomena which produce complex periodic data are far more common than those which produce simple sinusoidal data since few phenomena in nature are purely sinusoidal with no harmonics. Thus any data that is often considered sinusoidal is complex periodic in that higher harmonics are present (Fig. C.1). A.C. current, for instance, often considered sinusoidal, contains higher harmonics.

### C.2.1.3 Almost-Periodic Data

In the previous section, it was noted that periodic data can generally be reduced to a series of sine waves with commensurately related frequencies. Conversely, the data formed by summing two or more commensurately related sine waves will be periodic. However, the data formed by summing two or more since waves with arbitrary frequencies will generally not be periodic.

Almost periodic data differ from complex periodic data in that the frequencies of the various components of the data are not integral multiples of each other. This means that the period in which the record repeats itself is infinite.

Based upon these discussions, almost-periodic data is that type of non-periodic data which can be defined mathematically by a time-varying function of the form

$$y(t) = \sum_{n=1}^{\infty} Y_n \sin(2\pi f_n t + \theta_n) \qquad (C.12)$$

where $f_n/f_m \neq$ rational number in all cases.

An important property of almost-periodic data is the following, if the phase angles $\theta_n$ are ignored, Eq. (C.12) can be characterized by a discrete amplitude frequency spectrum similar to that for complex periodic data. The only difference is that the frequencies of the components are not related by rational numbers, as illustrated in Fig. C.5.

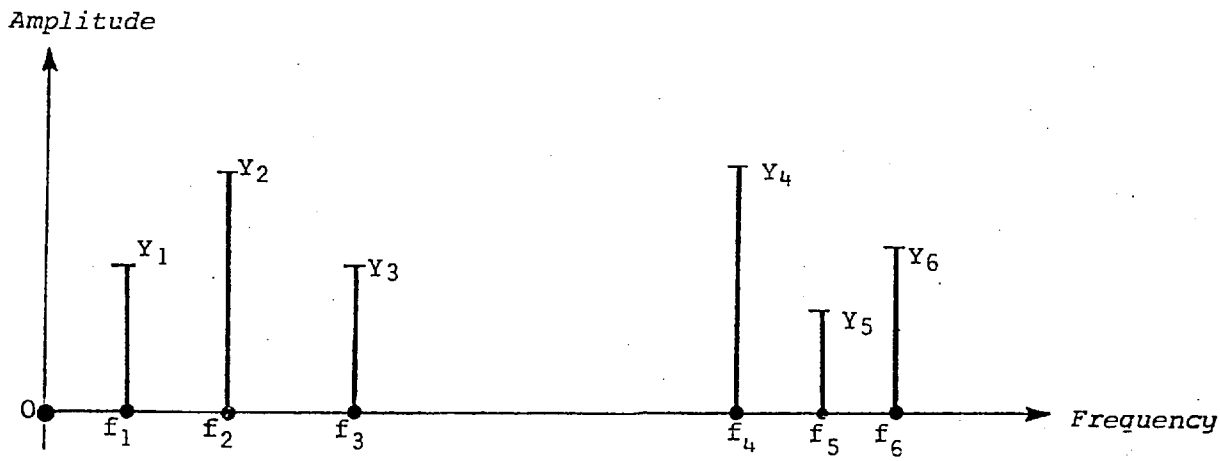


Fig. C.5 Amplitude-frequency diagram for an almost-periodic data

Any motion that is the result of a number of independent, unrelated periodic vibrations is almost periodic. Thus the motion of a weight suspended by 6 springs of arbitrary size and stiffness could be represented by an amplitude-frequency as illustrated in Fig. C.5. The vibration of a bridge subjected to vehicular traffic of all types is another example.

### C.2.1.4 Transient Non-periodic Data

This category includes all deterministic data not yet discussed; that is phenomena which are transient between one stationary state and another and can be described by some suitable time-varying function. Three simple examples of transient data are shown in Fig. C.6.

Examples of physical phenomena which produce transient data are numerous and diverse. For example, the data in Fig. C.6(a) could represent temperature of water in a kettle (relative to room temperature) after the flame is turned off. The data in Fig. C.6(b) might represent the free vibration of a damped mechanical system after an excitation force is ceased. The data in Fig. C.6(c) could represent the sudden closure of a valve or a switch at time t = c.

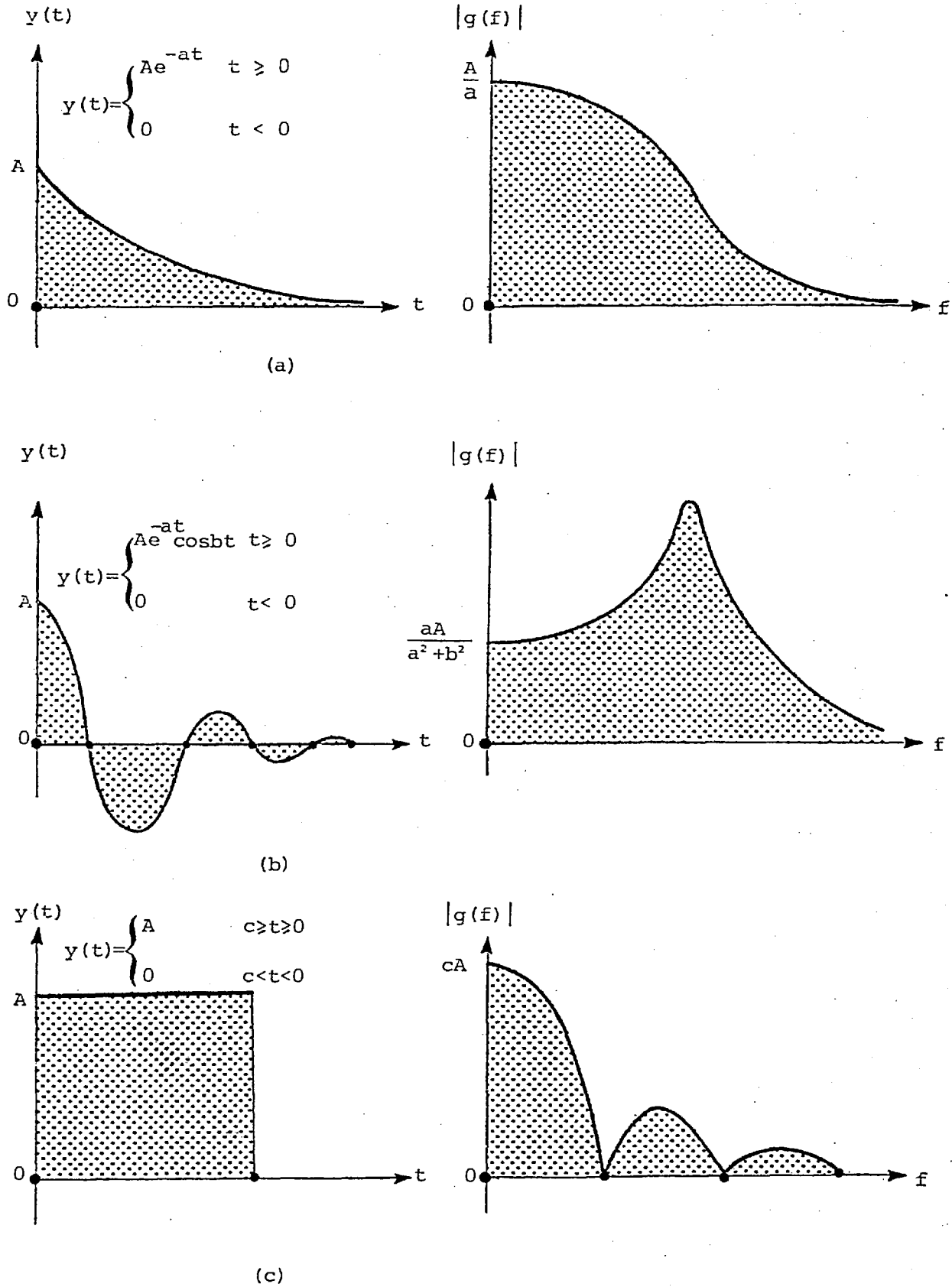


Fig. C.6 Illustrations of some transient data and their corresponding amplitude - frequency plots

It is obvious that in these transient data there are no discrete frequencies present and therefore the amplitude-frequency diagram will not be discrete but continuous, throughout all values of f. In parallel to the Fourier series analysis performed on the complex periodic data, it is possible to use a Fourier integral (Fourier integral will be discussed in detail in Section C.4) to arrive at an amplitude frequency diagram for transient conditions

$$g(f) = \int_{-\infty}^{+\infty} y(t) e^{-i2\pi ft} dt \qquad (C.13)$$

The Fourier spectrum g(f) is generally a complex number which can be expressed in complex polar notation as

$$g(f) = |g(f)| e^{-i\theta(f)} \qquad (C.14)$$

Here, $|g(f)|$ is the magnitude of g(f) and $\theta(f)$ is the argument. The amplitude-frequency plot for the three transient time histories are presented in Fig. C.6 (in terms of the magnitude $|g(f)|$).

## C.2.2 Classifications of Random (Stochastic or Probabilistic) Data

As discussed earlier, data which represents random physical phenomenon cannot be described by an explicit mathematical relationship because each observation of the phenomenon will be unique. In other words, any given observation will represent only one of many possible results which might have occurred. An example is when the output voltage from a thermal noise generator is recorded as a function of time. A specific voltage-time history record will be obtained, as shown in Fig. C.7. However, if a second thermal noise generator, of identical construction and assembly, is operated simultaneously a different voltage-time history record will result. In fact every thermal noise generator which might be constructed would produce a different voltage-time history record, as illustrated in Fig. C.7. Hence the voltage-time history for any generator is merely one example of an infinitely large number of time histories which might have occurred.

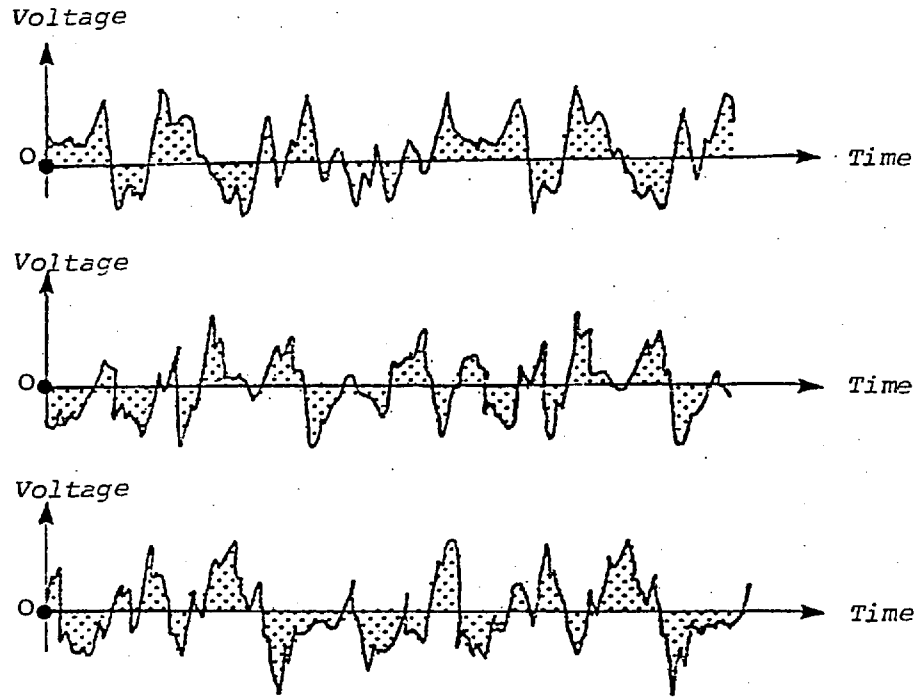


Fig. C.7 Sample records of thermal noise generator outputs

A single time history representing a random phenomenon is called a *sample function* (or a *sample record* when observed over a finite time interval). The collection of all possible sample functions which the random phenomenon might have produced is called a *random process* or a *stochastic process*. Hence a sample record of data for a random physical phenomenon may be thought of as one physical *realization* of a random process. The total collection of the records of a process is called an *ensemble*.

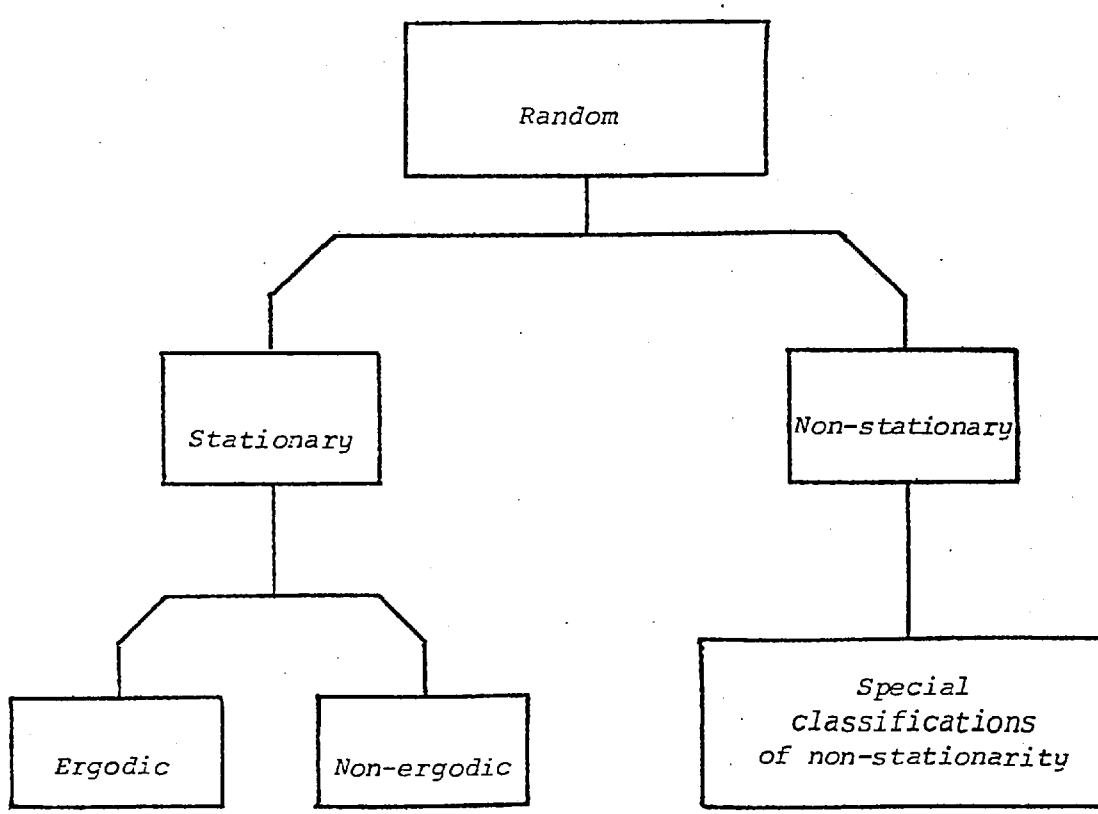


Fig. C.8 Classifications of random data

A random process may be categorized as being either *stationary* or *non-stationary*. Stationary random processes may be further categorized as being either *ergodic* or *non-ergodic*. Non-stationary random processes may be further categorized in terms of specific types of non-stationary properties. These various classifications for random processes are schematically illustrated in Fig. C.8. The meaning and physical significance of these various types of random processes will now be discussed in broad terms.

Considering the collection of sample functions (the ensemble) which forms the random process illustrated in Fig. C.9. The following terms are commonly used in connection with stochastic processes.

### C.2.2.1 Sample Mean

The mean value of the dependent variable over the sample function is defined as

$$\left.\begin{aligned} \mu_{y_k} = E[y_k(t)] = \lim_{T\to\infty} \frac{1}{T} \int_o^T y_k(t)\,dt \\ k = 1,2,3, \ldots, n \end{aligned}\right\} \quad (C.15)$$

Equation (C.15) gives the *sample mean* of y(t) over the kth sample. E[ ] is the short form for 'expected value' or mean value.

### C.2.2.2 Sample Autocorrelation

The correlation of the dependent variable at a point t with the same variable at another point some time $\tau$ later is defined as

$$\left.\begin{aligned} R_{y_k}(t,\tau) &= E[y_k(t) \cdot y_k(t+\tau)] \\ R_{y_k}(t,\tau) &= \lim_{T\to\infty} \frac{1}{T} \int_o^T y_k(t) \cdot y_k(t+\tau)\,dt \\ & \qquad k = 1,2, \ldots, n \end{aligned}\right\} \quad (C.16)$$

Eq. (C.16) expresses the autocorrelation (correlation of a record to itself) of the kth sample for a particular time lag $\tau$.

### C.2.2.3 Ensemble Mean

The mean value (first moment) of the random process at some time $t_1$ can be computed by taking the instantaneous value of each sample function of the ensemble at time $t_1$, summing the values, and dividing by the number of sample functions. That is, for the random process {y(t)}, where the symbol { } is used to denote an ensemble of sample functions, the mean value $\mu_y(t_1)$ is given by

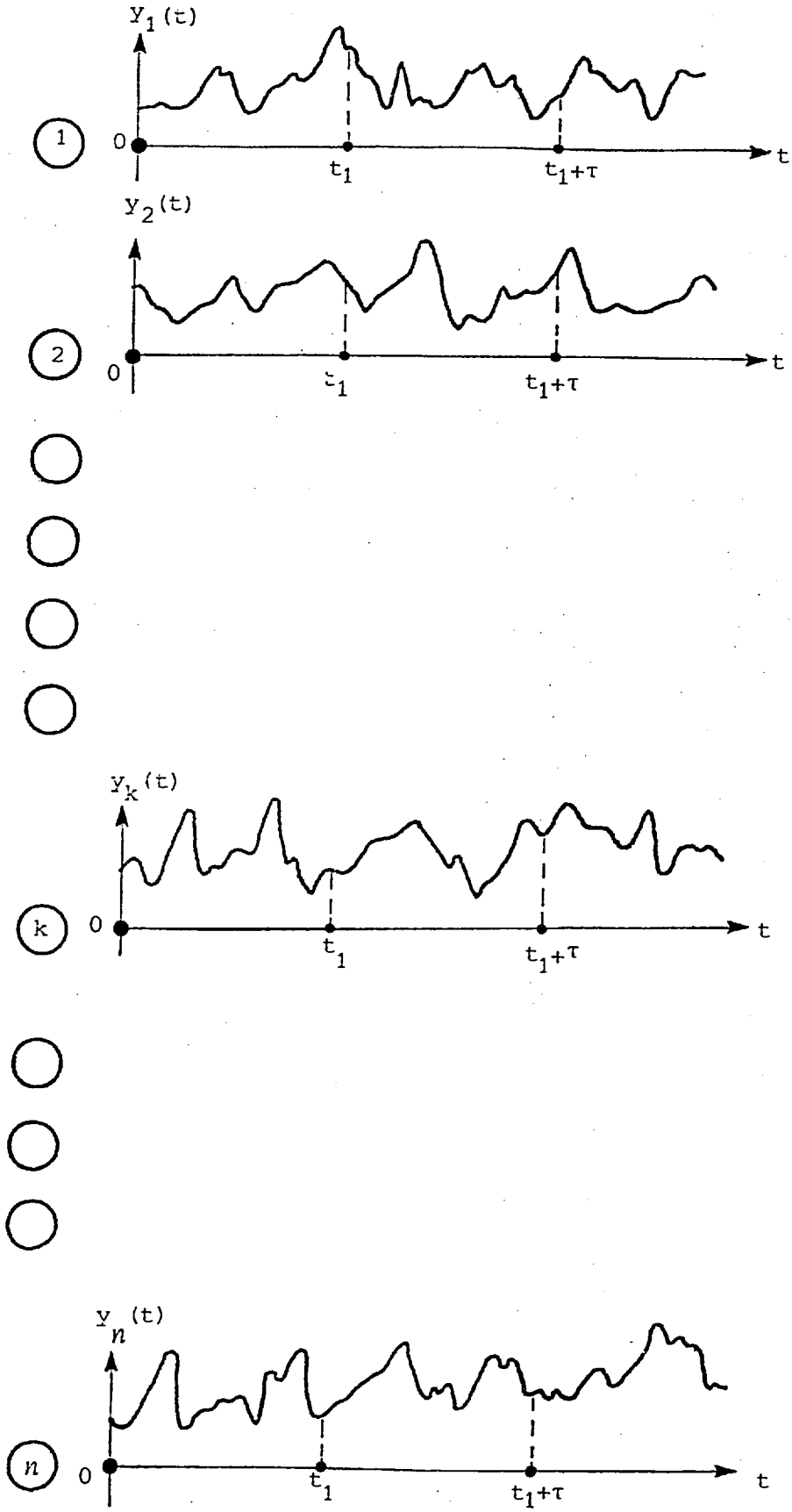


Fig. C.9 Ensemble of $n$ sample functions of a stochastic process

$$\mu_y(t_1) = E[y(t_1)] = \lim_{n\to\infty} \frac{1}{n} \sum_{k=1}^{n} y_k(t_1) \qquad \text{(C.17)}$$

### C.2.2.4 Ensemble Autocorrelation

In a similar manner, the autocorrelation function (often abbreviated as ac.f.) between the values of the random process at two different times can be computed by taking the ensemble average of the product of instantaneous values twice at $t_1$ and $(t_1+\tau)$. That is, the autocorrelation function $R_y(t_1,\tau)$

$$\left.\begin{aligned} R_y(t_1,\tau) &= E[y_k(t_1).y_k(t_1+\tau)] && \text{(a)} \\ R_y(t_1,\tau) &= \lim_{n\to\infty} \frac{1}{n} \sum_{k=1}^{n} y_k(t_1).y_k(t_1+\tau) && \text{(b)} \end{aligned}\right\} \text{(C.18)}$$

where the final summation assumes each sample function is equally likely.

### C.2.2.5 Stationary Random Processes

For the general case where $\mu_y(t_1)$ and $R_y(t_1,\tau)$ defined in Eqs (C.17) and (C.18) vary as time $t_1$ varies, the random process $\{y(t)\}$ is said to be *non-stationary*. For the case where $\mu_y(t_1)$ and $R_y(t_1,\tau)$ do not vary with time, the random process $\{y(t)\}$ is said to be *weakly stationary* or stationary in the wide sense. For weakly stationary random processes, the mean value is a constant and the autocorrelation function is dependent only upon the time displacement $\tau$. That is, $\mu_y(t_1) = \mu_y$ and $R_y(t_1,\tau) = R_y(\tau)$.

An infinite collection of higher-order moments and joint moments for the random process $\{y(t)\}$ could also be computed. For the special case where all possible moments and joint moments are time invariant, the random process $\{y(t)\}$ is said to be *strongly stationary* or stationary in the strict sense. However, in practice, verification of weak stationarity will justify an assumption of strong stationarity.

A time wave record from the sea, where there is neither the effect of wind acceleration nor the presence of tide (or tide effect has been artificially removed), is assumed to be stationary. If a tidal fluctuation is left in the record, the ensemble mean and autocorrelation would change as t changes and the record would therefore be non-stationary.

### C.2.2.6 Ergodic Random Processes

In the previous section the properties of a random process and how they can be determined by computing ensemble averages at specific instants of time was discussed. In most cases, however, it is also possible to describe the properties of a stationary random process by computing time-averages over specific sample functions in the ensemble. For example, considering the kth sample function for the random process illustrated in Fig. C.9, the mean value $\mu_{y_k}$ and the autocorrelation function $R_{y_k}(t,\tau)$ for the kth sample function are given by

$$\left.\begin{aligned} \mu_{y_k} &= \lim_{T\to\infty} \frac{1}{T} \int_0^T y_k(t)\,dt \qquad \text{(a)} \\ R_{y_k}(t,\tau) &= \lim_{T\to\infty} \frac{1}{T} \int_0^T y_k(t)\,y_k(t+\tau)\,dt \qquad \text{(b)} \end{aligned}\right\} \text{(C.19)}$$

If the random process $\{y(t)\}$ is stationary, and $\mu_{y_k}$ and $R_{y_k}(t,\tau)$ defined in Eq. (C.19) do not differ when computed over different sample functions, the random process is said to be *ergodic*. For ergodic random processes, the time-averaged mean value and autocorrelation function (as well as all other time-averaged properties) are equal to the corresponding ensemble averaged value. That is, $\mu_{y_k} = \mu_y$ and $R_{y_k}(t,\tau) = R_y(\tau)$. It is important to note that only stationary random processes can be ergodic.

Ergodic random processes are clearly an important class of random processes since all properties of ergodic random processes can be determined by performing time-averages over a single sample function, in this way it can be seen that this is a very strict condition. It means that if a wave recorder is positioned at a certain point in a lake then the mean of its record and the autocorrelations must be the same as those for all other similar wave records taken in all other similar lakes at similar points and under similar conditions, before the process can be called ergodic. Fortunately this is approximately true in nature and therefore all wave records are assumed to be part of ergodic processes and in most cases each wave characteristic can be measured properly, from a single observed time history record, although ergodicity cannot be proven.

### C.2.2.7 Non-stationary Random Processes

Non-stationary random processes include all random processes which do not meet the requirement for stationarity defined in Section C.2.2.5. Unless further restrictions are imposed, the properties of a non-stationary random process are generally time-varying functions which can only be determined by performing instantaneous averages over the ensemble of sample functions forming the process. In actual practice, it is often not feasible to obtain a sufficient number of sample records to permit the accurate measurement of properties by ensemble averaging. This fact has tended to impede the development of practical techniques for measuring and analyzing non-stationary random data.

In many cases, the non-stationary random data produced by actual physical phenomena can be classified into special categories of non-stationarity which simplify the measurement and analysis problem. For example, some types of random data might be described by a non-stationary random process $\{y(t)\}$ where each sample function is given by $y(t) = A(t)Q(t)$. Here, $Q(t)$ is a sample function from a stationary random process $\{Q(t)\}$ and $A(t)$ is a deterministic multiplication factor. If non-stationary random data fit a specific model of this type, ensemble averaging is not needed to describe satisfactorily the data. The various desired properties can be estimated from a single sample record, as is true for erogidc stationary data.

### C.2.2.8 Self-stationary Random Processes

The concept of stationarity as defined in Section 2.2.5, relates to the ensemble averaged properties of a random process. However, in actual practice, data in the form of individual time history records for a random phenomenon are frequently referred to as being stationary or non-stationary. A slightly different concept of stationarity is involved here. When a single time history record is referred to as being stationary, it generally means that the properties computed over short time intervals do not vary 'significantly' from one interval to

the next. The word significantly is used here to denote that observed variations are greater than would be expected, owing to normal statistical sampling variations. Hence the single sample record is stationary within itself. This concept of stationarity is sometimes called *self-stationarity* to avoid confusion with the classical definition.

To clarify the idea of self-stationarity, a single sample record $y_k(t)$ obtained from the kth sample function (Fig. C.9) of a random process $\{y(t)\}$ is considered where a mean value and autocorrelation function are obtained by time averaging over a short interval T with a starting time of $t_1$ as follows

$$\left.\begin{aligned} \mu_{y_k} &= \frac{1}{T}\int_{t_1}^{t_1+T} y_k(t)\,dt \qquad \text{(a)} \\ R_{y_k}(t,\tau) &= \frac{1}{T}\int_{t_1}^{t_1+T} y_k(t)y_k(t+\tau)\,dt \qquad \text{(b)} \end{aligned}\right\} \text{(C.20)}$$

For the general case where the sample properties defined in Eq. (C.20) vary significantly as the starting time $t_1$ varies, the individual sample record is said to be *self-nonstationary*. For the special case where the sample properties defined in Eq. (C.20) do not vary significantly as the starting time $t_1$ varies, the sample record is said to be *weakly self-stationary*. If this requirement is met for all higher order moments and joint moments, the sample record is said to be *strongly self-stationary*. It is important to note here that a sample record obtained from an ergodic random process will be self-stationary.

## C.3 BASIC DESCRIPTIVE PROPERTIES OF RANDOM DATA

Various descriptive properties for stationary random data will now be defined. It is assumed that the data is ergodic, so that the properties of the data can be determined from time-averages of individual sample records.

### C.3.1 Mean Square Values (Mean Values and Variances)

The general intensity of any set of random data may be described in rudimentary terms by a *mean-square value*, which is simply the average of the squared values of the time history. In equation form, the mean square value $\psi_y^2$ for a sample time history record $y(t)$ is given by

$$\psi_y^2 = \lim_{T\to\infty} \frac{1}{T} \int_0^T y^2(t)dt \tag{C.21}$$

The positive square root of the mean square value is called the *root mean square* (often abbreviated as r.m.s.).

It is often desirable to think of physical data in terms of a combination of a *satic* or *time-invariant component* and a *dynamic* or *fluctuating component*. The static component may be described by a *mean value* which is simply the average of all values. In equation form, the mean value $\mu_y$ is given by

$$\mu_y = \lim_{T\to\infty} \frac{1}{T} \int_0^T y(t)dt \tag{C.22}$$

The dynamic component may be described by a *variance* which is simply the mean square value about the mean. In equation form, the variance $\sigma_y^2$ is given by

$$\sigma_y^2 = \lim_{T\to\infty} \frac{1}{T} \int_0^T [y(t) - \mu_y]^2 dt \tag{C.23}$$

The positive square root of the variance is called the *standard deviation*.

### C.3.2 Probability Density Functions

The probability density function (often abbreviated as p.d.f.) provides information concerning the properties of the data in the *amplitude domain*. For a continuous random data, the probability density function describes the probability that the data will assume a value within some defined range at any instant of time. Considering the sample time-history record $y(t)$

as illustrated in Fig. C.10. The probability that y(t) assumes a value between y and (y+Δy) may be obtained by taking the ratio $T_o/T$, where $T_o = \sum_{n=1}^{N} \Delta t_n$ and is the total length of time for which y(t) falls inside the range (y, y+Δy) during an observation time T. This ratio will approach an exact probability description as T approaches infinity. In equation form

$$\text{Prob}\,[y < y(t) \leq y + \Delta t] = \lim_{T\to\infty} \frac{T_o}{T} = \lim_{T\to\infty} \frac{\sum_{n=1}^{N} \Delta t_n}{T} \qquad (C.24)$$

For small Δy, an approximation to the probability density function is

$$\text{Prob}[y < y(t) \leq y + \Delta y] \simeq p(y)\Delta y \qquad (C.25)$$

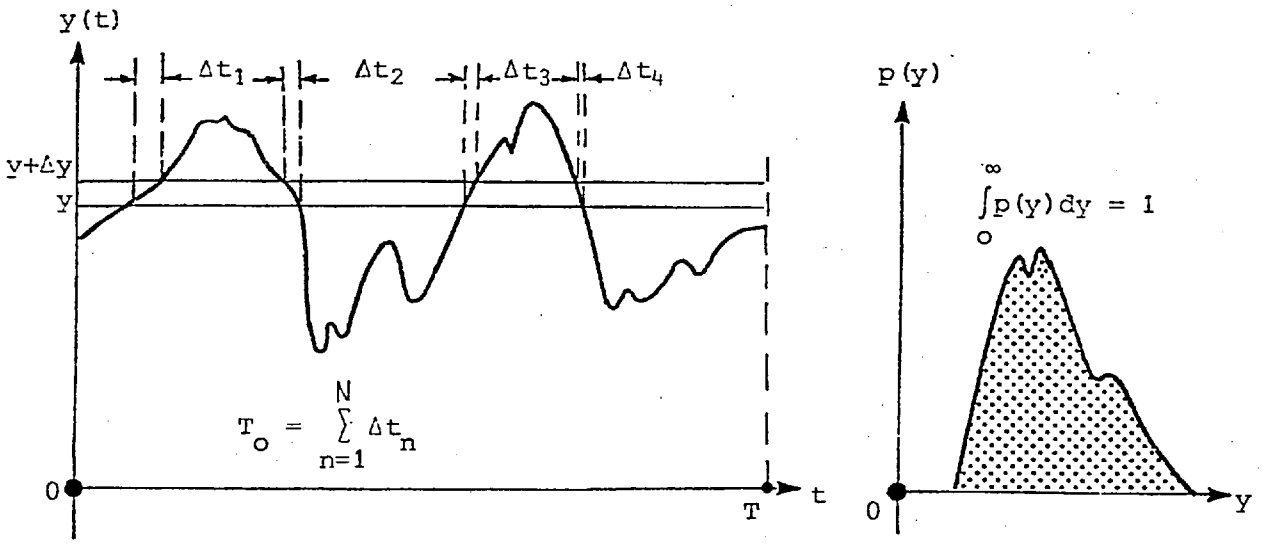


(a) *Probability measurement*

(b) *probability density function*

Fig. C.10

Thus

$$p(y) = \lim_{\Delta y\to 0} \frac{\text{Prob}[y<y(t)<y+\Delta y]}{\Delta y} = \lim_{\Delta y\to 0} \lim_{T\to\infty} \frac{1}{T} \frac{\sum_{n=1}^{N} \Delta t_n}{\Delta y} \qquad (C.26)$$

The probability density function p(y) is always a real-valued, non-negative function.

The probability that an instantaneous value of y(t) is less than or equal to some value of y is defined by P(y), which is in turn equal to the integral of the probability density function from minus infinity to y. This function P(y) is known as the *probability distribution function*, or *cumulative probability distribution function*, and should not be confused with the probability density function p(y). Specifically

$$P(y) = \text{Prob}[y(t) \leq y] = \int_{-\infty}^{y} p(\xi)\,d\xi \qquad (C.27)$$

The distribution function P(y) is bounded by zero and one, since the probability of y(t) being less than $-\infty$ is clearly zero while the probability of y(t) being less than $+\infty$ is unity (a certainty). The probability that y(t) falls inside any range $(y_1, y_2)$ is given by

$$P(y_2) - P(y_1) = \text{Prob}[y_1 < y(t) \leq y_2] = \int_{y_1}^{y_2} p(y)\,dy \qquad (C.28)$$

In terms of the probability density function p(y), the mean value of y(t) is given by

$$\mu_y = \int_{-\infty}^{+\infty} y p(y)\,dy \qquad (C.29)$$

In words, the mean value is a weighted linear sum of y(t) over all values of y. Similarly, the mean square value is given by

$$\psi_y^2 = \int_{-\infty}^{+\infty} y^2 p(y)\,dy \qquad (C.30)$$

Hence the mean square value is a weighted linear sum of $y^2(t)$ over all values of y.

### C.3.2.1 Illustrations

To help clarify the practical significance of probability density functions, it is convenient to consider seven examples of time history records which might occur in practice: (a) constant (b) square wave, (c) sawtooth wave, (d) sine wave, (e) sine wave plus random noise, (f) narrow-band random noise, and (g) wide-band random noise. Typical time history records for each of these examples are presented in Fig. C.11. In all cases, the mean value is assumed to equal zero ($\mu_y = 0$) for convenience.

It is important to note here that a sine wave is usually thought of as being deterministic since it can be described in detail by the equation $y(t) = Y \sin(2\pi f_o t + \theta)$. However, a sine wave may also be thought of as a sample function from a random process $\{y(t)\} = \{Y\sin(2\pi f_o t + \theta_k)\}$, where the initial phase angle $\theta_k$ for each sample function $y_k(t)$ is a random variable. Such an interpretation is made here to justify describing a sine wave in probabilistic terms.

A typical plot of a probability density function versus instantaneous value [p(y) versus y] for each of the last six illustrations of Fig. C.11 is presented in Fig. C.12. The last four examples in this figure illustrate a definite trend with the probability density plot changing pattern from the sine wave case to the wide-band random noise case.

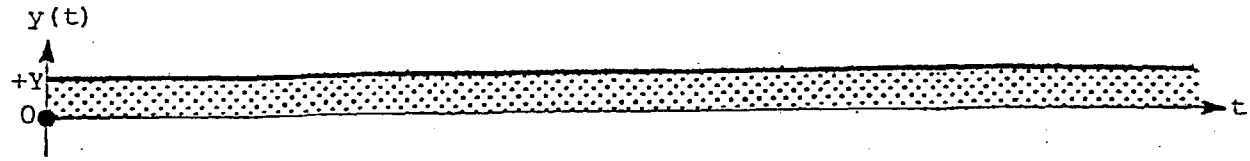


(a) *Constant*

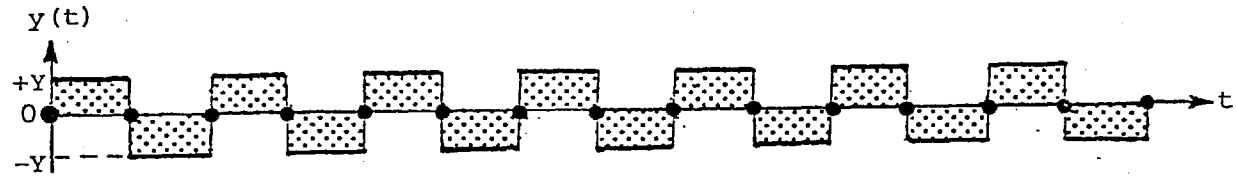


(b) *Square wave*

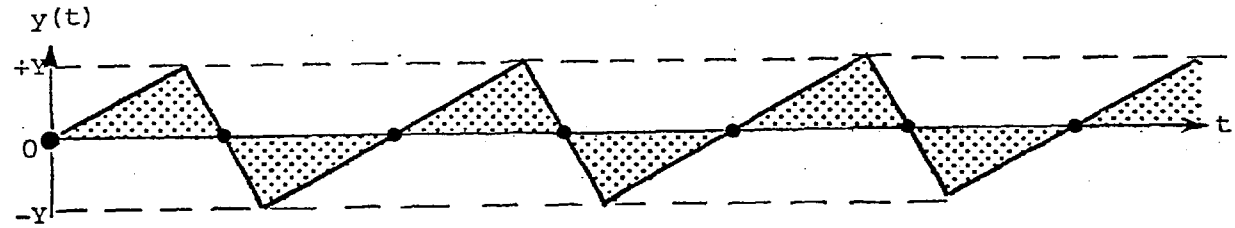


(c) *Sawtooth wave*

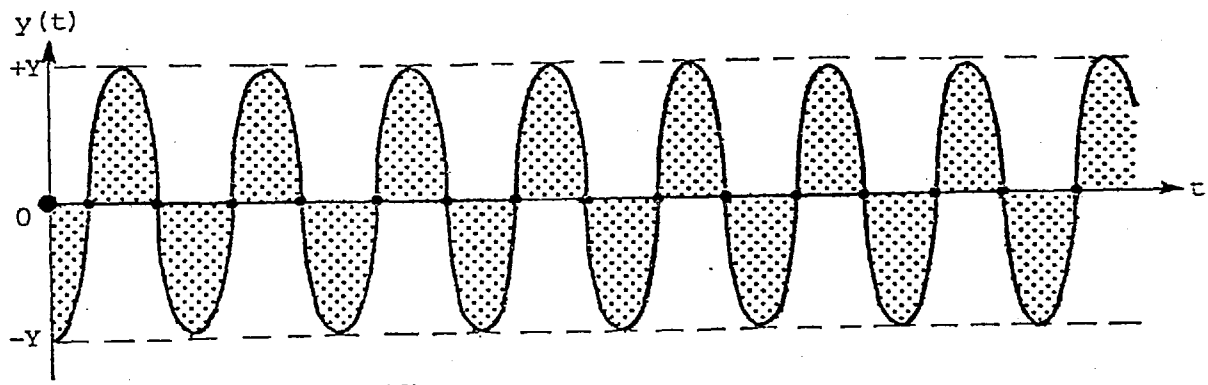


(d) *Sine wave*

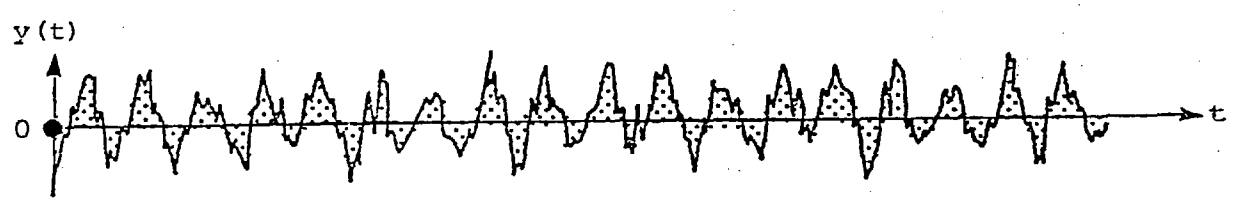


(e) *Sine wave plus random noise*

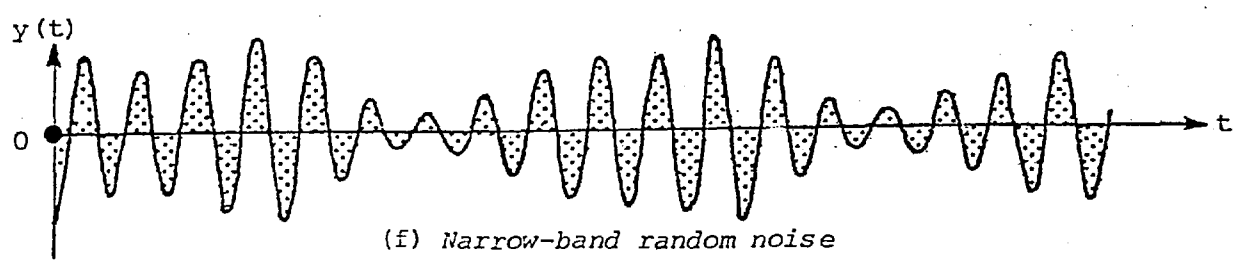


(f) *Narrow-band random noise*

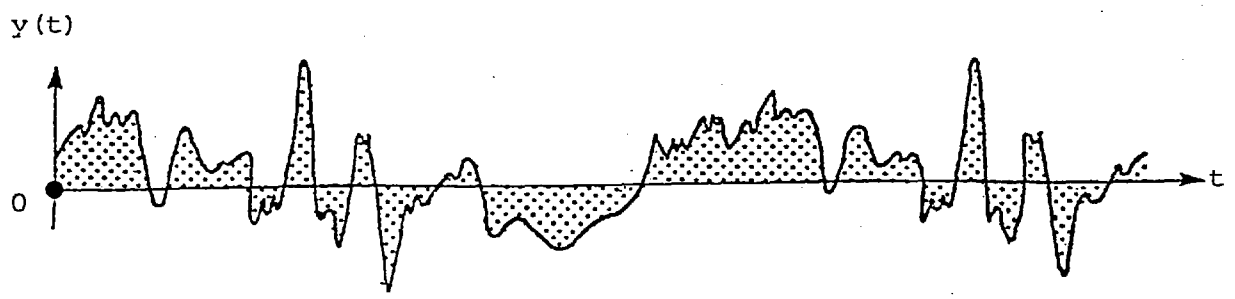


(g) *Wide-band random noise*

Fig. C.11 Seven special time histories

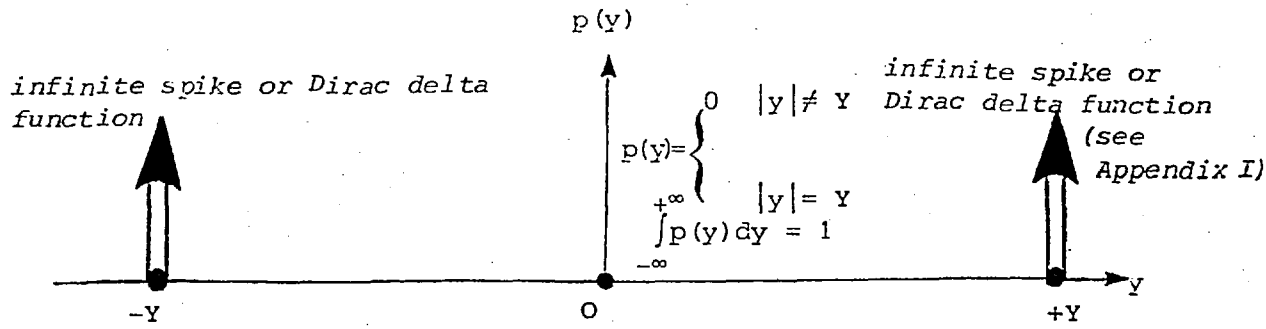


(a) *Probability density function plot of a square wave*

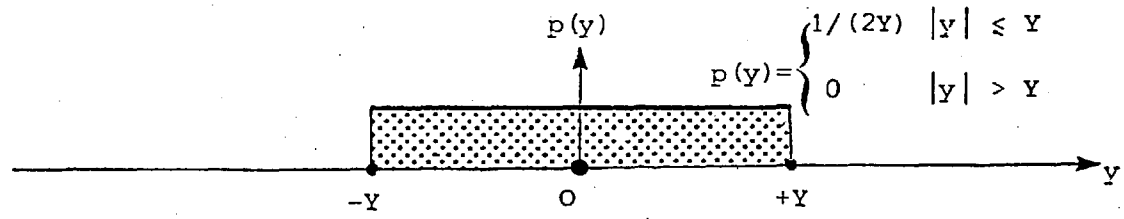


(b) *Probability density function plot of sawtooth wave*

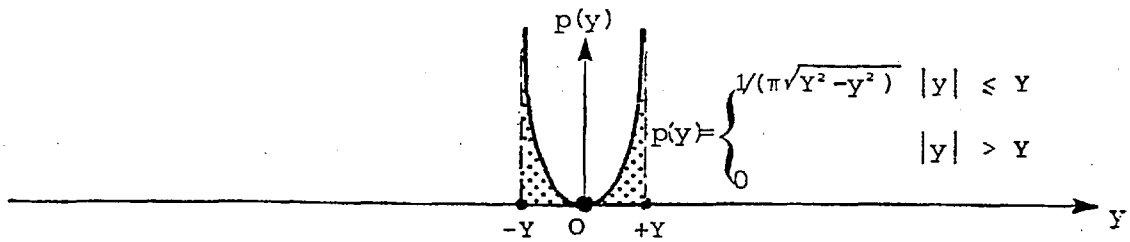


(c) *Disch-shaped probability density function plot of a sine wave*

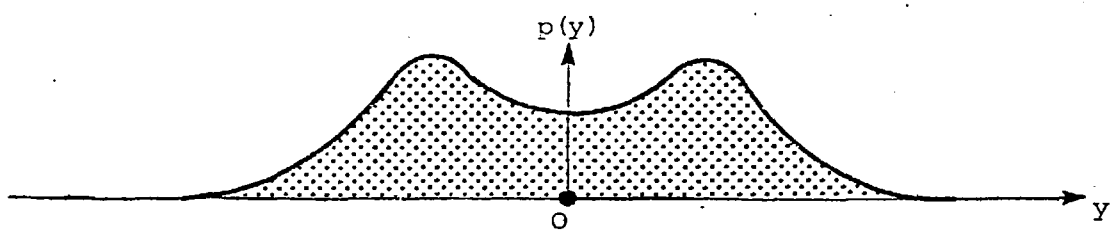


(d) *Probability density function plot of a sine wave plus random noise*

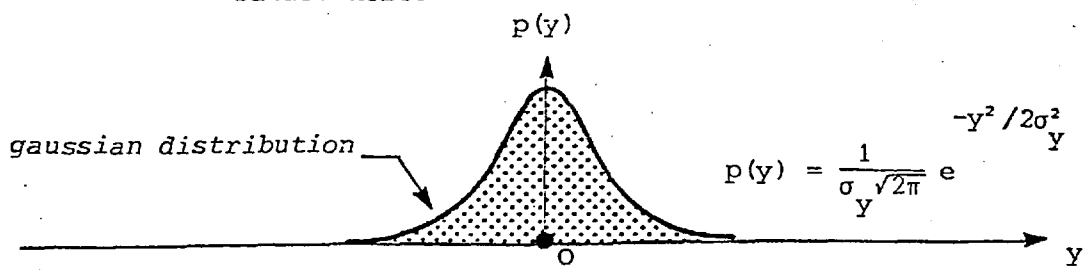


(e) *Bell-shaped probability density function plot of a narrow-band random noise*

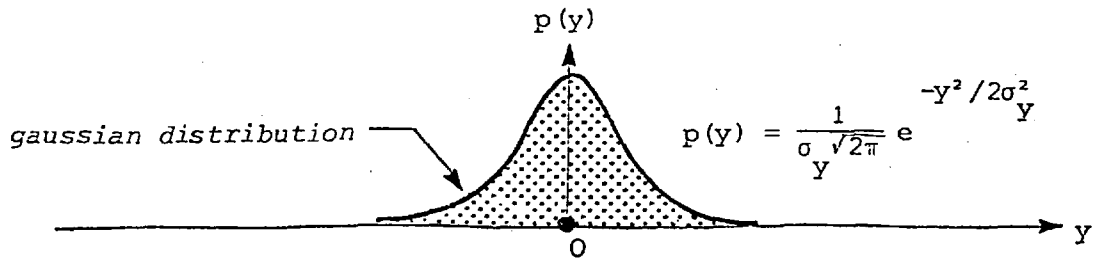


(f) *Bell-shaped probability density function plot of a wide-band random noise*

Fig. C.12 Probability density functions

### C.3.2.2 Applications

The principal application for a probability density function measurement of physical data is to establish a probabilistic description for the instantaneous values of the data. However, from Fig. C.12, it is seen that the probability density function could also be used to distinguish between sinusoidal and random data.

### C.3.3 Sampling Theory

Sampling theory is a study of the relationships between a population and samples drawn from that population. It has great value when used in many connections. For example it is useful in the *estimation* of unknown population quantities (such as population mean, variance, etc.); often called *population parameters* or more briefly *parameters*, from a knowledge of corresponding sample quantities (such as sample mean, variance, etc.); often called *sample statistics* or more briefly *statistics*.

### C.3.3.1 Unbiased Estimates

One desirable property for an estimator is that of unbiasedness. If the mean of the sampling distribution of a statistic equals the corresponding population parameter, the statistic is called an *unbiased estimator* of the parameter. In this thesis it is convenient to denote the unknown parameter by $\mu$ and the estimator by $\hat{\mu}$. $\hat{\mu}$ is an unbiased estimator of $\mu$ if $E(\hat{\mu}) = \mu$, otherwise it is known as a *biased estimator*. The corresponding values of such statistics are called *unbiased* and *biased estimates* respectively.

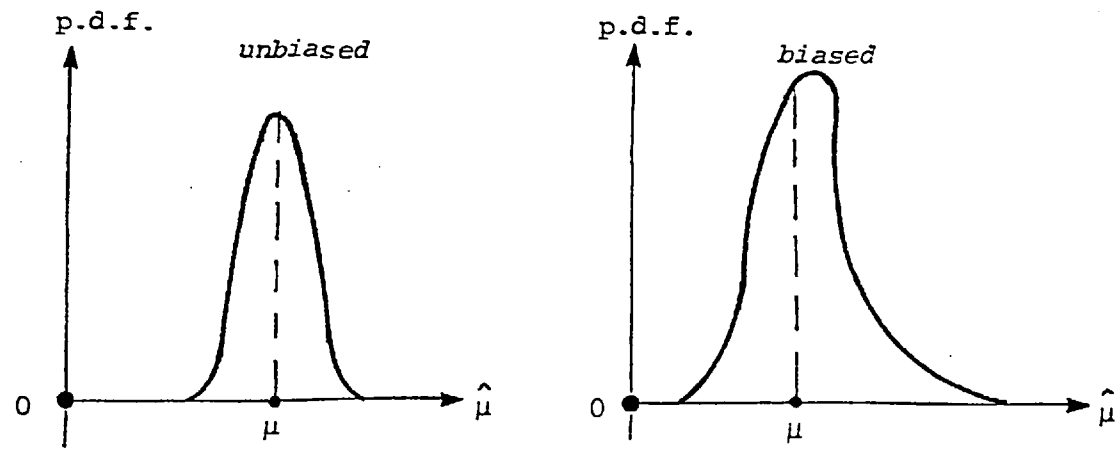


Fig. C.13 Types of estimators

### C.3.3.2 Consistent Estimates

A further desirable property of a good estimator is consistency; roughly speaking, this signifies that the larger the sample size n the closer the statistic will be to the true value. An estimator, $\hat{\mu}$, is said to be *consistent* if

$$\left.\begin{aligned} &E(\hat{\mu}) \to \mu \qquad \text{as } n \to \infty \qquad \text{(a)} \\ &\mathrm{Var}(\hat{\mu}) \to 0 \qquad \text{as } n \to \infty \qquad \text{(b)} \end{aligned}\right\} \text{(C.31)}$$

property (C.31a) holds for unbaised estimates,

### C.3.4 Digitising of Continuous Data

The process of *digitising* consists of converting data into discrete numbers. Among the various types of sampling, the most important one is the *equispaced sampling* which will be considered in this context. In order to digitise a continuous record, a positive quantity $\Delta t$ called the sampling interval, is required. The constant quantity $\Delta t$ is the time interval between sampled values of y(t). The number of values sampled per unit time is called the *sampling rate* and is equal to $1/\Delta t$.

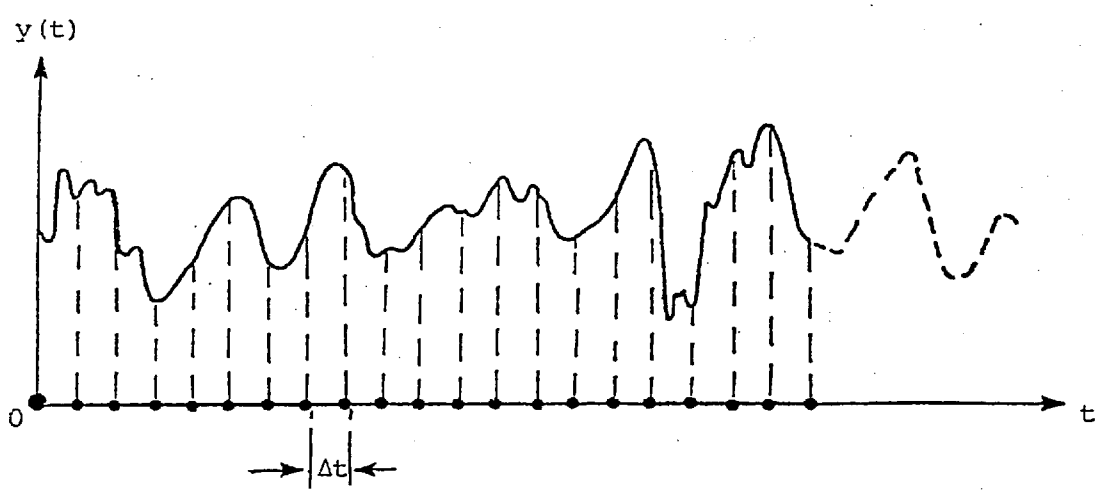


Fig. C.14 Equispace sampling of a continuous record

An illustration of equispaced sampling of continuous data is shown in Fig. C.14. The continuous function y(t) is replaced, by the discrete time series

$$y_i = y[(i-1)\Delta t]_{i=1,2,3,\ldots,N} \qquad \text{(C.32)}$$

The number of the data N is normally known as the *sample size*.

### C.3.4.1 Raw Data

When a continuous record is digitised, the collected data is not arranged numerically and as such is called *raw data*.

### C.3.4.2 Ordered Array (Ranked Array)

In array is an arrangement of raw data in ascending or descending order of magnitude. Such ranking enables a reader to perceive several aspects of the data at a glance, such as the smallest number, the largest number, the *range*, i.e.the difference between the largest and the smallest number.

## C.3.5 Calculation of the Mean Value

For a digitised time series of size N, the sample mean value is given by

$$\bar{y} = \frac{1}{N} \sum_{i=1}^{N} y_i \qquad (C.33)$$

where N is the number of data samples and $y_i$ are the data values. The quantity $\bar{y}$ calculated here is an unbiased estimate of the true mean value $\mu_y$.

## C.3.6 Calculation of the Standard Deviation

The sample standard deviation for a digitsed time series of size N is given by

$$s = \left[ \frac{1}{(N-1)} \sum_{i=1}^{N} (y_i - \bar{y})^2 \right]^{\frac{1}{2}} \qquad (C.34)$$

The quantities s and $s^2$ calculated here are unbiased estimates of the true standard deviation and variance, $\sigma_y$ and $\sigma_y^2$, respectively.

## C.3.7 Coefficient of Dispersion

The standard deviation is expressed in the same units as the mean, however it is more useful to measure the spread in relative terms by dividing the sample standard deviation by the sample mean. This dimensionless ratio is known as the *coefficient of dispersion*. If every observation in a set of data is multiplied by the same constant, the dispersion coefficient is unaffected.

## C.3.8 Skewness

*Skewness* is the degree of asymmetry of a probability density function. If the probability density function of a distribution has a longer 'tail' to the right of the central maximum than to the left, the distribution is said to be *skewed to the right* or to have *positive skewness*. If the reverse is true it is said to be *skewed to the left* or to have *negative skewness*. The population skewness coefficient is defined as the dimensionless ratio of the third central moment* to the second central moment on the power 3/2, or

$$g = \frac{\int_{-\infty}^{+\infty} (y-\mu_y)^3 p(y)\,dy}{\sigma_y^3} \qquad \text{(C.35)}$$

where $p(y)$, $\mu_y$, $\sigma_y$ are respectively the probability density function, the population mean and the population standard deviation. A distribution is *symmetrical (bell-shaped)* about its mean if g is zero.

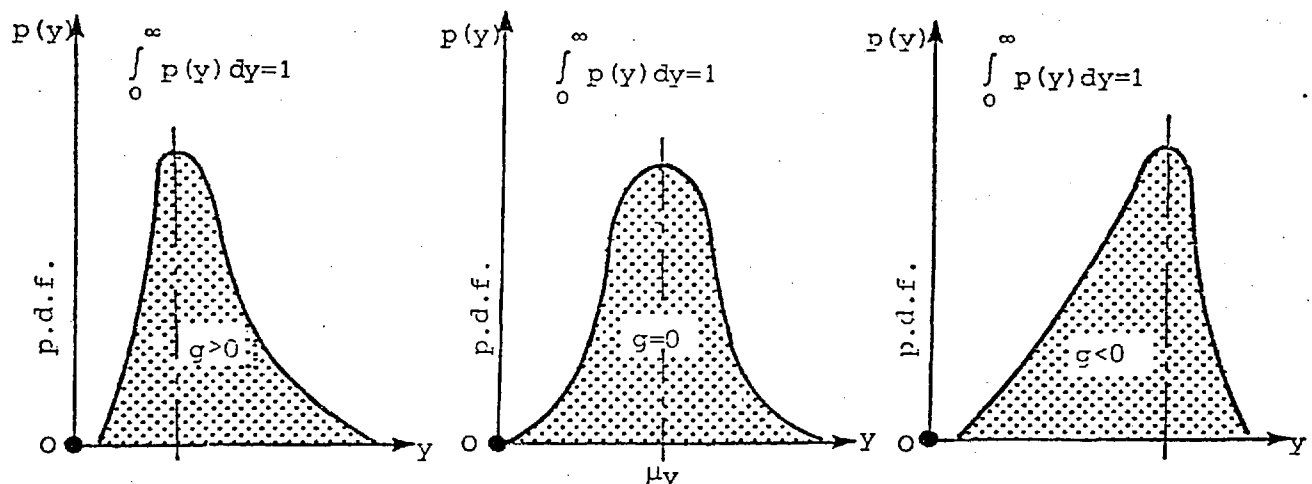


(a) *Skewed to the right* (b) *Symmetrical or bell-shaped* (c) *Skewed to the left*

Fig. C.15

For a digitised time series of size N, the unbiased estimate of the skewness coefficient is

$$\hat{g} = \frac{N^2}{(N-1)(N-2)} \frac{\sum_{i=1}^{N} (y_i-\bar{y})^3/N}{s^3} \qquad N>2 \qquad \text{(C.36)}$$

where $s^2$ is the sample variance.

If every observation in a set of data is multiplied by the same constant or a constant is added, the skewness coefficient is unaffected.

*If $x_1, x_2, \ldots x_n$ are the n values assumed by the variable x, the quantity $m_r = \sum_{j=1}^{N} (x_j-\bar{x})^r/N$ where $\bar{x}$ is the arithmetic mean is called the rth central moment.

## C.3.9 Kurtosis

*Kurtosis* is the degree of peakedness of a probability density function and is usually taken relative to a normal distribution. The population kurtosis coefficient is

$$\gamma = \frac{\int_{-\infty}^{+\infty} (y-\mu_y)^4 p(y)\,dy}{\sigma_y^4} - 3 \qquad \text{(C.37)}$$

A probability density function having a relatively high peak such as the curve of Fig. C.16 for which $\gamma > 0$ is called *leptokurtic*. Those for which $\gamma < 0$ are called *platykurtic* and will be flat-topped. The normal distribution, ($\gamma = 0$), which is not peaked or flat-topped is called *mesokurtic*.

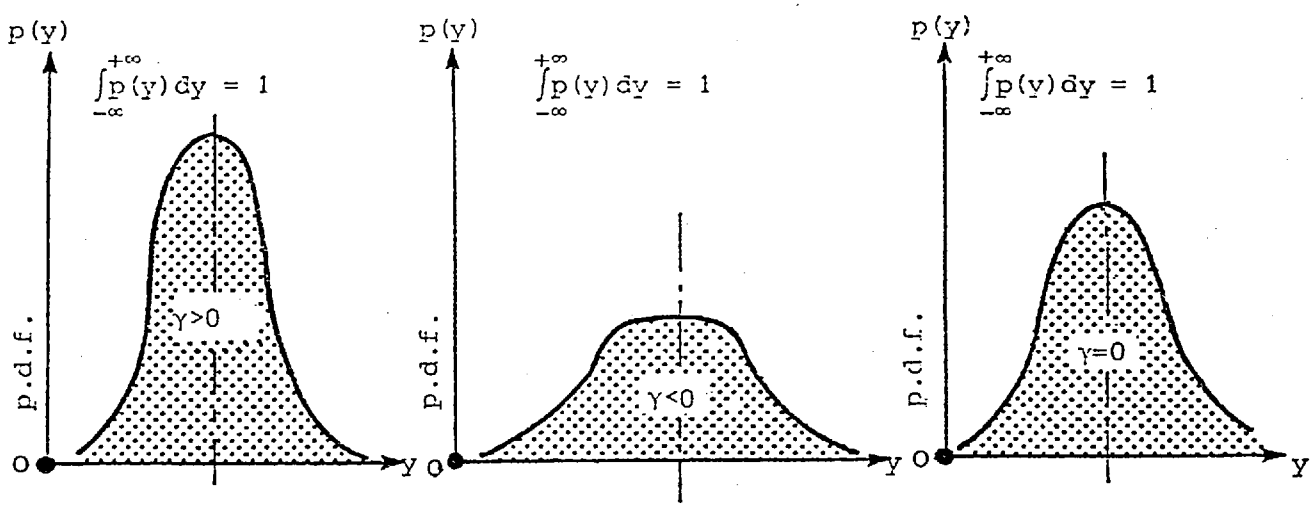


(a) *Leptokurtic* (b) *Platykurtic* (c) *Mesokurtic*

Fig. C.16

For a digitised time series of size N, the estimate of the kurtosis coefficient is

$$\hat{\gamma} = \frac{N^3}{(N-1)(N-2)(N-3)} \frac{\sum_{i=1}^{N} (y_i-\bar{y})^4/N}{s^4} - 3 \qquad \text{(C.38)}$$

## C.3.10 Percentile

Assuming y(t) is a continuous random variable with a probability density function of p(y), the value $t_k$ is defined to be (100k)th *percentile* for y(t) if the area under p(y) to the right of $t_k$ is k, where $0 < k < 1$; that is; the (100k)th percentile has the property that

$$\text{Prob}[y \geq t_k] = k \tag{C.39}$$

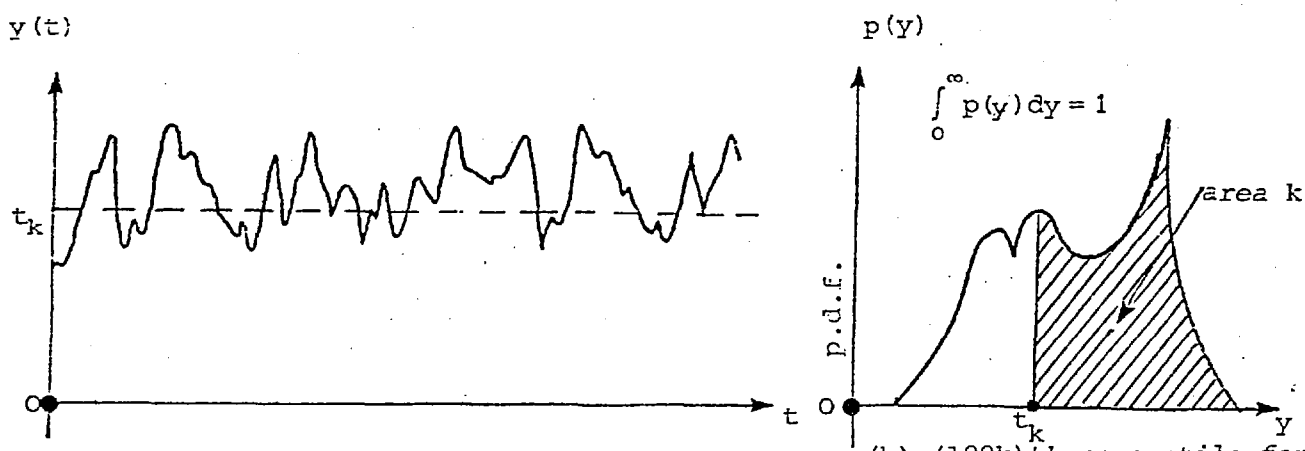


(a) *A continuous random variable*

(b) (100k)*th percentile for a random variable* y(t)

Fig. C.17

Figure C.17 shows a graphical representation of $t_k$ for a general probability density function. The way in which the area changes as $t_k$ moves depends on the particular probability density function assumed for y(t). The commonly used values for 100k are the integers between 0 and 100 (hence the reason for the name). *Median* $m_y$ is introduced as a measure of the middle of the distribution and splits the area under the probability density function into two equal parts; in particular, then, since the area to the left of $m_y$ must be 0.5, the median is identical with the 50th percentile

$$m_y = t_{0.5} \tag{C.40}$$

Percentiles can be used to measure any desired aspect of the distribution of a random variable. The most frequently used measure of variability is based on the percentiles in the *interquartile range* $I_r$ (Fig. C.18), defined to be the difference between the 75th and the 25th percentiles

$$I_r = t_{0.75} - t_{0.25} \tag{C.41}$$

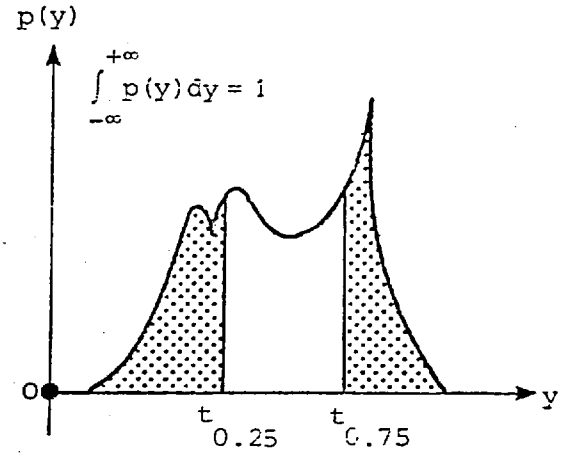


Fig. C.18 Interquartile range

$I_r$, then, gives the length of an interval, centred about the median $m_y$, which includes 50% of the total probability. Thus, as $I_r$ increases, it is necessary to take a larger interval about $m_y$ to include 50% of the probability.

### C.3.10.1 Percentile for a Digitised Time History Record

Given a continuous time history record y(t) is digitised and then arranged in descending order of magnitude. The quantities, $v_1, v_2, \ldots v_k, \ldots v_N$ form a ranked array, and are referred to as the *order statistics* of the digitised sample record. It can be shown (Larson, 1975) that an average, over repeated samples, the proportion of population values greater than or equal to $v_1$ is $1/(N+1)$. *This is true whatever the form of the continuous probability density function in the population;* similarly the proportion of population values greater than $v_2$ is $2/(N+1)$, the proportion greater than $v_3$ is $3/(N+1)$, up to the proportion greater than $v_n$ is $N/(N+1)$. In short, the expected proportion of population values greater than $v_j$ is $j/(N+1)$ for $j = 1,2, \ldots, N$, hence $v_j$ is the $[100j/(N+1)]$th percentile of the data set.

### C.3.11 Autocorrelation Functions

The autocorrelation function provides information concerning the properties of the data in the *time domain*. For random data autocorrelation function describes the general dependence of the values of the data at one time on the values at another time. Considering the sample time history record y(t) illustrated in Fig. C.19. An estimate of the autocorrelation between the values of y(t) at times t and $(t+\tau)$

can be obtained by taking the product of two values and averaging over the observation time T. The resulting average product will approach an exact autocorrelation function as T approaches infinity. In equation form

$$R_y(\tau) = \lim_{T\to\infty} \frac{1}{T} \int_0^T y(t)y(t+\tau)\,dt \qquad (C.42)$$

The quantity $R_y(\tau)$ is always a real-valued even function with a maximum at $\tau = 0$, and may be either positive or negative. In equation form

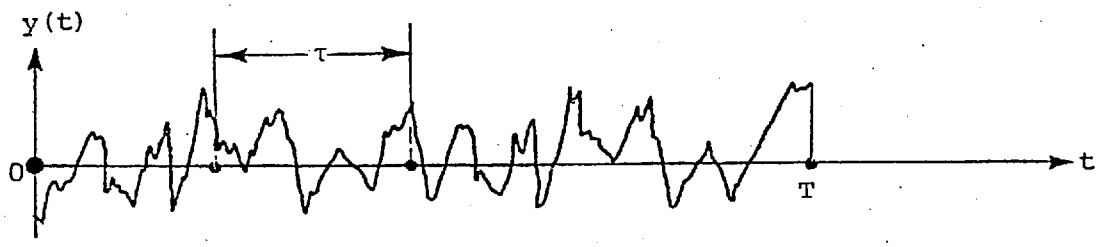


Fig. C.19 Autocorrelation measurement

$$R_y(-\tau) = R_y(\tau) \qquad (C.43)$$

$$R_y(0) \geq |R_y(\tau)| \quad \text{for all } \tau \qquad (C.44)$$

In terms of the autocorrleation function, the mean value of y(t) is given (excluding such special cases as sine waves) by

$$\mu_y = \sqrt{R_y(\infty)} \qquad (C.45)$$

In words, the mean value of y(t) is equal to the positive square root of the autocorrelation as the time displacement becomes very long. Similarly, the mean square value of y(t) is given by

$$\psi_y^2 = R_y(0) \qquad (C.46)$$

That is, the mean square value is equal to the autocorrelation at zero time displacement.

## C.3.12 Autocovariance Functions

The *autocovariance function* (often abbreviated as acv.f.) is the autocorrelation function after the mean of the record has been substracted

$$\gamma_y(\tau) = \lim_{T\to\infty} \frac{1}{T} \int_0^T (y(t) - \mu_y)(y(t+\tau) - \mu_y)dt \qquad (C.47)$$

For a record where $\mu_y = 0$

$$\gamma_y(\tau) = R_y(\tau) \qquad (C.48)$$

Also as $\tau\to\infty \quad \gamma_y(\tau) \to 0$

## C.3.13 Autocorrelation Coefficients

Given a time series, $y(t)$, with the population mean $\mu_y$, the *autocorrelation coefficient* is defined by the expression

$$\rho_\tau = \frac{E[(y(t) - \mu_y) \cdot (y(t+\tau) - \mu_y)]}{\sqrt{E[y(t) - \mu_y]^2 \cdot E[y(t+\tau) - \mu_y]^2}} \qquad (C.49)$$

in which $\rho_\tau$ expresses the correlation which exists between all pairs of observations $y(t)$ and $y(t+\tau)$ as a function of their spacing $\tau$.

For a finite data sample, estimates of the population values of $\rho_\tau$ are given by the serial correlation coefficients, $r_\tau$. Given a series of N observations, $y_t$, with a mean, $\bar{y}$, two over-lapping sequences each containing $(N-\tau)$ items of data, $y_1, y_2, y_3 \cdots y_{N-\tau}$, and $y_{\tau+1}$, $y_{\tau+2}$, $y_{\tau+3}$, ..., $y_N$ are selected and their coefficient of correlation, $r_\tau$, computed for $\tau = 1,2,3,\ldots,\tau_{max}$, where $\tau_{max}$ should not exceed 0.25 N (Matalas, 1967). When $\tau_{max}$ is small compared with N, the following expression given by Kendall and Stuart (1968) is known to be both adequate and economical in computer time

$$r_\tau = \frac{\frac{1}{N-\tau} \sum_{t=1}^{N-\tau} (y_t - \bar{y})(y_{t+\tau} - \bar{y})}{\frac{1}{N} \sum_{t=1}^{N} (y_t - \bar{y})^2} \qquad (C.50)$$

### C.3.13.1 Correlograms

A plot of $r_\tau$ as the ordinate against the lag, $\tau$, as the abscissa, in which adjacent points are joined by straight lines, is referred to as a *correlogram*.

#### C.3.13.1.1 Illustrations

Typical correlograms for four time histories of the Fig. C.11 are presented in Fig. C.20. If y(t) is a sine wave, i.e. $y(t) = a\cos(2\pi f_o t)$, where a is a constant, then it can easily be shown that

$$r_\tau \simeq \cos(2\pi f_o \tau) \tag{C.51}$$

The important feature of this correlogram is that it persists periodically over all lags with the same period as the underlying sine wave, but the phase angle information is lost.

The sharply peaked correlogram which diminished rapidly to zero (for large N, $r_\tau \simeq 0$ for all non-zero values of $\tau$), as illustrated in Fig. C.20(d), is typical of wide-band random data. For the limiting case of hypothetical white noise (random data with energy distributed uniformly over all frequencies), the correlogram is a Dirac delta function (see Appendix I) at zero time displacement ($\tau = 0$).

The correlogram for the sine wave plus random noise is simply the sum of the correlograms for the sine wave and random noise separately, as illustrated in Fig. C.20(b). Alternatively, the correlogram for the narrow-band random noise in Fig. C.20(c) appears to be a decaying version of a sine wave correlogram. An important feature, however, is that this correlogram will diminish to zero for large time displacements. The four examples in Fig. C.20 illustrate a definite trend in the correlogram changing pattern from the sine wave case to the wide-band random noise case, just as was true for the probability density function.

#### C.3.13.1.2 Applications

The principal application of an autocorrelation function in the measurement of physical data is to establish the influence of values at any time over values at a future time. The correlogram, which forms the basis of an autocorrelation analysis, reflects the structure of the time series, taking a wide variety of forms depending upon the dominance of the deterministic and stochastic components within the observed data. If the time series is completely random, the (population)

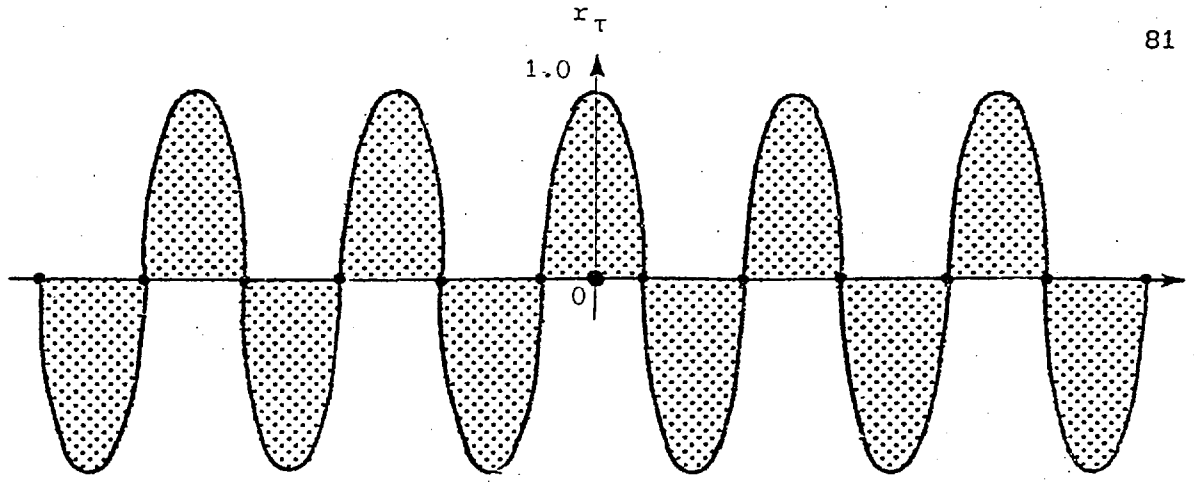


(a) *Correlogram plot of a sine wave*

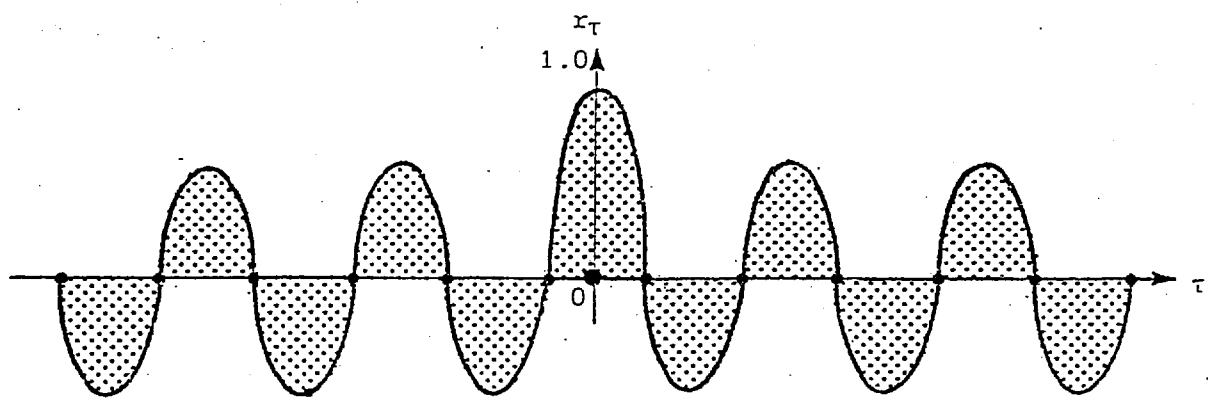


(b) *Correlogram plot of a sine wave plus random noise*

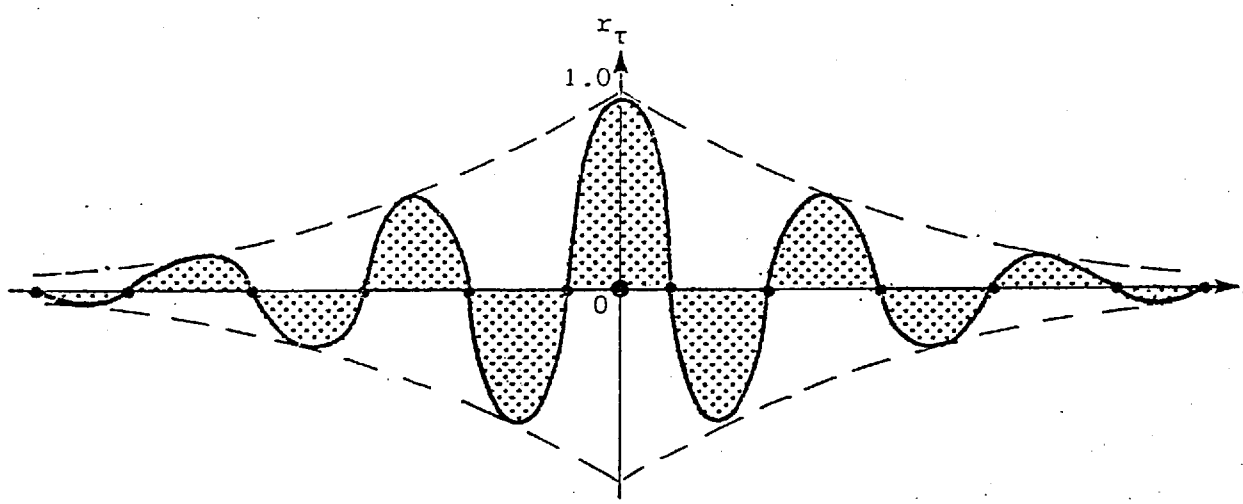


(c) *Correlogram plot of a narrow-brand random noise*

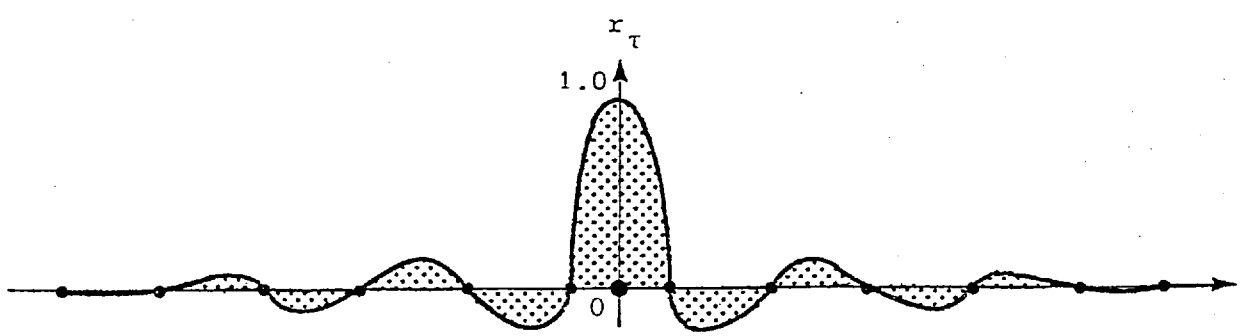


(d) *Correlogram plot of a wide-band random noise*

Fig. C.20

autocorrelation function is zero for all lags other than zero lag, and the (sample) correlogram will only deviate by small amounts from zero because of sampling effects. As the length of the series increases, these sampling effects decrease. In contrast, a sine wave, or any other deterministic data, will have a correlogram which persists over all time displacements. If the series is composed of both deterministic and stochastic components, regular peaks in the correlogram provide a strong indication of the presence of a cyclic component. A correlogram provides a powerful tool for detecting deterministic data which might be masked if presented in a random background. There are other less obvious applications for correlograms, but these are generally better interpreted from the Fourier Transform, the *power spectral density function*, which is discussed in the next section.

### C.3.14 Power Spectral Density Functions

The power spectral density function is a natural tool for considering the frequency properties of a time series. Inference regarding the power spectral density function is called an analysis in the *frequency domain*.

The power spectral density function has been defined as the 'average power' of the process, expressed as a function of frequency. If the average power of a process y(t) is defined as

$$\bar{P}_y = \lim_{T\to\infty} \frac{1}{T} \int_0^T y^2(t)dt = \psi_y^2 \qquad (C.52)$$

then the power contribution between frequencies f and (f+Δf) is

$$\bar{P}_y(f,f+\Delta f) = \psi_y^2(f,f+\Delta f) = \lim_{T\to\infty} \frac{1}{T} \int_0^T y^2(t,f,\Delta f)dt \qquad (C.53)$$

where $y(t,f,\Delta f)$ is the portion of y(t) in the frequency range from f to f+Δf. For small Δf, a power spectral density function $G_y(f)$ can be defined such that

$$\bar{P}_y(f,f+\Delta f) = \psi_y^2(f,f+\Delta f) \simeq G_y(f)\Delta f \qquad (C.54)$$

Therefore

$$G_y(f) = \lim_{\Delta f\to 0} \frac{\psi_y^2(f,f+\Delta f)}{\Delta f} = \lim_{\Delta f\to 0}\lim_{T\to\infty} \frac{1}{(\Delta f)T} \int_0^T y^2(t,f,\Delta f)dt \qquad (C.55)$$

The quantity $G_y(f)$ is always a real-valued, non-negative function.

Frequenty, for simplicity, the engineer eliminates the negative values of f, and for $f \geq 0$ the *one-sided* power spectral density function is given by

$$\int_0^\infty G_y(f)\,df = \psi_y^2 \tag{C.56}$$

Normally, the mean $\mu_y$ is subtracted from the time series. In this case the above relationship may be written as

$$\int_0^\infty G_y(f)\,df = \sigma_y^2 \tag{C.57}$$

### C.3.14.1 Normal Power Spectral Density Functions

It is sometimes necessary to compare time series which have different scales of measurement, and in these circumstances it is useful to normalize G(f) by dividing by the variance $\sigma_y^2$ and plot $G(f)/\sigma_y^2$ versus frequency f, the result is called the *normal power spectral density function*.

### C.3.14.2 Illustrations of Some Power Spectral Density Functions

Typical power spectral density functions ($G_y(f)$ versus f) for five time histories of Fig. C.11 are shown in Fig. C.21. These plots are called *power spectra*. It may be of interest to point out that power spectral density analysis has to be used with extreme care for periodic functions. The power spectral density function for a sine wave (Fig. C.3), as illustrated in Fig. C.21(b), is defined by

$$G_y(f) = \frac{Y^2}{2}\,\delta(f-f_o) \tag{C.58}$$

where $\delta(f-f_o)$ denotes a Dirac delta function at $f = f_o$. In words, the power spectral density function for a sine wave is infinitely large at the frequency of the sine wave and is zero at all other frequencies. However, the integral of the power spectral density function over any frequency range that includes the sinusoidal frequency has a finite value equal to the mean square value $Y^2/2$ of the sine wave. The spike spectrum for a sinusoidal process only results if the spectrum analysis is performed over an integer number of periods of the function. If it is performed over any length of the process, the resulting power spectral density function will not be a single infinite spike but a finite spectrum extending on both sides of the spike and having a negative power (dashed

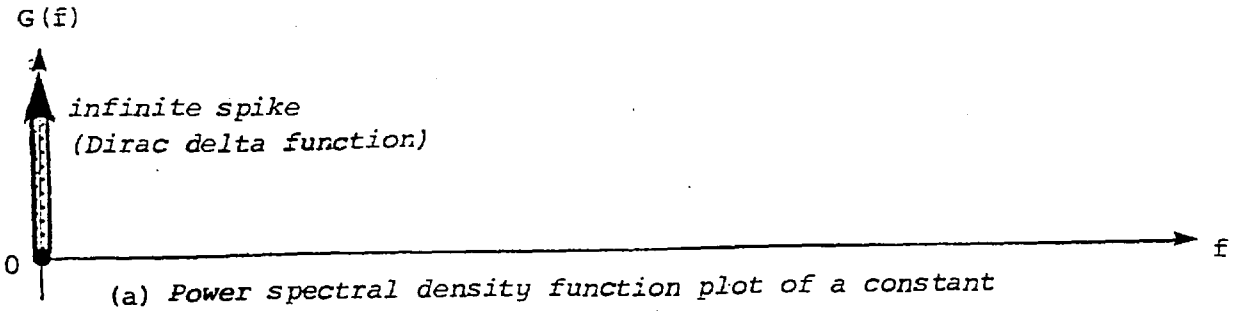


(a) *Power spectral density function plot of a constant*

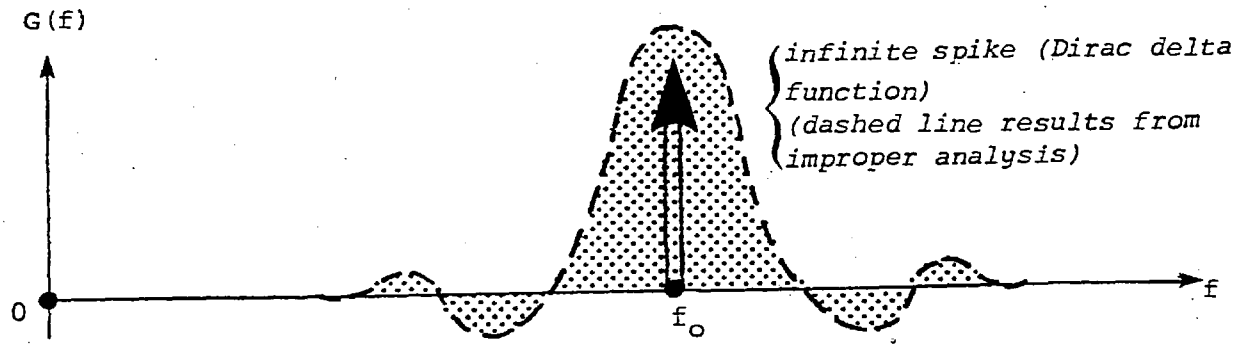


(b) *Power spectral density function plot of a sine wave*

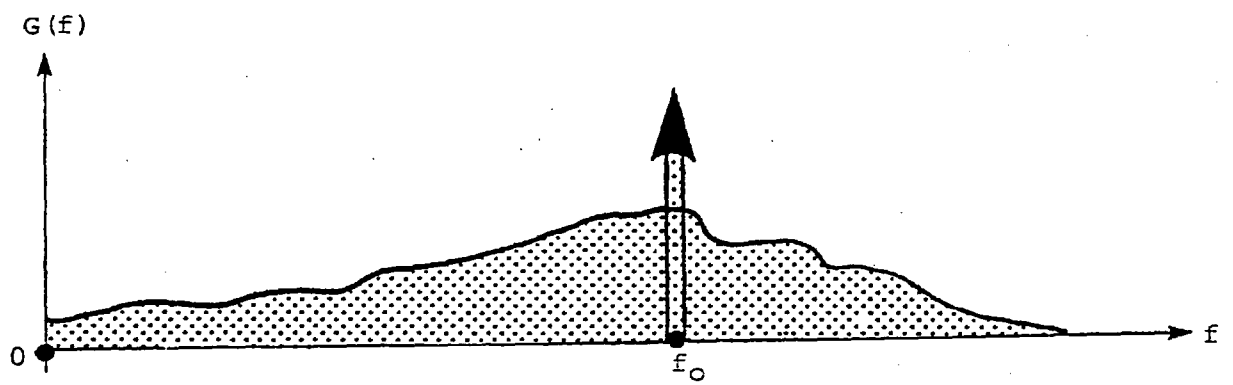


(c) *Power spectral density function plot of a sine wave plus random noise*

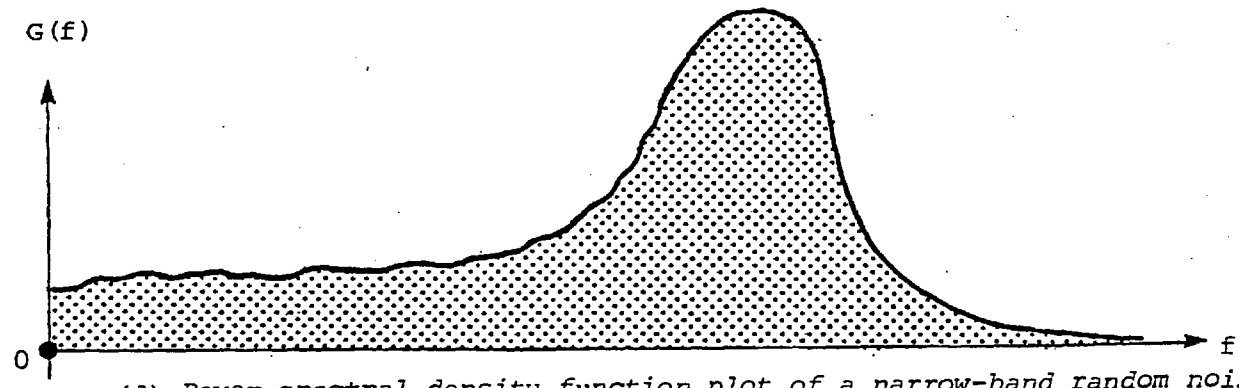


(d) *Power spectral density function plot of a narrow-band random noise*

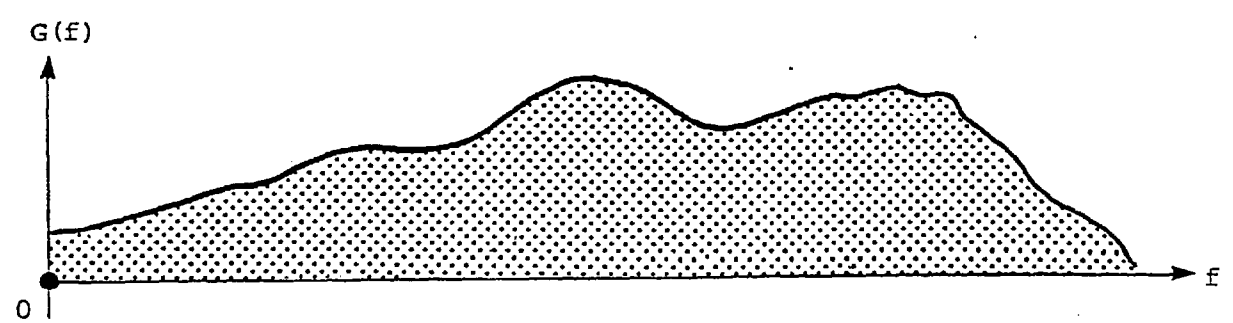


(e) *Power spectral density function plot of a wide-band random noise*

Fig. C.21 Power spectral density function plots

line). This is not the true power spectral density function (this problem will be discussed in detail in Section C.4) and therefore care must be taken to ensure that the analysis is synchronized with the process if periodic functions are present.

The relatively smooth and broad power spectrum illustrated in Fig. C.21(e) gives rise to the descriptive term 'wide-band' for this type of random data. For the hypothetical case of white noise, by definition, this spectrum is uniform over all frequencies. The power spectrum for the sine wave plus random noise is simply the sum of the power spectra for the sine wave and random noise separately, as illustrated in Fig. C.21(c). On the other hand, the power spectrum for the narrow-band noise in Fig. C.21(e) is sharply peaked as for a sine wave (hence the term 'narrow-band'), but still smoothly continuous as for random noise. Once again, the last four examples in Fig. C.21 illustrate a definite trend in the power spectrum changing pattern from the sine wave case to the wide-band noise case.

The adjective 'power', which is often prefixed to 'spectral density function' derives from the engineer's use of the word in connection with the passage of an electric current through a resistance. For a sinusoidal input, the power is directly proportional to the square of the amplitude of the oscillation. For a more general input, the power spectral density function describes how the power is distributed with respect to frequency. There are a number of other popular definitions of power spectra; *power spectrum*, *spectrum energy spectrum*, *energy density spectrum* and *energy density function* (often abbreviated as e.d.f.) are all used as synonymous terms, and when one of these terms is considered, a careful check must be made to understand the meaning of this term, because strictly speaking, mathematically, they may have a different meaning.

### C.3.14.3 Application of Power Spectral Density Functions to Water Waves

#### C.3.14.3.1 Average Power of the Process

The average power of any process is defined by Eq. (C.52) and is the mean square value of the process. If the water surface elevation is denoted by $y(t)$ and the still water surface by $\mu_y$, then it is customary to call the deviation from the still water surface $y_o(t)$, where

$$y_o(t) = y(t) - \mu_y \tag{C.59}$$

Therefore $y_o(t)$ is the fluctuation in water surface elevation about a zero mean. From Eq. (C.52) it can be concluded that

$$\overline{P}_{y_o} = \lim_{T\to\infty} \frac{1}{T} \int_o^T y_o^2(t)dt = E[y_o^2(t)] \tag{C.60}$$

where T refers to the length of the record. Further from Eqs. (C.21) and (C.23), it follows that

$$\overline{P}_{y_o} = \sigma_y^2 \tag{C.61}$$

C.3.14.3.2 Sinusoidal Waves

The sinusoidal wave process may be described by the following equation

$$y_o(t) = a \sin(2\pi f_o t) \tag{C.62}$$

where a is the amplitude of the water surface fluctuation. From Eqs. (C.60) and (C.61), it is concluded that

$$\overline{P}_{y_o} = \sigma_y^2 = a^2/2 \tag{C.63}$$

Using small amplitude wave theory, the expression for average total wave energy (kinetic plus potential) per unit surface area may be described as

$$\overline{e}_w = \rho g a^2/2 \tag{C.64}$$

Therefore, for sinusoidal waves

$$\left.\begin{aligned} &\overline{e}_w = \rho g \overline{P}_{y_o} = \rho g \sigma_y^2 \quad (a) \\ &\frac{\overline{e}_w}{\rho g} = \sigma_y^2 * \quad (b) \end{aligned}\right\} \tag{C.65}$$

*It has been shown (Thompson and Gilberd, 1971) that for complex waves of a random nature (e.g. sea waves), the variance is equal to the energy of the wave $\overline{e}_w/\rho g = \sigma_y^2 = \int_o^{+\infty} G_y(f)df$.

Hence the function $G_y(f)$ is called the energy spectrum. More correctly, $G_y(f)$ is the energy density function of the waves since it gives information on the density of energy at different frequencies. The variance may be regarded as the total energy.

### C.3.14.3.3 Almost Periodic Waves

The mathematical expression for wave motion which is *almost periodic* is

$$y_o(t) = \sum_{n=1}^{\infty} a_n \sin(2\pi f_n t + \theta_n) \tag{C.66}$$

and from Eqs. (C.60) and (C.61), it follows that

$$\left.\begin{aligned} \overline{P}_{y_o} = \sigma^2_{y_o} &= \lim_{T\to\infty} \frac{1}{T} \int_o^T \left[\sum_{n=1}^{\infty} a_n \sin(2\pi f_n t + \theta_n)\right]^2 dt \\ \overline{P}_{y_o} = \sigma^2_{y_o} &= \sum_{n=1}^{\infty} a_n^2/2 \end{aligned}\right\} \tag{C.67}$$

Thus the total average power is the sum of the powers contributed by each individual wave component. The corresponding discrete power spectrum is shown in Fig. C.22.

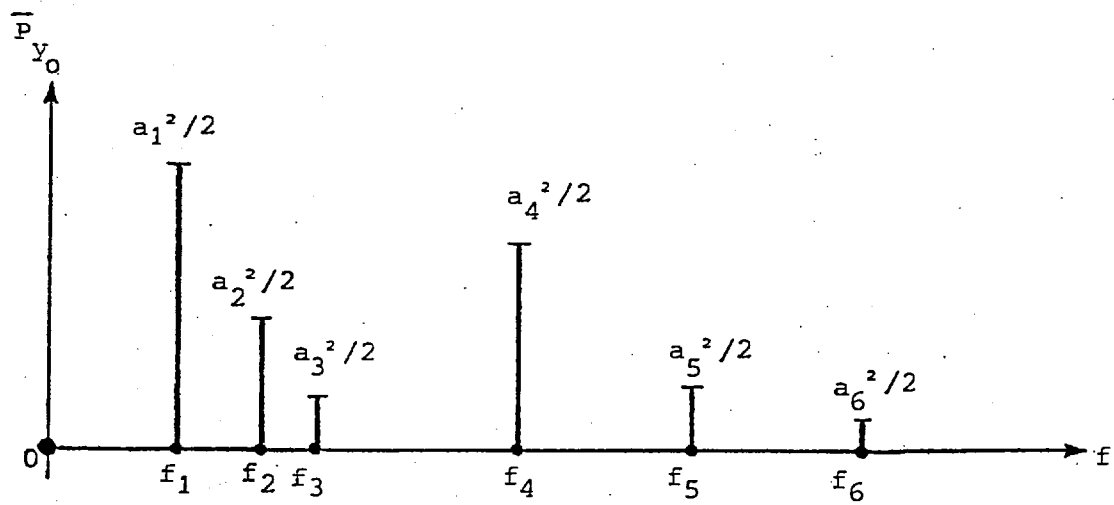


Fig. C.22 Discrete power spectral density function of an almost periodic wave

### C.3.14.3.4 Ergodic Random Waves

From the previous section, it can be concluded that

$$\overline{P}_{y_o} = \sigma_y^2 = \int_o^{\infty} G(f)df \qquad f \geq 0 \tag{C.68}$$

The average power of the recorded process is equal to the area under the power spectral density function. If the assumption is made that the total process can be described by a number of linearly superimposed sinusoidal waves, Eqs. (C.65) applies and therefore the average power calculated from the recorded process can be related to the average wave energy.

This is where the confusion between 'Power Density Spectrum' and 'Energy Density Spectrum' originated. It is the power density spectrum of the recorded process $y_o(t)$ (the distribution of power with frequency) that is computed. This power spectrum can only be related to the wave energy density if the above assumption is made.

### C.3.14.4 Importance of Energy Density Functions

The energy density function may be used to detect oscillations or cycles in the time series. Its advantage over correlogram is its ability to detect cycles of noncommensurable periods. The curve of energy density function specifies the allocation of energy (or power) among all the frequencies present. Peaks in the energy density function correspond to frequencies which account for a large percentage of the total energy (Fig. C.23). The inverses of these frequencies then give the periods of significant cycles in the time series, the significance being judged by the amount that a particular cycle contributes towards the variance of the whole time series.

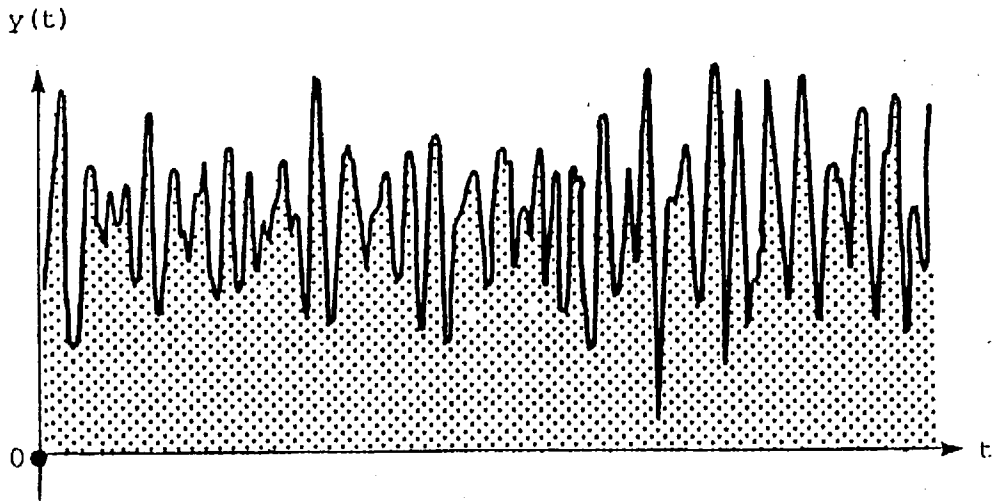


(a) *High frequency data*

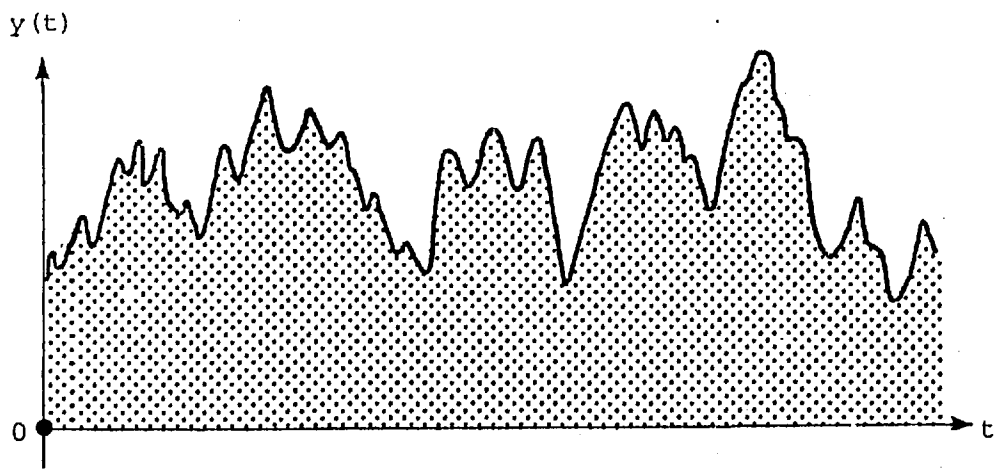


(c) *Low frequency data*

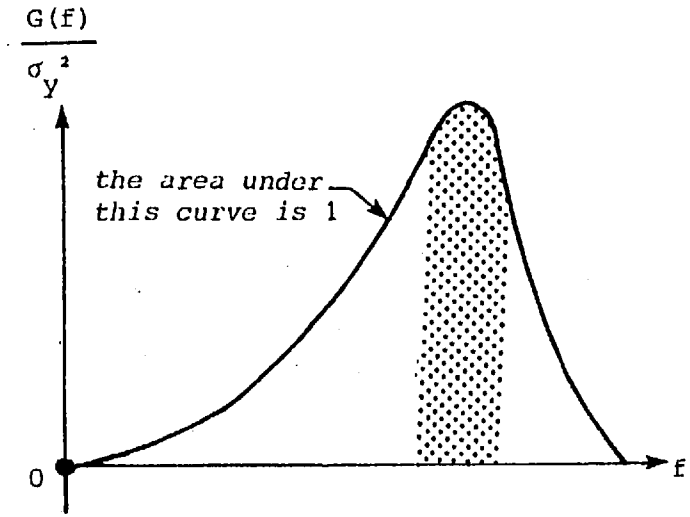


(c) *Power spectral density function plot of a high frequency data*

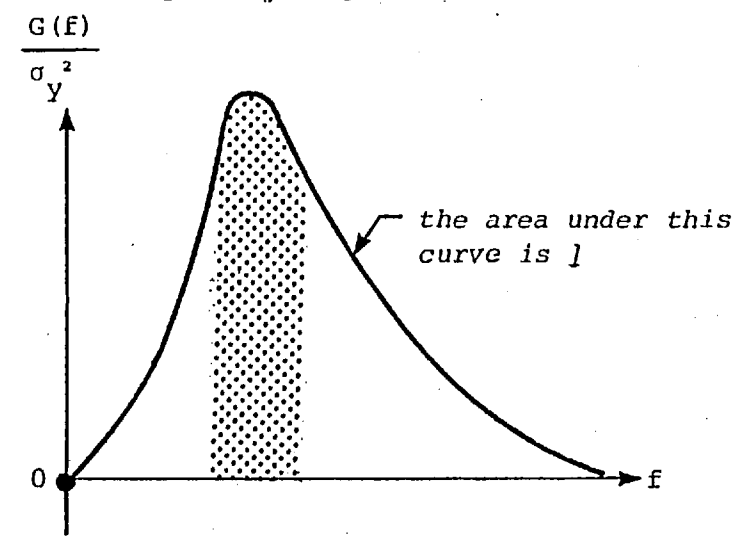


(d) *Power spectral density function plot of a low frequency data*

Fig. C.23 Comparison of two different types of data

## C.4 SPECTRAL ANALYSIS USING FOURIER TRANSFORM TECHNIQUES

The techniques of spectral analysis were greatly influenced by an important development made by Cooley and Tukey (1965) who perfected a numerical method called the Fast Fourier Transform. The employment of modern digital computers to facilitate these numerical treatments has made the Fast Fourier Transform particularly important.

The author felt that it was necessary to start from the simplest concepts and from these to develop a coherent presentation of the subject. Firstly a brief review is presented of Fourier series and of Fourier Transforms and their application to spectral analysis. Areas of particular difficulty when using Fourier Transforms are discussed in some detail.

### C.4.1 Representation of a Periodic Function by a Fourier Series

A function f(t) can be represented by a Fourier series if it is continuous over some interval T. The following identity applies

$$f(t) = \sum_{n=-\infty}^{\infty} H_n \, e^{i\omega n t} \tag{C.69}$$

where

$$\omega = 2\pi/T = 2\pi f \tag{C.70}$$

and

$$H_n = \frac{1}{T} \int_{-T/2}^{T/2} f(t) e^{-in\omega t} dt \tag{C.71}$$

In this thesis, for convenience, the angular frequency, $\omega$, will be used in mathematical formulae for conciseness, but the frequency f is often used for interpretation.

### C.4.2 The Fourier Integral and Transform

The Fourier integral theorem follows from (C.69) and (C.71) if the interval integration in (C.71) is extended to $T \to \infty$. Assuming f(t) satisfies the Dirichlet conditions* over any interval the following integral

$$M = \int_{-\infty}^{+\infty} |f(t)| dt \tag{C.72}$$

* If f(t) is a bounded periodic function which in any one period has at most a finite number of local maxima and minima and a finite number of points of discontinuity, then the Fourier series of f(t) converges to f(t) at all points where f(t) is continuous, and converges to the average of the right-and-left-hand limits of f(t) at each point where f(t) is discontinuous

exists. By introducing a new variable $\omega_n$ defined as

$$\left.\begin{aligned} \omega_n &= \frac{2\pi n}{T} = 2\pi n f = n\omega \qquad n = 0,1,2,3, \ldots . && \text{(a)} \\ \Delta\omega_n &= \frac{2\pi n}{T} - \frac{2\pi(n-1)}{T} = \frac{2\pi}{T} = 2\pi f && \text{(b)} \end{aligned}\right\} \quad \text{(C.73)}$$

Eq. (C.69) can be rewritten as

$$\left.\begin{aligned} f(t) &= \sum_{\omega_n=-\infty}^{\infty} H(\omega_n) e^{i\omega_n t} && \text{(a)} \\ \text{where} \\ H(\omega_n) &= \frac{1}{T}\int_{-T/2}^{T/2} f(t) e^{-i\omega_n t} dt && \text{(b)} \end{aligned}\right\} \quad \text{(C.74)}$$

As $T \to \infty$, $\Delta\omega_n \to 0$ and Eq. (C.74a) degenerates into a double integral. Removing the subscript n, Eq. (C.74a) can be written as

$$f(t) = \int_{\omega=-\infty}^{\infty} \left[\frac{1}{2\pi} e^{i\omega t} \int_{t=-\infty}^{\infty} f(t) e^{-i\omega t} dt\right] d\omega \qquad \text{(C.75)}$$

This is known as the Fourier integral. From this it is possible to define

$$\left.\begin{aligned} f(t) &= \frac{1}{\sqrt{2\pi}} \int_{-\infty}^{+\infty} H_1(\omega) e^{i\omega t} d\omega && \text{(a)} \\ \text{and} \\ H_1(\omega) &= \frac{1}{\sqrt{2\pi}} \int_{-\infty}^{+\infty} f(t) e^{-i\omega t} dt && \text{(b)} \end{aligned}\right\} \quad \text{(C.76)}$$

Eqs. (C.76a) and (C.76b) are called a *Fourier Transform pair.* If Eq. (C.76b) is considered to be the *forward transform,* then Eq. (C.76a), which recovers the original function f(t) from its transform, can be called the *inverse transform.* The *scale factor* $1/\sqrt{2\pi}$ is chosen arbitrarily so that the transform in either direction has the same scale factor. If another factor is chosen for the forward transform then that for the inverse must be adjusted accordingly, i.e., if $1/2\pi$ is chosen for Eq. (C.76a) then 1 must be taken for Eq. (C.76b). In terms of the frequency f, the Eqs. (C.76a) and (C.76b) representing the Fourier transform pair can be written as (choosing the scale factors equal to 1 and $\pi/2$ respectively)

$$g(f) = F[f(t)] = \int_{-\infty}^{+\infty} f(t)e^{-2\pi ift}dt \quad \text{(a)}$$

$$f(t) = \int_{-\infty}^{+\infty} g(f)e^{2\pi ift}dt \quad \text{(b)} \qquad \text{(C.77)}$$

where F[ ] is the short form for Fourier Transform.

### C.4.2.1 Convolution Integral

The *Convolution* or *Falung integral* is defined as

$$\int_{o}^{t} f(t-\xi)g(\xi)d\xi \qquad \text{(C.78)}$$

and is frequently denoted simply by $f(t)*g(t)$.

### C.4.2.2 Fourier Transform of Products of Two Functions

The Fourier transform of $f_1(t)f_2(t)$ is

$$F[f_1(t)f_2(t)] = \int_{-\infty}^{+\infty} g_1(\xi)g_2(f-\xi)d\xi = \int_{-\infty}^{+\infty} g_1(f-\xi)g_2(\xi)d\xi = g_1(f)*g_2(f) \qquad \text{(C.79)}$$

where $g_1(f)$ and $g_2(f)$ are, respectively, the Fourier Transforms of $f_1(t)$ and $f_2(t)$.

### C.4.3 Application of Fourier Transforms in Spectral Analysis

An important property of the power spectral function lies in its relationship to the autocovariance function. Specifically, for stationary data, the two functions are related by a Fourier transform (Jenkins and Watts, 1968) as follows

$$G_y(f) = \int_{-\infty}^{+\infty} \gamma_y(\tau)e^{-i2\pi f\tau}d\tau \qquad \text{(C.80)}$$

The reverse Fourier transform is

$$\gamma_y(\tau) = \int_{-\infty}^{+\infty} G_y(f)e^{i2\pi f\tau}df \qquad \text{(C.81)}$$

### C.4.4 Windows

Any experimental measurement is limited to a finite time-span. The record of data under consideration is obtained by looking at the signal for a period of T in Fig. C.24(a) and neglecting anything that happened before and after that period. Limiting the record length to a certain period T can be expressed mathematically by multiplying the infinite continuous record in Fig. C.24(b) by a *data window* as described by the relation

$$\left.\begin{aligned} w(t) &= 1, \qquad |t| \leq T/2 \qquad \text{(a)} \\ w(t) &= 0, \qquad |t| > T/2 \qquad \text{(b)} \end{aligned}\right\} \text{(C.82)}$$

The finite sample $y(t)w(t)$ is equivalent to looking at the infinite record through a window $w(t)$ which ensures that the record is zero everywhere outside the sample. This window itself has a Fourier transform $W(f)$

$$\left.\begin{aligned} W(f) &= \int_{-T/2}^{T/2} e^{-2\pi i f t}\,dt = \int_{-T/2}^{T/2} [\cos(2\pi f t) - i\sin(2\pi f t)]\,dt \\ &= \sin(\pi f T)/(\pi f) = T\,\frac{\sin(\pi f T)}{(\pi f T)} = T\,J(\pi f T) \end{aligned}\right\} \text{(C.83)}$$

where $J(u)$ is defined as

$$J(u) = \frac{\sin u}{u} \qquad \text{(C.84)}$$

The function $J(u)$ is plotted in Fig. C.25.

### C.4.5 Fourier Transform of a Sine Wave

It is important to fully appreciate the role played by the data window when a Fourier Transform is applied to the resultant record (Bergland, 1969). In order to demonstrate these effects, it is instructive to retrace the mathematical developments of a wave of infinite duration and also that of a wave of finite duration. The analysis in each of the two cases demonstrates the use of window functions.

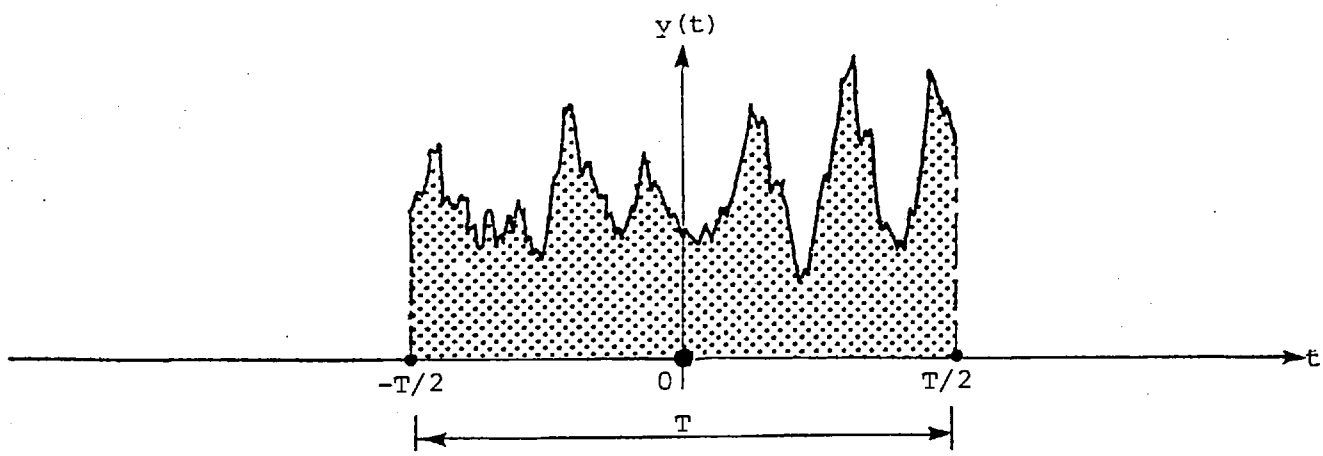


(a) *Sample of duration* T

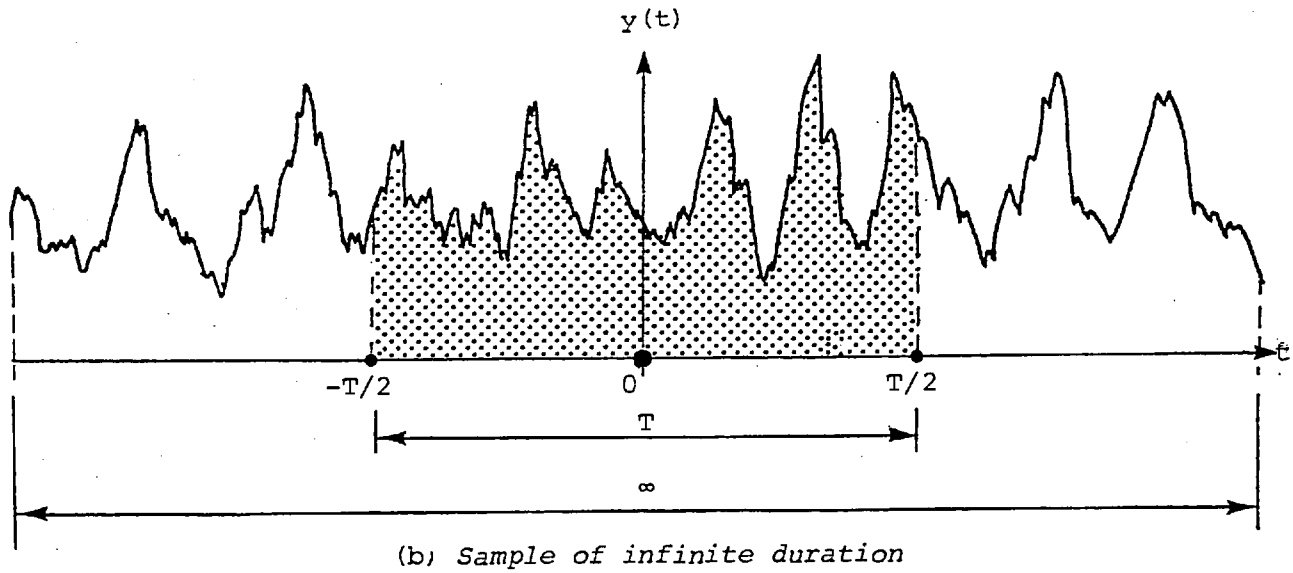


(b) *Sample of infinite duration*

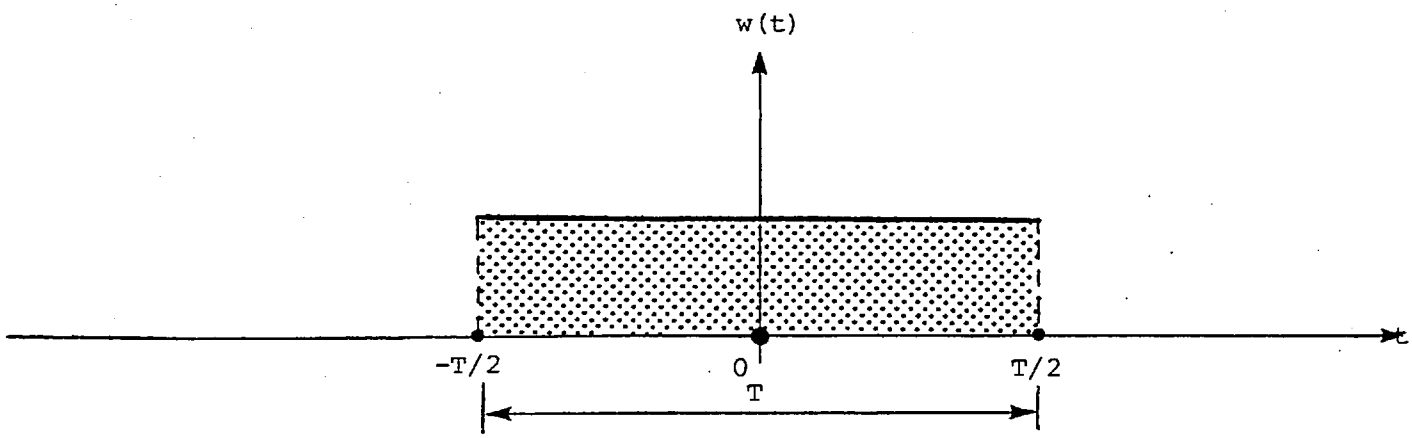


(c) *Rectangular data window of duration* T

Fig. C.24

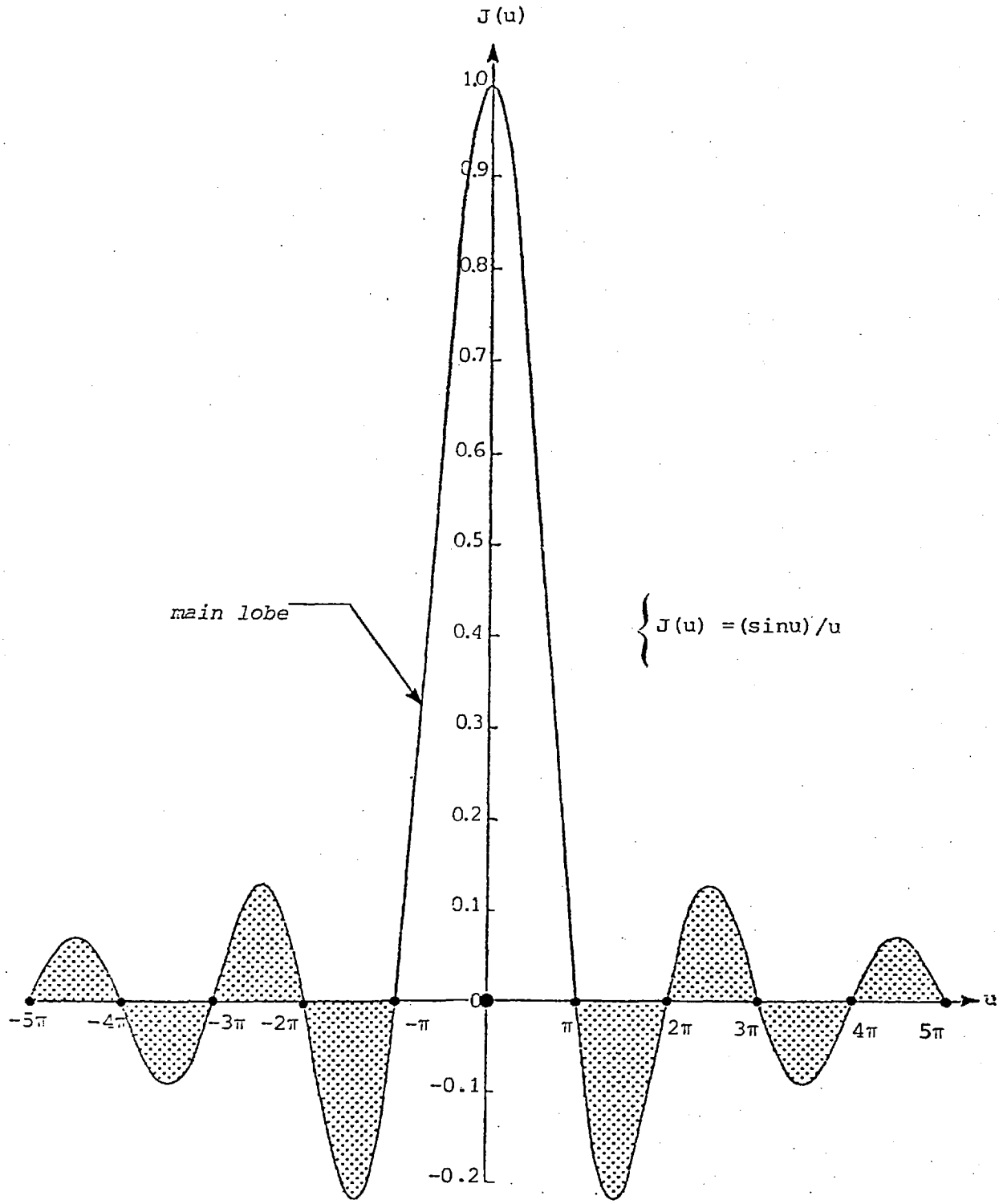
J(u)
1.0
0.9
0.8
0.7
0.6
0.5
0.4
0.3
0.2
0.1
0
-0.1
-0.2
main lobe
J(u) = (sinu)/u
-5π
-4π
-3π
-2π
-π
π
2π
3π
4π
5π
u

Fig. C.25

### C.4.5.1 The Infinite Continuous Record

Given a cosine wave of amplitude Y and frequency $f_o$ defined for all values of time t by

$$y(t) = Y\cos(2\pi f_o t) \tag{C.85}$$

Viewed through a window of infinite extent its Fourier Transform is given by

$$\left.\begin{aligned} F[y(t)] &= \int_{-\infty}^{+\infty} y(t)e^{-2\pi ift}dt \quad (a)\\ F[y(t)] &= \int_{-\infty}^{+\infty} Y\cos(2\pi f_o t)e^{-2\pi ift}dt \quad (b)\end{aligned}\right\} \tag{C.86}$$

With the *Euler relationship**, the trigonometric function can be replaced by the sum of the two complex exponential terms. Thus

$$F[y(t)] = \frac{Y}{2}\int_{-\infty}^{+\infty}[e^{2\pi it(f_o-f)} + e^{-2\pi it(f_o+f)}]dt \tag{C.87}$$

Using the relationships presented in Appendix I, the above equation can be written as

$$F[y(t)] = g(f) = \tfrac{1}{2}Y\{\delta(f-f_o) + \delta(f+f_o)\} \tag{C.88}$$

This 'mapping' of a cosine wave from the time domain into frequency space is illustrated in Fig. C.26.

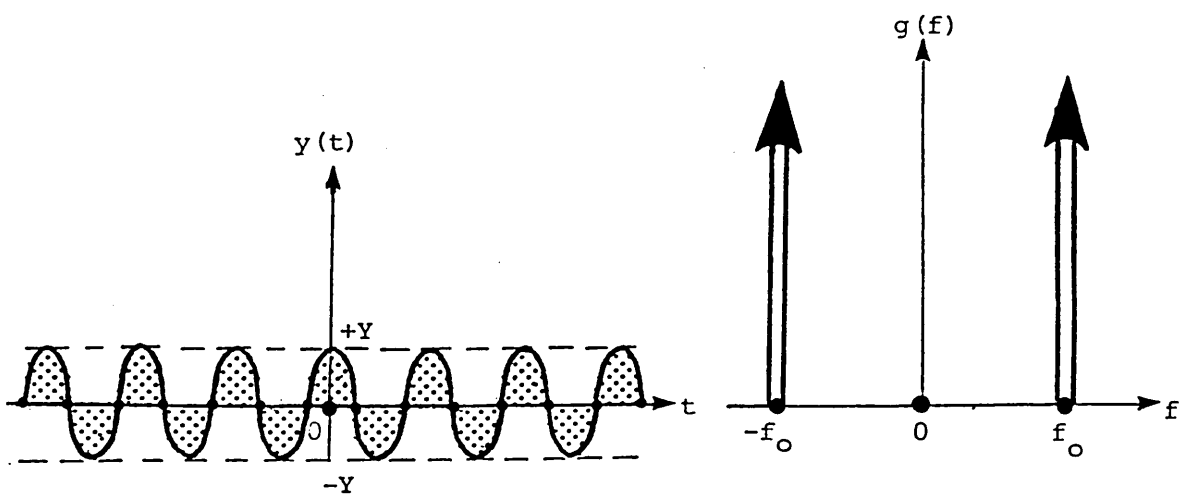


Fig. C.26 A cosine wave and its Fourier Transform

It must be emphasised that the ordinate of the Dirac pulses is indefinite. The area under each pulse, however, has a finite value, thus

$$A = \int_{-\infty}^{+\infty}\frac{Y}{2}[\delta(f-f_o) + \delta(f+f_o)]df = Y \tag{C.89}$$

* Euler relationship is defined as $e^{i\theta} = \cos\theta+i\sin\theta$, and its obvious companion is $e^{-i\theta} = \cos\theta-i\sin\theta$.

### C.4.5.2 The Finite Continuous Record

Now confining attention to the case where $y(t) = Y\cos(2\pi f_o t)$ is viewed through a finite window $w(t)$, where

$$w(t) = 1, \quad |t| \leq T/2 \qquad \text{(a)}$$
$$w(t) = 0, \quad \text{otherwise} \qquad \text{(b)} \qquad \text{(C.90)}$$

Seeing the function $y(t)$ through a window $w(t)$ is expressed mathematically by forming the product of these two functions. The Fourier Transform of this product can be evaluated most readily by calling on the Convolution integral as defined by Eqs. (C.78) and (C.79). The Fourier Transform of $w(t)$ is found from Eq. (C.83) as

$$W(f) = T\,\frac{\sin[(T/2)2\pi f]}{(T/2)2\pi f} \qquad \text{(C.91)}$$

Using the relationship (C.79), it can be written that

$$F[y(t)] = G(f)*W(f)$$
$$= \frac{AT}{2}\int_{-\infty}^{+\infty}\{\delta[\zeta-(f-f_o)] + \delta[\zeta-(f+f_o)]\}\,\frac{\sin(T/2)\pi\zeta}{(T/2)2\pi\zeta}\,d\zeta \qquad \text{(C.92)}$$

where $G(f)$ is the Fourier Transform of the infinite cosine wave. Now, using the so called 'shifting property' of the Dirac delta function (Appendix I), it follows that

$$G(f) * W(f) = \frac{YT}{2}\left\{\frac{\sin[2\pi T(f-f_o)/2]}{2\pi T(f-f_o)/2} + \frac{\sin[2\pi T(f+f_o)/2]}{2\pi T(f+f_o)/2}\right\} \qquad \text{(C.93)}$$

Using the relationship (C.91), the Convolution $G(f)*W(f)$ becomes

$$G(f)*W(f) = g(f) = \frac{YT}{2}\{J[\pi T(f-f_o)] + J[\pi T(f+f_o)]\} \qquad \text{(C.94)}$$

The 'mapping' of this finite portion of a cosine wave is indicated in Fig. C.27. The ordinates in the frequency space are now finite everywhere and the maximum is $(YT/2)[1 + \sin(2\pi f_o T)/(2\pi f_o T)]$.

It is of interest to examine the area under the curve defined by Eq. (C.94) and to compare it to that given by Eq. (C.89). Here, it can be written

$$A = \frac{YT}{2}\int_{-\infty}^{+\infty}\left\{\frac{\sin[2\pi T(f-f_o)/2]}{2\pi T(f-f_o)/2} + \frac{\sin[2\pi T(f+f_o)/2]}{2\pi T(f+f_o)/2}\right\}df \qquad \text{(C.95)}$$

This integral* reduces to the following after some mathematical manipulation

$$A = Y \qquad \text{(C.96)}$$

---

* It should be noted that $\sin u/u$ is an even function and $\int_o^\infty \frac{\sin mu}{u}\,du = \pi/2$, 0, or $-\pi/2$, as m is positive, 0, or negative (Dwight, 1961).

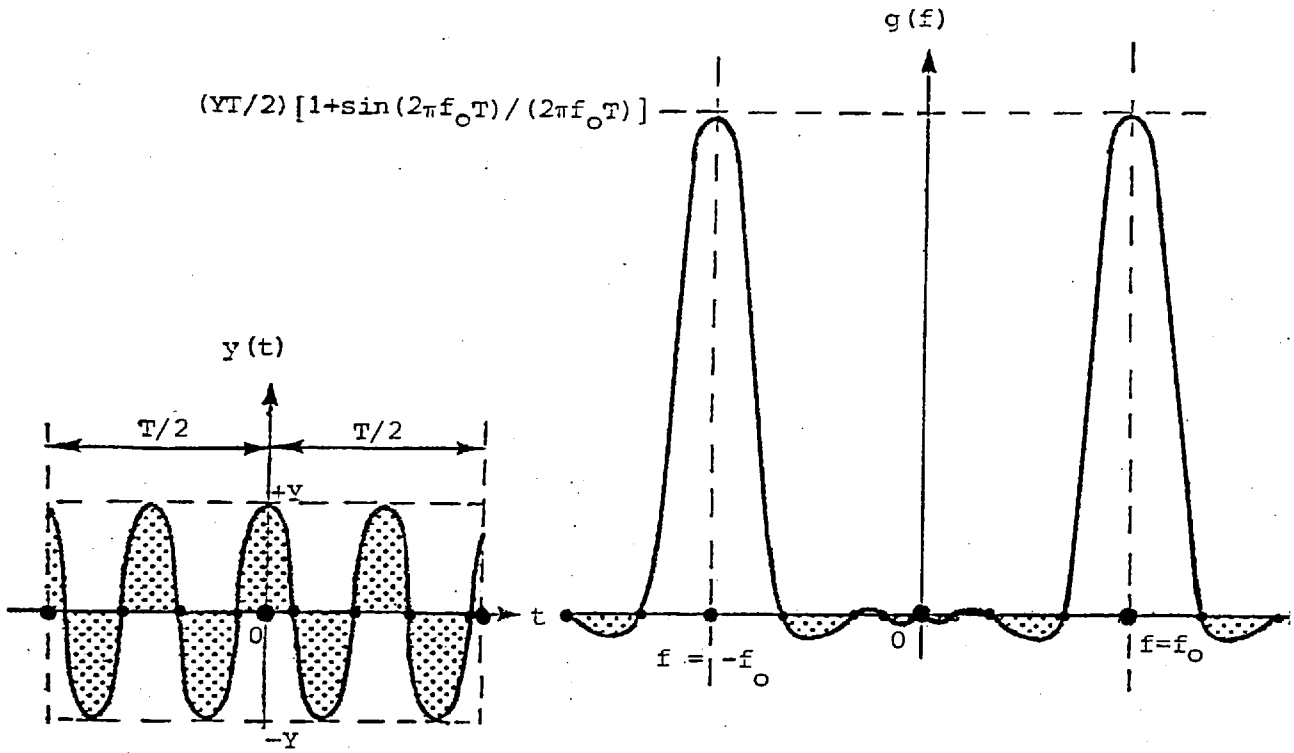


Fig. C.27 Truncated cosine-wave and its Fourier Transform

This means, that the area under the transformed function remains the same, whether a finite or an infinite record is used. The only difference lies in how this area is distributed over the frequency-axis.

Since the Fourier Transform is a *linear operator* it is apparent from Eq. (C.94), that if several frequencies are present in a signal the transforms are superimposed in the frequency domain. Thus the ordinate at $f = f_o$ would be, for several frequencies including $f_o$, the sum of the maximum due to the $f_o$ frequency and the contributions from all other frequencies present. The magnitude of these contributions depends on the amplitude $Y_1$ and the frequency difference $(f_o - f_1)$, where $Y_1$ and $f_1$ are the amplitude and frequency of some second signal. For two different cosine waves Eq. (C.94) becomes

$$\left.\begin{aligned} F[y(t)] = g(f) &= G(f) * W(f) \\ &= \frac{YT}{2}\left\{\frac{\sin[2\pi T(f-f_o)/2]}{2\pi T(f-f_o)/2} + \frac{\sin[2\pi T(f+f_o)/2]}{2\pi T(f+f_o)/2}\right\} \\ &+ \frac{Y_1 T}{2}\left\{\frac{\sin[2\pi T(f-f_1)/2]}{2\pi T(f-f_1)/2} + \frac{\sin[2\pi T(f+f_1)/2]}{2\pi T(f+f_1)/2}\right\} \end{aligned}\right\} \quad (C.97)$$

where

$$y(t) = Y\cos(2\pi f_o t) + Y_1 \cos(2\pi f_1 t) \quad (C.98)$$

### C.4.5.3 The Finite Record with Discrete Values Only

When the data is only available in digital form, this can be thought of as passing the signal through a window consisting of a 'Dirac comb', as illustrated in Fig. C.28. Since the finite record length is specified by the width T of the continuous window w(t), the Dirac comb itself can be considered infinite in extent.

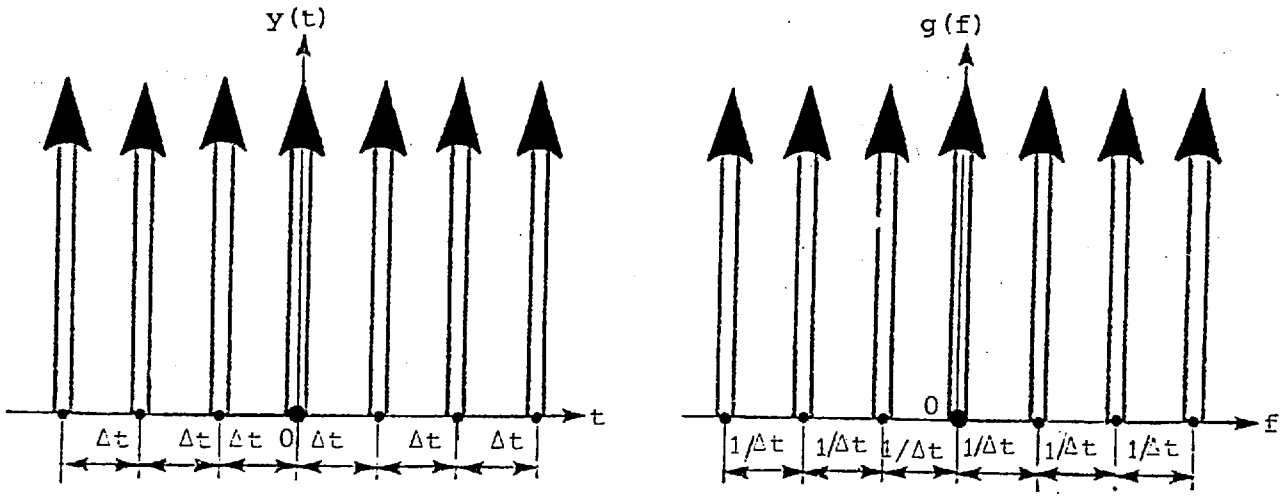


Fig. C.28 The Dirac comb and its Fourier Transform

To obtain the Fourier transform of the finite and discrete data, it is necessary to employ the Convolution integral again. To achieve this it is first necessary to derive the Fourier transform of the Dirac comb.

The Dirac comb can be expressed analytically as

$$c(t) = \sum_{n=-\infty}^{\infty} (t-n\Delta t) = \nabla(t,\Delta t) \qquad \text{(C.99)}$$

Using Eq. (77a) the Fourier transform of (C.99) can be written as

$$C(f) = \int_{-\infty}^{+\infty} \sum_{n=-\infty}^{n=+\infty} \delta(t-n\Delta t)\, e^{-2\pi i f t} dt \qquad \text{(C.100)}$$

The order of integration and summation can be interchanged. Then, if the identity (I.2) is applied to each element of the summation and the substitution n = -m is made, the final expression for C(f) becomes

$$C(f) = \sum_{m=-\infty}^{\infty} e^{2\pi i f m \Delta t} \qquad \text{(C.101)}$$

In fact Lighthill (1961) has shown that

$$\sum_{m=-\infty}^{\infty} \delta(\Omega - ma') = \frac{1}{a'} \sum_{m=-\infty}^{\infty} e^{2\pi i m\Omega/a'} \tag{C.102}$$

Letting $\Delta t = 1/a'$, the Fourier series to the right of Eq. (C.101) becomes

$$\sum_{m=-\infty}^{\infty} e^{2\pi i f m \Delta t} = \frac{1}{\Delta t} \sum_{m=-\infty}^{\infty} \delta\left(f - \frac{m}{\Delta t}\right) \tag{C.103}$$

Hence the Fourier Transform of a Dirac comb leads to another Dirac comb, so that

$$C(f) = \frac{1}{\Delta t} \sum_{m=-\infty}^{\infty} \delta\left(f - \frac{m}{\Delta t}\right) = \frac{1}{\Delta t} \nabla(f, 1/\Delta t) \tag{C.104}$$

The introduction of the Dirac comb modifies the transform of the original cosine function (taken as an example) further. The resultant transformation is obtained by employing the transforms represented by Eqs. (C.94) and (C.104).

In other words, the product $y(t).w(t).c(t)$ in the time domain corresponds to, in the frequency domain, the convolution of the respective Fourier Transforms $G(f)*W(f)*C(f)$

$$\left.\begin{aligned} g(f) = G(f)*W(f)*C(f) = \int_{-\infty}^{+\infty} \frac{YT}{2} \left\{ \frac{\sin[2\pi T(\xi - f_o)/2]}{2\pi T(\xi - f_o)/2} + \frac{\sin[2\pi T(\xi + f_o)/2]}{2\pi T(\xi + f_o)/2} \right\} \\ \times \frac{1}{\Delta t} \sum_{m=-\infty}^{\infty} \delta\left(f - \frac{m}{\Delta t} - \xi\right) d\xi \end{aligned}\right\} \tag{C.105}$$

Integrating and making use of the shifting property of the Dirac delta function, the final result is

$$\left.\begin{aligned} g(f) = \frac{YT}{2} \sum_{m=-\infty}^{\infty} \frac{1}{\Delta t} \left\{ \frac{\sin\left[2\pi T \frac{(f - m/\Delta t) - f_o}{2}\right]}{2\pi T \frac{(f - m/\Delta t) - f_o}{2}} + \frac{\sin\left[2\pi T \frac{(f - m/\Delta t) + f_o}{2}\right]}{2\pi T \frac{(f - m/\Delta t) + f_o}{2}} \right\} \\ = \frac{YT}{2} \sum_{m=-\infty}^{\infty} \frac{1}{\Delta t} \left\{ J\left[\pi T\left(f - \frac{m}{\Delta t} - f_o\right)\right] + J\left[\pi T\left(f - \frac{m}{\Delta t} + f_o\right)\right] \right\} \end{aligned}\right\} \tag{C.106}$$

Equation (C.106) represents a *continuous* rather than a discrete function of frequency in the frequency domain. It consists of a sum of damped sine curves, and has the appearance shown in Fig. C.29.

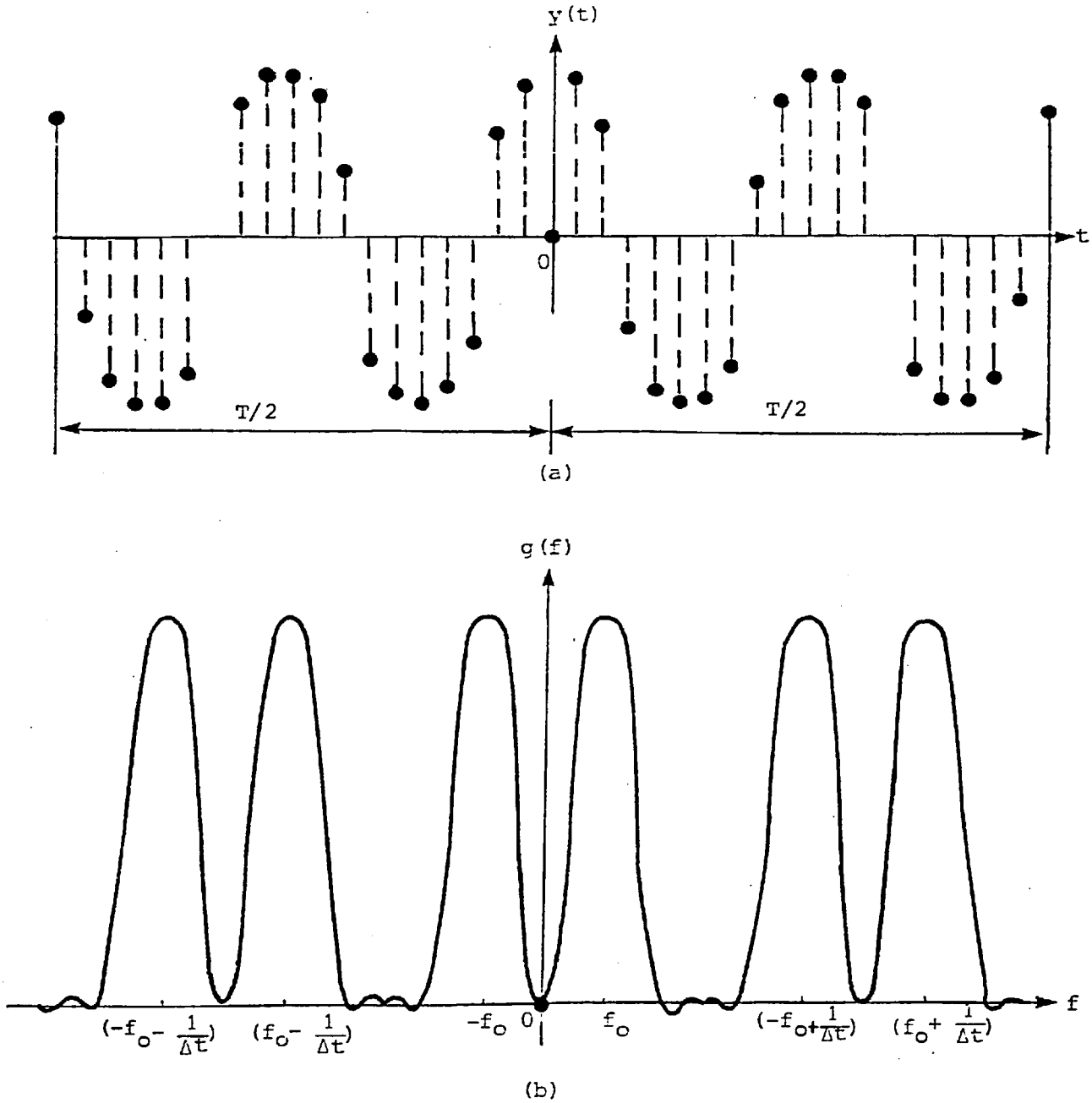


Fig. C.29 Digitised truncated cosine function and its Fourier Transform

### C.4.6 Leakage

A rectangular data window of width T defined in the time domain by Eqs. (C.82) and illustrated in Fig. C.24(c) was shown to have a Fourier Transform represented by Eq. (C.83). Referring to Fig. C.25, this frequency window consists of a series of damped sinusoidal oscillations or lobes. It has a value of unity where u = 0 and decays to zero at $u = \pm\infty$. The amplitude maxima of the function $J(u) = \frac{\sin u}{u}$ occur at $u = 0, 3\pi/2, 5\pi/2, 7\pi/2, 9\pi/2$ etc. and the successive magnitudes of the function are 1.0, -0.212, 0.127, -0.091, 0.071 etc. The first zeroes of the function on either side of the peak occur at $u = \pm\pi$ or $\pi fT = \pm\pi$ or $f = \pm 1/T$, i.e. the larger T the narrower the major lobe of the function.

The effect of the finite sample of the cosine wave can now be seen by comparing the infinite and finite duration results (Eqs. (C.88) and (C.94)). The infinite duration case has two spikes at $f = \pm f_o$ whereas in the finite duration case the spikes have become two principal lobes (compare Fig. C.26 with Fig. C.27) about $f = \pm f_o$ with finite heights and widths. These widths get smaller as the sample length increases, i.e. the lobes become more like a spike as the sample length approaches infinity. Thus the window has the effect of spreading or smearing the result in the frequency domain.

The presence of side lobes introduces certain distortions in the frequency domain. The energy associated with a frequency $f_o$ can contribute to that registered by adjacent frequencies. This phenomenon is usually referred to as *leakage*. Indeed if the window is rectangular, the side lobes in the frequency domain (Fig. C.25) are unacceptably large. The most common method of combating this difficulty involves modifying the shape of the data window by reducing the abrupt termination of w(t) in Fig. C.24(c) at $t = \pm T/2$. Among the best known modified data windows are 'Hanning' or 'Hamming' windows. Their principal aim is to suppress, to some extent, the unwanted side lobes, thereby curtailing energy leakage into adjacent frequency ranges.

### C.4.6.1 Hanning Window

The Hanning window (*cosine-hump window*) has the form

$$\left.\begin{aligned} w(t) &= 0.5[1 + \cos(\pi t/T)], \quad -T \leq t \leq T \qquad \text{(a)} \\ w(t) &= 0, \qquad\qquad\qquad\quad \text{otherwise} \qquad\qquad \text{(b)} \end{aligned}\right\} \text{(C.107)}$$

For T = 20, the function is illustrated in Fig. C.30(a). Its Fourier Transform $W_1(f)$ may be calculated as

$$W_1(f) = F[w(t)] = \int_{-\infty}^{+\infty} w(t) e^{-2\pi i f t} dt \qquad \text{(C.108)}$$

With the Euler relationship, the trigonometric function can be replaced by the sum of the two complex exponential terms. Thus

$$W_1(f) = \tfrac{1}{2} \int_{-T}^{T} [1 + \tfrac{1}{2}(e^{\pi i t/T} + e^{-\pi i t/T})] e^{-2\pi i f t} dt \qquad \text{(C.109)}$$

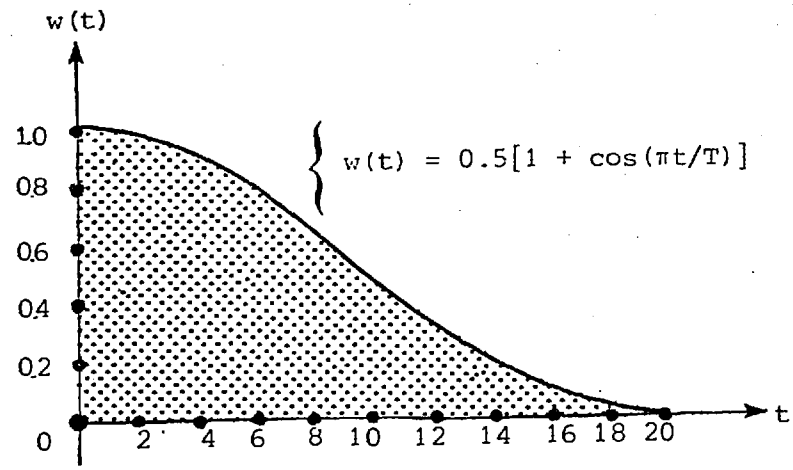


(a) *The Hanning window with* T = 20

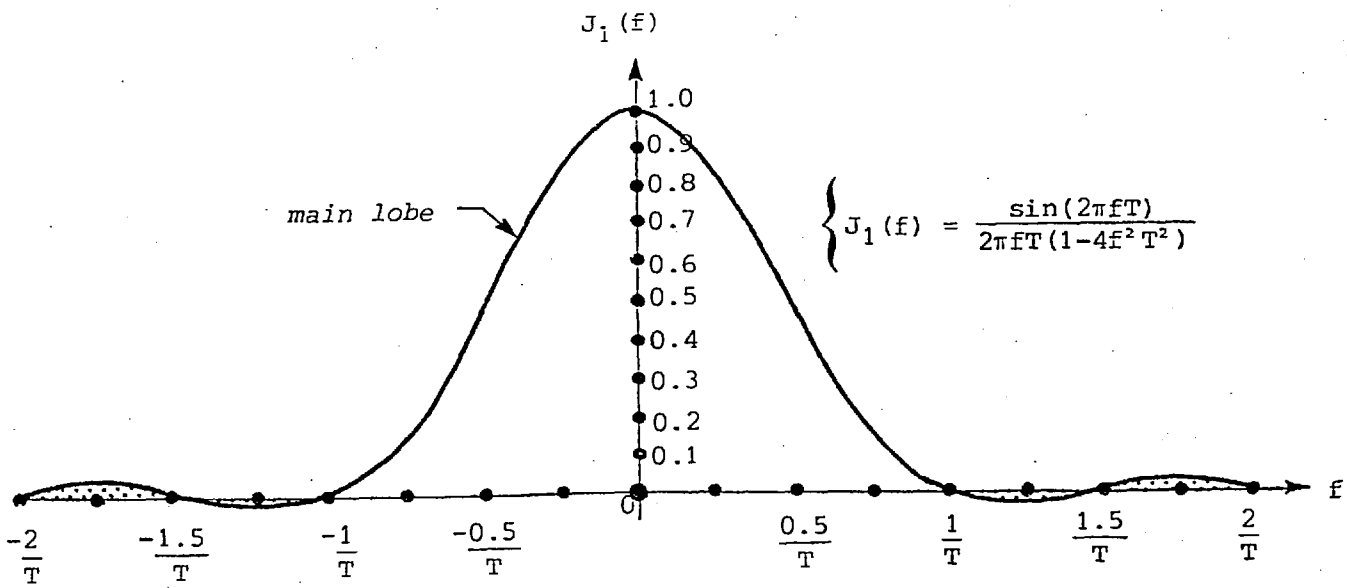


Fig. C.30

After some manipulation this integral reduces to

$$W_1(f) = \frac{\sin(2\pi fT)}{2\pi f(1-4f^2T^2)} \tag{C.110}$$

or

$$W_1(f) = TJ_1(f) \tag{C.111}$$

where $J_1(f)$ is defined as

$$J_1(f) = \frac{\sin(2\pi fT)}{2\pi fT(1-4f^2T^2)} \tag{C.112}$$

The above function is plotted in Fig. C.30(b). It has a value of unity where f = 0 and decays to zero at f = ±∞. From Eq. (C.112), it follows that

$$\left\{\begin{matrix} f = 0 \\ J_1(f) = 1 \end{matrix}\right\} \quad \left\{\begin{matrix} f = \frac{1}{2T} \\ J_1(f) = 0.5 \end{matrix}\right\} \quad \left\{\begin{matrix} f = \frac{3}{4T} \\ J_1(f) = \frac{8}{15} \end{matrix}\right\} \quad \left\{\begin{matrix} f = \frac{1}{T} \\ J_1(f) = 0 \end{matrix}\right\} \quad \left\{\begin{matrix} f = \frac{5}{4T} \\ J_1(f) = -\frac{8}{105} \end{matrix}\right\} \tag{C.113}$$

The spectral side lobe magnitudes of this window represent only a few percent of the main lobe magnitude hence virtually all the leakage is held within the main lobe.

## C.5 POWER SPECTRUM OF DIGITISED DATA

It is understood that power spectral density function is the name given to the methods of estimating the spectrum of a time series. This thesis is mainly concerned with purely indeterministic processes, which have a continuous spectrum, but the techniques can also be used for deterministic processes to identify components in the presence of noise.

### C.5.1 Fourier Series Representation (Harmonic Analysis)

In this section an attempt is made to modify the generalized form of the Fourier series discussed in Section C.4 so as to make it suitable for stochastic rather than deterministic functions of time. The common periodic functions are sine and cosine and Fourier analysis is basically concerned with approximating a function by a sum of sine and cosine terms, called the Fourier series representation.

Early attempts at discovering hidden periodicities in a continuous signal of duration T consisted of making the time series discrete by sampling the values of the signal at a spacing of $\Delta t$, then approximating by a sum of sine and cosine terms. This produces $N = T/\Delta t$ sample values $y_r$, where

$$y_r = y(r\Delta t) \qquad r = 1,2, \ldots, N \tag{C.114}$$

For convenience it is assumed that N is even. It should be noted that periodic functions which pass through the sample values may be chosen in an infinite number of ways. For example, the finite Fourier series containing N terms may be written as

$$\tilde{y}(t) = [a_o \cos(0) + b_o \sin(0)] + \sum_{p=1}^{(N/2-1)} [a_p \cos(\frac{2\pi p}{N\Delta t} t) + b_p (\frac{2\pi p}{N\Delta t} t)] + [a_{N/2} \cos(\frac{\pi t}{\Delta t}) + (0) \sin(\frac{\pi t}{\Delta t})] \tag{C.115}$$

Equation (C.115) contains N constants, $a_p$ and $b_p$, which can be determined so that the discrete and continuous values coincide at the points $t = r\Delta t$, that is, $\tilde{y}(t) = y_r$. It follows that the function $\tilde{y}(t)$ provides an *approximation* to the original continuous function $y(t)$ in the interval $0 < t < T$.

On substituting $t = r\Delta t$ in Eq. (C.115) and setting $\tilde{y}(r\Delta t) = y_r$, a set of N equations for the N unknown constants is obtained. The final expressions for the coefficients are

$$\left.\begin{aligned} a_o &= \frac{1}{N}\sum_{r=1}^{N} y_r = \bar{y} \qquad \text{(mean value of } y_r\text{)} \\ a_p &= \frac{2}{N}\sum_{r=1}^{N} y_r \sin\left(\frac{2\pi p}{N} r\right) \\ b_p &= \frac{2}{N}\sum_{r=1}^{N} y_r \sin\left(\frac{2\pi p}{N} r\right) \end{aligned}\right\} p = 1,2, \ldots, \left(\frac{N}{2} - 1\right)$$

$$a_{N/2} = \frac{1}{N}\sum_{r=1}^{N} (-1)^r y_r \qquad \text{(C.116)}$$

The Fourier series representation (C.115) has N parameters to describe N observations and so can be made to fit the data exactly*. The overall effect of the Fourier analysis is to partition the variability of the series into components at frequencies $\frac{1}{N\Delta t}, \frac{2}{N\Delta t}, \ldots, \frac{1}{2\Delta t}$. This is illustrated in Fig. C.31.

As it has already been defined, the frequency $f_1 = \frac{1}{N\Delta t}$ is the fundamental frequency of the record and corresponds to a period equal to the length of the record. The dimension of $f_1$ is cycles per second (Hz) when t is measured in seconds (sec). The highest frequency present is $1/2\Delta t$ (Hz), which corresponds to a period of two sampling intervals, the component at frequency $f_p = p/N\Delta t$ is called the *pth harmonic*. For $p \neq N/2$, it is often useful to write the pth harmonic in the equivalent form

$$a_p \cos\left(\frac{2\pi pt}{N\Delta t}\right) + b_p \sin\left(\frac{2\pi pt}{N\Delta t}\right) = R_p \cos\left(\frac{2\pi pt}{N\Delta t} + \phi_p\right) \qquad \text{(C.117)}$$

where

$$\left.\begin{aligned} R_p &= \text{amplitude of the pth harmonic} = \sqrt{a_p^2 + b_p^2} \qquad \text{(a)} \\ \phi_p &= \text{phase of pth harmonic} = \tan^{-1}(-b_p/a_p) \qquad \text{(b)} \end{aligned}\right\} \text{(C.118)}$$

---

* Just as a polynomial of degree (N-1) involving N parameters can be found which goes exactly through N observations in a polynomial regression.

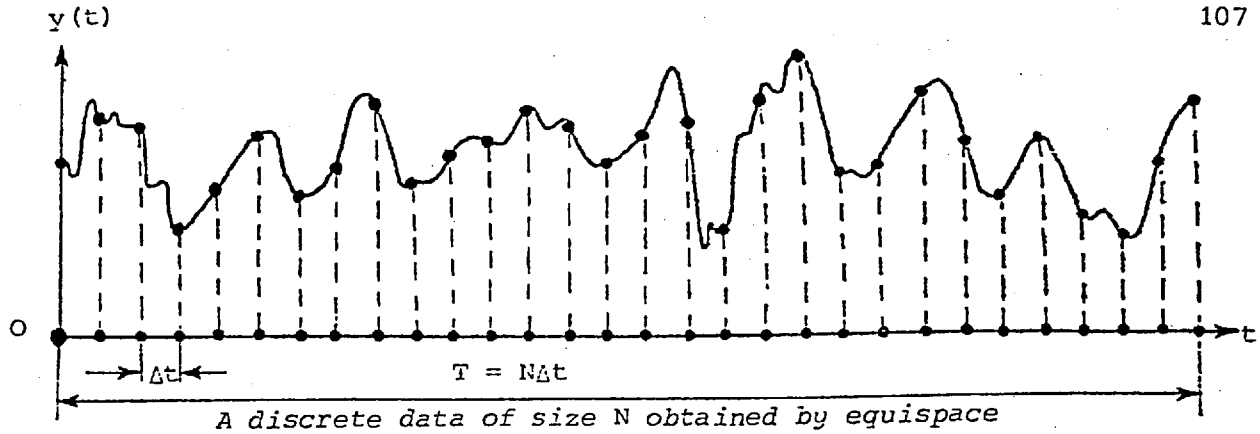


*A discrete data of size N obtained by equispace sampling of a continuous signal*

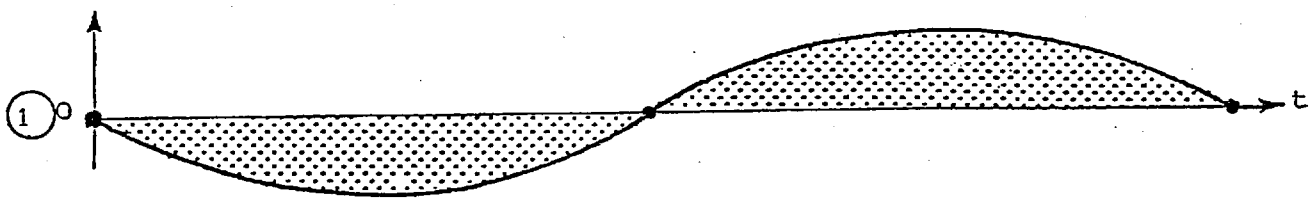


*Fundamental frequency* $f_1 = \frac{1}{N\Delta t} = 1/T$ $T_1 = N\Delta t$

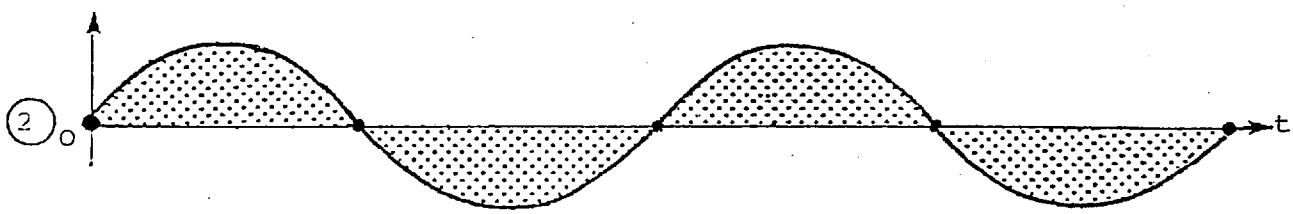


*2nd harmonic* $f_2 = 2/N\Delta t$ $T_1 = N\Delta t/2$

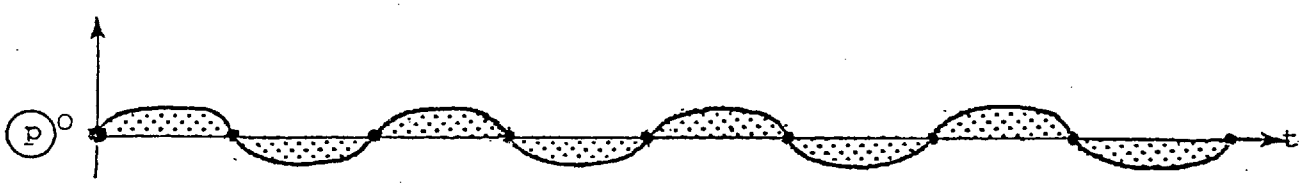


*pth harmonic* $f_p = p/N\Delta t$ $T_p = N\Delta t/p$

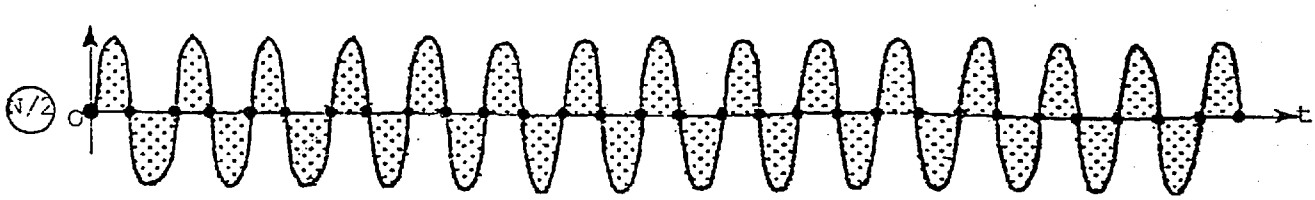


*(N/2) harmonic* $f_{N/2} = 1/2\Delta t$ $T_{N/2} = 2\Delta t$

Fig. C.31

### C.5.1.1 Parseval's Theorem

It is known that the mean square value of the record is

$$\frac{1}{N}\sum_{r=1}^{N} y_r^2 \tag{C.119}$$

*Parseval's theorem* states that for $p \neq N/2$, the contribution of the pth harmonic to the total sum of the squares is given as $NR_p^2/2 = N(a_p^2 + b_p^2)/2$. Hence

$$R_o^2 + \sum_{p=1}^{(N/2\ -1)} R_p^2/2 + a_{N/2}^2 = \frac{1}{N}\sum_{r=1}^{N} y_r^2 \tag{C.120}$$

It must be emphasised here that $a_o$ (which is the mean or average value of $y_r$) is equal to $R_o$. The above relationship can be written as

$$\frac{1}{N}\sum_{r=1}^{N} (y_r - R_o)^2 = \sum_{p=1}^{(N/2\ -1)} R_p^2/2 + a_{N/2}^2 \tag{C.121}$$

The left-hand side of Eq. (C.121) is effectively the variance of the observations although the divisor is N rather than the more usual (N-1). Thus $R_p^2/2$ is the contribution of the pth harmonic to the variance, and Eq. (C.121) shows how the total variance is partitioned.

### C.5.2 Transformation of Data to Zero Mean Value

In order that subsequent formulae and calculations may be simplified, it is desirable at this time to transform the data so that it has a zero mean value. If a new time history record is defined as $y_o(r\Delta t) = y(r\Delta t) - \bar{y}$, then $y_o(r\Delta t)$ has data values given by

$$\left.\begin{aligned} \textit{residual} = y_o(r\Delta t) &= y(r\Delta t) - \bar{y} \\ & \qquad r = 1,2, \ldots, N \end{aligned}\right\} \tag{C.122}$$

It should be noted that $\overline{y_o(r\Delta t)} = 0$. The reason* for representing the original data values by $y_o(r\Delta t)$ instead of $y(r\Delta t)$ is to have the $y_o(r\Delta t)$ notation indicating a zero sample mean value. Subsequent formulae will now be stated in terms of the transformed data values $y_o(r\Delta t)$.

* In wave studies $y_o(r\Delta t)$ is the 'wave height' or fluctuation in water surface about a zero mean.

## C.5.3 Fourier Line Spectrum-Raw Periodogram

If $R_p^2/2$ is plotted against $f_p = p/n\Delta t$, a *discrete* or *Fourier line spectrum* will be obtained. Because the energy is concentrated around particular frequencies and not spread throughout all frequencies, it is inappropriate to plot a line spectrum. However, $R_p^2/2$ can be regarded as the contribution to variance in the range $\frac{p}{N\Delta t} \pm \frac{1}{2N\Delta t}$, and a *histogram* can be plotted whose height in the range $\frac{p}{N\Delta t} \pm \frac{1}{2N\Delta t}$ is such that

$$\left.\begin{aligned} R_p^2/2 &= \text{area of histogram rectangle} \\ &= \text{height of histogram} \times \frac{2}{2N\Delta t} \\ &= I(f_p) \times \frac{1}{N\Delta t} \end{aligned}\right\} \quad (C.123)$$

Therefore

$$\left.\begin{aligned} I(0) &= 0 \\ I(f_p) &= \frac{N\Delta t}{2} R_p^2 \qquad p = 1,2,3, \ldots, (N/2 - 1) \end{aligned}\right\} \quad (C.124)$$

As usual, (C.124) does not apply for $p = N/2$; $a_{N/2}^2$ may be regarded as the contribution to variance in the range $[(\frac{1}{2\Delta t} - \frac{1}{2N\Delta t}), \frac{1}{2\Delta t}]$ so that

$$I(\tfrac{1}{2\Delta t}) = 2N\Delta t \cdot a_{N/2}^2 \qquad (C.125)$$

The plot of I(f) against f(Fig. C.32) is usually called *raw periodogram*.

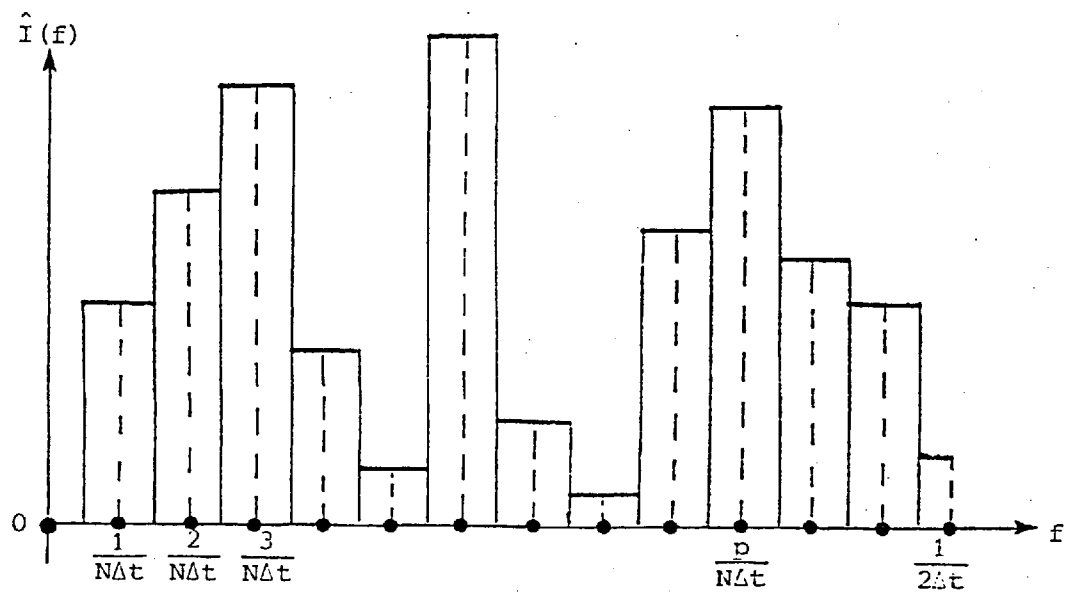


Fig. C.32 A raw periodogram

The total area under the raw periodogram is equal to the variance of the time series. Expression (C.124) may readily be calculated directly from the data by combining Eqs. (C.116), (C.118a) and (C.124)

$$I(f_p) = (2\Delta t/N)\{[\sum_{r=1}^{N} y_r \cos(\frac{2\pi p}{N} r)]^2 + [\sum_{r=1}^{N} y_r \sin(\frac{2\pi p}{N} r)]^2\} \quad (C.126)$$

From Fig. C.32, it can be seen that $1/(N\Delta t)$ is the lowest frequency and $1/(2\Delta t)$ is the highest frequency which can be detected from the periodogram of data sampled at $\Delta t$ (hence the signal $\tilde{y}(t)$ is said to be *band limited*). The frequency $f_N = \frac{1}{2\Delta t}$ (Hz) or $\omega_N = \pi/\Delta t$ (radians per sec) is called *Nyquist folding frequency, cutoff frequency* or simply *Nyquist frequency*.

The periodogram appears to be a natural way of estimating the power spectral density function, however it will be explained that for a process with a 'continuous' spectrum it provides a poor estimate and needs to be modified.

### C.5.4 Hanning Window for a Digitised Time Series

For a digitised record of size N, the Hanning window weighting function $w_r$ takes the form

$$\left.\begin{aligned} w_{(n+1)} &= 0.5[1 - \cos(\frac{n\pi}{M})] \\ &= 0.5\{1 + \cos[\frac{(M-n)\pi}{M}]\} \\ & \qquad n = 0,1,2, \ldots, (M-1) \end{aligned}\right\} \quad (C.127)$$

for the first M values of the data and the form

$$\left.\begin{aligned} w_n &= 0.5\{1 - \cos[\frac{(N-n)\pi}{M}]\} \\ & \qquad n = (N-M+1), \ldots, N \end{aligned}\right\} \quad (C.128)$$

for the last M values, before spectral estimation.

The ratio M/N is between 1/20 and 1/3. For example if $100 < N < 200$, a value of M of about N/6 may be appropriate, while if $1000 < N < 2000$ a value of M less than N/10 may be appropriate (Chatfield, 1975).

## C.5.5 Properties of the Raw Periodogram

The raw periodogram derived from the Fourier coefficients of any time series, e.g. a wave record, is highly erratic unless it is given special treatment. This holds true no matter how long a sample is taken from the signal or how high a sampling rate is used.

In order to understand this behaviour, it must be remembered that the estimated raw periodogram exhibits a certain deviation from the true energy density function. This is evident since one data sample is only a finite record (in time) of an infinite number of possible infinitely long realizations of the process. Clearly, the averaging of the raw periodogram calculated from many data samples should give a result closer to the true energy density function.

Tucker (1957) gave an insight into the problem of the variability of the periodogram for the case of a gaussian random sea. He showed that the elements of the periodogram calculated from a sequence of statistically independent data values having a gaussian distribution are independently distributed as a $\chi^2_2$ (Appendix II); i.e. the I(f) calculated from repeated data samples of the same process has a chi-squared distribution with 2 degrees of freedom.

From Appendix II, it immediately follows that the coefficient of dispersion of the raw periodogram is 100%. In effect, a raw periodogram is a very poor estimate of the true continuous spectrum G(f) of the process. Although

$$\underset{N\to\infty}{E[\hat{I}(f)]} \Rightarrow G(f) \qquad \text{(C.129)}$$

i.e. the periodogram is asymptotically unbiased, Chatfield (1975) has proved that the estimator I(f) is *not a consistent* estimator of G(f). A well-behaved estimator has the property that its variance decreases with increased record length (or sample size), yet the variance of I(f) does not decrease as N increases

$$\mathrm{Var}[\hat{I}(f)] \not\Rightarrow 0 \qquad \text{as } N \Rightarrow \infty \qquad \text{(C.130)}$$

From the above discussion, it can be concluded that the raw periodogram is highly unstable. The change that is required to make the raw periodogram part of a consistent estimating procedure involves applying a smoothing procedure to the raw periodogram ordinates.

### C.5.6 Smoothing

This approach smooths the periodogram by simply grouping the periodogram ordinates in sets of size m and then the average value of each group is found. In this case

$$\hat{G}(f) = \frac{1}{m} \sum_{j=n}^{(m+n-1)} \hat{I}(f_j) \qquad n \text{ is an integer} \qquad (C.131)$$

where $f_j = j/N\Delta t$ and $j$ varies over m consecutive integers so that $f_j$ is symmetrical about f. In order to estimate G(f) at f = 0, the relationship (C.131) has to be modified in an obvious way, treating the raw periodogram as being symmetrical about 0. Only at this point is m assumed to be odd (obviously if m is an even number, one unit should be added to it), with $m^* = (m-1)/2$, $\hat{G}(0)$ may be written as

$$\hat{G}(0) = 2 \sum_{j=1}^{m^*} \hat{I}(f_j)/m \qquad (C.132)$$

The other ordinates are obtained by the following relation

$$\hat{G}(f_k') = \sum_{j=[m^*+(k-1)m+1]}^{m^*+km} \hat{I}(f_j)/m \qquad \left.\begin{array}{l} f_k' = (m^*+km + \frac{1-m}{2})/(N\Delta t) \\ k = 1,2, \ldots, \ell \\ \text{where } \ell \text{ is an integer} \\ \text{less or equal to} \\ (N/2 - m^*)/m \end{array}\right\} \qquad (C.133)$$

If $(m^* + \ell m) \neq N/2$, $[N/2 - (m^* + \ell m)]$ is the number of remaining raw periodogram ordinates (which is less than m), assuming the raw periodogram to be symmetrical about $f_{N/2} = 1/2\Delta t$, if $(m^* + \ell m + 1) < N/2$ then

$$\hat{G}(\frac{1}{2\Delta t}) = [\hat{I}(\frac{1}{2\Delta t}) + 2 \sum_{j=m^*+\ell m+1}^{(N/2-1)} \hat{I}(f_j)]/(N-2m^*-2\ell m-1) \qquad (C.134)$$

But if $(m^* + \ell m + 1) = N/2$ then

$$\hat{G}(\frac{1}{2\Delta t}) = \hat{I}(\frac{1}{2\Delta t}) \qquad (C.135)$$

#### C.5.6.1 Properties of the Smoothed Periodogram

Whereas the raw periodogram is an asymptotically unbiased but inconsistent estimate of the true spectrum, smoothing changes the properties of the estimator. Jenkins and Watts (1968) showed that the smoothed periodogram is such that $X = \nu\hat{G}(f)/G(f)$ is approximately distributed as $\chi^2_\nu$, where $\nu = 2m$. This means that the random variable X has got 2m degrees of freedom. From Appendix II, it immediately follows that

$$\left.\begin{aligned} \mathrm{Var}[\nu\hat{G}(f)/G(f)] &= \nu^2\ \mathrm{Var}[\hat{G}(f)/G(f)] = 2\nu \\ \mathrm{Var}[\hat{G}(f)/G(f)] &= 2/\nu = 1/m \\ \text{The coefficient of dispersion of } [\hat{G}(f)/G(f)] &= 1/\sqrt{m} \end{aligned}\right\} \quad (C.136)$$

The above relationships immediately lead to the conclusion that a smaller sample variance and hence a more stable estimate of the smoothed periodogram can only be achieved for a large number of degrees of freedom or m.

### C.5.6.2 Recommendation for the Value of m

There seems to be relatively little advice in the literature on the choice of m. It seems advisable to try several values in the region of N/40. A high value should give an idea where the large peaks occur in the spectrum $\hat{G}(f)$, but the curve is likely to be too smooth. A low value of m will produce a curve with a large number of peaks, some of which may be spurious.

Care should be taken in the choice of m, the effects of 'variance'and'frequency resolution' are in opposite directions. The larger the value of m the smaller the variance of the resulting estimate is but if m is too large then interesting features of $\hat{G}(f)$, such as peaks, may be smoothed out and hence pass unnoticed. Any gain in stability through an increase in m is accompanied by a loss in frequency resolution, a compromise must usually be found between these two conflicting objects. If a smooth and continuous spectrum is expected, as would be the case for a turbulent flow signal, emphasis should be placed on obtaining a stable spectral estimate by increasing m to the detriment of frequency-resolution. If, however, the process under study exhibits one or more energy peaks along the frequency axis which must be identified, then the value of m must be limited to a minimum. Thus the loss of information caused by the smoothing process is reduced.

### C.5.6.3 Confidence Limits for the Smoothed Periodogram

Since $[\nu\hat{G}(f)/G(f)]$ is approximately distributed as $\chi^2_\nu$ where $\nu = 2m$, it follows that (Fig. II.1).

$$\text{Prob}[\chi^2_{(1-\alpha/2),\nu} < \nu\hat{G}(f)/G(f) < \chi^2_{\alpha/2,\nu}] = 1-\alpha \qquad \text{(C.137)}$$

so that the 100(1-α)% confidence interval for G(f) is given by

$$\left.\begin{aligned} \text{the upper confidence limit} &= \frac{\nu\hat{G}(f)}{\chi^2_{(1-\alpha/2),\nu}} \quad \text{(a)} \\ \text{the lower confidence limit} &= \frac{\nu\hat{G}(f)}{\chi^2_{\alpha/2,\nu}} \quad \text{(b)} \end{aligned}\right\} \text{(C.138)}$$

Thus the true spectrum G(f) is said to fall between the upper and lower confidence limits and to have a 100(1-α) percent confidence.

### C.5.7 3 Point Smoothing

This method is based on smoothing the raw periodogram using the weights (1/4, 1/2, 1/4) to give the estimates

$$\left.\begin{aligned} \hat{G}(0) &= 0.5\,\hat{I}(0) + 0.5\,\hat{I}\left(\frac{1}{N\Delta t}\right) \\ \hat{G}\left(\frac{k}{N\Delta t}\right) &= 0.25\,\hat{I}\left[\frac{(k-1)}{N\Delta t}\right] + 0.5\,\hat{I}\left(\frac{k}{N\Delta t}\right) + 0.25\,\hat{I}\left[\frac{(k+1)}{N\Delta t}\right] \\ &\qquad k = 1,2,3,\ \ldots\ (N/2-1) \\ \hat{G}\left(\frac{1}{2\Delta t}\right) &= 0.5\,\hat{I}\left(\frac{1}{2\Delta t} - 1\right) + 0.5\hat{I}\left(\frac{1}{2\Delta t}\right) \end{aligned}\right\} \text{(C.139)}$$

Eq. (C.139) is implemented easily on a binary digital computer when compared to the previous smoothing procedure.

### C.5.8 Aliasing

When a continuous function is sampled at constant time intervals equal to Δt sec, values between sampled data points are discarded. In general an analogue signal of a wave can be thought of as a sum of a great number of sinusoidal functions of varying amplitude and frequency. If the sampling rate is too slow in relation to the highest frequencies present, too much information is discarded. As is illustrated in

Fig. C.33 through sampling, the high frequency components are indistinguishable from lower frequency elements. It should be noted that for the given sampling interval it is impossible to tell which of the two harmonics is being observed. Thus, the power attributed to the more slowly varying harmonic will be, in some senses, the combined power

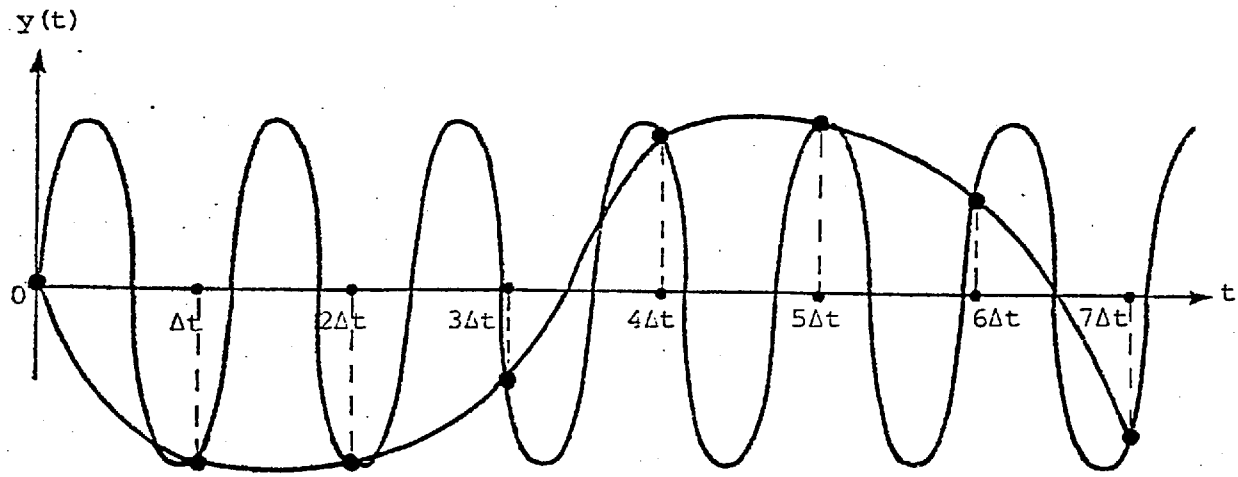


Fig. C.33 Illustration of two sinusoids made indistinguishable by sampling at intervals of length $\Delta t$.

of all harmonics which are made indistinguishable from it (i.e., are *aliased* with it) by sampling. This effect is commonly called *aliasing*.

### C.5.8.1 Theorem

A continuous time series, with spectrum $G_c(f)$ for $0 < f < \infty$, is sampled at equal intervals of length $\Delta t$. The resulting discrete time series has spectrum $G_d(f)$ defined over $0 < f < 1/2\Delta t$. Then $G_c(f)$ and $G_d(f)$ are related

$$G_d(f) = \sum_{\delta=0}^{\infty} G_c\left(f + \frac{\delta}{\Delta t}\right) + \sum_{\delta=1}^{\infty} G_c\left(-f + \frac{\delta}{\Delta t}\right) \qquad \text{(C.140)}$$

The implications of this theorem are now considered. Firstly, it is noted that if the continuous series contains no variation at frequencies above the Nyquist frequency, so that $G_c(f) = 0$ for $f > 1/2\Delta t$, then $G_d(f) = G_c(f)$. In this case no information is lost by sampling.

But more generally, the effect of sampling will be that variation at frequencies above the Nyquist frequency $1/2\Delta t$ will be 'folded back' and produce an effect over the 'visible' frequency $0 < f \leq f_N = 1/2\Delta t$ in $G_d(f)$.

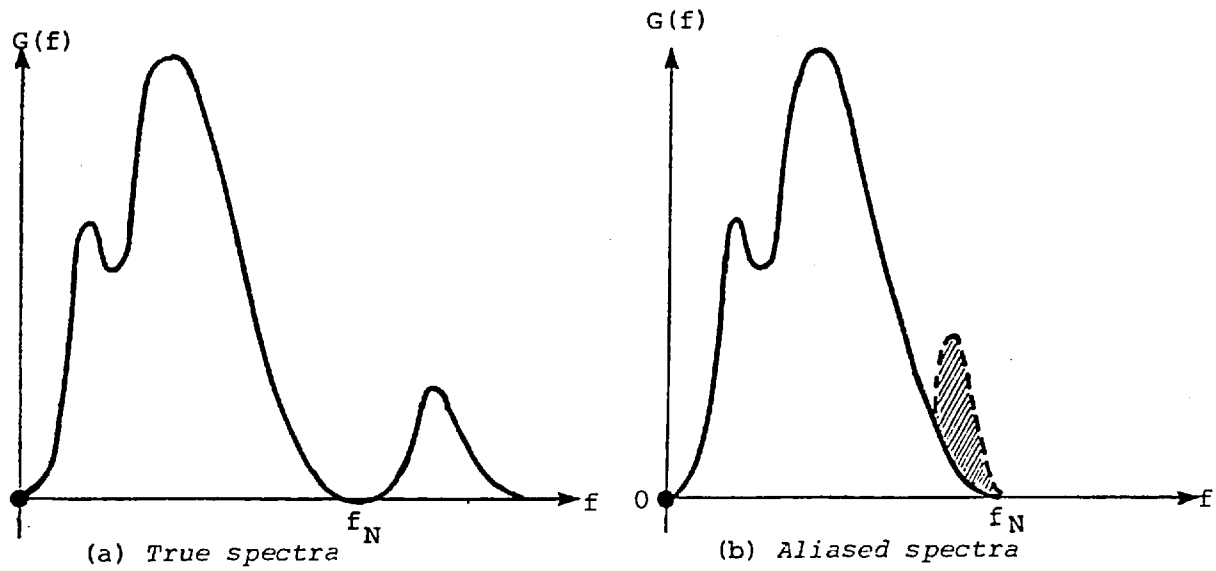


Fig. C.34 Aliased power spectra due to folding

For any frequency f in the range $0 \leq f \leq f_N$, the higher frequencies which are aliased with f are defined by

$$(2f_N \pm f),\ (4f_N \pm f),\ \ldots\ ,\ (2nf_N \pm f), \qquad \text{(C.141)}$$

Variation at all these frequencies in the continuous series will appear as variation at frequency f in the sampled series.

## C.5.9 Fast Fourier Transform

Until recently the energy density functions of the stationary time series have been calculated indirectly through autocovariance functions. Many authors such as Chatfield (1975) have pointed out that an algorithm developed around the basic Eqs. (C.116) requires a number of operations proportional to $N^2$ for a series of N data. For large data series this leads to prohibitive running times even when modern computers are employed. The advent of the F.F.T. algorithm makes the calculations of the energy density function much faster than the classical procedure via autocovariance function.

A history of the F.F.T. is described by Cooley, Lewis and Welch (1967), the ideas going back to the early 1900's. But it was the work of Cooley and Tukey (1965) which first stimulated the application of the technique to time series analysis. The details of this technique is given by Otnes and Enochson (1972), Bingham, Godfrey and Tukery (1967) and Bendat and Piersol (1971).

The F.F.T. technique substantially reduces the time required to perform a Fourier analysis on a computer, and is also more accurate. Much bigger reductions in computing can be made when N is highly composite (i.e. has many factors). In particular if N is of the form $2^n$ (e.g. N = 256, 512, 1024 etc.), then the number of operations will be of the order $N\log_2 N$ instead of $N^2$. Singleton (1969) gives a general computer programme.

### C.5.10 Recommendation for Sampling Rate and Length of the Record

Two basic parameters are needed for the analysis of a time varying stationary random process. The first is the length T of the record and the second is the time interval $\Delta t$ (or the sampling rate $1/\Delta t$) at which the record is sampled to give the N data values for analysis. The selection of the sampling rate is determined by the desire to avoid aliasing. Thus it is necessary to have *a prior* knowledge of the highest frequencies containing appreciable energy that are present in the sampled record. Given such an estimate of the highest frequency $f_{max}$ which may be derived from results of previous experiments at similar conditions, the sampling rate is specified (Thompson and Gilberd, 1971) by

$$\left.\begin{aligned} &\frac{1}{\Delta t} \leq 4f_{max} && \text{(a)} \\ &\Delta t \leq 1/4f_{max} && \text{(b)} \end{aligned}\right\} \quad \text{(C.142)}$$

It is evident that $T = N\Delta t = 2^n\Delta t$.

## C.6 QUANTIZATION ERROR

Analysis of random data is usually done by using a digital computer. This implies that the continuous or analog signal will have to be sampled in the manner of C.3.4 and the sampled values converted to digital form. No matter how fine the scale, a choice between two consecutive values is required. This matter is illustrated on Fig. C.35.

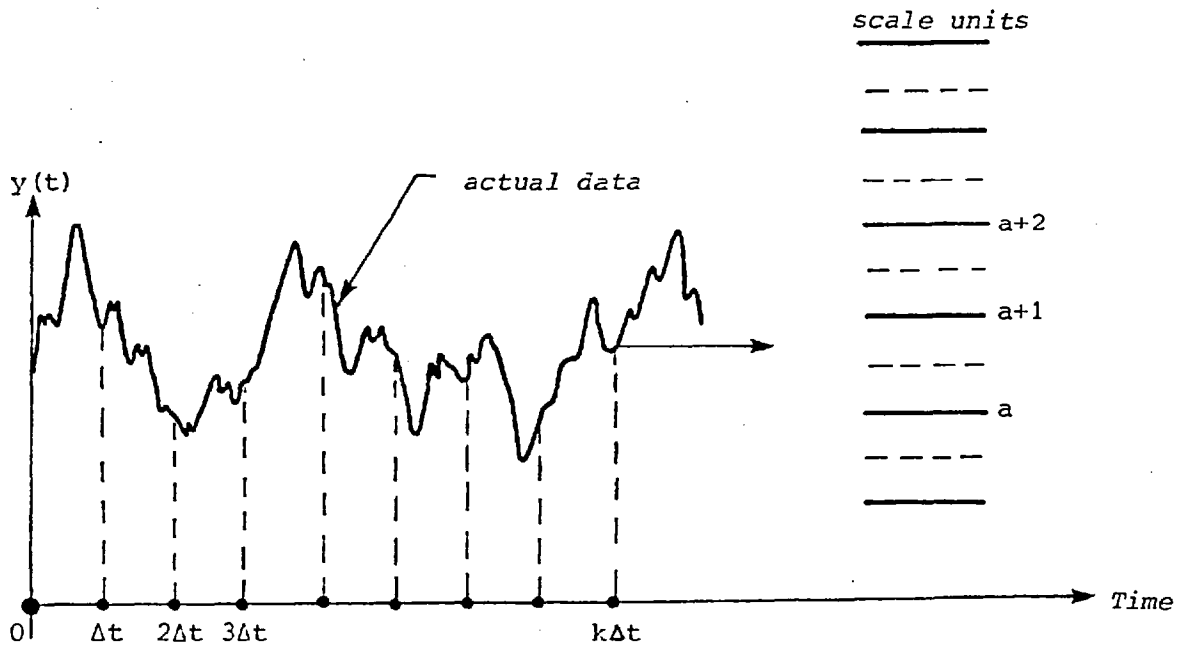


Fig. C.35 Quantization error

In this figure one would choose a+1 as the closest numerical value to the data at time kΔt.

If it is assumed that the quantization errors follow a 'uniform probability distribution' over 'one scale unit', then these errors will have a mean value of zero and a standard deviation of approximately 0.29 scale unit. This is easily shown as follows.

Let p(y) be the quantization error probability density function defined by

$$\left.\begin{aligned} p(y) &= 1, \quad -0.50 \leq y \leq 0.50 \quad \text{(a)} \\ &= 0, \quad \text{otherwise} \quad \text{(b)} \end{aligned}\right\} \quad \text{(C.143)}$$

Then, the mean value $\mu_y$ is clearly zero since p(y) is symmetric about y = 0, and the variance

$$\sigma_y^2 = \int_{-\infty}^{+\infty} (y-\mu_y)^2 p(y)\,dy = \int_{-\infty}^{+\infty} y^2\,dy = 1/12 \qquad \text{(C.144)}$$

The standard deviation

$$\sigma_y = \sqrt{1/12} \simeq 0.29 \text{ scale unit} \qquad \text{(C.145)}$$

This is the root mean square value of the quantization error, which may be considered as a root mean square noise on desired signals.

To apply this result, if the full range of a signal is quantized at 256 scale units, the root mean square noise-to-signal ratio is 0.29/256 = 0.001. This illustrates that, for most practical problems, quantization errors should be negligible when signals are quantized at 256 or more scale units.

## C.7 JOINT PROPERTIES OF RANDOM DATA

Thus far, the attention has been confined to the analysis of a single record. The statistical functions in Section C.3 are useful to describe the properties of data from individual random processes. It is often desirable to describe certain common or joint properties of different data from two or more random processes. For example, it may be of interest to study the height of waves at various points on the surface of the sea. The average properties of the wave height at each point could be described using the statistical functions discussed in Section C.3. However, there may be additional important information in similar joint statistical functions which can be computed for the wave heights at two points on the sea.

One of the main types of statistical function used to describe the joint properties of sample records from two random processes is the *cross-correlation function*. It is effectively an extension of the basic formulations used to describe the properties of individual sample records which produces information concerning joint properties in time domain.

This joint descriptive property for two sets of stationary random data will now be defined in broad terms. Once again, the discussions will assume ergodicity so that the joint time-averaged properties of single pairs of sample time history records can be considered.

### C.7.1 Cross-Correlation Functions

The cross-correlation function for two sets of random data describes the general dependence of the values of one set of data on the other. Given the pair of time history records $x(t)$ and $y(t)$ illustrated in Fig. C.36. An estimate for the cross-correlation function of the values of $x(t)$ at time $t$ and $y(t)$ at time $(t+\tau)$ may be obtained by taking the average product for the two values over the observation time $T$, as is done for autocorrelation functions in Section C.3. The resulting average product will approach an exact cross-correlation function as $T$ approaches infinity. That is,

$$R_{xy}(\tau) = \lim_{T\to\infty} \frac{1}{T} \int_0^T x(t)y(t+\tau)\,dt \qquad (C.146)$$

The function $R_{xy}(\tau)$ is always a real-valued function which may be either positive or negative. Furthermore, $R_{xy}(\tau)$ does not necessarily have a maximum at $\tau = 0$ as was true for autocorrelation functions, nor is $R_{xy}(\tau)$ an even function as was true for autocorrelation functions.

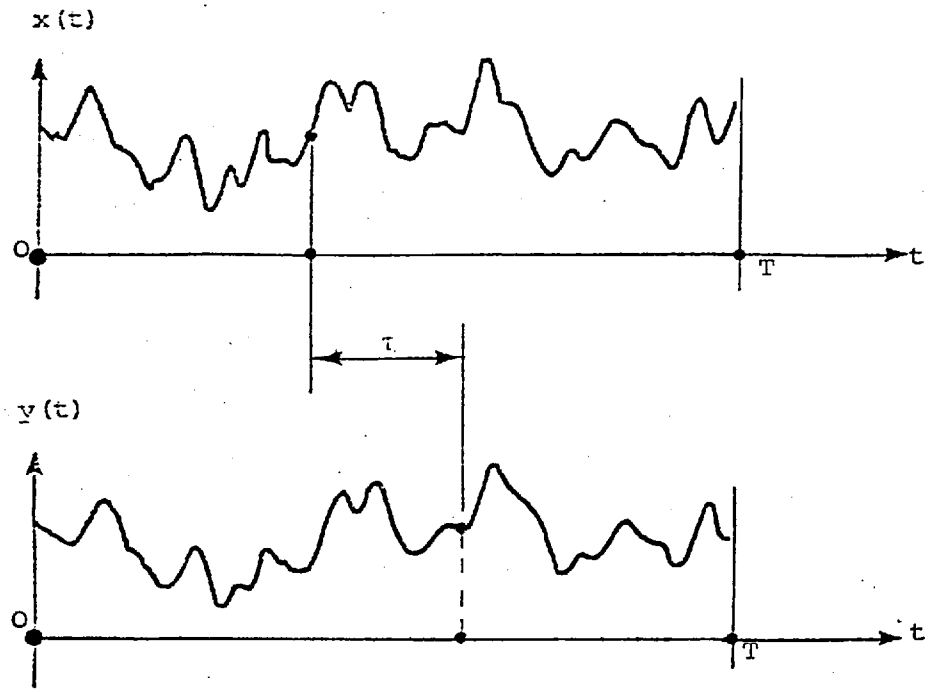


Fig. C.36 Cross-correlation measurement

However, $R_{xy}(\tau)$ does display symmetry about the ordinate when x and y are interchanged, that is

$$R_{xy}(\tau) = R_{yx}(-\tau) \tag{C.147}$$

When $R_{xy}(\tau) = 0$, x(t) and y(t) are said to be *uncorrelated*.

## C.7.2 Estimation of the Cross-Correlation Functions

For two digitised time series of size N, the unbiased estimates for the sample cross-correlation functions* are defined by

$$\hat{R}_{xy}(\tau) = \begin{cases} \dfrac{1}{N-\tau} \displaystyle\sum_{t=1}^{N-\tau} \{(x_t - \bar{x})[y_{(t+\tau)} - \bar{y}]\} & \text{(a)} \\ \qquad \tau = 0,1,2,..,m & \\ \dfrac{1}{N-\tau} \displaystyle\sum_{t=1-\tau}^{N} \{(x_t - \bar{x})[y_{(t+\tau)} - \bar{y}]\} & \text{(b)} \\ \qquad \tau = -1,-2,..,-m & \end{cases}$$

$$\hat{R}_{yx}(\tau) = \begin{cases} \dfrac{1}{N-\tau} \displaystyle\sum_{t=1}^{N-\tau} \{(y_t - \bar{y})[x_{(t+\tau)} - \bar{x}]\} & \text{(c)} \\ \qquad \tau = 0,1,2,..,m & \\ \dfrac{1}{N-\tau} \displaystyle\sum_{t=1-\tau}^{N-\tau} \{(y_t - \bar{y})[x_{(t+\tau)} - \bar{x}]\} & \text{(d)} \\ \qquad \tau = -1,-2,..,-m & \end{cases} \tag{C.148}$$

* They may also be called *cross-covariance functions* after the mean of each record has been removed.

It should be noted that the two cross-correlation functions $\hat{R}_{xy}(\tau)$ and $\hat{R}_{yx}(\tau)$ differ by the interchange of $x_t$ and $y_t$ data values.

The sample cross-correlation function $\hat{R}_{xy}(\tau)$ may be normalized to have values between +1 and -1 by dividing by

$$\{[\sum_{t=1}^{N}(x_t-\bar{x})^2]\ [\frac{1}{N}\sum_{t=1}^{N}(y_t-\bar{y})]\}^{\frac{1}{2}}. \tag{C.149}$$

This defines a sample cross-correlation coefficient

$$\left.\hat{\rho}_{xy}(\tau) = \frac{\hat{R}_{xy}(\tau)}{\{[\frac{1}{N}\sum_{t=1}^{N}(x_t-\bar{x})^2]\ [\frac{1}{N}\sum_{t=1}^{N}(y_t-\bar{y})^2]\}^{\frac{1}{2}}}\right\} \tag{C.150}$$

$$\tau = 0,1,2,\ ..,\ m$$

which theoretically should satisfy $-1 \leq \hat{\rho}_{xy}(\tau) \leq 1$. A similar formula exists for $\hat{\rho}_{yx}(\tau)$.

### C.7.3 Cross-Correlogram

A plot of $\hat{\rho}_{xy}(\tau)$ as the ordinate against the lag, $\tau$, as the abscissa, in which adjacent points are jointed by straight lines, is referred to as a *cross-correlogram*.

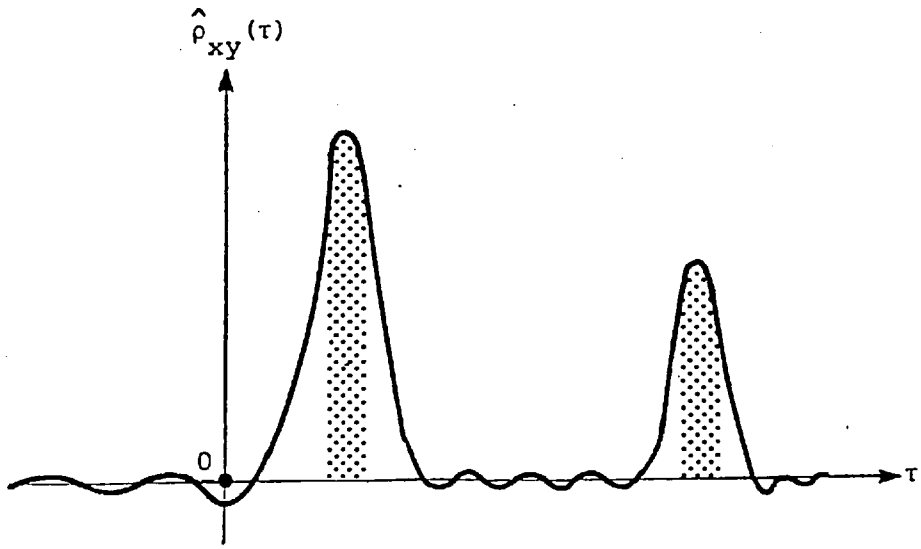


Fig. C.37 Typical cross-correlogram plot

It should be noted that the plot will sometimes display sharp peaks which indicate the existance of correlation between x(t) and y(t) for specific time displacements.

### C.7.3.1 Applications

Cross-correlograms have many important applications including the following.

It may be of interest to determine the time required for a signal to pass through a given system. Assuming the system is linear, a cross-correlogram measurement between the input and output may yield such time delay information directly. As the output from the system is displaced in time relative to the input, the cross-correlogram plot will peak at that time displacement equal to the time required for the signal to pass through the system (Jenkins and Watts, 1968).

# CHAPTER D

# WALL JETS

## D.1 PLANE TURBULENT WALL JETS

The term 'wall jet' was introduced by Glauert (1956) to describe the flow that develops when a jet, consisting of a fluid similar to that of its surroundings, impinges tangentially (or at an angle) to a plane surface and spreads out over the surface (the surrounding fluid is assumed to be stationary). He studied such a flow in two and three dimensions, and pointed out that it has features common to both the *free jet* and the *ordinary boundary layer*. Thus, the spreading fluid is retarded by the frictional resistance of the wall and the inner part of the flow (Fig. D.1) may be expected to have a structural similarity to a boundary layer, whereas entrainment of still fluid occurs near the outer edge of the flow which is therefore likely to resemble a free jet in character.

Considering a plane jet of thickness d and with a uniform velocity $U_o$ issuing from a nozzle tangentially to a smooth flat surface which is submerged in a semi-finite expanse of the same fluid as shown in Fig. D.1. This is known as 'classical wall jet'. In this figure, $\bar{x}$ denotes the longitudinal distance from the efflux section. If experimental observations of the distribution of the U velocity in the y-direction at different x stations were made, it would be seen that at any x station, the magnitude of U increases from zero at the wall to a maximum value of $U_{max}$ at $y = \delta$, it then decreases to zero at some large value of y. The region from the wall to the maximum velocity level is known as the 'inner layer' or *wall region* or 'boundary layer' and the region above this is generally known as the 'outer layer' or the 'free-mixing'region. These two regions overlap at the point of maximum velocity.

From the profile of the velocity distribution curve (Fig. D.1) it is evident that this type of flow is a class of shear flow because of the spatial variation of the velocity in the direction normal to bed. Turbulent motion in shear flows is self-sustaining, in the sense that turbulence arises as a consequence of shear and shear persists as a consequence of turbulent fluctuations.

Extensive investigation on wall jets has shown that the flow in such a jet has a self-preserving form. This means that the variation of any *mean flow quantity* over any plane could be expressed non-dimensionally through scales of velocity and length. For a classical wall jet, the

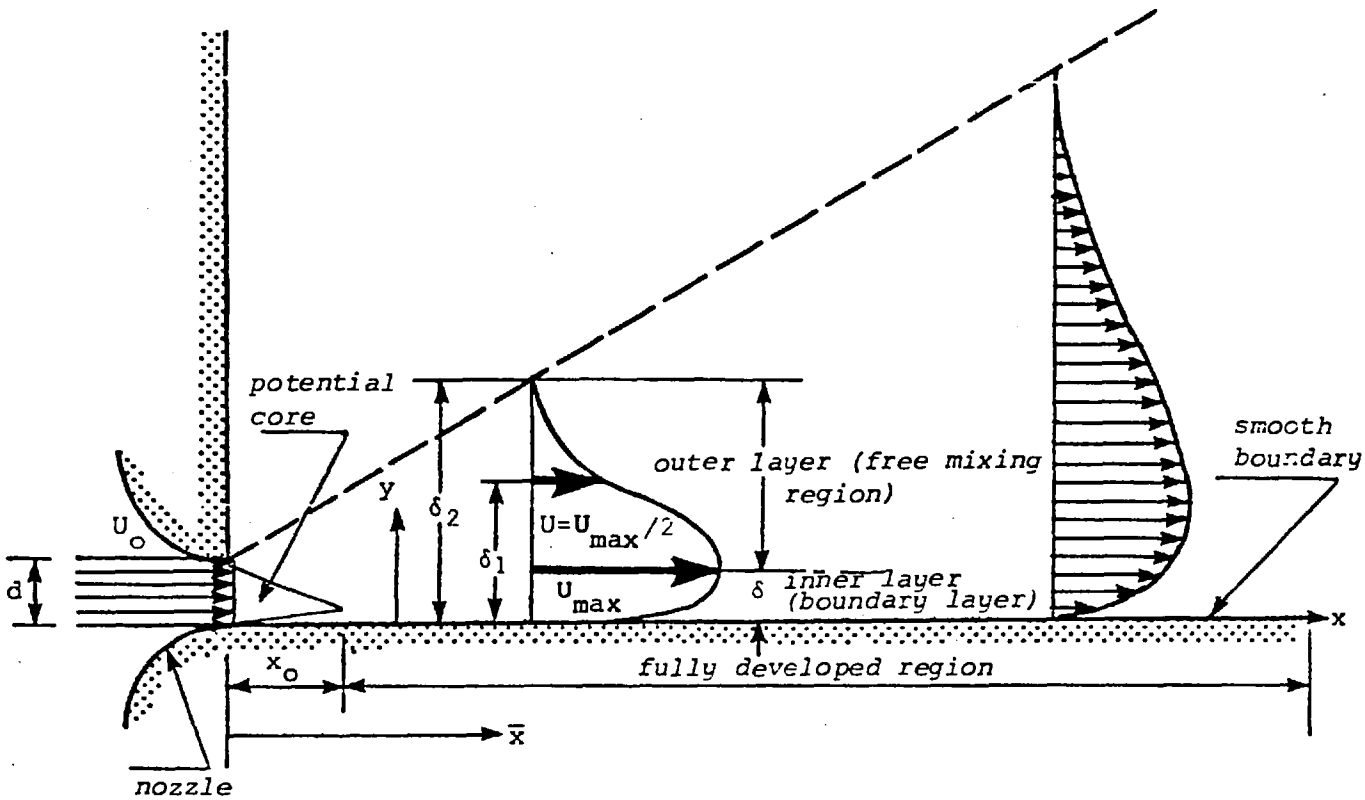


Fig. D.1 Definition sketch of plane turbulent wall jets

maximum velocity at each section $U_{max}$ is taken as the 'velocity scale' and the normal depth from the bed to the point where the velocity is half of maximum velocity $\delta_1$ (Fig. D.1) is taken as the length scale. For a wall jet, the principal mean flow quantities of interest are the maximum velocity $U_{max}$, the length scale $\delta_1$, the inner layer $\delta$, the total thickness $\delta_2$ in addition to the wall shear $\tau_o$. The existence of similarity reduces the difficulty of treating the wall jet problem and a mathematical treatment can be applied in terms of a characteristic velocity scale $U_{max}$ and a length scale $\delta_1$, which are functions of x only.

### D.1.1 Equation of Motion

In tensor notation, the equation of motion for momentum transfer under steady-flow conditions is written as

$$\rho \frac{\partial U_i}{\partial t} + \rho U_j \frac{\partial U_i}{\partial x_j} = - \frac{\partial P}{\partial x_i} + \frac{\partial}{\partial x_j} (\mu \frac{\partial U_i}{\partial x_j}) + \frac{\partial}{\partial x_j} (-\rho \overline{u_i u_j}) + F_i \qquad (D.1)$$

where

| | | |
|---|---|---|
| i,j,k | = | subscripts in tensor notation |
| x | = | co-ordinate position |
| t | = | time variable |
| U | = | turbulent mean velocity |
| u | = | turbulent fluctuating velocity |
| $\rho$ | = | mass density of fluid |
| $\mu$ | = | dynamic viscosity |
| F | = | body force |
| P | = | pressure at any point |

The nine products $\rho\overline{u_i u_j}$ are referred to as the Reynolds stresses and the terms $\partial/\partial x_j(\rho\overline{u_i u_j})$ are the partial derivatives of these products. The subscripts indicate which component of a quantity is considered, and the repetition of a subscript in a term indicates a summation to be carried out over the possible components. For the case under consideration, if the x-axis is taken as the axial direction of the jet, the y-axis normal to the x-axis and in the direction of the height of the nozzle and the z-axis as the third axis of the co-ordinate system orthogonal to the other two axes; Eq. (D.1) can be written as

$$\frac{\partial U}{\partial t} + U\frac{\partial U}{\partial x} + V\frac{\partial U}{\partial y} + W\frac{\partial U}{\partial z} = -\frac{1}{\rho}\frac{\partial P}{\partial x} + \nu\left(\frac{\partial^2 U}{\partial x^2} + \frac{\partial^2 U}{\partial y^2} + \frac{\partial^2 U}{\partial z^2}\right) + -\left(\frac{\partial\overline{u^2}}{\partial x} + \frac{\partial\overline{uv}}{\partial y} + \frac{\partial\overline{uw}}{\partial z}\right) + \frac{F_1}{\rho} \qquad \text{(D.2)}$$

$$\frac{\partial V}{\partial t} + U\frac{\partial V}{\partial x} + V\frac{\partial V}{\partial y} + W\frac{\partial V}{\partial z} = -\frac{1}{\rho}\frac{\partial P}{\partial y} + \nu\left(\frac{\partial^2 V}{\partial x^2} + \frac{\partial^2 V}{\partial y^2} + \frac{\partial^2 V}{\partial z^2}\right) + -\left(\frac{\partial\overline{uv}}{\partial x} + \frac{\partial\overline{v^2}}{\partial y} + \frac{\partial\overline{vw}}{\partial z}\right) + \frac{F_2}{\rho} \qquad \text{(D.3)}$$

$$\frac{\partial W}{\partial t} + U\frac{\partial W}{\partial x} + V\frac{\partial W}{\partial y} + W\frac{\partial W}{\partial z} = -\frac{1}{\rho}\frac{\partial P}{\partial z} + \nu\left(\frac{\partial^2 W}{\partial x^2} + \frac{\partial^2 W}{\partial y^2} + \frac{\partial^2 W}{\partial z^2}\right) -\left(\frac{\partial\overline{uw}}{\partial x} + \frac{\partial\overline{vw}}{\partial y} + \frac{\partial\overline{w^2}}{\partial z}\right) + \frac{F_3}{\rho} \qquad \text{(D.4)}$$

U,V and W and u,v and w are the turbulent mean and fluctuating velocities in the x,y and z co-ordinate direction and $\nu$ is the kinematic viscosity. The continuity equation is written as

$$\frac{\partial U}{\partial x} + \frac{\partial V}{\partial y} + \frac{\partial W}{\partial z} = 0 \qquad (D.5)$$

To apply Eqs. (D.2), (D.3), (D.4) and (D.5) when analysing the flow described in Fig. D.1, the following assumptions must be made.

(a) The mean flow velocity in the direction transverse to the main flow is very small compared with the main flow velocity.

(b) Changes in the quantities in the direction of main flow are correspondingly slow with respect to those in the transverse direction.

(c) The body force effects are negligible.

Since the mean flow is two-dimensional, $W = 0, \partial/\partial z$ of any mean quantity is zero; $\overline{uw} = 0$; $\overline{vw} = 0$ and since the mean flow is steady $\partial U/\partial t = 0$ and $\partial V/\partial t = 0$. Further, since the transverse extent of the flow is small, U is generally much larger than V over a large portion of the jet and the velocity and stress gradients in the y-direction are much larger than those in the x-direction. With these considerations, the equations of motion can be shown to reduce to the form

$$\left.\begin{aligned} U\frac{\partial U}{\partial x} + V\frac{\partial U}{\partial y} &= -\frac{1}{\rho}\frac{\partial P}{\partial x} + \nu\frac{\partial^2 U}{\partial y^2} - \frac{\partial \overline{uv}}{\partial y} - \frac{\partial \overline{u^2}}{\partial x} && \text{(a)}\\ 0 &= -\frac{1}{\rho}\frac{\partial P}{\partial y} - \frac{\partial \overline{v^2}}{\partial y} && \text{(b)}\\ \frac{\partial U}{\partial x} + \frac{\partial V}{\partial y} &= 0 && \text{(c)} \end{aligned}\right\} \quad (D.6)$$

Integrating (D.6b) with respect to y from y to a point located outside the jet, it can be concluded that

$$p = p_\infty - \rho\overline{v^2} \qquad (D.7)$$

where $p_\infty$ is the pressure outside the jet. Differentiating the above equation and substituting in (D.6a), it can be written that

$$U\frac{\partial U}{\partial x} + V\frac{\partial U}{\partial y} = -\frac{1}{\rho}\frac{dp_\infty}{dx} + \nu\frac{\partial^2 U}{\partial y^2} - \frac{\partial \overline{uv}}{\partial y} - \frac{\partial}{\partial x}(\overline{u^2} - \overline{v^2}) \qquad (D.8)$$

The last term in the above equation is smaller than the other terms and could be neglected. The reduced equations of motion are

$$\left.\begin{aligned} U\frac{\partial U}{\partial x} + V\frac{\partial U}{\partial y} &= -\frac{1}{\rho}\frac{dp}{dx} + \nu\frac{\partial^2 U}{\partial y^2} - \frac{\partial\overline{uv}}{\partial y} \quad &(a)\\ \frac{\partial U}{\partial x} + \frac{\partial V}{\partial y} &= 0 \quad &(b)\end{aligned}\right\} \quad (D.9)$$

where $P_\infty$ is simply written as P for convenience. In Eq. (D.9a), the last term can be rewritten as

$$-\frac{\partial\overline{uv}}{\partial y} = +\frac{1}{\rho}\frac{\partial}{\partial y}(-\rho\overline{uv}) = \frac{1}{\rho}\frac{\partial\tau_t}{\partial y} \quad (D.10)$$

where $\tau_t$ stands for the turbulent shear stress, which is quite large compared to the mean viscous shear stress (Schlichting, 1960). Further, because in a large number of practical problems the pressure gradient in the axial direction is negligibly small and also to study the jet under relatively simpler conditions, it is assumed that $dP/dx \simeq 0$. The equations of motion of the plane turbulent wall jet with a zero pressure gradient in the axial direction will reduce to the following form

$$\left.\begin{aligned} U\frac{\partial U}{\partial x} + V\frac{\partial U}{\partial y} &= -\frac{1}{\rho}\frac{dP}{dx} + \nu\frac{\partial^2 U}{\partial y^2} + \frac{1}{\rho}\frac{\partial\tau_t}{\partial y} \quad &(a)\\ \frac{\partial U}{\partial x} + \frac{\partial V}{\partial y} &= 0 \quad &(b)\end{aligned}\right\} \quad (D.11)$$

### D.1.2 Similarity Analysis of Equations of Motion

The investigations of Förthmann (1936), Glauert (1956) and Eichebrenner and Dumargue (1962) have shown that, strictly speaking, the velocity profiles in the fully-developed region of a plane turbulent wall jet cannot be similar; but, if a small region near the boundary is neglected, the velocity distribution is indeed similar. This means that a curve $f(\eta)$ defined as

$$f(\eta) = U/U_{max} \quad (a)$$

where

$$\eta = y/\delta_1 \quad (b) \qquad (D.12)$$

exists whose co-ordinates are constant and independent of the history of the flow. $U_{max}$ and $\delta_1$ are normally assumed to be of the following simple form

$$U_{max} \sim x^p \quad (a)$$

$$\delta_1 \sim x^q \quad (b) \qquad (D.13)$$

Based on experimental observations and also from a dimensional consideration

$$\tau_t/\rho U^2_{max} = g(\eta) \qquad (D.14)$$

Based on the above assumptions, the individual terms of Eq. (D.11) can be evaluated as follows

$$U = U_{max} f(\eta) \qquad (D.15)$$

By differentiating Eq. (D.15), it can be concluded that

$$\frac{\partial U}{\partial x} = \frac{\partial}{\partial x}(U_{max} f) = f \frac{dU_{max}}{dx} + U_{max} \frac{df}{d\eta} \frac{\partial \eta}{\partial \delta_1} \frac{d\delta_1}{dx}$$

$$\frac{\partial U}{\partial x} = fU'_{max} - U_{max} f' \frac{y}{\delta_1^2} \delta_1' = fU'_{max} - U_{max} f' \frac{\eta}{\delta_1} \delta_1' \qquad (D.16)$$

where $f' = df/d\eta$; $\delta_1' = d\delta_1/dx$; $U'_{max} = dU_{max}/dx$. Hence

$$U \frac{\partial U}{\partial x} = U_{max} U'_{max} f^2 - \frac{U^2_{max} \delta_1'}{\delta_1} \eta f f' \qquad (D.17)$$

In order to evaluate the second term in relationship (D.11a), an expression for V can be obtained by integrating the continuity equation

$$
\begin{aligned}
v &= \int_o^y \frac{\partial V}{\partial y}\, dy = -\int_o^y \frac{\partial U}{\partial x}\, dy \\
&= \int_o^y \left(\frac{U_{max}\,\delta_1'}{\delta_1}\,\eta f' - U_{max}' f\right) dy \\
&= U_{max}\delta_1' \int_o^y \frac{\eta f'}{\delta_1}\, dy - U_{max}' \int_o^y f\, dy \\
&= U_{max}\delta_1' \int_o^\eta \eta f'\, d\eta - U_{max}'\delta_1 \int_o^\eta f\, d\eta \\
&= U_{max}\delta_1' \left(\eta f - \int_o^\eta f\, d\eta\right) - U_{max}\delta_1 \int_o^\eta f\, d\eta
\end{aligned}
\qquad \text{(D.18)}
$$

The partial derivative of U with respect to y is

$$\frac{\partial U}{\partial y} = \frac{\partial}{\partial y}(U_{max} f) = U_{max} f' \frac{\partial \eta}{\partial y} = \frac{U_{max} f'}{\delta_1} \qquad \text{(D.19)}$$

Hence

$$v \frac{\partial U}{\partial y} = \frac{U_{max}^2 \delta_1'}{\delta_1}(\eta f f' - f' \int_o^\eta f\, d\eta) - U_{max} U_{max}' f' \int_o^\eta f\, d\eta \qquad \text{(D.20)}$$

The third term on the right-hand side of Eq. (D.11a) can be written as

$$\frac{1}{\rho}\frac{\partial \tau_t}{\partial y} = \frac{1}{\rho}\frac{\partial}{\partial y}(\rho U_{max}^2 g) = U_{max}^2 \frac{dg}{d\eta}\frac{\partial \eta}{\partial y} = \frac{U_{max}^2 g'}{\delta_1} \qquad \text{(D.21)}$$

where $g' = dg/d\eta$. The second term on the right-hand side of (D.11a) may be written as

$$\nu \frac{\partial^2 U}{\partial y^2} = \nu \frac{\partial}{\partial y}\left(\frac{U_m f'}{\delta_1}\right) = \frac{\nu U_{max}}{\delta_1^2} f'' \qquad \text{(D.22)}$$

where $f'' = d^2 f/d\eta^2$. Substituting (D.17), (D.20), (D.21) and (D.22) in (D.11a) leads to the following relationship

$$g' = \frac{\delta_1 U_{max}' f^2}{U_{max}} - \delta_1' f' \int_o^\eta f\, d\eta - \frac{\nu f''}{\delta_1 U_{max}} \qquad \text{(D.23)}$$

For most of the wall jet problems of practical interest, $U_{max}\,\delta_1/\nu$ is large and hence the last term in Eq. (D.23) can be neglected. From the assumptions made in (D.13), it follows that

$$\left.\begin{aligned} &\frac{\delta_1 U'_{max}}{U_{max}} \propto x^{q-1} && \text{(a)}\\ &\delta_1' \propto x^{q-1} && \text{(b)} \end{aligned}\right\} \quad \text{(D.24)}$$

and in this case, the Eq. (D.23) will result in $q = 1$.

### D.1.3 Integral Momentum Equation

The equation of motion may be written in the following form

$$\left.\begin{aligned} &U\frac{\partial U}{\partial x} + V\frac{\partial U}{\partial y} = -\frac{1}{\rho}\frac{dP}{dx} + \frac{1}{\rho}\frac{\partial}{\partial y}\left(\mu\frac{\partial U}{\partial y} + \tau_t\right) && \text{(a)}\\ \text{or}\quad &U\frac{\partial U}{\partial x} + V\frac{\partial U}{\partial y} = -\frac{1}{\rho}\frac{dP}{dx} + \frac{1}{\rho}\frac{\partial \tau}{\partial y} && \text{(b)} \end{aligned}\right\} \quad \text{(D.25)}$$

where $\tau$ is the total stress which is the sum of the viscous stress and the apparent stress. Multiplying Eq. (D.25b) by $\rho$ and integrating with respect to y from $y = 0$ to $y = \infty$ leads to

$$\rho\int_0^\infty U\frac{\partial U}{\partial x}\,dy + \rho\int_0^\infty V\frac{\partial U}{\partial y}\,dy = \int_0^\infty \frac{\partial \tau}{\partial y}\,dy = \int_0^\infty \tau = -\tau_o \qquad \text{(D.26)}$$

where $\tau_o$ is the wall shear stress. The individual terms of the above equation are elvaluated here. Using the Liebnitz rule* (Wylie, 1966), the first term can be written as

$$\rho\int_0^\infty U\frac{\partial U}{\partial x}\,dy = \tfrac{1}{2}\int_0^\infty \frac{\partial}{\partial x}(\rho U^2)\,dy = \tfrac{1}{2}\frac{d}{dx}\int_0^\infty \rho U^2\,dy \qquad \text{(D.27)}$$

Using the continuity equation, the second term may be written as

* According to the Leibnitz rule, if $F(t) = \int_{a(t)}^{b(t)} \phi(x,t)\,dx$, where a and b are differentiable functions of t and where $\phi(x,t)$ and $\frac{\partial \phi(x,t)}{\partial t}$ are continuous in x and t, then

$$\frac{dF}{dt} = \int_{a(t)}^{b(t)} \frac{\partial \phi(x,t)}{\partial t}\,dx + \phi[b(t),t]\frac{db(t)}{dt} - \phi[a(t),t]\frac{da(t)}{dt}$$

$$\left.\begin{aligned} \rho\int_o^\infty V\frac{\partial U}{\partial y}\,dy &= \rho\Big(UV\Big|_o^\infty - \int_o^\infty U\frac{\partial V}{\partial y}\,dy\Big) \\ &= \rho\int_o^\infty U\frac{\partial U}{\partial x}\,dy = \tfrac{1}{2}\frac{d}{dx}\int_o^\infty \rho U^2\,dy \end{aligned}\right\} \quad (D.28)$$

Hence Eq. (D.26) can be written in the following form

$$\tfrac{1}{2}\frac{d}{dx}\int_o^\infty \rho U^2\,dy + \tfrac{1}{2}\frac{d}{dx}\int_o^\infty \rho U^2\,dy = \frac{d}{dx}\int_o^\infty \rho U^2\,dy = -\tau_o \qquad (D.29)$$

However if $U = U_{max} f(\eta)$ and $dy = \delta_1\, d\eta$ as before, the above relationship may be written as

$$\left.\begin{aligned} &\frac{d}{dx}\int_o^\infty \rho U_{max}^2 f^2(\eta)\,\delta_1 d\eta = -\tau_o \qquad (a) \\ \text{or} \\ &f^2(\eta)\,d\eta\Big[\frac{d}{dx}\int_o^\infty \rho U_{max}^2\,\delta_1\Big] = -\tau_o \qquad (b \end{aligned}\right\} \quad (D.30)$$

From the assumptions of (D.13), it can be concluded that

$$\left.\begin{aligned} &U_{max}^2\,\delta_1 \propto x^{(2p+q)} \qquad (a) \\ &\frac{d}{dx}\,(U_{max}^2\,\delta_1) \propto x^{2p+q-1} \qquad (b) \end{aligned}\right\} \quad (D.31)$$

If it is assumed that

$$\tau_o \propto x^{\delta} \qquad (D.32)$$

Then, from Eq. (D.30b) it follows that

$$2p + q - 1 = \delta \qquad (D.33)$$

With q being equal to 1, the above relationship will reduce to

$$2p = \delta \qquad (D.34)$$

However most experimental workers such as Narasimha, Narayan and Parthasarathy (1973) correlate $U_{max}$ and x by the use of a power law expression of the form

$$\frac{U_{max}}{U_o} = A_1 (x/d)^p \qquad (D.35)$$

Values quoted for the constants in Eq. (D.35) often vary widely, p ranges from -0.49 to -0.62, and $A_1$ from about 3 to 7. However, if p is assumed to be -0.5, then from relationship (D.34), it immediately follows that $\delta = -1$. This means that $\tau_o$ decreases inversely with x. Thus for the classical plane turbulent wall jet, it follows that

$$\left.\begin{aligned} U_{max} &\propto 1/\sqrt{x} && \text{(a)} \\ \delta_1 &\propto x && \text{(b)} \\ \tau_o &\propto 1/x && \text{(c)} \end{aligned}\right\} \quad (D.36)$$

### D.1.4 Dimensional Considerations

In presenting experimental results on turbulent wall jets most researchers such as Bradshaw and Gee (1962) and Kohan (1969) have demonstrated their results by using the slot height d and jet exit velocity $U_o$ as well as the jet momentum flux $M_j$ from the nozzle. If the momentum flux $M_j$ which is approximately preserved (Rajaratnam, 1976) is accepted as the main parameter in this problem, for a fully-developed wall jet the following relationships can be written

$$\left.\begin{aligned} U_{max} &= f_1(M_j, \rho, x, \nu) && \text{(a)} \\ \delta_1 &= f_2(M_j, \rho, x, \nu) && \text{(b)} \\ \tau_o &= f_3(M_j, \rho, x, \nu) && \text{(c)} \end{aligned}\right\} \quad (D.37)$$

Application of the Buckingham $\pi$ theorem gives the following results

$$\left.\begin{aligned} U_{max}/\sqrt{M_j/\rho x} &= g_1(R_j) && \text{(a)} \\ \delta_1/x &= g_2(R_j) && \text{(b)} \\ \tau_o/(M_j/x) &= g_3(R_j) && \text{(c)} \end{aligned}\right\} \quad (D.38)$$

where $g_1, g_2$ and $g_3$ are functions of the nozzle Reynolds number (Reynolds nubmer of the jet) defined as

$$R_j = U_o d/\nu \tag{D.39}$$

Experimental results have generally indicated that if $R_j$ is greater than $10^4$, the variation of $g_1(R_j)$, $g_2(R_j)$ and $g_3(R_j)$ with $R_j$ is small and in this case the above relationships reduce to the following simpler forms

$$\left.\begin{aligned} \frac{U}{U_{max}}/U_o &= C_1/\sqrt{x/d} && \text{(a)} \\ \delta_1 &= C_2 x && \text{(b)} \\ c_f &= \tau_o/(\rho U_o^2/2) = C_3/(x/d) && \text{(c)} \end{aligned}\right\} \tag{D.40}$$

where $c_f$ is called a *skin-friction coefficient*.

### D.1.5 Experimental Results

The first experimental study of a plane turbulent wall jet appears to have been made by Förthmann (1936). His observations on the velocity distributions indicated that the flow becomes fully established for x greater than about 15d. Further experiments on the plane wall jets have been performed by Zerbe and Selna (1946), Sigalla (1958), Schwarz and Cosart (1961) and Myers, Schauer and Eustis (1963). For wall jets, in general, the velocity distribution in the inner layer is better described by a power law of the form

$$\frac{U}{U_{max}} = (y/\delta)^n \tag{D.41}$$

where $n$, like $\delta$ and $U_{max}$, is a function of x. For the classical wall jet, Förthmann (1936) found that the velocity distribution in the boundary layer follows the one-seventh power law ($n=1/7$), as in the Blasius law. However, experimental observations of Schwarz and Cosart (1961) and Myers et al. (1963) have shown that with the Reynolds number, $R_j$, in the range $10^4$ to $10^5$, the value of the exponent is closer to 1/14. Further Myers et al. (1963) found that the logarithmic law is valid in the form

$$U/U_* = 5.6 \log(yU_*/\nu) + 4.9 \qquad (D.42)$$

with $U_* = \sqrt{\tau_o/\rho}$, whereas Mathieu and Thailland (1963) have reported different values for the coefficients in Eq. (D.42) (4.45 instead of 5.6, and 10.3 instead of 4.9).

The velocity distribution of the entire wall jet has been found to be similar by Sigalla (1968), Schwarz and Cosart (1961) and Myers et al. (1963), thereby confirming the earlier observations of Förthmann (1936). The co-ordinates of the similarity curve based on the available experimental

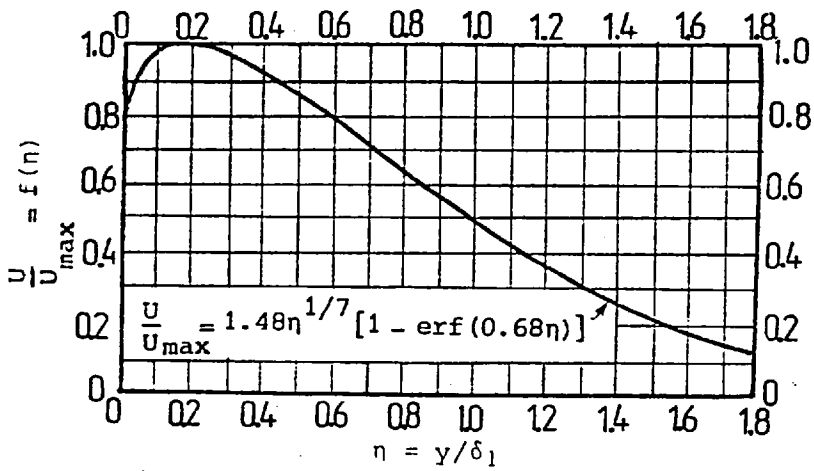


Fig. D.2

data given in Table D.1. Verhoff (1963) derived an empirical relationship to describe the similarity curve which he gave as

$$\frac{U}{U_{max}} = 1.48\eta^{1/7}[1 - erf(0.68\eta)] \qquad (D.43)$$

where erf is the 'error function' defined by

$$erf(\eta) = \frac{2}{\sqrt{\pi}} \int_0^{\eta} e^{-t^2} dt \qquad (D.44)$$

The portion of the curve in Fig. D.2, in which $f(\eta)$ increases from zero to unity, resembles the inner layer.

| η | f(η) |
|---|---|
| 0.00 | 0.000 |
| 0.02 | 0.790 |
| 0.05 | 0.900 |
| 0.08 | 0.950 |
| 0.10 | 0.980 |
| 0.10 | 0.980 |
| 0.16 | 1.000 |
| 0.20 | 0.995 |
| 0.30 | 0.950 |
| 0.40 | 0.890 |
| 0.50 | 0.825 |
| 0.60 | 0.760 |
| 0.70 | 0.690 |
| 0.80 | 0.625 |
| 0.90 | 0.560 |
| 1.00 | 0.500 |
| 1.10 | 0.450 |
| 1.20 | 0.405 |
| 1.30 | 0.360 |
| 1.40 | 0.310 |
| 1.50 | 0.260 |
| 1.60 | 0.220 |
| 1.70 | 0.170 |
| 1.80 | 0.125 |
| 2.00 | 0.055 |
| 2.10 | 0.030 |
| 2.20 | 0.005 |
| 2.25 | 0.000 |

Table D.1 Coordinates for the velocity-distribution curve of the classical plane turbulent wall jet

As has already been described, the velocity profile of a wall jet is divided into two regions of inner and outer layers, separated by the position at which the correlation $\overline{uv} = 0$. The investigations of Eskinazi and Yeh (1956) showed that for asymmetrical velocity profiles, the positions of the zero value of the fluctuating correlation $\overline{uv}$ is *not* at the point of maximum velocity. For the wall jet, this phenomenon was indicated by Mathieu (1959). However, since the determination of this position is impractical for mean flow considerations, the location of the maximum velocity is normally chosen as the dividing point.

The experimental results of Myer et al. (1963), which are available in tabular form, are shown plotted in Fig. D.3 as $(U_o/U_{max})^2$ versus x/d, where x is measured from a virtual origin not generally coincident with the position of the slot. Rajaratnam (1965) reported that the virtual

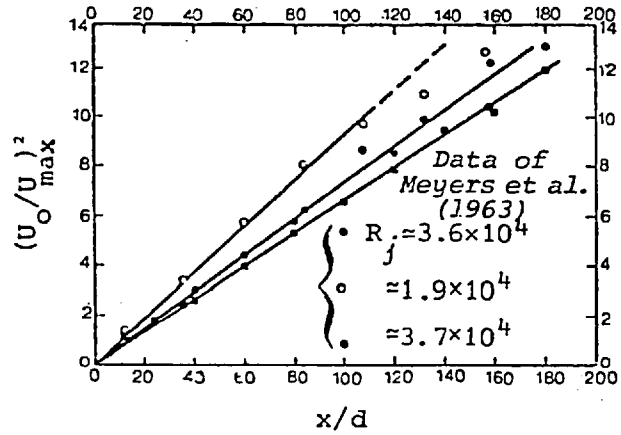


Fig. D.3 Variation of the velocity scale for plane wall jets

origin is located roughly 10d behind the nozzle. From the Fig. D.3 it can be seen that most of the points are well described by straight lines passing through the (centre of the) nozzle. Most of the available observations on the decay of the velocity scale are reproduced in Fig. D.4 from Rajaratnam and Subramanya (1967) and the average curve is well described by the equation

$$\frac{U}{U_{max}} / U_o = 3.5/\sqrt{\bar{x}/d} \qquad (D.45)$$

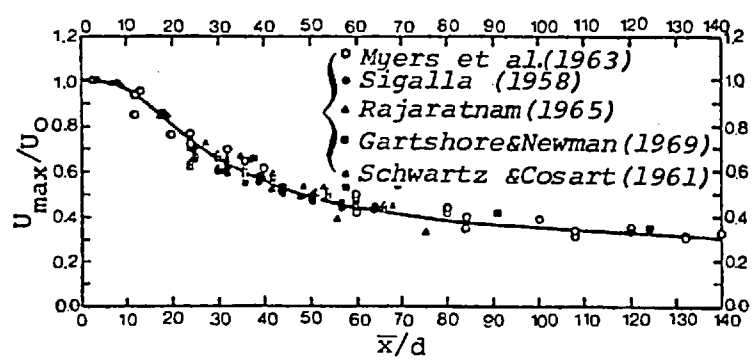


Fig. D.4 Correlation of the velocity scale for plane wall jets

for $\bar{x}/d$ at least up to 100. The Reynolds number of the jet has not been found to influence the above relationship to any appreciable extent.

Some of the results regarding the length scale are shown in Fig. D.5. Most experimental workers such as Kohan (1969) correlate $\delta_1$ and x by the use of a power law expression of the form

$$\frac{\delta_1}{d} = A_2(x/d)^t \qquad (D.46)$$

In Eq. (D.46) x is measured from a virtual origin (it is normally assumed that the virtual origin is located 10d behind the nozzle). Most investigators have assumed t to be equal to 1 and $A_2$ to be equal to 0.068. In this case, the length scale can be presented by the following simple relationship

$$\delta_1 = 0.068x \qquad \text{(a)}$$

or

$$\delta_1/d = 0.68 + 0.068\,\bar{x}/d \qquad \text{(b)} \qquad (D.47)$$

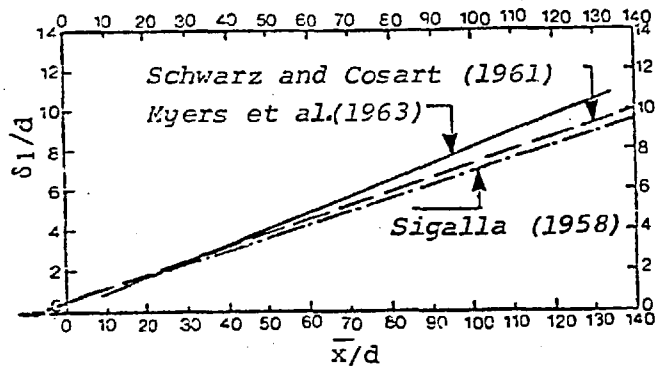


Fig. D.5 Growth of the length scale for plane wall jets

The coefficient in Eq. (D.47a) has been found to have slightly different values by other investigators. Rajaratnam (1965) expressed a view that the Reynolds number of the jet would not significantly influence the relationship (D.46). However a subsequent investigation by Kohn (1969) led to the following expression for $A_2$

$$A_2 = (-4.05 \pm 0.61)10^{-7}R_j + 0.08 \qquad (D.48)$$

It has been found (Narasimha, Narayan and Parthasarathy, 1973), that

$$\delta \simeq 0.16\,\delta_1 \tag{D.49}$$

and that the upper boundary of the jet (Fig. D.1) is fixed approximately at

$$\delta_2 \simeq 2.25\delta_1 \tag{D.50}$$

Dimensional and analytical considerations predicted that $\tau_o \propto 1/x$. The variation of the skin-friction coefficient $c_f$ defined as (D.40c) could be expressed by the equation (Mayer et al. 1963)

$$c_f = \frac{\tau_o}{\rho U_o^2/2} = \frac{0.20}{(x/d)(U_o d/\nu)^{1/12}} \tag{D.51}$$

The results of Sigalla (1958) on $\tau_o$, obtained with the Preston tube, are known to be about 15% less than the results of Mayer et al. (1963). However, Sigalla recommended the empirical equation

$$c_f' = \frac{\tau_o}{\rho U_{max}^2/2} = \frac{0.0565}{(U_{max}\delta/\nu)^{1/4}} \tag{D.52}$$

If $Q$ is the *forward flow* per unit width of the wall jet, the following can be written

$$Q = \int_o^\infty U dy \tag{D.53}$$

By using relationships (D.12a) and (D.12b), the above equation may be written as

$$Q = U_{max}\delta_1 \int_o^\infty f d\eta \tag{D.54}$$

Using the relationships developed for the velocity and length scales, and the curve for the velocity distribution, the value of $Q$ can be calculated at any point.

## D.2 PLANE TURBULENT FREE JET AND WALL JET

The aim of this section is to compare the plane turbulent free jet diffusing in an infinite stagnant ambient environment with the corresponding plane turbulent wall jet on a smooth boundary with regard to the three important characteristics, namely the velocity distribution and the variation of the velocity and length scales, in the region of developed flow.

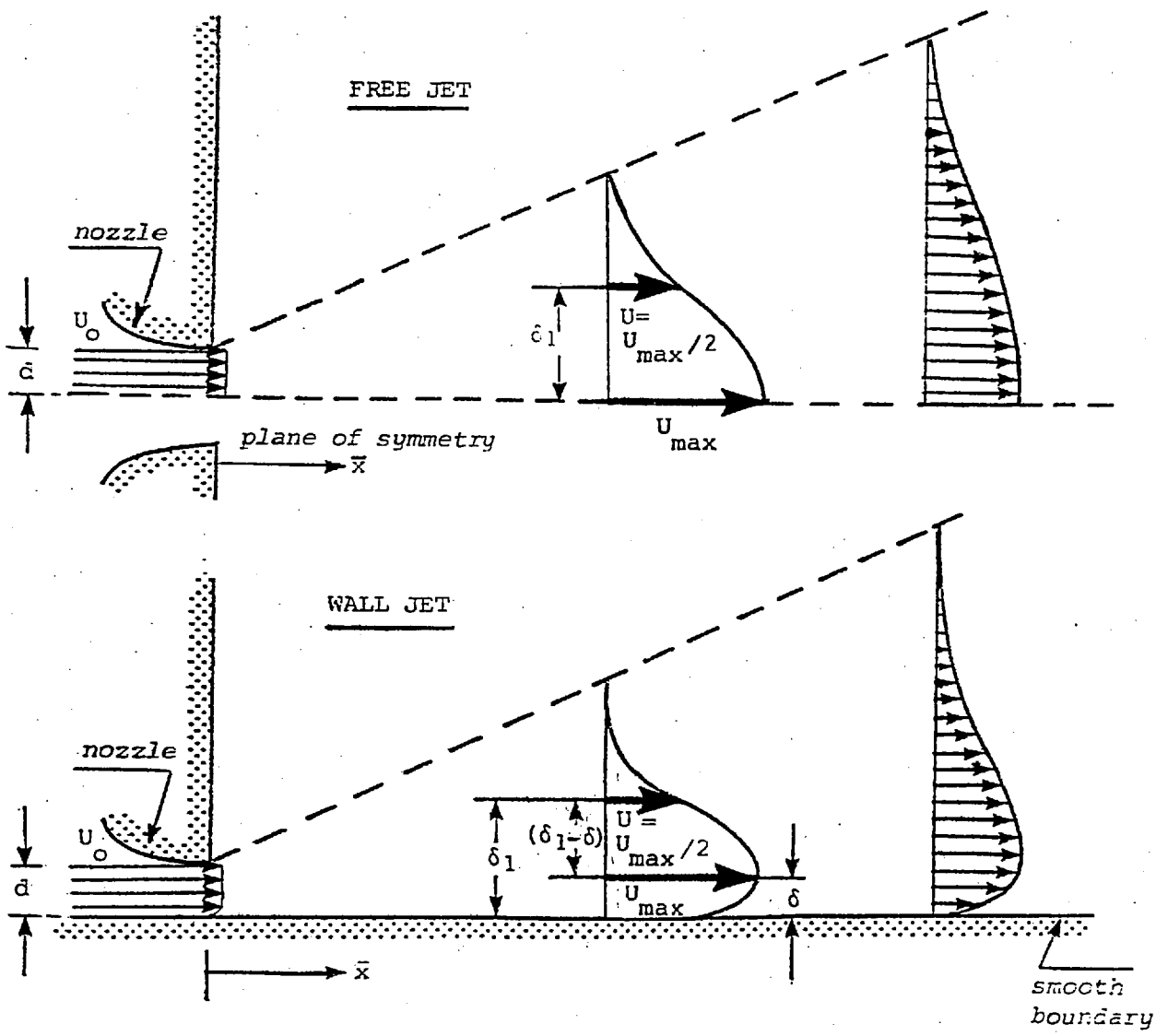


Fig. D.6 The plane free jet and wall jet

## D.2.1 The Free Jet

Figure D.6 shows a free jet of thickness 2d with an almost uniform velocity $U_o$ diffusing in an infinite stagnant surrounding. It has been found (Yevdjevich, 1966) that the length of the potential core is about 11.8 to 13.2d. If $\bar{x}$ is the longitudinal distance from the nozzle, for $\bar{x}/d$ greater than approximately 12, the transverse mean velocity distribution is similar and is satisfactorily described by the theoretical solutions of Tollmien (1933) and Görtler (1942). The velocity scale for the similarity profile is the maximum velocity $U_{max}$ at the section and the length scale is the transverse distance $\delta_1$ between the planes where the mean velocities are respectively equal to $U_{max}$ and $U_{max}/2$.

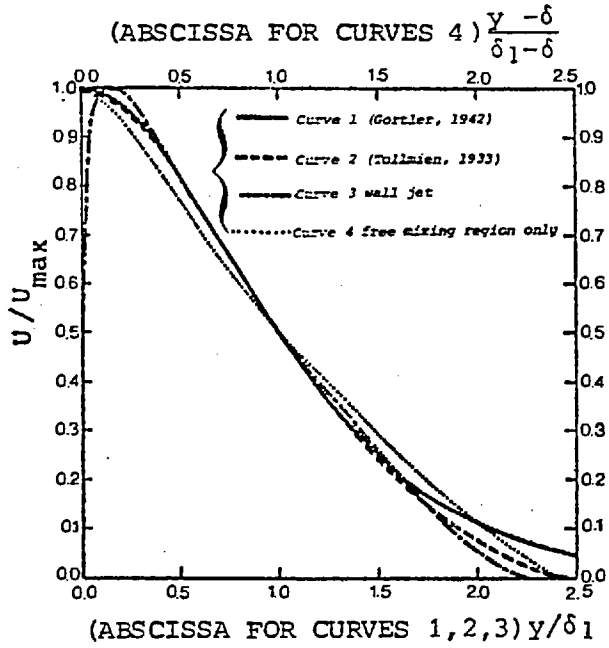


Fig. D.7

The velocity distributions given by Tollmien (1933) and Görtler (1942) are shown in Fig. D.7, where the dimensionless abscissa is $y/\delta_1$, y being the normal distance from the axis of the jet.

## D.2.2 The Wall Jet

Considering a jet, consisting of a fluid similar to that of its surroundings, impinges tangentially to a plane surface and spreads over the surface (the surrounding fluid is assumed to be stationary). As has already been defined, the mean velocity distribution is essentially similar. From Fig. D.7, it can be seen that, except in the boundary layer region (i.e. $y < \delta$) and a very small portion of the outer free mixing region (i.e. $y > \delta$), the wall jet profile agrees well with that of the free jet, especially with the curve of Tollmien.

It is interesting to compare the free jet curve with the free mixing region portion of the wall jet. The abscissa of the free mixing region curve of the wall jet is $(y-\delta)/(\delta_1-\delta)$ and the ordinate is $U/U_{max}$. Knowing that $\delta = 0.16\delta_1$ and by using Table D.1, the co-ordinates of the free mixing region curve of the plane wall jet can easily be obtained (Table D.2). This curve is plotted in Fig. D.7, and it can be seen that it is slightly different from the others, however for practical purposes, this difference could possibly be neglected.

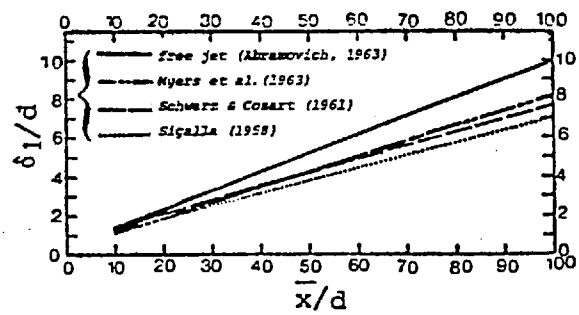


Fig. D.8

The variations in the length scale as given by Sigalla (1958), Schwarz and Cosart (1961), Myers et al. (1963) are plotted in Fig. D.8. It can be seen that the curve of Schwarz and Cosart (1961) is a good average for the wall jet data. Based on this, it can be seen that the length scale $\delta_1$ of the wall jet grows at 0.7 times the rate of that of the free jet.

| $\eta_1 = \frac{y-\delta}{\delta_1-\delta}$ <br> $\delta = 0.16\delta_1$ | f(η) |
|---|---|
| 0.000 | 1.000 |
| 0.048 | 0.995 |
| 0.167 | 0.950 |
| 0.286 | 0.890 |
| 0.405 | 0.825 |
| 0.524 | 0.760 |
| 0.643 | 0.690 |
| 0.762 | 0.625 |
| 0.881 | 0.560 |
| 1.000 | 0.500 |
| 1.119 | 0.450 |
| 1.238 | 0.405 |
| 1.357 | 0.360 |
| 1.476 | 0.310 |
| 1.595 | 0.260 |
| 1.714 | 0.220 |
| 1.833 | 0.170 |
| 1.952 | 0.125 |
| 2.071 | 0.085 |
| 2.190 | 0.053 |
| 2.309 | 0.030 |
| 2.429 | 0.005 |
| 2.488 | 0.00 |

Table D.2 Co-ordinates for the velocity-distribution of the free mixing region of the wall jet

# CHAPTER E

# EXPERIMENTAL SET-UP AND MEASURING TECHNIQUES

## E.1 GENERAL

The experimental work that was undertaken in the study of a supercritical water flow deflected by a plane, smooth, vertical transverse wall is described in this chapter. The apparatus and the procedure used for producing the fast flow is described in detail first. The methods used to measure the water flow rate, mean pressure field, mean flow direction and the mean velocity profile and to record the complicated wave patterns occurring at the retaining wall is also described. Finally, the facilities for and the procedure used in the analysis of the experimental measurements, together with an outline of the experimental programme performed are given in this chapter. However, before describing the details of the experimental apparatus and the different measuring techniques, some basic uncertainties in the measurements must be defined.

## E.2 TOLERANCE ON MEASUREMENT

All physical measurements are inaccurate to some degree and it is therefore essential that every measurement should be accompanied by an assessment of the *uncertainty* involved.

### E.2.1 Uncertainty

Uncertainty applies to a *measurement* rather than an instrument. The total uncertainty of a measurement is defined as the range in which the true value is likely to lie, at a stated level of probability. Thus, the uncertainty of a measurement is not a fixed value but a function of the level of confidence with which the uncertainty of the measurement is quoted, i.e. the higher the confidence level, the greater the uncertainty. The level most often used in industry is 95 percent and this figure has been adopted in this investigation.

#### E.2.1.1 Categories of Uncertainties

Basically there are three types of uncertainty which must be considered.

(a) Spurious uncertainties (human erros and instrument malfunctions)

(b) Random uncertainties (experimental and reading uncertainties)

(c) Systematic uncertainties (which may be either constant or variable).

Spurious uncertainties are uncertainties which can invalidate a measurement. Such uncertainties cannot be incorporated into a statistical analysis and the suspect measurement must be discared. During experiments steps should be taken to avoid such uncertainties or to recognize them and discard the results.

Random uncertainties are uncertainties that affect the ability to reproduce measurements. The propagation of uncertainties is based upon the standard deviation of the uncertainties. The standard deviation of a set of n measurements of a quantity $y$ under *steady* conditions may be estimated from the following equation

$$s_y = \left[ \frac{\sum_{i=1}^{n} (y_i - \bar{y})^2}{(n-1)} \right]^{\frac{1}{2}} \qquad \text{(E.1)}$$

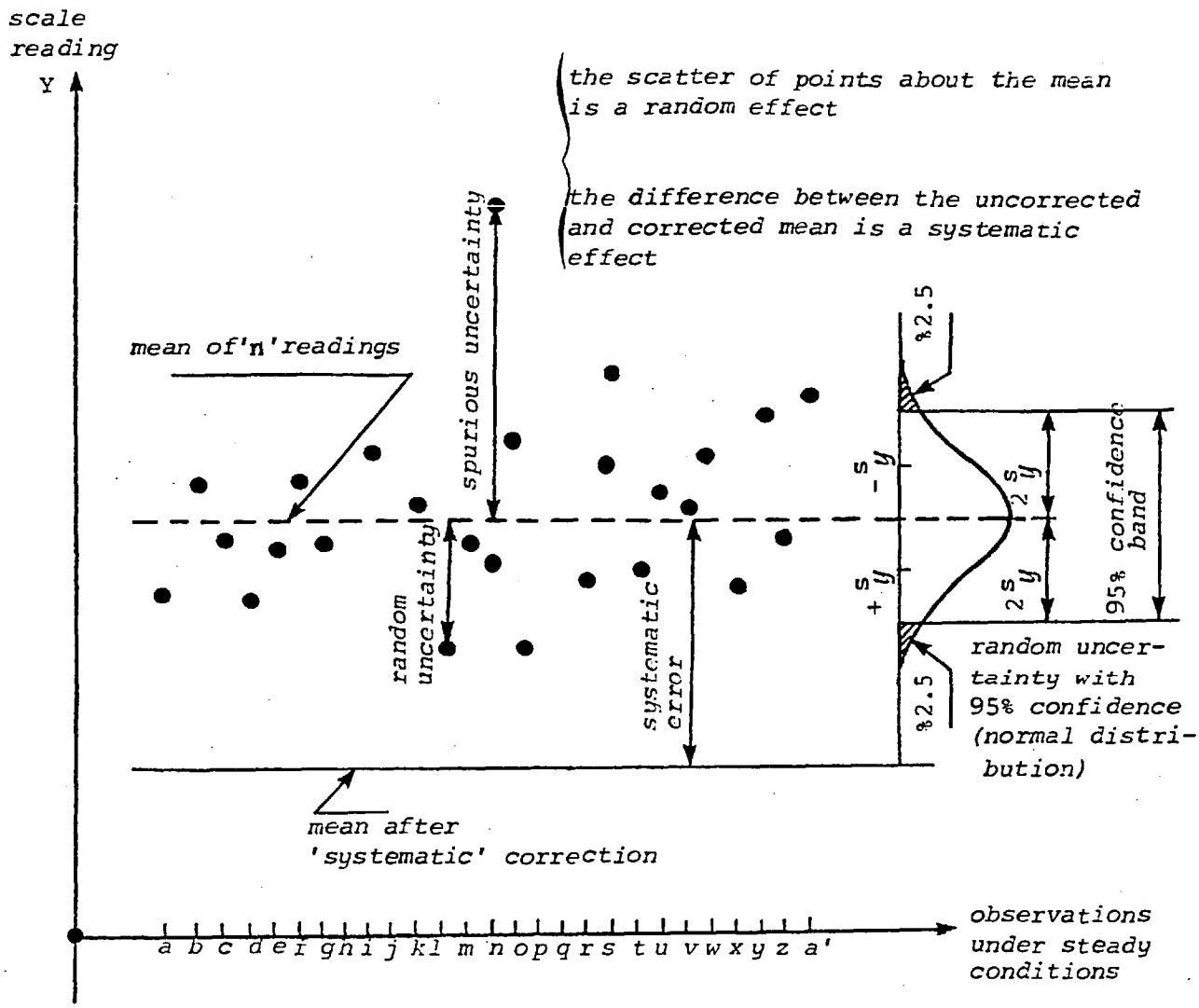


Fig. E.1 A simple example of random and systematic effects

where

$\bar{y}$ = arithmetic mean of the n measurements of the variable $y$

$y_i$ = value obtained by the ith measurement of the variable $y$

n = total number of measurements of $y$.

The *relative standard deviation* $s'_y$ equals $s_y$ divided by the observed mean. Hence

$$s'_y = \frac{1}{\bar{y}} \left[ \frac{\sum_{i=1}^{n} (y_i - \bar{y})^2}{(n-1)} \right]^{\frac{1}{2}} \qquad \text{(E.2)}$$

The mean value will also be subject to a random uncertainty. The *standard deviation of the mean* $s_{\bar{y}}$ is given by

$$s_{\bar{y}} = s_y / \sqrt{n} \qquad \text{(E.3)}$$

For practical purposes, it can be assumed that the distribution of the uncertainties in a set of measurements under steady conditions can be adequately approximated by a *normal* distribution. In this case, the

uncertainty of the mean is twice $s_{\bar{y}}$ at the 95% confidence level (assuming that n is a fairly large number). However, more correctly, the uncertainty is a function of both the number of readings, n, and the confidence level, the uncertainty of the mean can be expressed (Hayward, 1977) as

$$r_m = t_c s_y/\sqrt{n} \qquad \text{(E.4)}$$

where $t_c$ is the value of the mathematical function known as *Student* $t$ which is dependent on both the confidence level and the number of readings. For the 95% confidence level, some typical values for $t_c$ are given in Table E.1.

| n | 4 | 8 | 10 | 12 | 20 | ∞ |
|---|---|---|---|---|---|---|
| $t_c$ | 3.148 | 2.36 | 2.26 | 2.20 | 2.09 | 1.96 |
| $t_c/\sqrt{n}$ | 1.074 | 0.834 | 0.715 | 0.635 | 0.467 | 0 |

Table E.1 Values of $t_c$ for a 95% confidence level

It can be seen from the above table that the value of $t_c$ increases quite rapidly when n is small. If an infinite number of readings are taken, the random uncertainty of the mean becomes zero.

Systematic uncertainties are uncertainties which cannot be reduced by increasing the number of measurements whilst the equipment and experimental conditions remain unchanged. Whenever there is evidence of a systematic uncertainty of known sign, the mean uncertainty should be added to (or subtracted from) the measurement results. In deciding whether an uncertainty is to be regarded as random or systematic, the true criterion should be whether the values assigned to the uncertainty were derived from a statistical analysis of a number of measurements or whether it was only possible to estimate limiting values on a non-statistical basis. Following on from this the random and systematic uncertainties should be treated separately and the overall uncertainty of measurements should have a random and systematic component.

### E.2.2 Repeatability

*Repeatability*, unlike uncertainty, which is a property of a measurement, is a property of an *instrument*. Its British Standard definition (B.S.I., 1975), is "the ability of a measuring instrument to give identical indications, or responses, for repeated applications of the same value of

the measured quantity under stated conditions of use". This means that if a typical reading of the instrument stands at 95% of being within $\pm R$ of the mean of an infinite number of repeated readings, then the repeatability of the instrument is $R$.

### E.2.3 Combination of Uncertainties

The overall uncertainty arises from several contributary uncertainties, which may themselves be composite uncertainties. The total uncertainty is the *square root of the sum of squares* or *'root-sum-squaring'* of the separate percentage uncertainties.

When the uncertainty in a result $\psi$ is desired, where $\psi = \psi(v_1, v_2, \ldots, v_n)$, then a very good approximation is given by

$$w_\psi = \left[ \left(\frac{\partial \psi}{\partial v_1} w_1\right)^2 + \left(\frac{\partial \psi}{\partial v_2} w_2\right)^2 + \left(\frac{\partial \psi}{\partial v_3} w_3\right)^2 + \ldots + \left(\frac{\partial \psi}{\partial v_n} w_n\right)^2 \right]^{\frac{1}{2}} \tag{E.5}$$

where $w_1, w_2, \ldots w_n$ are the uncertainty intervals in $v_1, v_2, \ldots, v_n$, respectively and $w_\psi$ is the uncertainty of the result $\psi$. The above procedure for estimating uncertainties was proposed by Kline and McClintock (1953) and is known as the 'second power equation'.

### E.2.4 Accuracy

The overall uncertainty of a measurement arises from the combined effect of several separate sources of uncertainty. The *accuracy* of a measurement is taken as the square root of the sum of the squares of repeatability and other uncertainties.

### E.2.5 Method of Least Squares

The *least squares method* (often abbreviated as l.s.m.) states that the most probable value of any observed quantity is such that the sum of the squares of the deviations of the observations from this value is minimum. Further details of this are given in Appendix III.

## E.3 THE LABORATORY ARRANGEMENT

### E.3.1 General Layout

The general layout of the laboratory equipment is shown in Plate IV. The main features of the equipment used in this experimental work were a smooth-steep chute of 180 mm width, a smooth horizontal channel and a smooth retaining wall. The geometry of the chute approach was improved on the sides by fitting streamlined plates upstream of the leading edges of the chute (Fig. E.2). The channel was made of perspex of 16 mm thickness and 180 mm width. The retaining wall was made of a steel plate of 5 mm thickness. The side wall was made of 3 mm aluminium sheet (in order to provide a smooth surface). The pointgauge (Plate IV) was supported on a carriage such that a depth reading could be taken at any point in the channel.

### E.3.2 Supply and Disposal of Water

The main supply of water in the hydraulics laboratory consists of a self-contained circuit in which the water from the sump is pumped into several constant head tanks and then distributed to the models, flumes and equipment of the laboratory. The water was supplied to the reservoir from one of the medium head tanks of the laboratory which maintained a water surface level of approximately 13 m above the reservoir.

The reservoir measured 2.3 m long by 1.2m width and was 0.9 m in height. A 100 mm durapipe supplied water to the reservoir and distributed through a manifold. A butterfly control valve was fitted 2 m upstream of the pipe outlet in the reservoir. A honeycomb baffle (Fig. E.2) as well as wire grids were positioned across the reservoir near the pipe outlet to help dissipate disturbances in the flow after it leaves the pipe outlet. Flow out of the model was directed through a drain channel to an underground sump.

### E.3.3 Control of Flow to the Chute

When undertaking experimental work, a researcher should be able to reproduce a particular experiment to sufficient accuracy. To


PLATE IV GENERAL VIEW OF MODEL

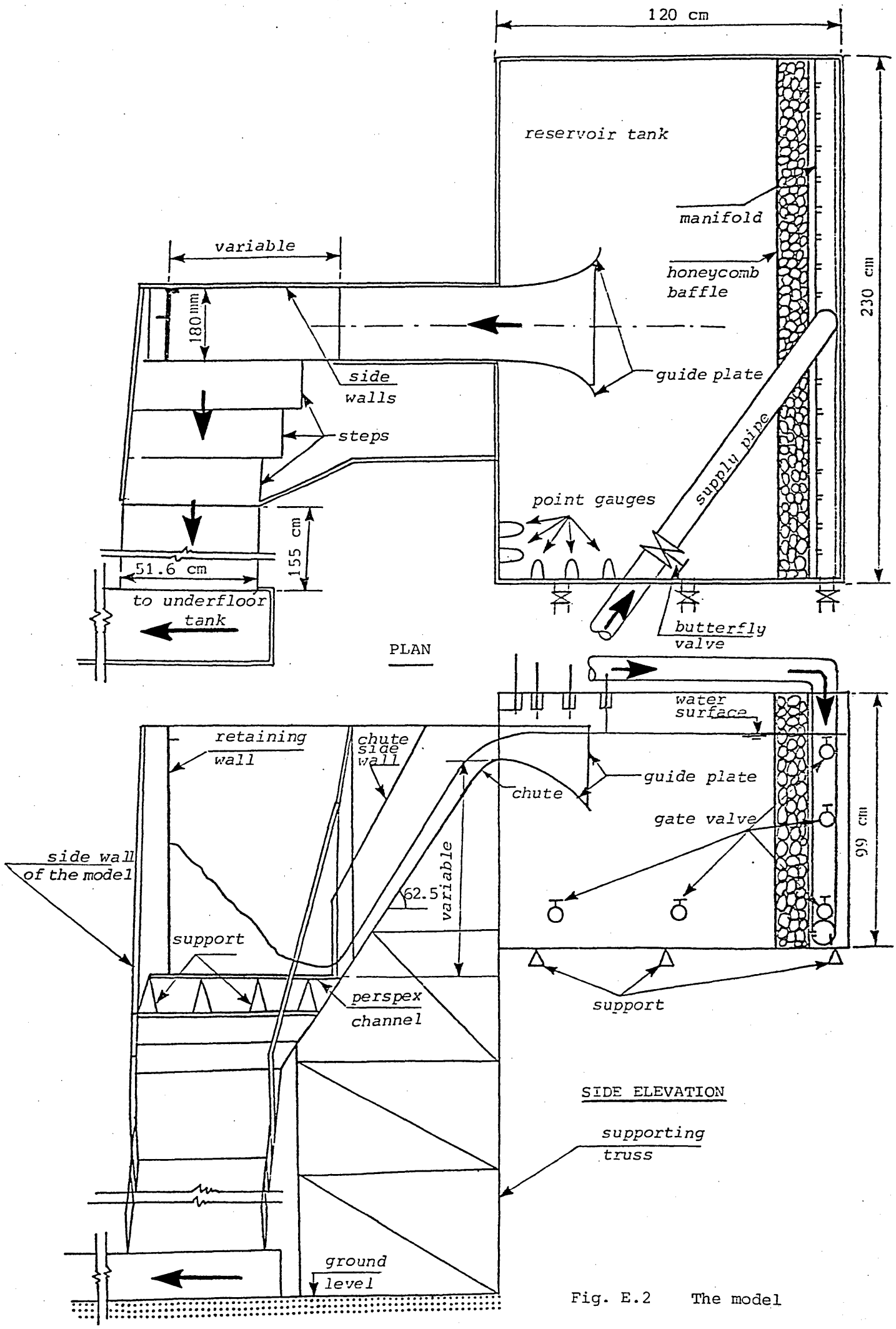


Fig. E.2 The model

achieve this, the water levels in the reservoir were controlled and measured by means of several point gauges which were fixed vertically to the interior face of the reservoir, close to butterfly valve (Fig. E.2). Each point gauge corresponded to a certain water level in the reservoir and hence to a certain experiment. The reservoir area was relatively large so as to dissipate to some extent any disturbances caused by the opening and shutting of the other valves. However, during the initial stages of the investigation, it was noticed that controlling the water level in the tank by means of the butterfly valve was tedious and time-consuming; it was also noticed that during lengthy experiments, the water level in the reservoir unexpectedly dropped or increased slightly. To combat this difficulty, fine adjustment of the water level in the reservoir was made possible by connecting 5 gate valves to the vertical side of the reservoir, near the butterfly valve (Plate V). As will be explained in the next sections, it was sometimes necessary to stop the water flow over the chute instantaneously; this was not possible by merely closing the valve of the water supply. To provide for this, gate valves A, B and C were fixed at the lowest part of the reservoir. By opening all the gate valves, the water flow over the chute could be stopped in a very short time.

### E.3.4. Water Flow Rate Measurements

The discharge from the model was measured volumetrically over a measured time interval with the water being collected in an underfloor volumetric tank, the plan area of which was 41.52 $m^2$. With the aid of the two air operated butterfly valves which opened and closed simultaneously, water flow was cut off from the underfloor tank and discharged into the laboratory sump. The water levels in the underfloor tank were measured by a metered rod provided with electric cells. A signal indicated the water level in the tank. This signal was only activated when a direct current electric circuit was closed by the point gauge tip touching the water surface. The device was mounted on a tripod and could read water level changes within ±0.1 mm.

The water outflow from the model generated irregular waves on the water surface in the underfloor tank. A smooth vertical plastic pipe 1.8 m long, of 8 mm thickness and 153 mm internal diameter enclosed the point gauge and suppressed the irregular disturbances. Water in the

PLATE V VIEW OF THE RESERVOIR

underfloor tank entered the pipe via a 20 mm gap at its lower end. The time of the discharge was measured by a stop-watch with the measurement having an uncertainty of ±0.1 seconds. For a given discharge, the discharge measurement was repeated at least three times and the arithmetic mean of the three measurements was considered the reliable value. The total uncertainty in discharge measurement was within ±1%.

### E.3.4.1 Calibration of the Spillway Crest

Many experimental formulae for the discharge of an overflow spillway have been developed. Most of the formulae can be expressed in the following general form

$$c_d = \frac{Q}{\frac{2}{3}\sqrt{2g}\, L H_1^{3/2}} \quad \text{(a)}$$

or

$$Q = \frac{2}{3}\sqrt{2g}\, c_d\, L\, H_1^{3/2} \quad \text{(b)} \qquad \text{(E.6)}$$

in which Q is the discharge over the spillway, $c_d$ is the *discharge coefficient*, L is the length of the weir crest (normal to the flow direction), g is the gravitational acceleration and $H_1$ is the total upstream energy head over the chute crest, *including* the velocity head in the approach channel. Often it is not possible to measure the energy head $H_1$ directly and it is therefore a common practice to relate the discharge to the upstream water level over the crest, H. In this case, Eq. (E.6b) can be written as

$$Q = c_d\, c_v\, \frac{2}{3}\sqrt{2g}\, L H^{3/2} \qquad \text{(E.7)}$$

where $c_v$ is a correction coefficient which allows for neglecting the velocity head. If an *overall discharge coefficient* $C_d$ is substituted for the product $c_d c_v \frac{2}{3}\sqrt{2g}\, L$, Eq. (E.7) may be written in terms of the head over the spillway crest as

$$Q = C_d\, H^{1.5} \qquad \text{(E.8)}$$

The measured values of Q and H are given in Table E.2.

| H mm | Q $cm^3/sec$ |
|---|---|
| 115.0 | 13269 |
| 90.0 | 8956 |
| 58.0 | 4471 |
| 46.5 | 3169 |
| 36.5 | 2189 |
| 88.5 | 8760 |
| 76.0 | 6898 |
| 66.6 | 5575 |
| 54.0 | 4014 |
| 125.2 | 15300 |
| 105.0 | 11507 |
| 12.3 | 405 |
| 23.7 | 1123 |

Table E.2

A simple linear regression with no constant and with dependent variable Q and independent variable $H^{1.5}$ gave $C_d = 10.65$ (Q in $cm^3/sec$ and H in mm), while the standard error of $C_d$ was 0.07 with the Pearson product-moment correlation coefficient r = 0.999 (Fig. E.3).

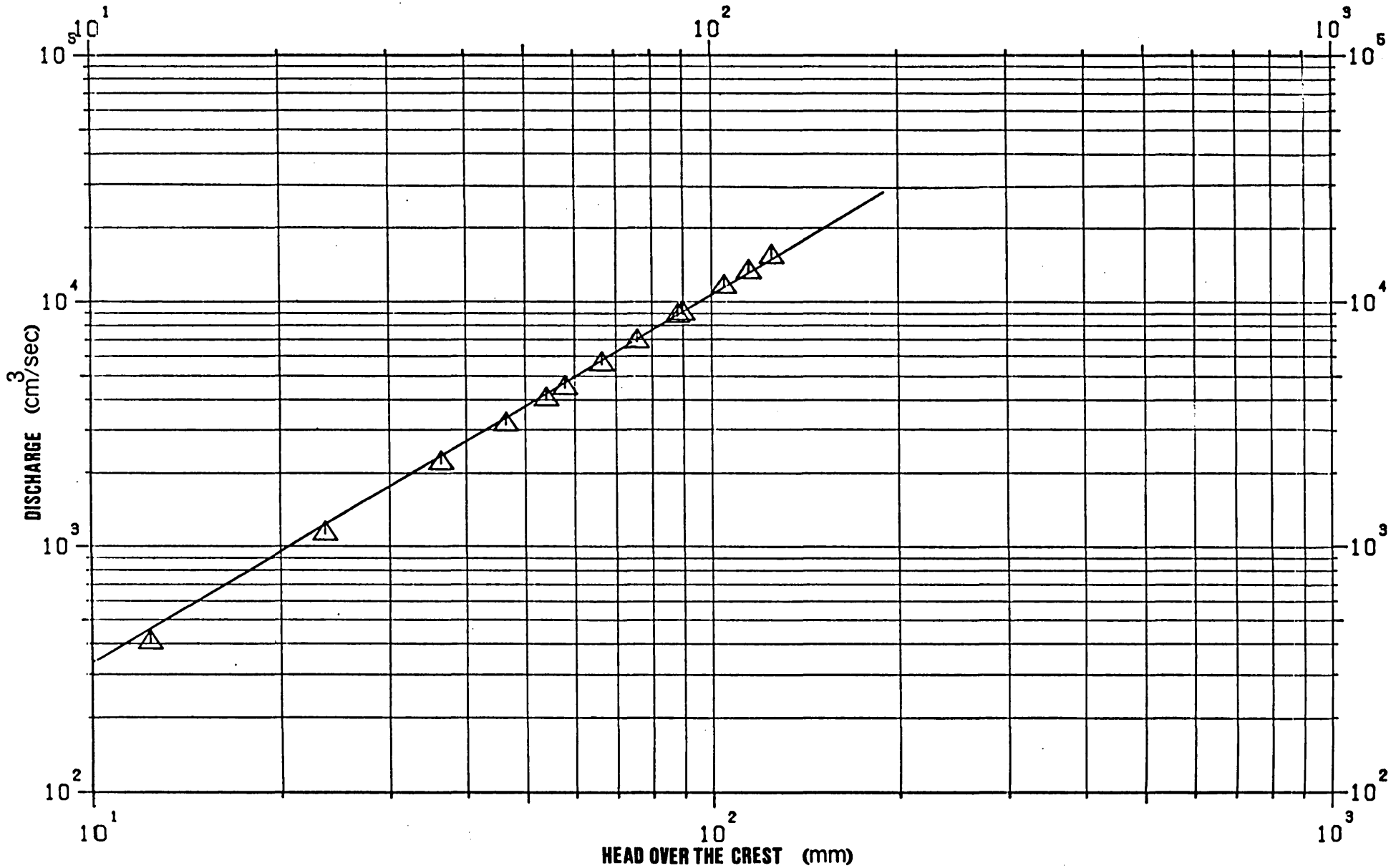


Fig. E.3 Calibration curve for the spillway crest

## E.4 MEASUREMENT OF MEAN FLOW PROPERTIES

In dealing with the fluctuating quantities of turbulent flows, it becomes necessary to employ a type of statistical approach. The *mean time average* of a quantity B is defined as

$$\overline{B} = \frac{1}{T}\int_{t}^{t+T} B\,dt \qquad (E.9)$$

where T is the interval over which the average is carried out and is large enough to render the quantity $\overline{B}$ independent of time. Thus, the mean time average represents the well-ordered part of the flow.

However, when attempting to measure mean-flow quantities in a fluctuating flow, the measuring systems (pressure transducers, liquid-filled manometers, etc.) may not indicate the true mean value. When considering the causes of uncertainty, it is necessary to consider the system as a whole and take into account the measuring system qualities such as *frequency response limitations, departures* from *linearity* etc.

### E.4.1 The Effect of Fluctuations

The instruments used to measure mean values in turbulent flows are often those developed for essentially steady situations such as strain gauges, manometers, pitot tubes etc. The response of these instruments is slow enough to provide steady readings, independent of the continual fluctuations. In using such instruments for turbulent flows, it is assumed, often tacitly, that the effect of the fluctuations on the indicated mean value is negligible, either because the fluctuations are small, or because their effects are averaged correctly by the instrument. Considering an intrument for which the relationship between the output (or the quantity being measured), S, and the input (or the reading), I, can be expressed in the form

$$S = K\,I \qquad (E.10)$$

where K is the *calibration factor,* which is very nearly constant (the operation of the instrument can be made simpler by treating K as if it were a constant). The instrument response to an input of $(\overline{I} + i)$ in which $i$ is the fluctuating part will be $\overline{S} + s$. From Eq. (E.10), it

follows that

$$\overline{S} = K\,\overline{I} \tag{E.11}$$

Such an instrument will record a simple time average, and calibration can be accomplished using *static* tests.

In the above relationships, it has been assumed, for convenience that K is a constant for all values of the input I. However, there is a disadvantage, since, at those points where the true value of K differs from the assumed (constant) value, an error will be introduced. Such an error is termed a *non-linearity error*. When the response is non-linear, the average value registered will contain a contribution from fluctuations. If the relationship between the input and the output is assumed to be of the following form

$$S = K\,I^n \tag{E.12}$$

in which K and n are constant, then the relationship between the fluctuating input and the output will be

$$\overline{S} + s = K(\overline{I} + i)^n = K\,\overline{I}^n\,(1 + \frac{i}{\overline{I}})^n \tag{E.13}$$

or

$$\overline{S}+s = K\,\overline{I}^n\,[1 + n\,\frac{i}{\overline{I}} + \frac{n(n-1)}{2}(\frac{i}{\overline{I}})^2 + \frac{n(n-1)(n-2)}{2\times 3}\,(\frac{i}{\overline{I}})^3 + \ldots] \tag{E.14}$$

On averaging the above relationship and using the fact that $\overline{i} = 0$ and $\frac{\sqrt{\overline{i^2}}}{\overline{I}} << 1$, Eq. (E.14) can be written as

$$\overline{S} \simeq K\,\overline{I}^n\,[1 + \tfrac{1}{2}n(n-1)\frac{\overline{i^2}}{\overline{I}^2}] \tag{E.15}$$

Here, if very high precision is sought in determination of the mean flow quantity, the static calibration is insufficient. In this case, either a *dynamic calibration* or a *theoretical correction* is required (Reynolds, 1974).

## E.5 MANOMETERS

In most practical circumstances for incompressible flow, and very often for compressible flow, the velocity, static and total pressures are measured with manometers, in which the pressure is balanced by the weight of a column of liquid of known density.

### E.5.1 Calibration of Manometers

Manometers using gauging fluid of known density such as water do not require calibration when operated with the tubes held vertical, their accuracy being dependent mainly on the precision with which the liquid heights can be read. In this investigation, the manometers were not calibrated.

### E.5.2 Lag in Leads

When making pressure-probe measurements in flow conditions which are essentially steady, one of the main considerations in choosing components for the manometer system is that of lag in obtaining steady readings after the changes in flow conditions or the location or attitude of the pressure probe. After any change, a finite time lapses before the new value is registered by the indicating or recording system. In general, in the case of water-filled manometers, water must flow in or out of the probe orifices. It is, therefore, usually an advantage to keep the liquid volume of the system as small as possible in order to minimise the time taken for these processes to be completed.

### E.5.3 System Response

In general, water manometers having an internal diameter of approximately 10 mm can only respond to frequencies which are less than 2 Hz and are seldom non-linear to a significant extent.

The influence of stream turbulence on the performance of pressure probes is of great importance. In this case, it is also necessary to examine the response of the system to fluctuating pressures and to consider whether a true mean pressure is registered by the manometer. If a length of tubing having a restricted inlet at the pressure-sensing end and

at the other end a manometer is considered, it can be said that a fluctuating external pressure at the inlet will cause a flow in and out of the inlet tube and a fluctuating pressure will also occur within the system. If the relationships which govern the exchange of energy from pressure to kinetic energy and then back to pressure are completely linear, then the mean level of pressure detected by the pressure-measuring device would equal that at the inlet to the system. Actual systems may not behave in this way for the following reasons

(a) At the change of section, the geometry of the section imposes a rectification of the pressure pulse. This effect may occur at any change of section throughout the system.

(b) The transfer of water along the entrance tube is only a linear function of the pressure difference across it when the flow in the tube is laminar. Non-linearities occur when it is turbulent or quickly changing, and further non-linearities are introduced for all conditions if the tube is short when it acts in some ways like an orifice.

(c) Non-linear elastic properties of the flexible tubing introduce a rectification of the pressure pulse.

(d) If a liquid manometer is used, there is the additional possibility of error being generated by the behaviour of the manometer itself. The water column of a manometer, which has an internal diameter of approximately 10 mm, responds to pressure fluctuations as a damped oscillatory system with a single degree of freedom, its natural frequency usually being about 1 Hz. If large amplitude oscillations of the liquid column are excited, large displacement of liquid throughout the system will result in the aggravation of errors arising from (a), (b) and (c) above; in addition, parts of the liquid system itself may cause rectification of the oscillating liquid flow. If a pressure transducer is used, its linearity and that of the associated electrical system are important.

In spite of all the possibilities listed above, satisfactory accuracies can usually be obtained from pressure probes when measuring mean flow quantities in most fluctuating flows, provided that the probe properties, such as sensitivity to flow direction, are taken into account. In most situations, the turbulent intensities are not greater than 20 per cent, which means that the effects of (b) and (c) can usually be ignored (Bryer and Pankhurst, 1971). In addition, the effects of (a) and (d) can be

largely overcome by introducing a length of narrow-bore capillary tubing at a positicn as close to the probe-sensing orifice as possible. The damping produced by the capillary tube should then be large enough to ensure that any rectification effect is small compared with the resistance of the tube to flow.

### E.5.4 Manometer Boards

Thirty individual glass manometers of 10 mm internal diameter were made (Plate VI), as it was desirable for simplicity and to save time to be able to measure a large number of pressures simultaneously. Flexible plastic tubing, 2.5 m long was used to connect the pressure-sensing probes with the manometers. The plastic tubing was of 3 mm bore and transparent, so that air blockages could be readily seen.

An elaborate flushing arrangement was made for each manometer. It consisted of a T-piece, with each end connected to soft transparent plastic tube 100 mm in length. Each soft tube had a clip; the clips were used for different purposes such as filling the manometer with water, filling the connecting tube to the pressure-sensing probe with water, disconnecting the manometer system from the flushing water and for removing air whenever it interfered with the pressure measurement. The ends (c) of all the manometers (Fig. E.4) were connected to a common pipe with a valve containing the flushing water which could be supplied at a strong pressure (Plate VII).

In the initial stage of experimentation, it was noticed that the plastic tubes containing water of the hydraulic laboratory went dark after a day or two unless the water was emptied after the experiment. To combat this problem, after working with the manometers, the water inside the system was discharged by means of an inflator which was used as a pump.


PLATE VI FRONT VIEW OF THE MANOMETER BOARD

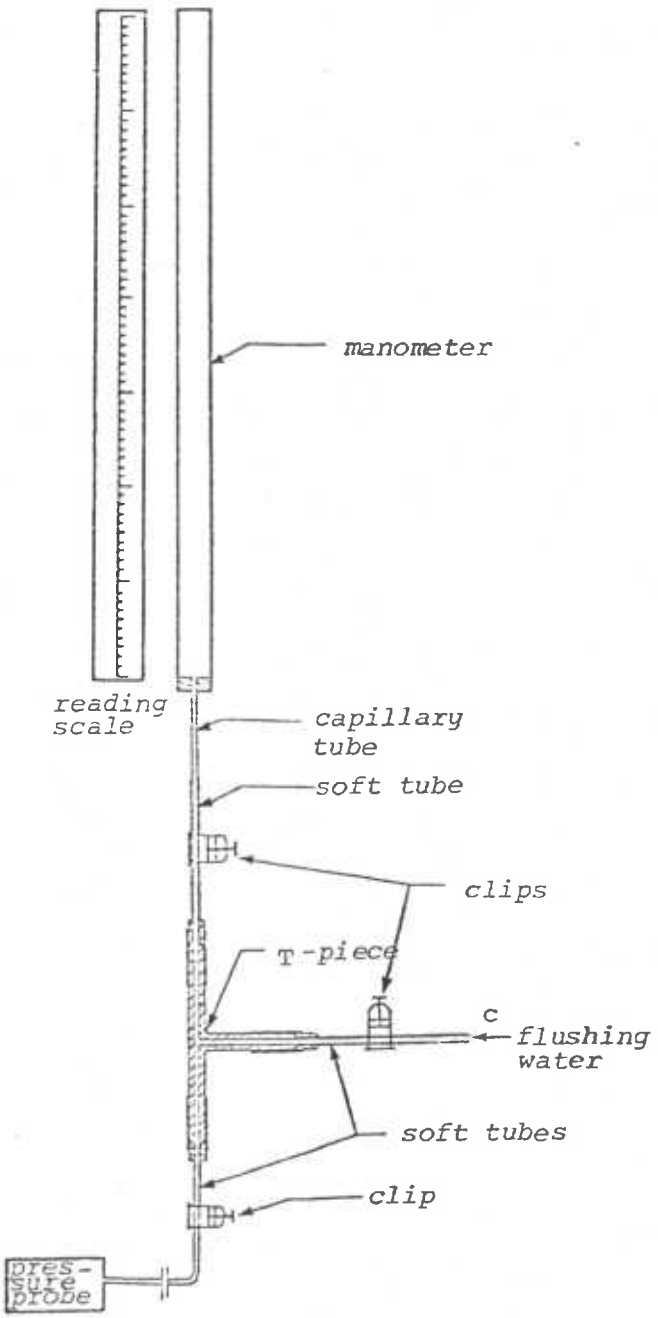


Fig. E.4 Schematic representation of a manometer with the flushing arrangement

PLATE VII REAR VIEW OF THE MANOMETER BOARD

## E.6 MEAN VELOCITY FIELD MEASUREMENTS

All the velocity profile measurements were made by means of a pitot-static tube with the static openings also being used to measure the pressure field. It is known that the pitot-static tube only gives the mean velocity. It can be used in water with some difficulty, to measure speeds as small as 30 mm $sec^{-1}$ (Preston, 1972). However, the pitot-static tube is a *slow-responding* instrument, and this is a big disadvantage in its use.

### E.6.1 Design of the Pitot-Static Tube

Tbe pitot-static tube used in this investigation was of 3 mm

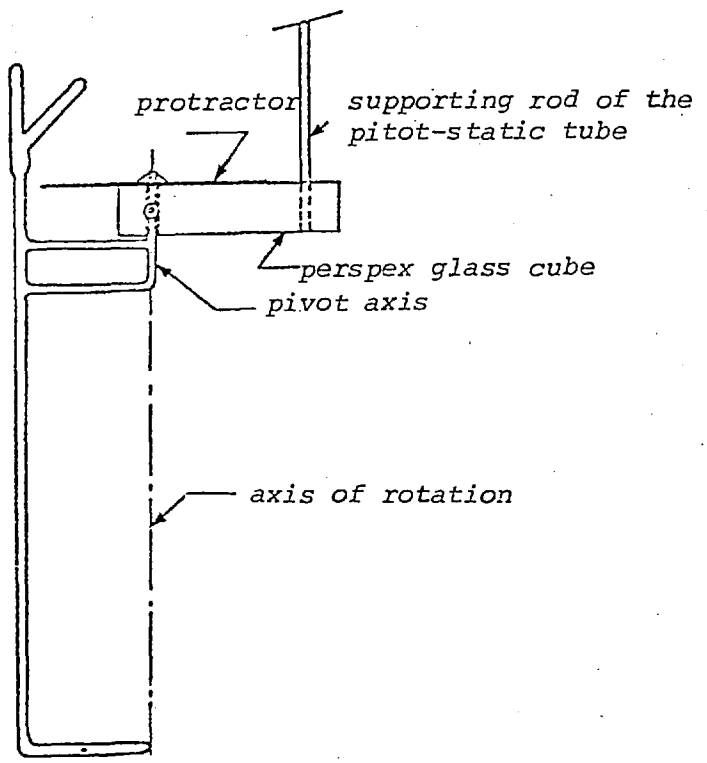


PROFILE

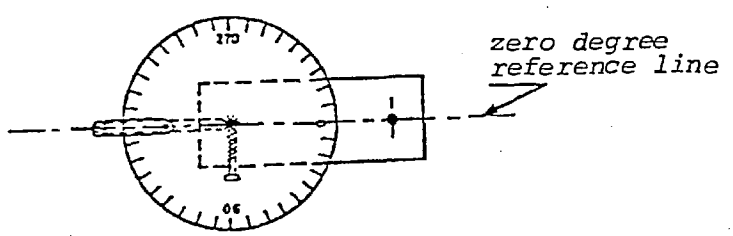


PLAN

Fig. E.5

external diameter and had a hemispherical nose (head) supported by a vertical stem at the downstream end. In order to make correct measurements, the pitot-static tube had to be aligned with the local flow direction; this was achieved by using a perspex cube and a protractor (Fig. E.5). The tip of the pitot-static tube was so positioned that it was directly below the pivot axis (axis of rotation) and was independent of the alignment chosen. Normal laboratory water manometers were used that could be read to $\pm 0.5$ mm. The velocities to be measured were generally large enough to induce an adequate velocity head which thereby insured sufficient accuracy in the manometer readings. Two lengths of 2 m flexible plastic tubing were used for connecting the pitot-static tube to the manometers. The plastic tubing was of the same material as that described in Section E.5.4. Also, an elaborate flushing arrangement similar to that explained earlier was made for the pitot-static tube to remove air whenever it interfered with the velocity measurement.

In contrast to the pitot tube, the static pressure, as measured by the manometers, is influenced appreciably by the position of the stem relative to the pressure holes and by the distance that the holes are downstream of the nose. The effect of the nose is to increase the velocity over the pressure holes and thus to depress the measured pressure below the true static value (Johansen and Ower, 1932), whereas the presence of the stem produces a 'damming' effect which tends to produce an error of opposite sign to that of the nose. Ower and Pankhurst (1966) have recommended that the static orifices should be 5 tube-diameters back from the base of the nose. Their results also showed that if the stem was then 8 diameters behind the static holes, the pressure at these holes would then be the stream static pressure. These recommendations were adhered to as far as possible in the design of the pitot-static probe.

### E.6.2 The Effect of Misalignment

In general, errors will arise if a pitot-static probe is not accurately aligned with the direction of flow, but before discussing this matter, the following terms must be defined.

(a) Yaw

*Yaw* is used to signify rotation about an axis passing through (or parallel to) the stem of the instrument.

(b) Pitch

*Pitch* is the angular deviation in the plane containing both head and stem. The angle of pitch is also referred to as an angle of *incidence*. As yawing the tube is much simpler than pitching it, most experimental results relate to angles of yaw rather than to angles of incidence. Pitch gives slightly different results for corresponding deviations about the axis of the stem. The investigation of Bryer and Pankhurst (1971) shows that if the direction of flow is uncertain by as much as $25^{\circ}$ or $30^{\circ}$, the hemispherical nose is much to be preferred. The maximum error that would be incurred due to misalignment within the angular range would be about 2%

## E.6.3 Theoretical Investigation of the Turbulence Effect on Flow Measurement by Pitot-Static Tube

In general, turbulent flow can be regarded as having a steady velocity $\vec{V}$ on which is superimposed a random turbulent velocity $\vec{v}$ which has a finite value at any instant but an average value of zero taken over a sufficiently long time interval. The turbulent velocity $\vec{v}$ can be resolved into components u , v and w parallel to the axes of a three-dimensional Cartesian system of co-ordinates with the x-axis aligned with the direction of mean flow. At any instant, the velocity component in the x-direction is $\bar{U}+u$ ; u may be positive or negative, but its

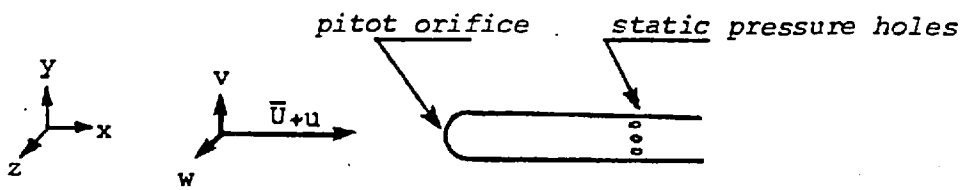


Fig.E.6 Pitot-static tube in a turbulent flow

average value is zero; and similarly for v ans w . The associated pressure changes, however, depend on the squares of the velocities, and the mean value of these are *not* zero.

The turbulent velocity components affect the readings of both the pitot and the static tube. Goldstein (1936) investigated these effects theoretically, neglecting the possible effects of factors such as frequency, damping, resonance, and lag in leads. Since pitot tubes are almost insensitive to yaw up to about ±15 degrees, he showed with fair confidence that the mean pressure recorded by a pitot orifice in incompressible flow is not $(\overline{p} + \frac{1}{2}\rho\overline{U}^2)$ but $[\overline{p} + \frac{1}{2}\rho\overline{U}^2 + \frac{1}{2}\rho(\overline{u^2} + \overline{v^2} + \overline{w^2})]$, where $\overline{u^2}$ etc. are the mean squares of the turbulent components u etc. However, it should be noted that the argument on which this conclusion is based only takes account of the turbulence intensity, and not of its *scale*. If the turbulence scale is large compared with the diameter of the pitot tube, the probe responds as if the flow-direction were continually varying in a random manner. This effect tends to reduce the recorded stagnation pressure (Bryer and Pankhurst, 1971). The relatively large insensitivity of the pitot tube to misalignment with the flow, however, suggests that this effect remains negligible unless the intensity of the transverse fluctuations are large.

The effect of stream turbulence on the reading of a static tube is known to be uncertain. Early work (Goldstein, 1936) suggested that the reading of static pressure exceeded the stream static pressure by $\frac{1}{4}\rho(\overline{v^2} + \overline{w^2})$. A subsequent analysis took into account the effects of turbulence scale, and concluded that the reading exceeded the stream static by twice this amount, i.e. by $\frac{1}{2}\rho(\overline{v^2} + \overline{w^2})$, when the turbulence scale is small compared with the diameter of the probe. But when the turbulence scale is very large, the tube was shown to read *low* by $\frac{1}{2}\rho(\overline{v^2} + \overline{w^2})$. The values of the correction between these two limits are not known quantitatively. The effects of turbulence scale on the readings of static probes of different sizes were examined by Bradshaw, Goodman and Dorothy (1968). Their experiments confirmed the above conclusion and showed that the readings of probes of a common size are closer to the static pressure than to the extreme theoretical predictions. Although these effects are often negligible in practice (Bryer and Pankhurst, 1971).

### E.6.4 The Turbulence Effect on Flow Measurements by Pitot-Static Tube

The turbulent velocity components affect the readings of both the pitot and the static tube. This manifests itself as fluctuations on the

manometers. An effective method of reducing the resulting unsteadiness of the manometer readings in such conditions depends, in principle, on the fact that a tube of given dimensions exerts a certain amount of damping on the motion of a pressure pulse along its length. The damping due to the total-head tube will obviously be less than that of the static tube on account of the larger resistance of the small static orifices. Hence, even if the same pulse acts simultaneously both at the mouth of the total-head tube and at the static holes, the fluctuations will not be damped to the same extent, by the time the pressures reach the manometers, unless some resistance is introduced in the total-head connecting tube. Such extra resistance may be provided by using a longer length of plastic (or rubber) tubing on the total-head side, but a more convenient and economical method is to insert a piece of capillary tube into the total-head connecting tube. The amount of capillary inserted can be altered until a sufficiently steady manometer reading is obtained (Ower and Pankhurst 1966).

Insertion of the viscous damping into the pressure leads would reduce the fluctuations of pressure to a negligible amount, so that the mean pressures transmitted would be the true time averages of the pressures at the pick up points (Ower and Pankhurst, 1966). Viscous damping may be used with success, for example, in the form of capillary tubing. The viscous element should offer the same resistance to motion in either direction, hence, if capillary tubing is used it should be at least 100 diameters long to reduce possible errors due to dissimilarity between its two ends. In this investigation, it had been found that approximately 50 mm of capillary tubing of 0.5 mm bore was sufficient to result in a greatly improved steadiness on the manometer.

However, it should be noticed that a system balanced in the manner mentioned above will not necessarily always give entirely steady readings even if the viscous damping is increased considerably. This is due to some non-stationarity in the turbulence pattern of the flow (Karki, 1976). In this investigation a very slight variability of the water surfaces in the manometers showed that in order to establish a reliable value for the mean readings, the manometer readings had to be repeated (Powell and Posey, 1959) sometimes as many as twenty times. At a fixed location, the readings of manometers normally took 20 minutes which meant that the process was tedious and time-consuming.

### E.6.5 The Calibration Factor for the Pitot-Static Tube

The *calibration factor* for a pitot-static probe is defined by

$$p_1 - p = K\tfrac{1}{2}\rho U^2 \qquad (E.16)$$

where $p_1$ denotes the pressure measured by the pitot orifice and $p$ that of the static side of the instrument. Tests have revealed that the calibration factor K, in incompressible flow, is a function of the probe Reynolds number, i.e.

$$K = F(R_{probe}) = F\left(\frac{U D}{\nu}\right) \qquad (E.17)$$

where

- F = some function of the Reynolds number of the pitot-static tube
- D = external diameter of the tube
- U = velocity of the undisturbed stream
- $\nu$ = coefficient of kinematic viscosity.

Viscous effects become significant when the Reynolds number is less than about 100. For most practical purposes the influence of the Reynolds number on a pitot-static probe is negligible except for specially made miniature instruments, or at very low water velocities.

#### E.6.5.1 Calibration of the Pitot-Static Tube

The simple 'well-known flow system' procedure where the probe is introduced into a known velocity profile was adopted for the calibration of the pitot-static tube.

The calibration was conducted in a horizontal flume which had a nominal width of 100 mm and a length of 2.8 m, a smooth aluminium bed and vertical glass side walls. The inflow to the flume could be maintained at a constant head by using an overflow pipe in the inlet box. The maximum depth of water possible in the flume was 310 mm. Water entered the flume under a full-width adjustable sluice gate which was made of a brass plate with a knife lower edge. Figure E.7 is a diagram of the equipment in which '$a$' is the gate opening, $H_1$ is the depth of the approaching flow

which has a mean velocity of $U_1$ and $a_c$ is the depth of flow at the vena contracta. The depth of the water upstream of the sluice gate, the opening of the gate and the depth of the water at the vena contracta were

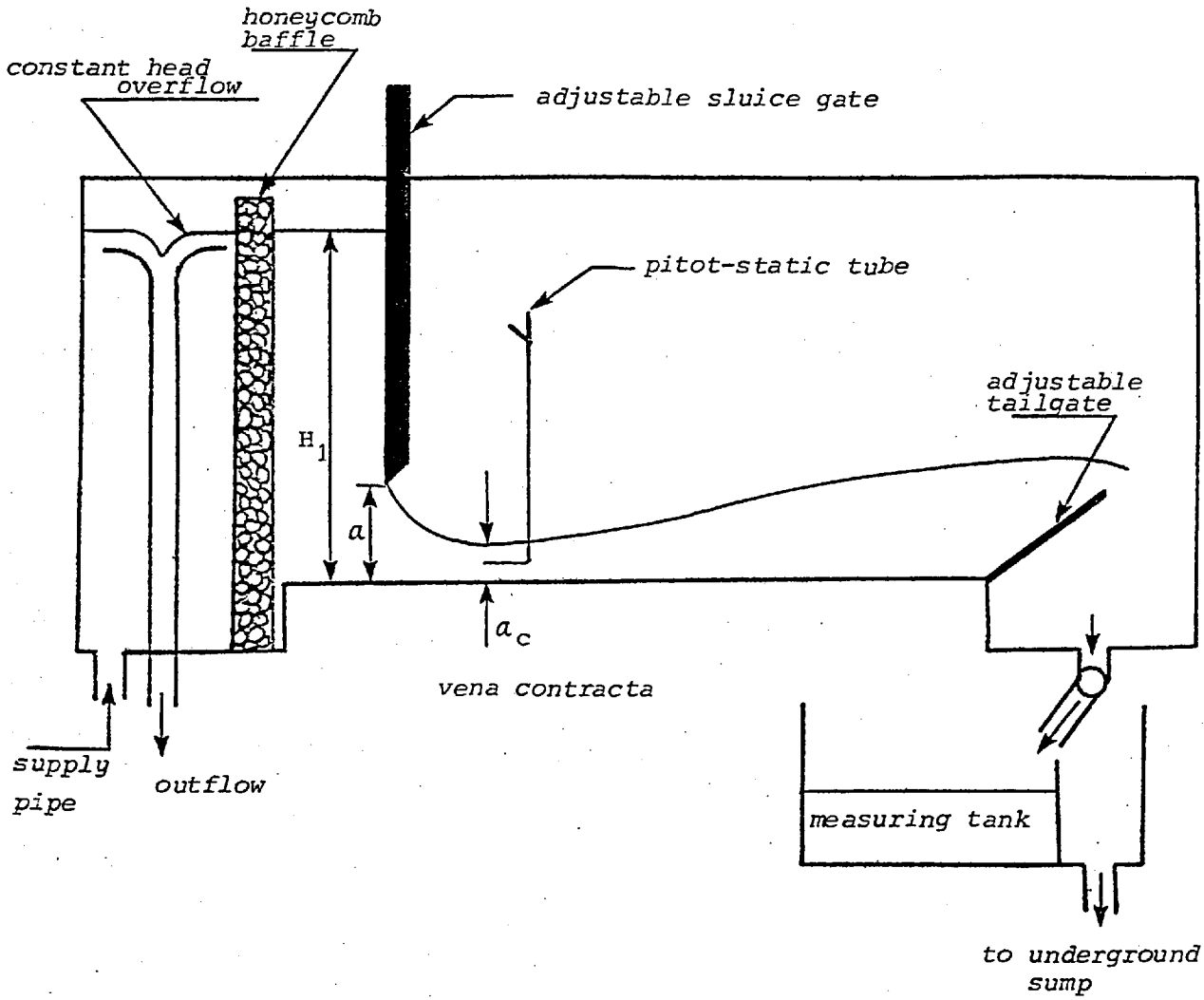


Fig. E.7 Layout and some details of experimental arrangement made for the calibration of the pitot-static tube

measured by a precision point gauge with the reading uncertainty being ±0.1 mm. The discharges were measured volumetrically over a measured time interval in a tank having an area of 0.912 $m^2$.

As the water emerged from the sluice gate, the free surface contracted to a minimum section known as the *vena contracta* (Plate VIII); this occurred at a distance from the gate approximately equal to '$a$'. Neglecting the viscous effects, the velocity distribution across the vena contracta section could be assumed to be uniform and parallel to the flume bottom and sides. The static and total pressures $p$ and $p_1$ were measured by means of two manometers with an uncertainty of 0.5 mm in the head reading; for low heads two inclined-tube manometers were used. The pitot-static tube was inserted in the vena contracta and was aligned with the flow direction. By changing the flow conditions different velocities at the vena contracta were achieved.

Calling on Eq. (E.16)

$$p_1 - p = K\tfrac{1}{2} U^2 \quad \text{(a)}$$

or

$$h_1 - h = K \frac{U^2}{2g} \quad \text{(b)} \qquad \text{(E.18)}$$

where $g$ is the acceleration due to gravity and $(h_1-h)$ is the difference of head between the dynamic and the static openings, i.e., the manometer head. The results of the experiment are tabulated in Table E.3. Performing a simple linear regression with no constant with dependent variable $U^2$ and independent variable $(h_1-h)$ gave $K = 1.032$, while the standard error of $K$ was 0.009 with the Pearson product-moment correlation coefficient $r = 0.998$ (Fig. E.8).

### E.6.6 Correction of Turbulent Flow Pitot-Static Tube Measurements

When the flow is *steady* and the probe installed properly, the flow velocity can be calculated, with an uncertainty of ±0.25 per cent (Reynolds, 1974). If the flow is turbulent (Fig. E.6), the pressures at the sensing points will fluctuate as the local flow direction and velocity vary. However, if the damping in the pressure lines are high enough, the recorded pressures will still be *nearly* steady. It is not possible to predict the instantaneous pressures just inside the sensing holes for a specified structure of ambient turbulence, but a plausible assessment of the effect

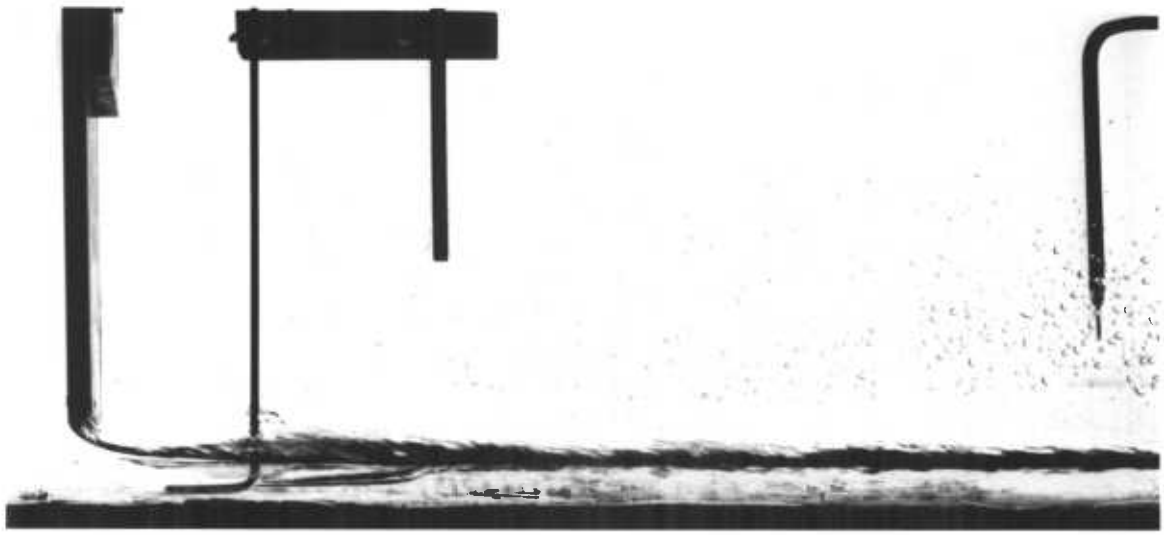

PLATE VIII CALIBRATION OF THE PITOT-STATIC TUBE IN THE NOMINAL 10 CM FLUME

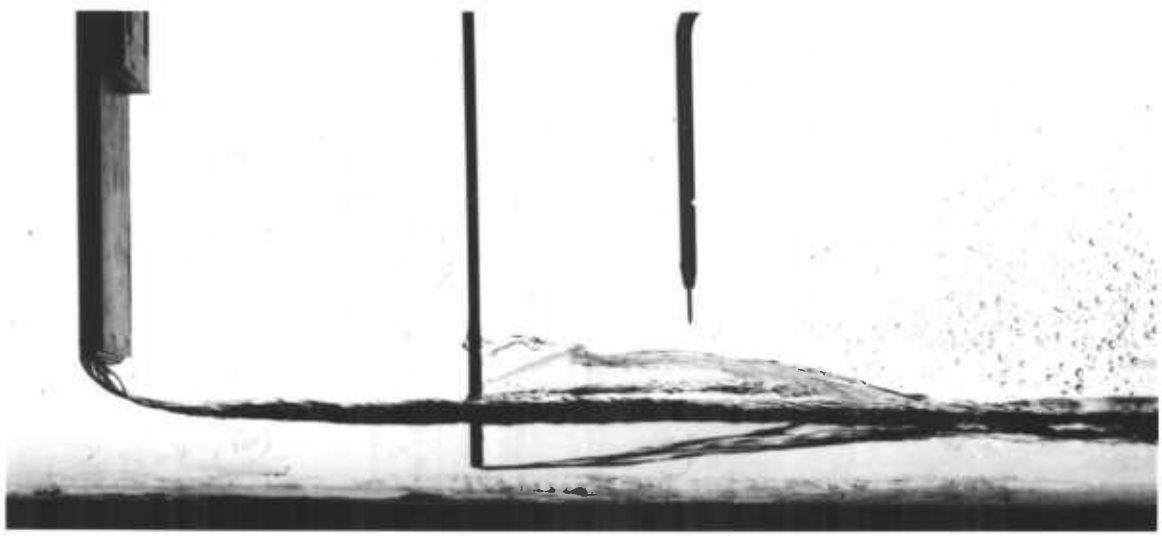

PLATE IX ASSEMBLY OF DIFFERENT MEMBERS OF THE 2-HOLE TRANSVERSE-CYLINDER YAWMETER IN THE NOMINAL 10 CM FLUME

| $H_1$ mm | $a$ mm | $a_c$ mm | $(h_1 - h)$ mm | Q *flow rate* $cm^3/sec$ | U cm/sec |
|---|---|---|---|---|---|
| 309.8 | 20.8 | 13.9 | 196.4 | 3373 | 233.3 |
| 290.8 | 20.8 | 13.3 | 275.0 | 3230 | 234.6 |
| 268.9 | 20.8 | 13.3 | 253.0 | 3072 | 221.3 |
| 245.3 | 20.8 | 13.6 | 230.0 | 2959 | 208.8 |
| 220.9 | 20.8 | 13.7 | 205.5 | 2797 | 196.3 |
| 199.5 | 20.8 | 13.8 | 182.5 | 2629 | 183.4 |
| 172.4 | 20.8 | 13.6 | 157.1 | 2403 | 169.3 |
| 151.0 | 20.8 | 13.7 | 136.1 | 2319 | 162.9 |
| 121.3 | 20.8 | 13.5 | 116.1 | 2092 | 148.5 |
| 92.2 | 20.8 | 13.2 | 80.0 | 1756 | 127.9 |
| 60.8 | 20.8 | 14.3 | 49.5 | 1417 | 95.0 |
| 36.9 | 20.8 | 14.7 | 27.5 | 1083 | 71.0 |
| 28.1 | 20.8 | 14.6 | 20.5 | 956 | 62.8 |

Table E.3 Calibration of the pitot-static tube

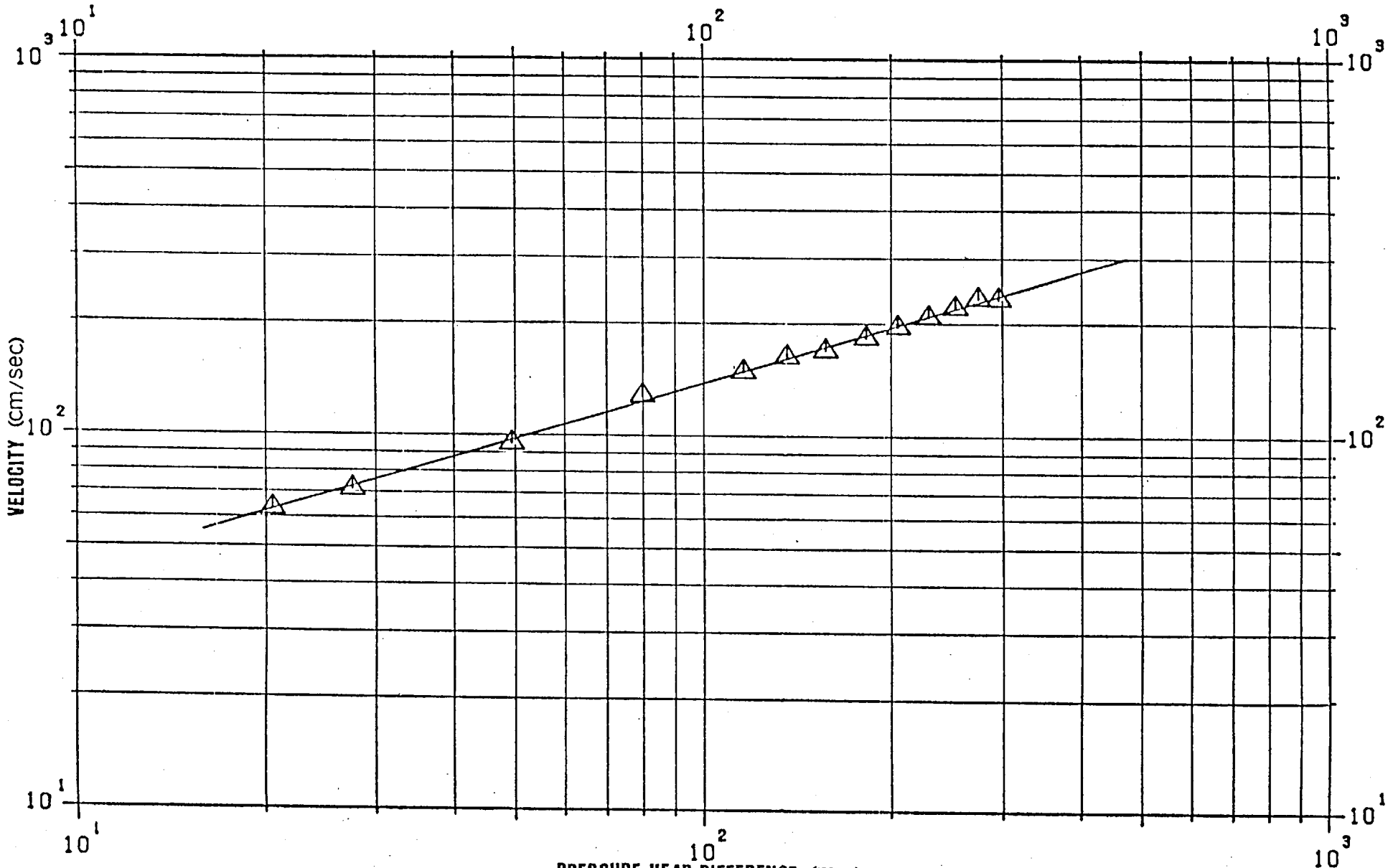


Fig. E.8 Calibration curve of the pitot-static tube

of the fluctuations can be obtained by assuming that the fluctuating pressure differential hs the form

$$\overline{P_1 - P} = \overline{P_1} - \overline{p} = K\tfrac{1}{2}\rho[\overline{U}^2 + K_1\,\overline{u^2} + K_2(\overline{v^2} + \overline{w^2})] \qquad (E.19)$$

with the constants $K_1$ and $K_2$ modified to account for distortions introduced within the pressure lines.

## E.6.7 Pitot-Static Tubes in Pressure Gradient Flows

It is known that when a pitot-static tube is used in *uniform* flows, and if $h = (h_1 - h)$ is the difference of head between the dynamic and the static openings, i.e., the manometer head, then the velocity U is given satisfactorily by Eq. (E.18b) which can be written in the following form

$$U = \sqrt{2gh/K} \qquad (E.20)$$

where, as already defined, g is the acceleration due to gravity and K is

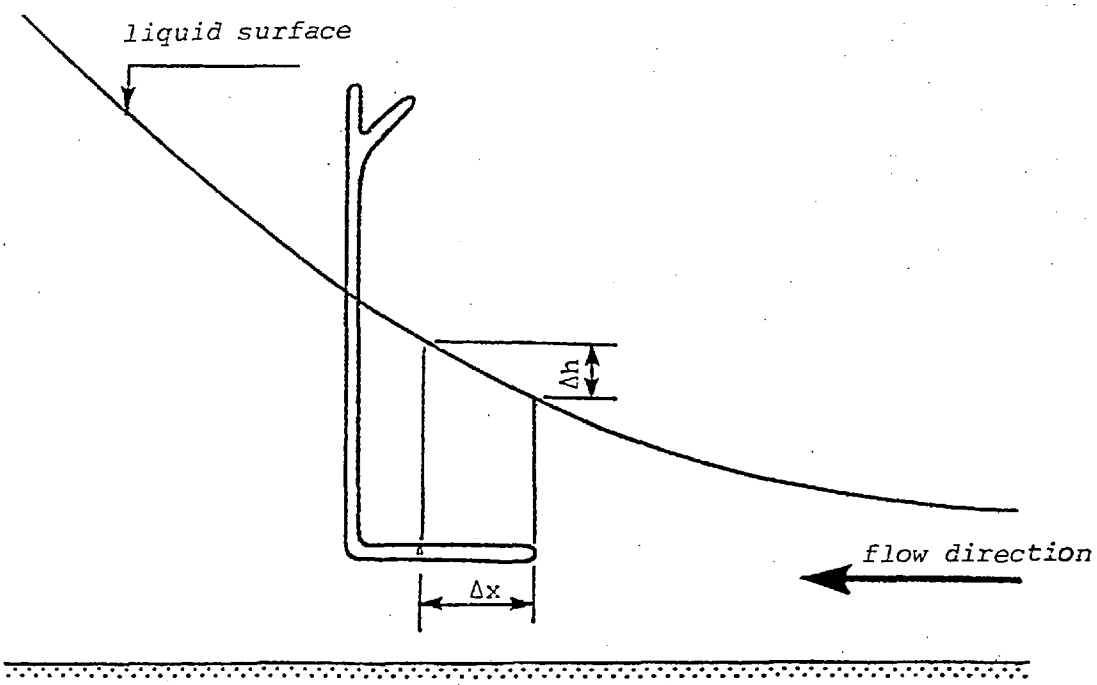


Fig. E.9 Pitot-static tube in adverse pressure gradient flow

the calibration factor. If now the same tube is placed in a flow with a *longitudinal pressure gradient* (assumed to be *adverse*) of dp/dx, and if $\Delta x$ is the longitudinal distance between two sets of holes, the difference of static pressure is $(\Delta p/\Delta x)\Delta x = \Delta p = \rho g \Delta h$, where $\rho g$ is the specific weight of the fluid. In this case, if $p_1$ denotes the pressure given by the pitot orifice and $p$ that of the static side of the instrument, the following relationships can be written

$$
\left.
\begin{aligned}
p_1 - p &= K \tfrac{1}{2} \rho U^2 && \text{(a)}\\
\frac{p_1}{\rho g} - \frac{p}{\rho g} &= K \frac{U^2}{2g} && \text{(b)}\\
h_1 - (h - \Delta h) &= K \frac{U^2}{2g} && \text{(c)}\\
\underbrace{h_1 - h}_{h} + \Delta h &= K \frac{U^2}{2g} && \text{(d)}\\
U &= \sqrt{\frac{2g}{K}(h+\Delta h)} = \sqrt{\frac{2gh}{K}}\left(1+\frac{\Delta h}{h}\right)^{\frac{1}{2}} = \sqrt{\frac{2gh}{K}}\, f(\beta) && \text{(e)}
\end{aligned}
\right\} \quad \text{(E.21)}
$$

where

$$\beta = \Delta h/h \qquad \text{(E.22)}$$

The $f(\beta)$ can be expanded as

$$f(\beta) = 1 + \frac{\beta}{2} - \frac{\beta^2}{8} + \frac{\beta^3}{16} - \frac{5\beta^4}{128} + \frac{35\beta^5}{1280} - \frac{21\beta^6}{1024} + \frac{33\beta^7}{2048} + \frac{429\beta^8}{32768} + \ldots \qquad \text{(E.23)}$$

The expression for $f(\beta)$ converges rapidly for $\beta < 1$ and the first five terms were found to give sufficient accuracy. The function $F(\beta)$ is shown plotted in Fig. E.10, it can be seen that when $\beta$ is close to unity, $f(\beta)$ could be as high as 1.40.

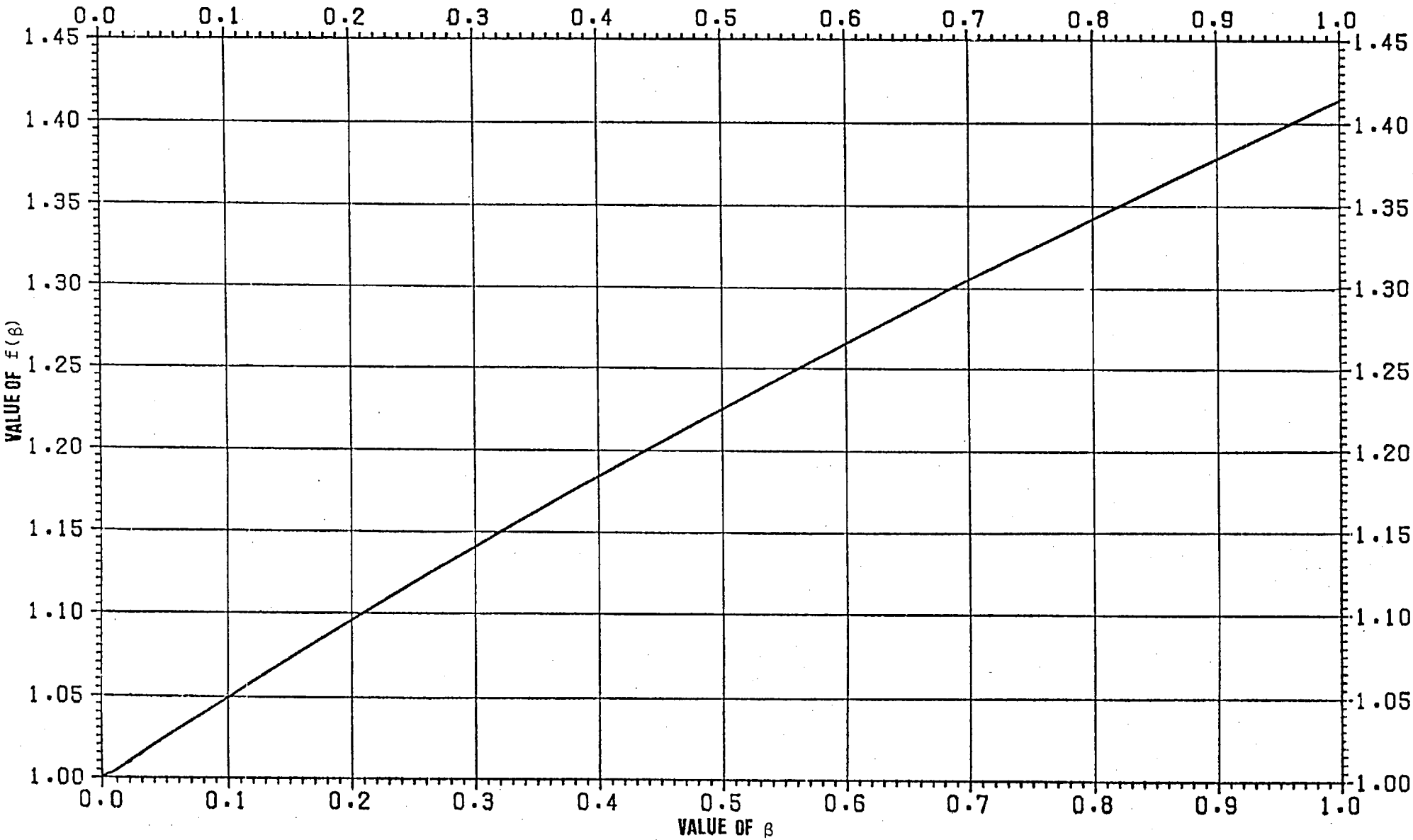


Fig. E.10 Correction for pitot-static tubes in adverse pressure gradient flows

## E.7 DETERMINATION OF THE MEAN FLOW DIRECTION

Pressure probes used as direction indicators have distinct advantages over alternative devices such as tufts, whose indication of direction cannot easily be related to any one point and whose introduction can produce more disturbance to the flow. Pressure probes also avoid certain errors associated with the inertial and gravitational forces affecting mechanical indicators.

There are two common methods by which flow direction can be measured with pressure-type yawmeters (in this thesis, the term 'yawmeter' is only used to describe those probes which are designed specifically as direction-sensing instruments). In either case the probes are similar and have a symmetrical arrangement of sensing holes. In the first case, known as the *alignment* or *null-reading* or *equibalanced* method, use is made of the equality of pressure at symmetrically opposite points on a symmetrical probe. The probe is orientated to a position at which the same pressure is recorded at each hole. The flow direction can then be related to the geometry of the probe. In the second method, no attempt is made to align the probe accurately, instead, the probe is kept stationary and the pressure differences between symmetrically opposite holes are measured and the flow direction is deduced from a *prior calibration* in which the probe is orientated in a steady known flow.

The types of instrument which are used without rotation, although of similar geometry to the null-reading types, should be designed for convenience so that the pressure differences are *linearly* related to the angles made by the probe axis to the flow direction; this enables the more convenient use of *constant calibrations* over at least part of the angle range for which the probe is designed. Pressure-type yawmeters possessing two or more sensing holes are more reliable than other types of direction-sensing instruments. Winternitz (1956) has investigated the sensitivity and the effects of changes in the probe Reynolds number (the probe Reynolds number is defined as $R_{probe} = \frac{UD}{\nu}$, where U is the speed of the undisturbed flow, D is the external diameter of the probe and $\nu$ is the coefficient of kinematic viscosity). When all these points of view are taken into account, the null-reading method is to be preferred.

The first of these methods is recommended where possible because it is a relatively simple matter to design probes which will give a high value for pressure difference per unit change in flow direction (high sensitivity). A further advantage lies in the comparatively short time required to obtain a steady manometer reading of nearly equal pressures

as against different pressures requiring a displacement of air and gauging fluid through the differential pressure manometer system. The method is especially suitable for two-dimensional flow measurements in which a single rotation is sufficient (about an axis perpendicular to the plane of two-dimensionality).

### E.7.1 Design of the Pressure-Type Yawmeter

A transverse-cylinder yawmeter of 5 mm external diameter was made for precise flow direction measurement (Fig. E.11). The body

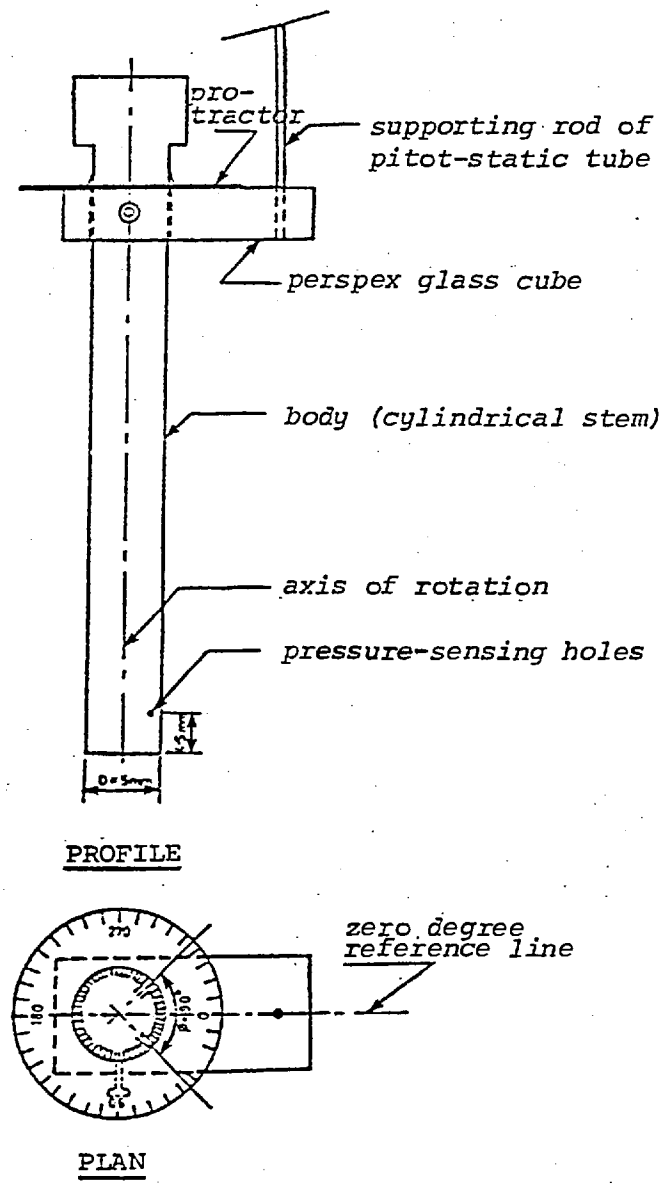


Fig. E.11 Schematic representation of the 2-hole transverse-cylinder yawmeter

(the cylindrical stem) and the two tubes inside were made of stainless steel. Two 0.5 mm diameter holes were drilled normal to the cylinder axis and 4.5 mm from the probe end. The directions of the sensing holes relative to each other were orthogonal. As the probe diameter was small, a cut-cylinder section was used at its lower end rather than a hemispherical section, due to difficulty in the manufacture of the latter type.

In order to assemble the different parts of the yawmeter, the probe and supporting rod were first inserted into a perspex cube. Then a protractor was positioned on the upper surface of the perspex cube, so that its centre was aligned with the vertical axis of the yawmeter stem. The direction of the line joining the centres of the cylindrical stem and the supporting rod was regarded as the zero degree reference line. Two 2 m lengths of flexible plastic tubing were used for connection to the tubes and the differential pressure manometer (water-air). In addition an elaborate flushing arrangement similar to that described in Section E.5.4 were made for the yawmeter probe to remove air whenever it interfered with flow-direction measurement.

In order to fix the position of the protractor relative to the yawmeter probe, the same arrangement as was made for the calibration of the pitot-static tube was used. The probe was placed in the vena contracta (Plate IX) of the incoming flow issuing from the sluice gate and was subsequently rotated until the readings on the differential pressure manometer were the same. Then the protractor and the yawmeter stem were glued together with the zero degree direction on the protractor aligned with the reference line mentioned above.

Designs with only one pair of off-centre pressure holes such as the one described above are normally difficult to manufacture but are basically more reliable and have a better all-round performance whilst generally offering less disturbance to the flow than any other type. They are convenient for two-dimensional flow investigation when used with rotation to give a null-reading alignment.

### E.7.2 Woollen Tufts

The direction of flow was observed also by means of woollen tufts approximately 20 mm in length tied to a 3.2 mm diameter rod. These woollen tufts were also used for visualizing and locating the separation points.

## E.8 MEASUREMENT OF THE MEAN WALL PRESSURE

The mean retaining wall pressure was measured by providing a large number of pressure tapping points (Fig. E.13). This method had the advantage of measuring the pressure distribution on the wall. The pressure holes were 0.5 mm in diameter. This is virtually the smallest diameter which can be used when a large number of pressure taps are dealt with. However, during the initial stages of this investigation, it was noticed that air from the water flow lodged just inside the pressure holes

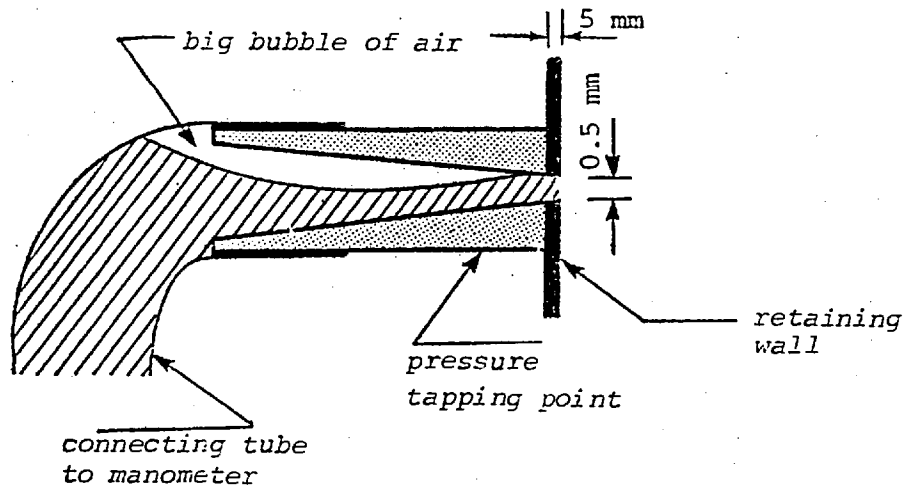


Fig. E.12

(Fig. E.12). At first, measuring the wall pressure by means of pressure taps seemed to be an impossible task. Subsequently, the reason for the formation of a large air bubble in the pressrue holes and a means of combatting this difficulty was discovered.

Previous investigation of *static pressure taps* has shown that in general the absence of a solid boundary over the area of the hole changes the local flow conditions. As shown theoretically by Thom and Apelt (1958) and observed by Ray (1956), fluid flow is deflected into the hole (Fig. E.14). Stream turbulence would make this situation worse. If a length of tubing having a restricted inlet at the pressure tapping point end and a manometer at the other end is considered, it can be said that a fluctuating external pressure at the inlet will cause a flow in and out of the pressure hole.

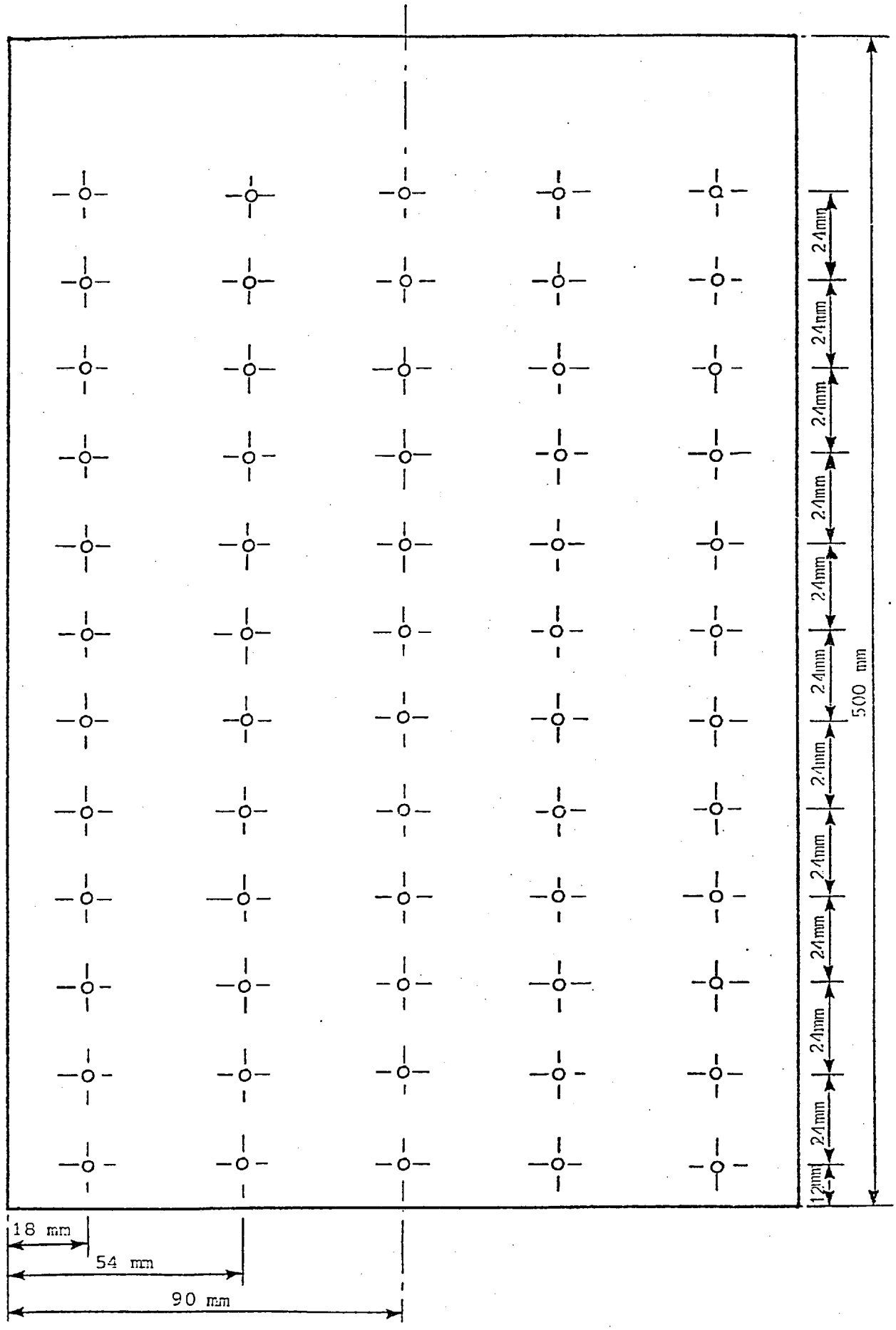


Fig. E. 13 The arrangement of the pressure taps on the retaining wall

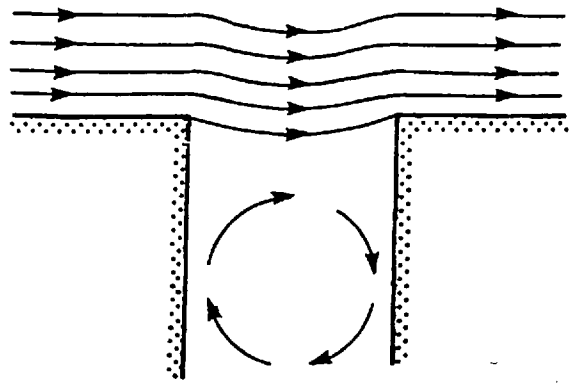

Fig. E.14 Flow behaviour at the static pressure hole

In the case of the pressure holes of the retaining wall when, due to the effects mentioned above, water enters the pressure taps, it is accompanied by air bubbles which are of limited size, 0.5 mm diameter. However, when there is a flow out of the pressure holes, unlike water, tiny air bubbles cannot descend and follow the internal conical geometry of the pressure taps, instead they accumulate and a large air bubble may occur inside each pressure hole.

To overcome this problem, another tube of 2 mm internal diameter was fixed at the back of the pressure tap (Fig. E.15). In this case, no

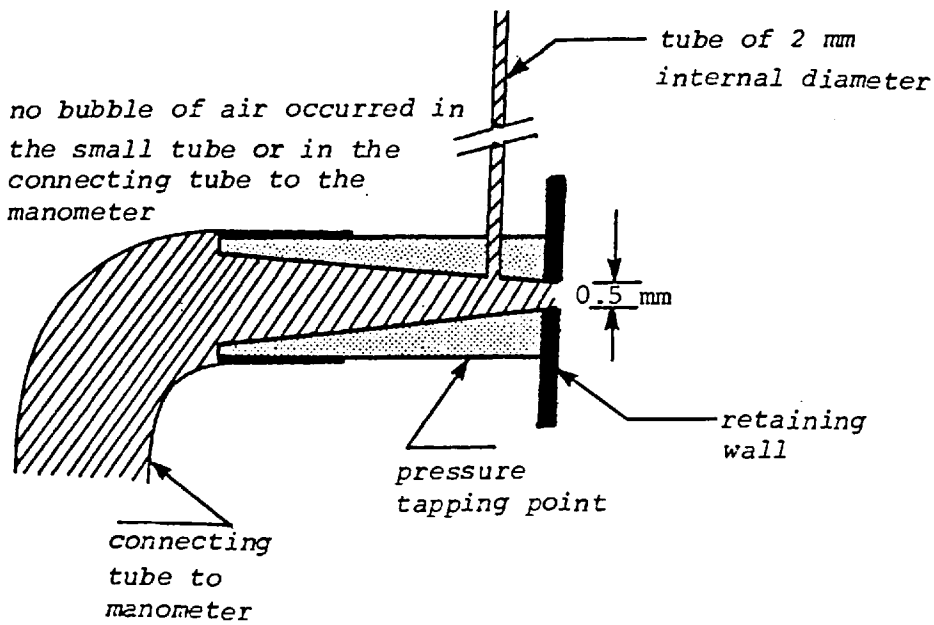


Fig. E.15

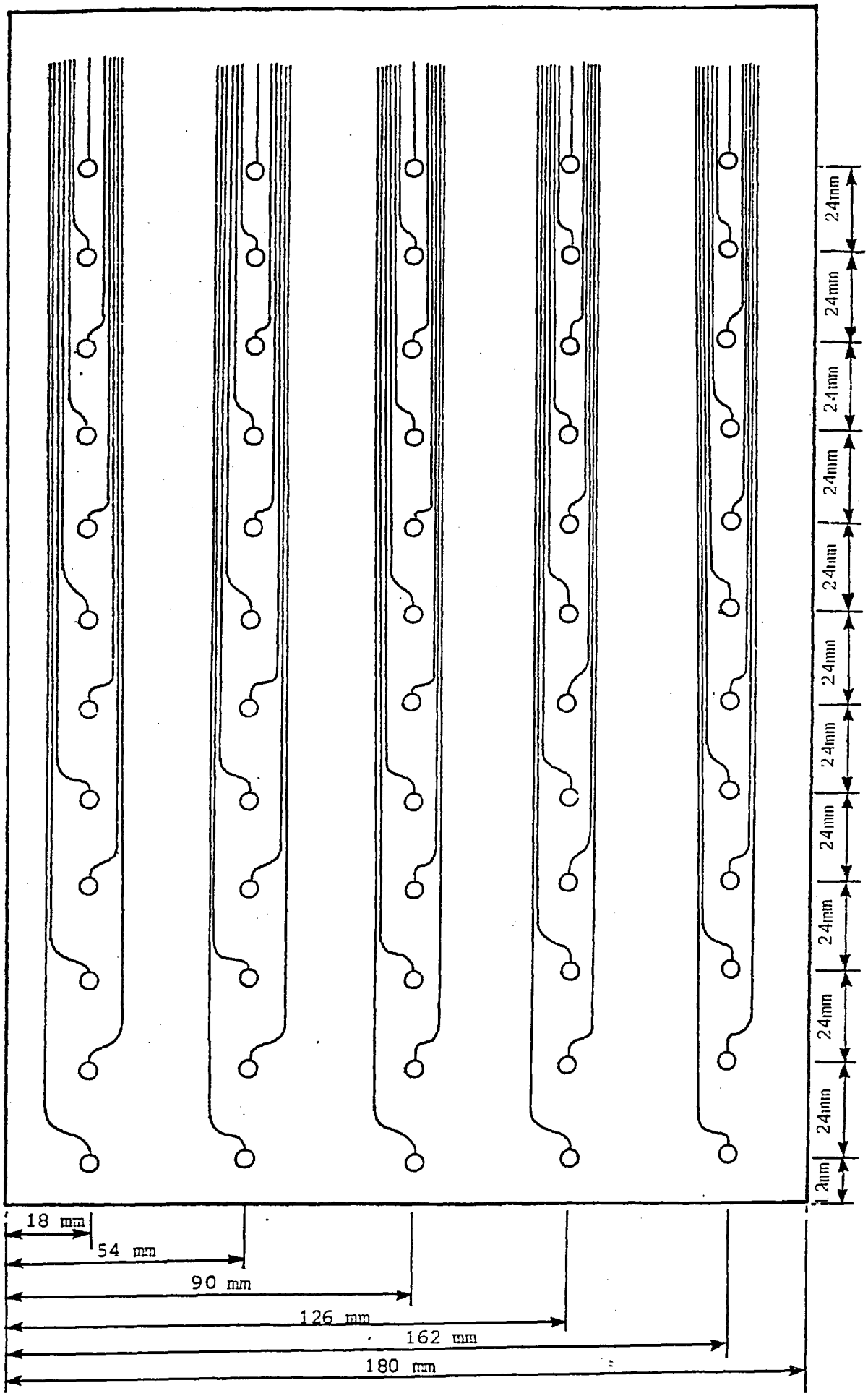


Fig. E.16 The rear view of the arrangement of the pressure taps on the retaining walls

visible air bubble was observed in the small tube or the connecting tube to the manometer. Perhaps, in this case, minute bubbles of air rise from the small tube and burst. A pressure hole having a sharp angle with

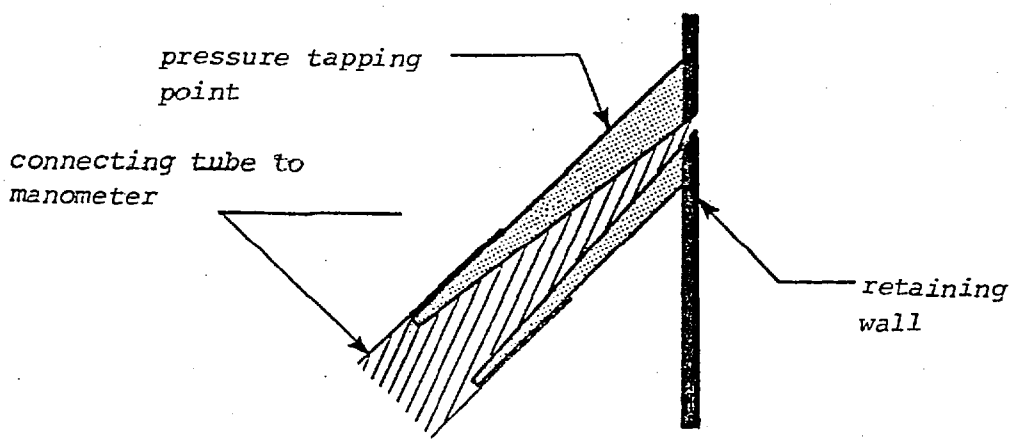


Fig. E.17

respect to the wall, instead of the conventional 90°, such as the one illustrated in Fig. E.17, might solve the problem; however, manufacturing and employing this type of pressure tap is extremely difficult.

## E.9 MEASUREMENT OF THE MEAN BED PRESSURE

The mean pressure on the channel bed was measured by providing a large number of small diameter piezometric tapping points. The channel

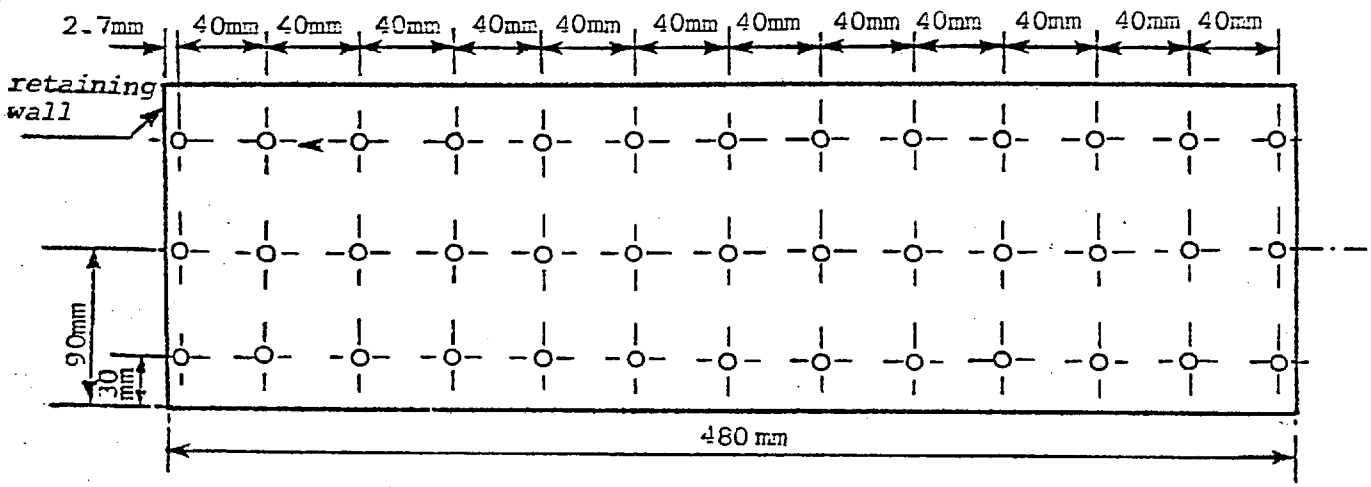


Fig. E.18 The arrangement of the static pressure taps on the channel bed

was divided into three sections of equal width and a row of 0.5 mm diameter pressure taps were located at the centre of each section (Fig. E.18).

## E.10 THE MEASUREMENT AND ANALYSIS OF WAVE HEIGHT

The complicated wave patterns occurring at the retaining wall were studied by employing a *capacitance-wire gauge* technique. This essentially simple method makes use of the fact that water is an efficient conductor of high frequency alternating currents. If a high frequency voltage is applied to a wire which has a non-conducting coating, then, when it is partially immersed in water, the wire acts as one plate of a capacitor, the coating as the dielectric and the surrounding water as the other plate.

In order to investigate the wave conditions occurring at the retaining wall, it was initially intended that three conventional laboratory wave gauge probes be fixed adjacent to the wall. However, the supporting rods of the probes would have interfered with the flow pattern. Instead, the retaining wall was divided into three equal vertical sections with a capacitance-wire gauge fixed in the middle of each section. The wire gauges were perpendicular to the channel bottom and partly immersed in the water flow. Each gauge consisted of a double length of coated wire of 0.4 mm diameter kept taut between a perspex cube fixed at the top of the wall and a non-conducting semi-circular disc at the bottom and fixed to the wall (Plate X). The three semi-circular discs were fixed to the bottom by means of screws, which were left uncoated in order to be conductive. Three screened low-noise cables were each connected to the retaining wall, the coated wires at one end and to the remainder of the wave height recording apparatus at the other end. A high frequency signal from an oscillator was applied between each wire and the painted metallic wall which conducted it to the water surrounding the wire (through the uncoated screw attached to each non-conducting semi-circular disc). As a wave passed each gauge, the immersed length of the wir changed, thus changing its capacitance and inducing an effect on the applied signal. The only source of error was that produced by surface tension which caused a slight damping of the readings.

High frequency fluctuating signals are unsuitable for use with recording instruments, and if they are used, it is first necessary to convert them to direct voltage outputs. In the experiment, this was done by three transducers, which used the fluctuations in capacitance of the gauges to produce corresponding frequency modulations of the applied carrier signals. Each modulated signal was then fed into a unit containing

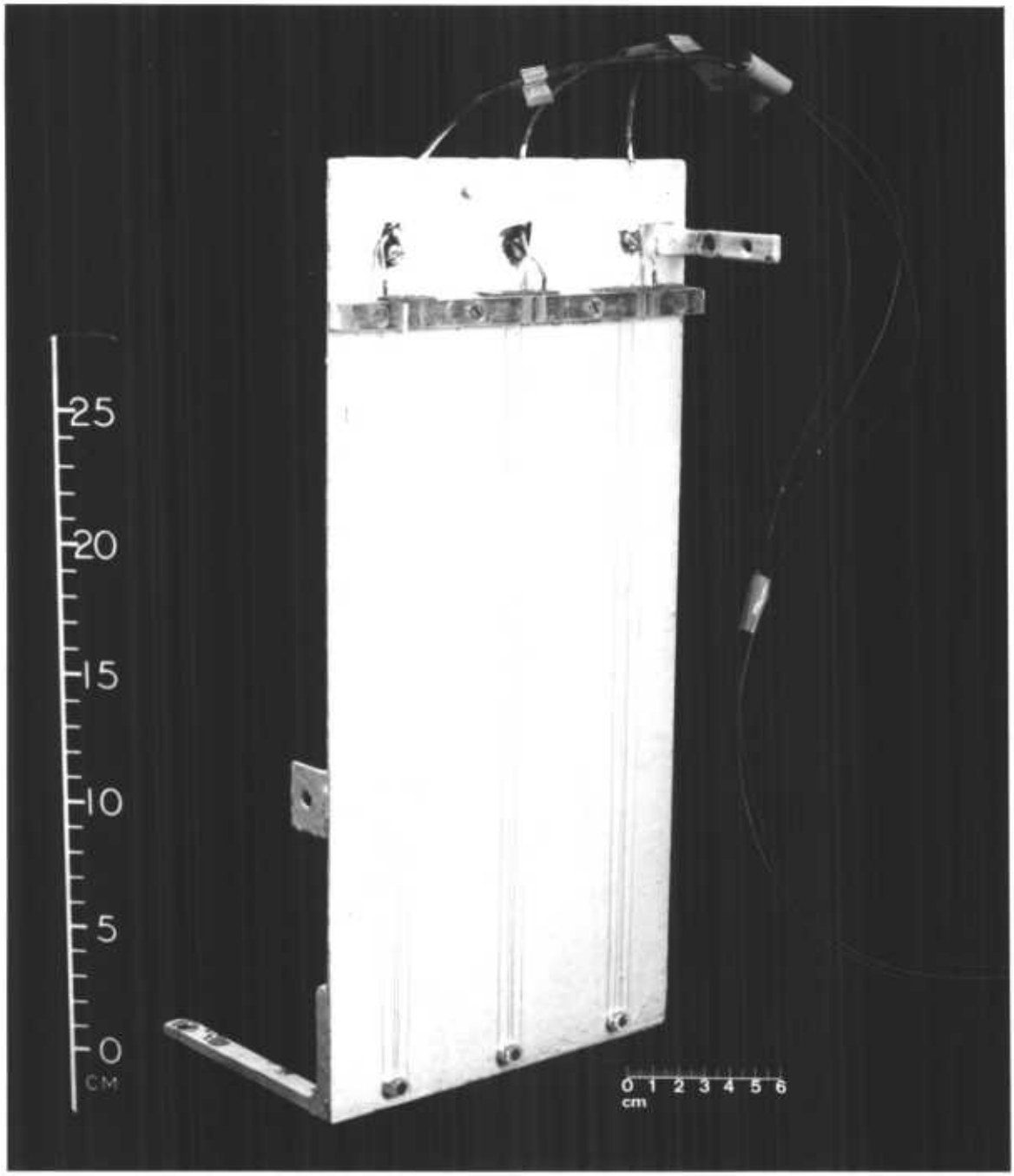


PLATE X VIEW OF RETAINING WALL INCORPORATING WAVE RECORDING APPARATUS

a frequency-discriminating circuit which converted the frequency change to a proportional change in the direct output voltage. The simultaneous water level signals belonging to three different points along the retaining wall were translated into curve-traces on photographic paper via an ultra-violet recorder (Type 1185).

The ultra-violet recorder is a machine similar in principle to a moving-paper/moving-pen recorder, but instead of the use of a pen, the record is produced by a thin beam of ultra-violet light. It is a general purpose instrument which can receive up to thirty-six channels of information to be recorded simultaneously. However, in this investigation, only three were required for recording wave heights. The thin beams of ultra-violet lights are focussed onto a roll of light-sensitive paper, 305 mm in width, and moving at a predetermined constant speed. The movement of each beam is controlled by a mirror mounted on a small galvanometer coil which responds in proportion to the direct voltage applied to it. Before taking a record, it was necessary to adjust each galvanometer alignment by rotating the galvanometer (using the adjusting tool) until the light image appeared at its correct position on the paper. Several paper speeds were available, anyone of which could be selected during running by means of a switch on the front panel. The paper speeds provided were 762, 508, 254, 152.4, 101.6, 50.8 and 38.1 mm/sec. The recording process was entirely electronic and had the advantages of high frequency response and very little lag.

### E.10.1 Calibration of the Wave Recorder Probes

The calibration of the wave gauges/transducers/recorder combination was a critical factor in the measurement of wave heights. It is known that the calibration varies with ambient temperature so the calibration procedure had to be accomplised in *as short a time as possible* to minimise temperature effects. It is also known that the calibration varies if the position of the connecting wires between wave gauges, transducers and the recording apparatus change. To prevent this source of error occurring, extreme care was taken that the connecting wires did not change position.

After the variable water level recordings were made, the water flow was stopped very quickly by opening all the gate valves connected

to the reservoirs. Still water levels produced by means of a *calibration well* (Plate XI) were measured, relative to the channel bottom, by a precision point gauge. The static calibration was achieved by relating still water levels, to the corresponding recordings made on the photographic paper. After the fixing lug of the calibration well was connected to that of the retaining wall by means of a plastic nut and bolt, the sides and bottom of the calibration well were efficiently sealed with plasticine at the bevelled edges. Water was allowed into the calibration well and after it had filled the well and became completely still, the point gauge in the stilling well was read. The corresponding water level in the stilling well was recorded on the photographic paper from the signal obtained from the wire recorder. The tap incorporated at the bottom of the calibration well was used to drain the water inside the well and in this way a new water level could easily be obtained. This step was repeated for 30 different depths in the stilling well during each run. Thus, knowing the reading of the point gauge and the corresponding signal shown on the photographic paper, the scale of the recording on the photographic paper could be determined.

The important requirement was that the calibration of each wave recording probe should be linear over the full range needed for wave measurement. This was found to be the case provided that the bottom part of the gauges, where the wires pass around the non-conducting discs, were kept well below the water-surface. Because a linear calibration depends on the wire insulation being uniform, care was taken when handling the wall holding the wire gauges at all times so that the coatings would not be damaged. As it was necessary in each run to adjust the three galvanometer alignments by rotating them using the adjusting tool in order that the three light images did not go beyond the width of the light-sensitive paper, the calibration process had to be repeated for each run.

### E.10.2. The Analyser

The water level records made on photographic paper were continuous traces of water levels against time. To transform these records into digital records, suitable for computer analysis, coordinates were read from the traces on to computer punched cards using an X-Y plotter.

The X-Y digital data reader equipment was supplied by P.C.D.

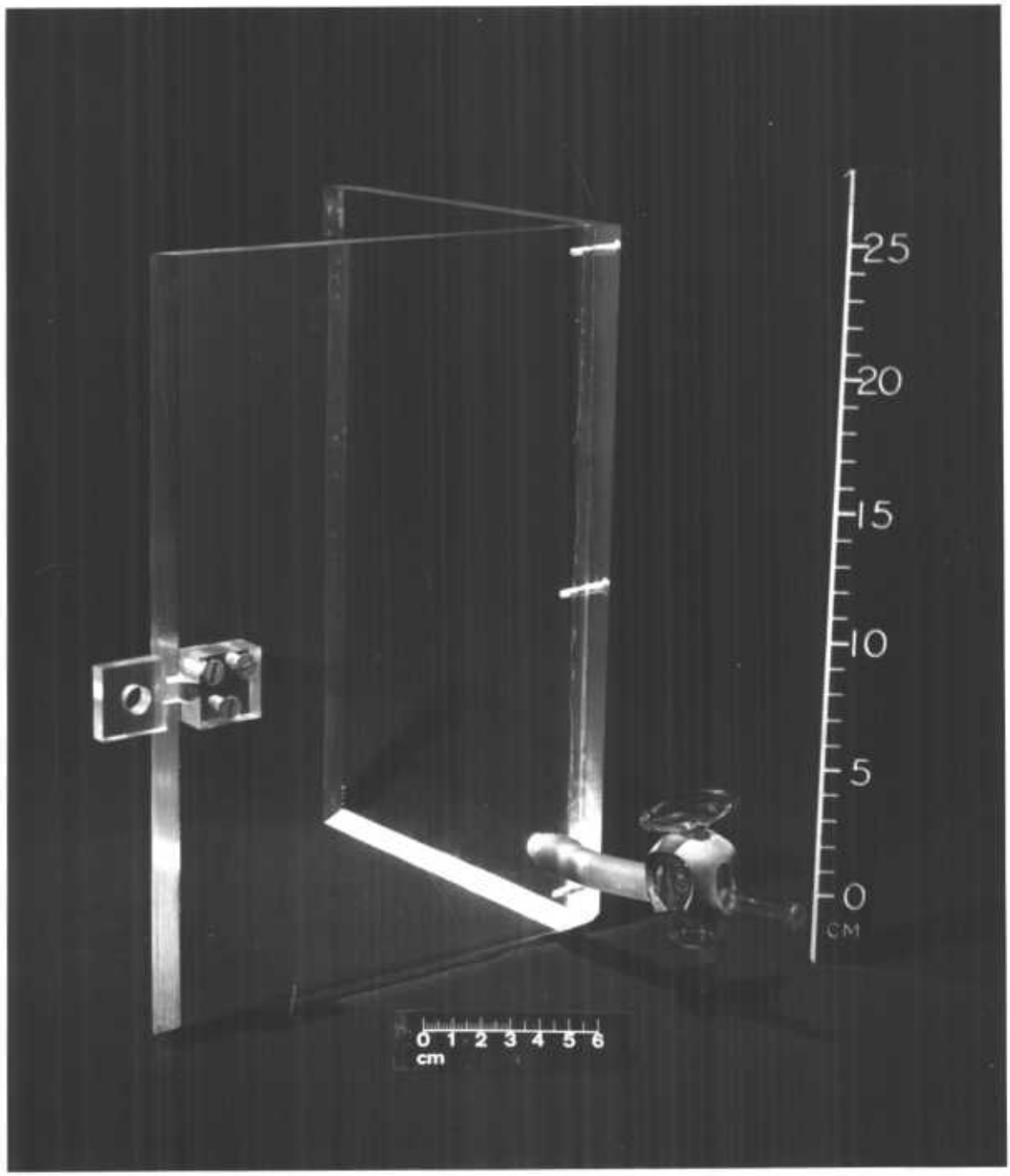


PLATE XI VIEW OF CALIBRATION WELL

(Farnborough)and was operated together with a 'Dynamco voltmeter'. Plate XII shows the analyser used and its different components. The reader, which was housed in a stressed-skin metal structure, contained three highly linear potentiometers associated with the X-Y outputs. Accurate readings were obtained through the use of the anti-parallax double ring magnifying reading sight with a magnification of 1:1.3. A 'carriage' (A), which carried the sight, moved horizontally across the unit and its position determined the X output. Facilities were also provided to move the carriage along the X axis by fixed increments of 2.5, 5, 10, 25 or 50 mm as selected, in this case, a 'selector switch' (B) permitted readings at regular intervals. The eyepiece was moved up and down the carriage manually to follow the plot being measured with its position specifying the Y output. Extreme freedom of movement of the sight helped to follow any curve whilst positive locking of the carriage in any X position permitted the multi-channel record to be read at a common X line. Up to six channels were available, each with individual scale and zero adjustments. The plotter was adjusted to read water levels along the Y axis, at fixed

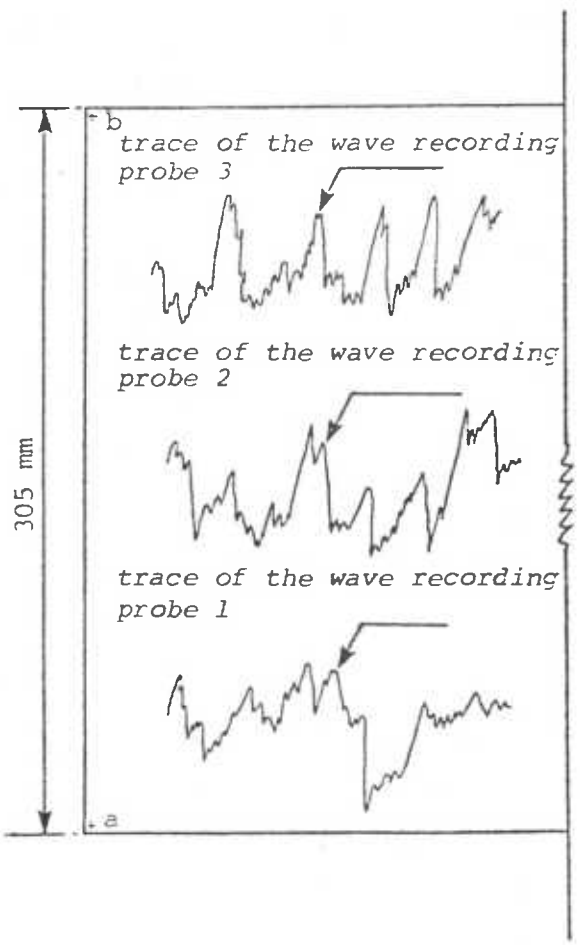


Fig. E.19 Three simultaneous water level traces on the light-sensitive paper

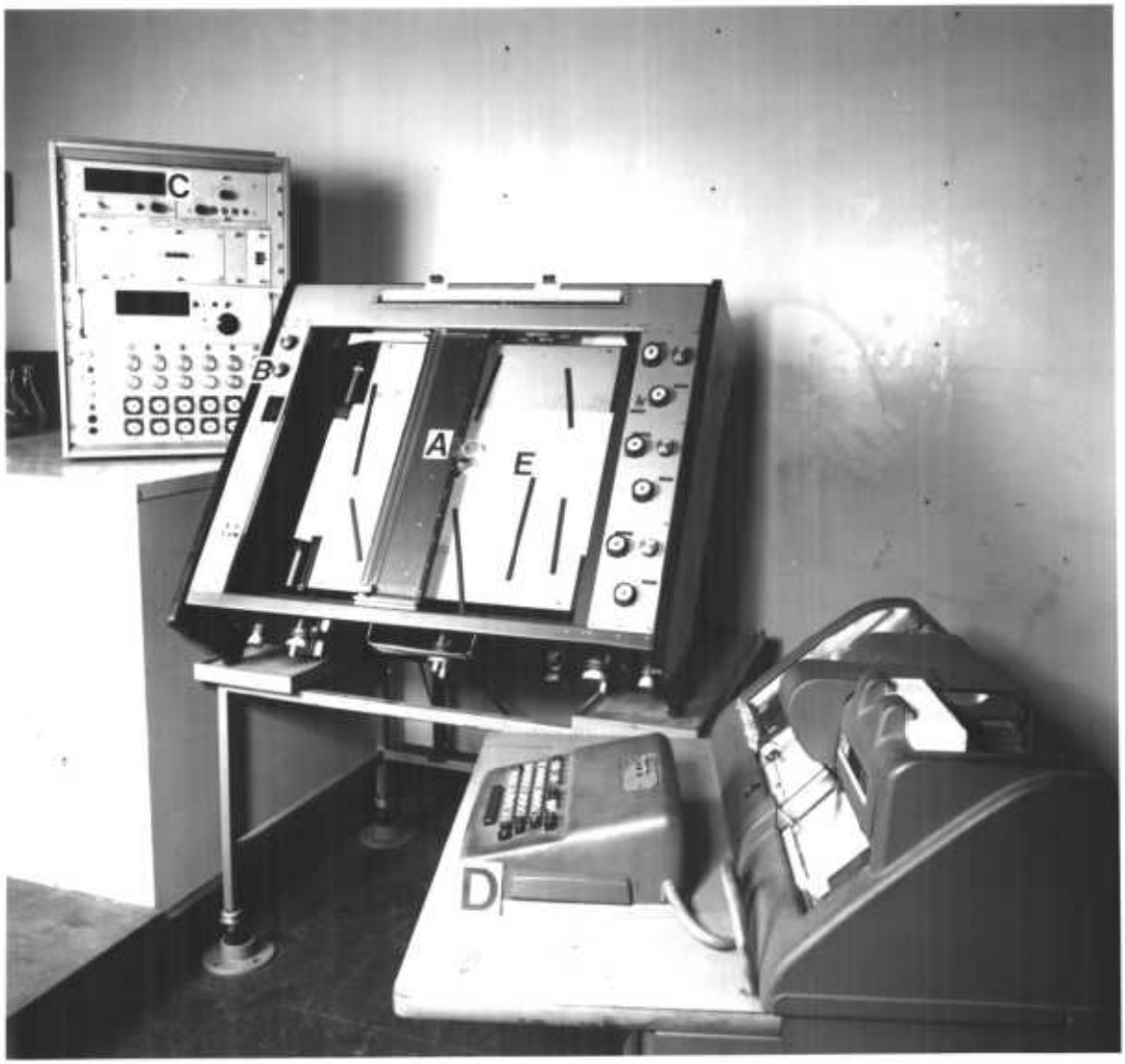


PLATE XII GENERAL VIEW OF X-Y DIGITAL DATA READER

**A** *Carriage*

**B** *Interval selector*

**C** *Control unit with X-Y display*

**D** *IBM-026 card punch*

**E** *Ground glass screen*

increments of time, along the X axis. Spools were provided to hold the continuous water level recording paper with magnetic strips to hold the edges of the paper to the reading area. The chart reader was electronically coupled to an IBM-026 card punch machine and the data displayed on the chart reader panel (C) was automatically punched onto cards.

However, as equispaced sampling was adopted in this investigation, only three channels out of six were required for recording the three vertical distances of the traces on the paper. The scale length for the vertical axis varied from 0, which corresponded to the point(a) chosen (Fig. E.19) very close to the lower edge of the paper, to 6000 which corresponded to the point (b) very close to the upper edge of the paper.

### E.10.3 Selection of Paper Speed and Digitisation Interval

The choice of paper speed was closely related to the time increment to be used in digitising the wave records, the physical limits of the recording and to the digitising equipment being used, once these limits were known.

In Section C.5.3, it was explained that $f_N = 1/2\Delta t$, called the Nyquist frequency, is the highest frequency which can be detected from the periodogram of data sampled at $\Delta t$. Table E.4 gives the Nyquist frequency corresponding to a given paper speed and a given digitisation interval.

| $\Delta X$ digitisation interval mm \ paper speed mm/sec $u_o$ | 762 | 508 | 254 | 152.4 | 101.6 | 50.8 | 38.1 |
|---|---|---|---|---|---|---|---|
| 2.5 | 152.4 | 101.6 | 50.8 | 30.5 | 20.3 | 10.2 | 7.6 |
| 5 | 76.2 | 50.8 | 25.4 | 15.2 | 10.2 | 5.1 | 3.8 |
| 7.5 | 50.8 | 33.9 | 16.9 | 10.2 | 6.8 | 3.4 | 2.5 |

Nyquist frequency (Hz)

Table E.4 The Nyquist frequency $f_N$ for a given paper speed and a given digitisation interval

In the initial stages of this investigation, since very little was known of the maximum frequency $f_{max}$ of the complicated wave patterns near the retaining wall , a very fast paper speed of 508 mm/sec was chosen to analyse the first water level recordings. Using the digitisation interval of 2.5 mm, the digitising time interval will be

$$\Delta t = 0.05 \text{ sec} \tag{E.24}$$

and the corresponding Nyquist frequency will be 101 Hz (Table 4). While in itself this appeared unrealistic, it allowed an examination of the spectra over a wide range of frequencies in order to find a more realistic cutoff frequency. This action was taken in the absence of any knowledge of the highest frequency response of the wave recording probes, the limit of which was probably caused by the surface tension drag of the water on the probe wires. However, in the initial stages of the investigation, the ordinates of the spectra were all found to be very small for frequencies higher than approximately 10 Hz.

The smallest digitisation interval (2.5 mm) was adopted for digitisation of all the records. Since it was known that the maximum frequency was $f_{max} = 10$ Hz, from Eq. (C.142), it was concluded that $\Delta t = 0.025$. By referring to Table E.4, it followed that the appropriate paper speed was 101.6 mm/sec; this was adopted for all the experiments. The paper speed of 101 mm/sec and digitisation interval of 2.5 mm resulted in sampling interval of $\Delta t = 0.025$ sec and a Nyquist frequency of $f_N = 20.3$ Hz. The frequencies close to the cut off frequency of 20.3 Hz contribute little or nothing to the total variance, and aliasing would be unlikely to occur.

### E.10.4 Number of Data Points and Length of Recording Paper

With the variable $\Delta t$ fixed, it was possible to look at the spectra produced by varying N. In the initial stages of investigation, according to the recommendation given in Section C.5.9, three values of N were considered - 1024, 512 and 256. With N = 1024, the best estimates were obtained, hence 1024 was chosen for all the experiments. In this case, for each experiment, the total length of approximately 4.5 m of light-sensitive paper was necessary; 2.6 m of this was for wave recordings and the remainder for calibration of the probes.

## E.10.5 Calibration Lines of the Wave Recording Probes

In this investigation, the digitised water levels obtained from the X-Y plotter had units of millivolts rather than of length as was desired. To transform the records to the correct units, the calibration lines were also assigned coordinates in millivolts. Thus conversions into correct units, based on calibrations in the laboratory, were applied as the data were entered. For each wave recording probe, this involved application of simple linear equation of the form

$$y = kp + c \qquad (E.25)$$

to, n(n around 30), pairs of measurements, $(y_1, p_1)$, ..., $(y_n, p_n)$ using *weighted* least squares method, where

p = data point in millivolts
y = corrected data point in mm
k,c = calibration constants

Typical calibration lines are illustrated in Fig. E.20, the lines were found by linear regression of p versus y (p as dependent variable and y as independent variable). Subscript 1 corresponds to a measurement from the wave gauge probe which is close to the channel outlet; subscript 2 represents a measurement from the wave gauge probe which is in the middle of the retaining wall and subscript 3 belongs to the wave gauge probe which is close to the side wall. The adjustment, in this case three simple linear equations, was applied within the computer programme as the data were entered in for analysis.

It should be noted here that one restriction imposed by employing the least squares method (Appendix III) is that the independent variable should not have any degree of uncertainty while in this case, there is uncertainty in both variables y and p. However, in the initial stages of the investigation, it was found that the linear regression of p versus y would generally result in a lower sum of squares of deviations about the regression (s.s.d) than that of y against p. For this reason, the linear regression where p was considered as a dependent variable and y as an independent variable was adopted for each probe in all experiments.

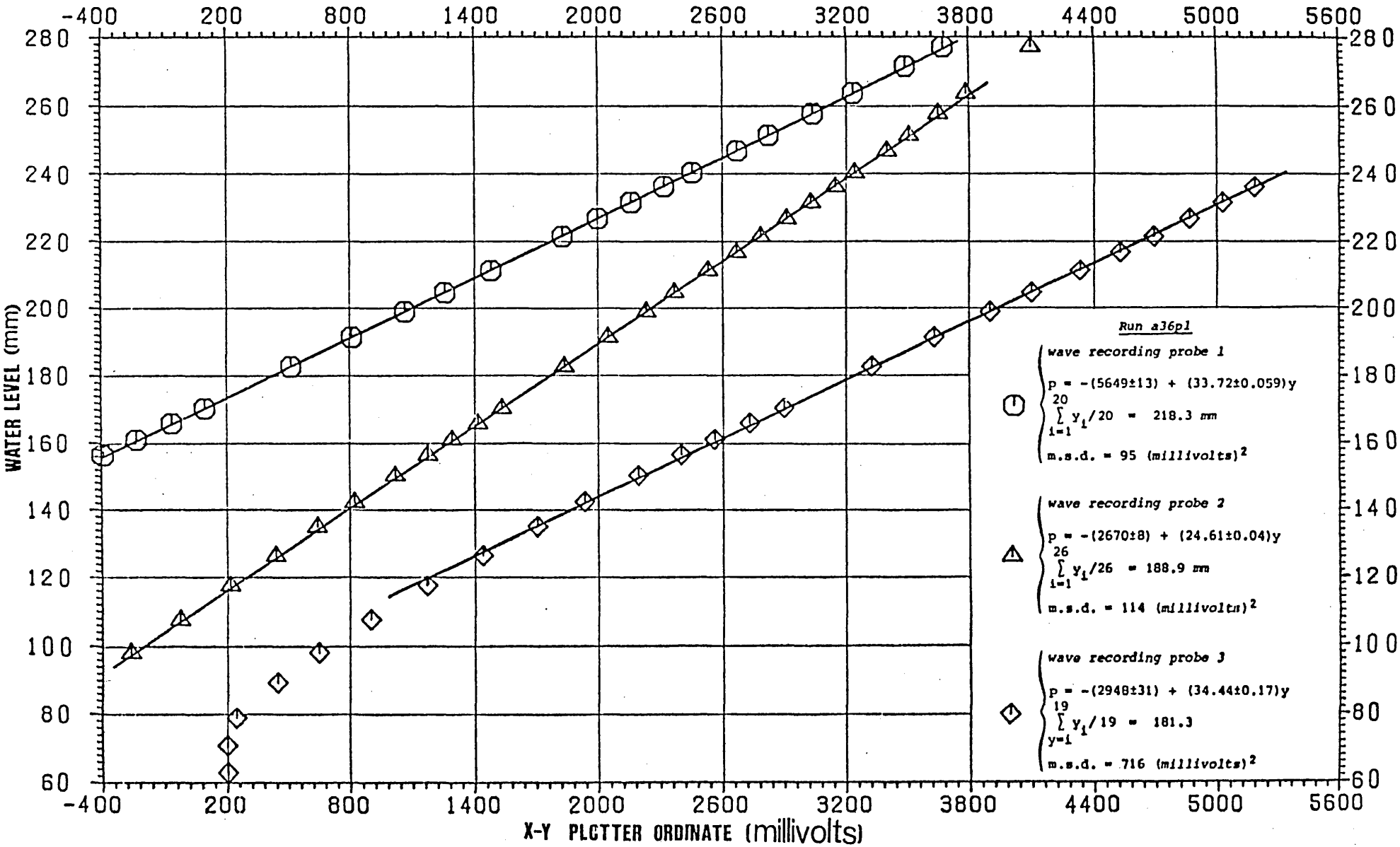


Fig. E.20 Calibration of the wave recording system

### E.10.6 Estimation of Uncertainty in Wave Height Measurement

There are several sources of uncertainty in the procedure used to measure and analyse the wave patterns near the retaining wall. The overall uncertainty in the measurement of wave heights is not a *single* value but varies with the magnitude of the measured wave height. It is necessary, therefore, to assess the total uncertainty for the worst cases. The contributary uncertainties can be summarized as follows:

(a) Uncertainty in *reading* of the water level by the *point gauge* in the calibration stilling well was ±0.1 mm.

(b) Linearity of the deflection on the recording paper produced by the galvanometer beam when compared with the deflecting current is another source of uncertainty. Non-linearity would increase as the beam gets further from the mean position. This effect manifests itself as a scatter of the experimental points around the line drawn by the weighted least squares method (Fig. E.20). From Appendix III, it follows that the uncertainty in the estimated value obtained by using least squares method is not a single value but varies with the number of data points, the confidence level used and also the value of the independent variable.

(c) The analyser *resolution limitation* was given by the manufacturer to be ±0.13 mm.

(d) The *linearity of the potentiometers* was given by the manufacturer to be better than ±0.1%.

(e) The *operational uncertainty* is the random uncertainty of a typical measurement made with the X-Y plotter. Its average value should be found by the operator.

The estimation of the total uncertainty was carried out for run *a36p1* and wave recording probe 2. For the calibration of the wave recording probes, the water depth in the calibration well was varied between approximately 50 and 280 mm. For the estimation of total uncertainty, the worst case for the probe 2 (see Fig. E.20), where the water depth in the stilling well was $y_o$ = 100 mm and the corresponding signal

appeared to be at 100 mm from the point 'a' (Fig. E.19) on the photographic paper was considered. The uncertainty due to the application of least squares method at a 95% confidence level could be calculated from Eq.(III.8d). In this case (see Fig. E.20), it follows that

$$\left.\begin{aligned} n &= 26 && \text{(a)}\\ \alpha &= 0.05 && \text{(b)}\\ \text{m.s.d.} &= 114.53 \text{ (millivolts)}^2 && \text{(c)}\\ \bar{y} &= 188.9 \text{ mm} && \text{(d)}\\ y_o &= 100 \text{ mm} && \text{(e)} \end{aligned}\right\} \text{(E.26)}$$

The value of $t_{0.025,24}$ is given by Chatfield (1975a) to be 2.064. Using the equation of calibration

$$p = -2670 + 24.61\, y \qquad \text{(E.27)}$$

for $y_o$ = 100 mm, the corresponding millivolts will be $p_o$ = -209 millivolts and hence the uncertainty will be

$$\left.\begin{aligned} & t_{\alpha/2,(n-2)}\left\{\text{m.s.d.}\left[1 + \frac{1}{n} + \frac{(y_o - \bar{y})^2}{\sum_{i=1}^{n}(y_i - \bar{y})^2}\right]\right\}^{\frac{1}{2}} \\ &= 24 \text{ millivolts} \end{aligned}\right\} \text{(E.28)}$$

The corresponding uncertainty in the water depth is ±0.97 mm. Using the root square method, the total uncertainty from the reading by the point gauge and from the application of the least squares method is $w_{y_o} = (0.97^2 + 0.1^2)^{\frac{1}{2}} = 1$ mm.

To evaluate the average operational uncertainty, a simple test was made. An accurate 0.3 m ruler was positioned by magnetic strips to the reading area and along the Y axis. The zero mark of the ruler corresponded to the point (a) (Fig. E.19) where the number displayed on the chart reader panel was zero. The 30 cm mark was read 20 times. However, due to operational error and also due to the uncertainties mentioned in

(c) and (d), the readings were evidently different. Using Eqs (E.1) and (E.4), the relative uncertainty was found to be 0.025. The total uncertainty in length was 300×0.025 = 7.5 mm. The combined uncertainty due to the non-linearity and resolution limitation in a 300 mm length of the ruler was $[(300\times0.001)^2+(0.13)^2]^{\frac{1}{2}}$ = 0.33 mm and hence the relative operational uncertainty was $[(7.5)^2-(0.33)^2]^{\frac{1}{2}}/300$ = 2.5%.

As the trace corresponding to 100 mm water depth in the stilling well appeared to be at approximately 100 mm from the point 'a' on the photographic paper (Fig. E.19), the combined uncertainty introduced by the non-linearity of the potentiometers, resolution limitation and operational error is

$$w_{h_o} = (0.13^2 + 0.1^2 + 2.5^2)^{\frac{1}{2}} = 2.5 \text{ mm} \qquad \text{(E.29)}$$

The total uncertainty in the wave height measurement is of the order of

$$\left.\begin{aligned} \frac{w_w}{w} &= \left[\left(\frac{w_{h_o}}{h_o}\right)^2 + \left(\frac{w_{y_o}}{y_o}\right)^2\right]^{\frac{1}{2}} \\ \frac{w_w}{w} &= \left[\left(\frac{2.5}{100}\right)^2 + \left(\frac{1}{100}\right)^2\right]^{\frac{1}{2}} = 2.7\% \end{aligned}\right\} \text{(E.30)}$$

## E.10.7 Estimation of Uncertainty in Frequency

A signal generator was used to determine the uncertainty in the speed of ultra-violet recorder. It was found that at a speed of 101 mm/sec the uncertainty was of the order of 2%. The X-Y plotter was found to have a reading uncertainty of ±1% along the X axis. Hence the total uncertainty in the frequency is of the order of

$$\left.\begin{aligned} \frac{w_f}{f} &= \left[\left(\frac{w_{u_o}}{u_o}\right)^2 + \left(\frac{w_{\Delta X}}{\Delta X}\right)^2\right]^{\frac{1}{2}} \\ \frac{w_f}{f} &= \left[\left(\frac{2}{100}\right)^2 + \left(\frac{1}{100}\right)^2\right]^{\frac{1}{2}} = 2.2\% \end{aligned}\right\} \text{(E.31)}$$

## E.11 EXPERIMENTAL PROGRAMME

The experimental study described here was mainly designed to provide information about the motion and the behaviour of a plane turbulent water jet of finite dimensions when deflected by a transverse wall.

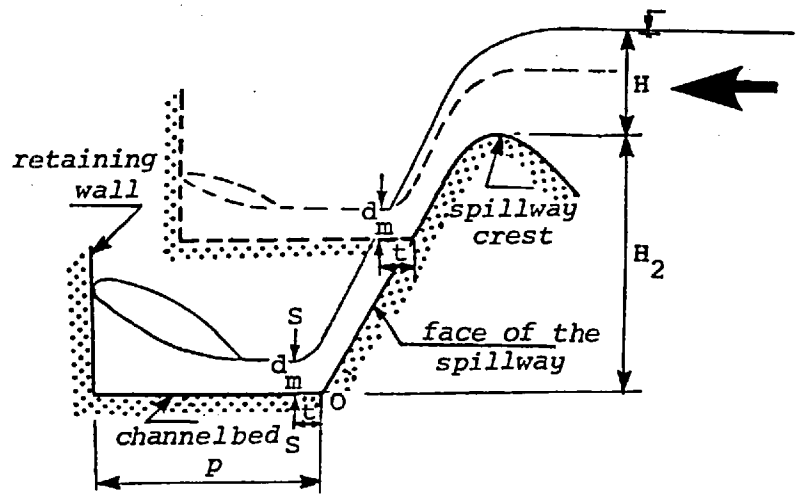


Fig. E.21

Fig. E.21 shows a schematic representation of a supercritical water flow issuing from an overflow spillway onto a smooth horizontal channel of the same width, with the flow being deflected by a plane smooth vertical transverse wall which is perpendicular to the initial flow direction. Observation of the flow indicated that as the water came down from the spillway, the free surface converged steadily until it attained a minimum depth at section S-S, situated close to the toe of the spillway and also became aligned parallel to the channel bed at this section. In Fig. E.21 $H_2$ is the height of the spillway crest above the channel bed, H is the water level over the spillway crest, $d_m$ is the depth of the flow at section S-S and t denotes the distance of section S-S from point O where the channel bed and the face of the spillway intersect.

With regard to the variables $d_m$, t, H and $H_2$, it was discovered that by varying the elevation of the channel bed with respect to the elevation of the spillway crest, the same depth of flow $d_m$ at section S-S would be located at the same distance t from the point O (where the channel bed and the face of the spillway intersect), irrespective of the different velocities arising at the toe of the spillway (Fig. E.21). Furthermore, it was observed that with the retaining wall at a fixed position with respect to the spillway, an increase in the discharge of the incoming flow from the

spillway caused the distance t to increase (i.e. the section S-S got closer to the retaining wall). This situation was very similar to a free flow under a sharp-edged sluice gate located in a horizontal rectangular channel of the same width; as was explained in Section 6.5.1. For the case of the sluice gate, as the water emerged from the sluice gate, the free surface contracted to a minimum section which is well known as the vena contracta. This normally occurred at a distance from the gate which was approximately equal to the gate opening and was independent of the water head upstream of the sluice gate (or alternatively the velocity of the water at the vena contracta).

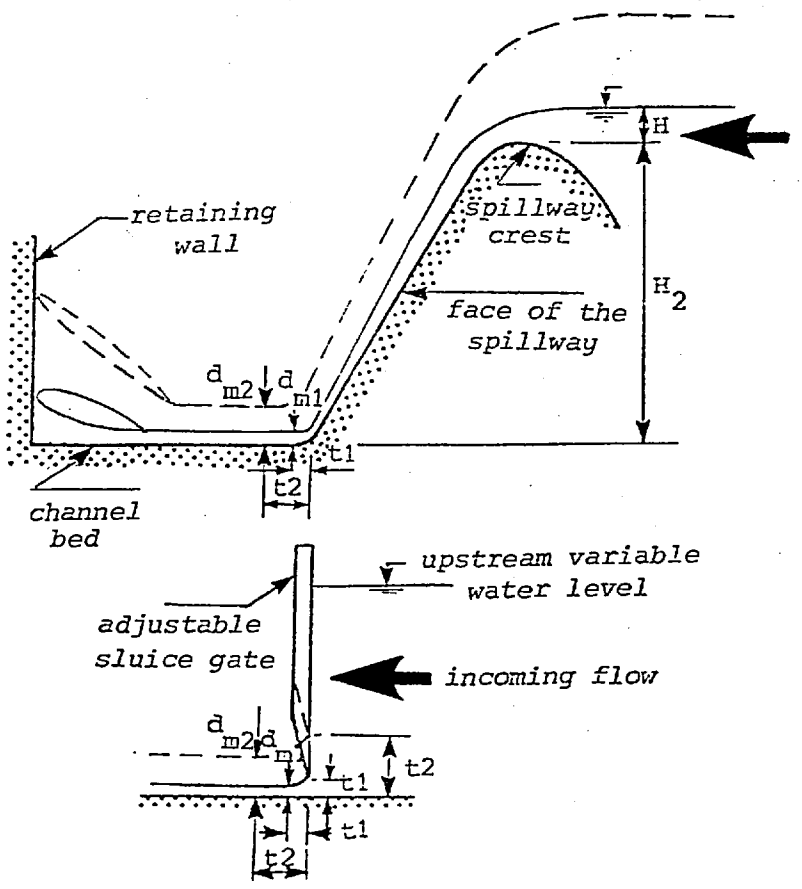


Fig. E.22 The flow under a sharp edged sluice gate and the flow from a spillway into a horizontal channel

The principal variables which governed the present experimental work were:

a) the height of the spillway crest with respect to the channel bed $H_2$.

b) the depth of the flow at the toe of the spillway $d_m$ (or the water level over the spillway crest H).

c) the position of the retaining wall with respect to the spillway *p*.

The angle between the spillway face and the horizontal was kept constant at 62.5° throughout all the experiments. Based on the three aforementioned variables, the experiments performed during this investigation can be classified into two principal groups *a* and *b*. In group *a*, the vertical distance between the horizontal channel bed and the spillway crest was 219mm and for group *b*, this distance was increased to 519mm. However, for both groups, the distance of the retaining wall from the point O (where the channel bed and the face of the spillway intersect) was changed from *p1*=480mm to *p2*=360mm and then to *p3*=240mm (where *p* refers to the position of the retaining wall with respect to the spillway). In this thesis each experiment is characterised by six figures. In the first instance a letter denotes the group which the experiment belongs to; then the second and third numbers give the depth of the flow at section S-S in mm to the nearest round number and the fourth and the fifth figures refer to the distance of the retaining wall from the spillway. For example, run *a36p1* represents the experiment belonging to the group *a* (where the vertical distance between the channel bed and the spillway crest was 219mm) and the depth of the flow at the toe of the spillway was 36mm and the distance of the retaining wall from the point O was 480mm.

A total of 21 experiments were undertaken. The important details of these experiments are given in Table E.5, in which,

$H_2$ = vertical distance between the spillway crest and the channel bed. Only two values (219mm and 519mm) were taken for $H_2$.

H = the water level above the spillway crest (varied between 36.4mm and 116.9mm).

Q = discharge over the spillway (varied between 2342$cm^3$/sec and 13464$cm^3$/sec).

*b* = the *impingement width* which was kept constant at 180mm throughout all the experiments. The impingement width was equal to the spillway width.

| Run | $H_2$ mm | H mm | Q $Cm^3/sec$ | b mm | $d_m$ mm | $\ell$ mm | $U_m$ Cm/sec | Fr | $R_j$ | $\frac{\ell}{d_m}$ | $\frac{b}{d_m}$ |
|---|---|---|---|---|---|---|---|---|---|---|---|
| *a08p1* | 219 | 36.4 | 2342 | 180 | 8 | 464 | 163 | 6.46 | 11370 | 58 | 22.5 |
| *a11p1* | 219 | 48.2 | 3568 | 180 | 11 | 461 | 180 | 5.92 | 17320 | 41.9 | 16.4 |
| *a14p1* * | 219 | 58.2 | 4734 | 180 | 14 | 456 | 188 | 5.37 | 22970 | 32.6 | 12.9 |
| *a25p1* * | 219 | 92 | 9398 | 180 | 25.1 | 433 | 208 | 4.32 | 45600 | 17.2 | 7.2 |
| *a36p1* * | 219 | 116.9 | 13464 | 180 | 36.4 | 425 | 206 | 3.55 | 65330 | 11.7 | 4.9 |
| *a08p2* | 219 | 36.4 | 2342 | 180 | 8 | 344 | 163 | 6.46 | 11370 | 43 | 22.5 |
| *a11p2* | 219 | 48.2 | 3568 | 180 | 11 | 341 | 180 | 5.92 | 17320 | 31 | 16.4 |
| *a14p2* * | 219 | 58.2 | 4734 | 180 | 14 | 336 | 188 | 5.37 | 22970 | 24 | 12.9 |
| *a25p2* * | 219 | 92 | 9398 | 180 | 25.1 | 313 | 208 | 4.32 | 45600 | 12.5 | 7.2 |
| *a36p2* * | 219 | 116.9 | 13464 | 180 | 36.4 | 305 | 206 | 3.55 | 65330 | 8.4 | 4.9 |
| *a08p3* | 219 | 36.4 | 2342 | 180 | 8 | 224 | 163 | 6.46 | 11370 | 28 | 22.5 |
| *a11p3* | 219 | 48.2 | 3568 | 180 | 11 | 221 | 180 | 5.92 | 17320 | 20.1 | 16.4 |
| *a14p3* * | 219 | 58.2 | 4734 | 180 | 14 | 216 | 188 | 5.37 | 22970 | 15.5 | 12.9 |
| *a25p3* * | 219 | 92 | 9398 | 180 | 25.1 | 193 | 208 | 4.32 | 45600 | 7.7 | 7.2 |
| *a36p3* * | 219 | 116.9 | 13464 | 180 | 36.4 | 185 | 206 | 3.55 | 65330 | 5.1 | 4.9 |
| *b08p1* * | 519 | 51 | 3874 | 180 | 8.1 | 464 | 266 | 10.31 | 18800 | 58 | 22.2 |
| *b11p1* * | 519 | 65 | 5578 | 180 | 11.2 | 461 | 277 | 8.95 | 27070 | 41.9 | 16.1 |
| *b14p1* * | 519 | 76.4 | 7114 | 180 | 13.9 | 456 | 284 | 8.12 | 34520 | 32.6 | 12.9 |
| *b17p1* * | 519 | 87 | 8646 | 180 | 17.1 | 453 | 281 | 7.18 | 41960 | 26.6 | 10.5 |
| *b14p2* * | 519 | 76.4 | 7114 | 180 | 13.9 | 336 | 284 | 8.12 | 34520 | 24 | 12.9 |
| *b14p3* * | 519 | 76.4 | 7114 | 180 | 13.9 | 216 | 282 | 8.12 | 34520 | 15.5 | 12.9 |

* the wave height records were digitised on these runs.

Table E.5 Details of the experiments

$\ell$ = *impingement length* which can be defined as the distance between the section S-S (Fig. E.21) and the retaining wall. If the impingement length is equal to or less than impingement width, the deflection of the water jet by the transverse wall can be called 'square impingement' or 'short impingement'. The values of the impingement length were varied between 185mm and 464mm were greater than the impingement width.

$d_m$ = the depth of the supercritical water flow as measured at section S-S along the channel centre line. The value of $d_m$ varied between 8mm and 36.4mm.

$U_m$ = average velocity of the supercritical water flow measured at section S-S. The average velocity was calculated from the following relationship

$$U_m = \frac{Q}{b d_m} \qquad \text{(E.31)}$$

The value of $U_m$ varied between 163Cm/sec and 284Cm/sec.

Fr = the Froude number associated with the shooting flow at section S-S. The Froude number was calculated from the following relationship

$$Fr = \frac{U_m}{\sqrt{g d/\alpha}} \qquad \text{(E.32)}$$

in which g is the acceleration due to gravity and $\alpha$ is the energy coefficient of the incoming supercritical water flow at section S-S. The procedure which was adopted to measure the coefficient of energy is described in Chapter F. The Froude number varied between 3.55 and 10.31.

$R_j$ = the Reynolds number of the supercritical water flow at section S-S which was calculated from the following relationship

$$R_j = \frac{U_m \, d_m}{\nu} \qquad \text{(E.33)}$$

where $\nu$ is the kinematic viscosity of water. The Reynolds number varied between $11.4 \times 10^3$ and $65.3 \times 10^3$.

$\frac{b}{d_m}$ = aspect ratio of the plane turbulent water jet which varied between 4.9 and 22.5.

$\frac{\ell}{d_m}$ = dimensionless impingement length which varied between 5.1 and 58.

It must be noted that observation of the flow indicated that with a constant discharge from the spillway, the flow depth $d_m$ and the position of the section where the free surface became horizonatal (distance t in Fig. E.21) were unaffected by changing the retaining wall position with respect to the spillway. The Froude number Fr and the coefficient of energy α of the supercritical water flow were also unaffected. This fact was extended for the case, when with a constant discharge from the spillway, the retaining wall was fixed close enough to the spillway (or alternatively when with the retaining wall at a fixed position with respect to the spillway, the discharge was high enough) such that the toe of the forced hydraulic jump was oscillating around the toe of the spillway. In the latter case, it could be assumed (Stepanov, 1958) that the Froude number and the nominal values of the flow depth $d_m$, the distance t and the velocity $U_m$ at the toe of the spillway were the same as the corresponding values where the retaining wall was further away.

E.11.1 Critical Point for the Flow Over the Spillway

With regard to the flow over the spillway, a few general observations concerning the air entrainment on the face of the spillway must be made.

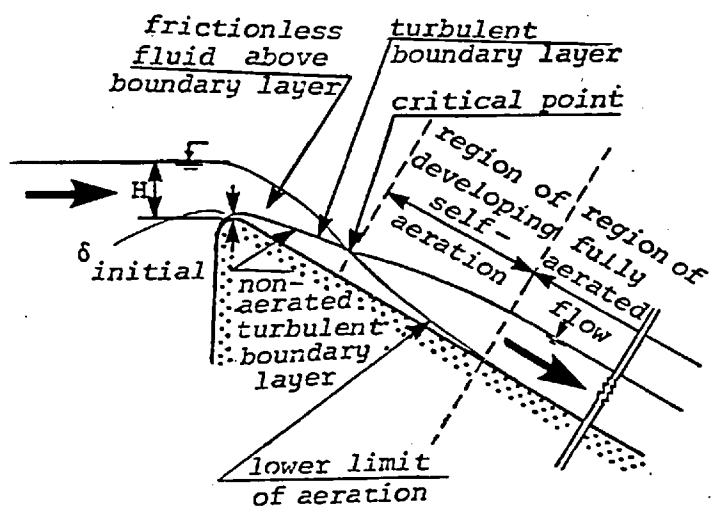


Fig. E.23 Definition sketch for a section of flow down a long steep spillway.

As shown in Fig. E.23, the flow domain over the *long spillways* can be divided into two regions, from the spillway bed to the boundary layer edge and from the boundary layer edge to the free surface. The latter region may be considered as a frictionless converging layer of water. It has been reasonably well established by several observers such as Bauer (1954) that for flow over the spillways incipient aeration does not occur on the slope until a point (or region) is reached at which the boundary layer thickness is equal to the flow depth. The point where the spillway face - induced boundary layer meets the free water surface is called the *critical point*. Examination of flows beyond the critical point have indicated that the upper boundary of the flow is violently agitated and hence is rather ill - defined. It consists of a zone which appears to be *white* due to the high degree of entrained air, while above this zone a spray of water droplets occurs which move more or less parallel to the flow and below which there is a region of discrete air bubbles suspended in the fluid. The reasoning behind this is that the emergence of the boundary layer is associated with velocity fluctuations normal to the surface which become strong enough to induce elements of fluid to be thrown clear of the parent motion. These elements return to the mainstream, carrying air which is then distributed throughout the flow by turbulence. As atmospheric air is drawn into and mixed with the flow to create the appearance of *white water*, the mixture increases in volume or bulks. This increase in volume implies that aerated flows require higher side walls than non-aerated flows.

It is known that by increasing the flow discharge and thus the flow depth, the points at which the surface roughening and the white water occur move downstream together with the critical point. Thus, in the design of spillways, for the design (maximum) discharge, uniform aerated flow will not necessarily occur unless the spillway is exceptionally long or the design discharge is relativley small. Furthermore, it is also known that the results from model studies which have been obtained in self-aerated flows in spillways cannot be reliably extrapolated to the prototype through the several orders of magnitude required to obtain full scale spillway quantities.

Several empirical methods such as those by Bauer (1954), Gangadariah, Lakshmana Rao and Seetharamiah (1970), Campbell, Cox and Boyd (1970) have been proposed for the prediction of the rate of boundary layer growth and the position of the critical point. In this investigation, for each experiment, a careful flow observation in addition to a check using Bauer's method were made to ensure that the boundary layer thickness was less than the flow depth before the flow entered the horizontal channel bed.

# CHAPTER F

# EXPERIMENTAL RESULTS AND DISCUSSION

## F.1 FLOW DIRECTION

Woollen tufts were used to observe the flow direction. The 2-hole transverse - cylinder yawmeter was employed for the measurement of the flow direction in region I and in the forward flow portion of region II. When the yawmeter was being used in region II, it was feared that air entrainment in the forced hydraulic jump might interfere with the flow direction measurement. For this reason, the flushing arrangement of the yawmeter was kept flushed except in the interval when the observations were being made. It was found that the air bubbles present in the forced hydraulic jump seldom presented difficulties.

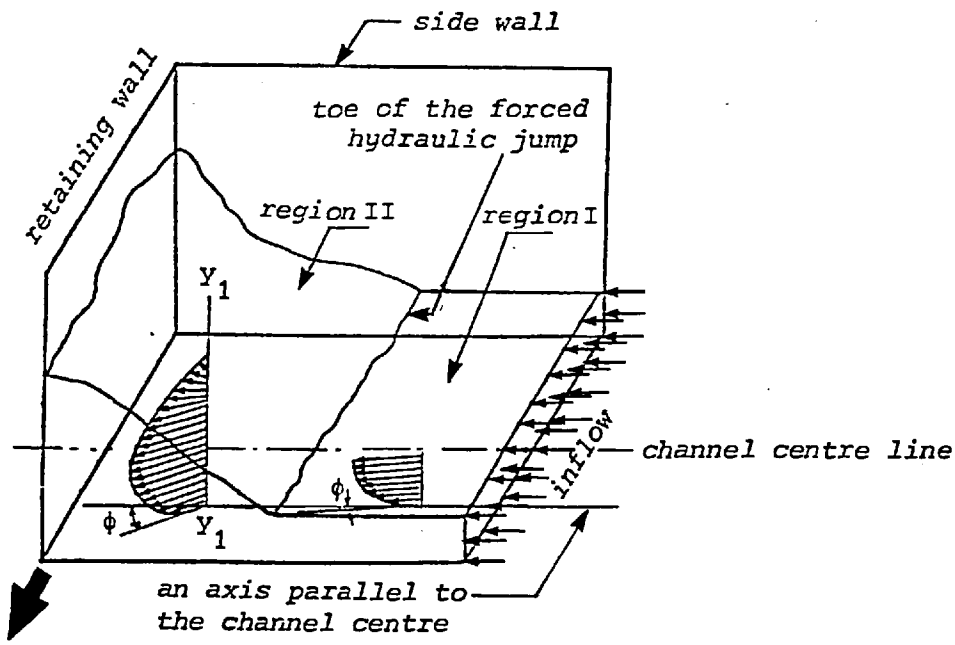


Fig. F.1 Flow direction

With regard to flow direction, it was assumed that the flow in region I and in the forward flow portion of region II was two-dimensional, with the velocity vectors parallel to the channel bed and the velocity plane at an angle $\phi$ to the channel centre line. This means that in both regions I and II for all points on an axis such as $y_1y_1$ perpendicular to

the channel bed (Fig. F.1), the velocity vectors were parallel to the channel bed and lay in a vertical plane at an angle $\phi$ with the channel centre line. This assumption only introduced an appreciable error in the zone close to the top of the forward flow of region II where the velocity vectors were considerably inclined with respect to the channel bed and in the backward flow of region II. During this investigation, no measurements of flow direction were made in the backward flow of region II and in region III.

Using the yawmeter, the assumption that the flow was two-dimensional, as explained above, was tested for several runs and was found to be approximately true. It was observed that in any plane perpendicular to the channel bed and parallel to the channel centre (longitudinal section), the magnitude of redirection $\phi$ increased as the flow approached the retaining

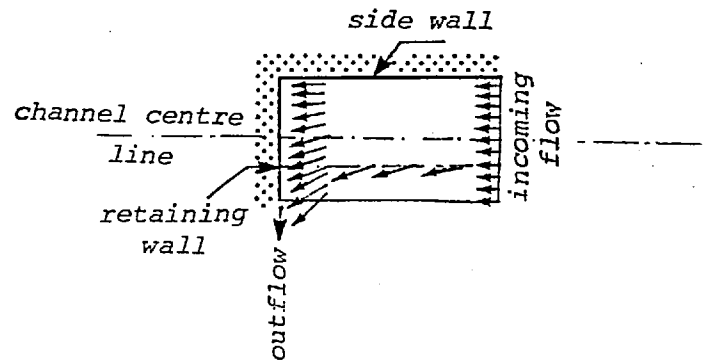


Fig.F.2 Redirection of the Flow

wall. Moreover, for any plane perpendicular to the bed and parallel to the retaining wall (transverse - cross section), the angle $\phi$ increased from the side wall towards the outflow. Also, it was found that with the retaining wall at a fixed position with respect to the spillway, an increase in the discharge from the spillway caused the magnitude of $\phi$ at any given point in both regions I and II to increase. Figs. F.7,F.13 and F.14 show the magnitude of the redirection $\phi$ at different points along the channel centre line for several runs. In these figures, x denotes the longitudinal distance from the retaining wall in the upstream direction. It can be seen that the amount of redirection along the channel centre line was small, being limited to $1^{o}$ in region I and $12^{o}$ in region II.

## F.2 FLOW CHARACTERISTICS OF REGION I

### F.2.1 Theory of the Boundary Layer

When viscosity is significant in a problem, for example in the present investigation, the expedient of separting the flow into two domains can be used, as suggested by L. Prandtl (1904) in his original statement of the boundary layer concept. Prandtl considered that in many flow situations particularly those involving fluids of low viscosity, of which water is a good example, the viscous effects are confined to a relatively narrow zone which is adjacent to the boundary; the major part of the flow therefore behaves as if the fluid were non-viscous. Prandtl then proposed that these two domains be treated separately. The domain where viscous effects are large is called the boundary layer; the domain of negligible viscous effects is termed the zone of *near-potential flow*, indicating that the flow is only different from the potential flow of the non-viscous fluid. On the spillway studied here, for example, both domains exist contiguously-the near-potential flow region being dominant at the upstream end of the spillway with the boundary layer increasing in thickness in the direction of flow. The flow within the boundary layer is complicated by the presence of rotational flow and the internal shear stress, which reaches a maximum at the spillway bed. However, in order to achieve a better understanding of the boundary layer development in the present investigation, it is necessary to briefly review the analytical background to the boundary layer development along smooth flat plates.

#### F.2.1.1 Parameters of Turbulent Boundary Layers

The boundary layer which is simplest to study is that formed by the flow along one side of a thin flat plate parallel to the direction of the oncoming fluid. The fluid, originally having a velocity $U_\infty$ in the

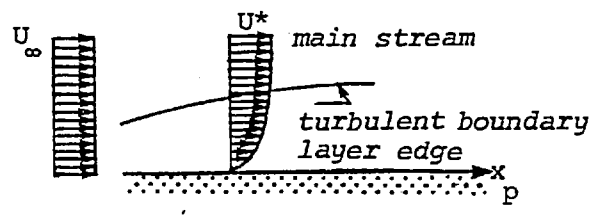


Fig. F.3 Boundary layer on a flat plate.

direction of the plate, is retarded in the neighbourhood of the surface and the boundary layer begins at the leading edge of the plate. As a greater proportion of the fluid slows down the thickness of the layer increases. This means that as the boundary layer becomes thicker, more fluid decelerates from its original undisturbed velocity, so that the momentum of the fluid in the direction parallel to the solid surface steadily decreases.

Since the velocity within the boundary layer increases to the velocity of the main stream asymptotically, an arbitrary convention must be adopted to define the thickness of the layer. One possible definition of the thickness is that distance from the solid surface in which the velocity reaches 99% of the local main-stream velocity component $U^*$. The two other parameters which are used to describe the boundary layer are the displacement thickness and the momentum thickness. The displacement thickness $\delta_d$, is the distance by which the near-potential flow has been displaced from the surface due to the presence of the boundary layer and is defined as

$$\delta_d = \int_o^\delta (1 - \frac{U}{U^*})\, dy \qquad (F.1)$$

in which U is the velocity at a distance y above the plate and $\delta$ denotes the boundary layer thickness. The momentum thickness $\delta_m$, is a similar length parameter associated with the momentum defect suffered by the fluid because of friction and is defined by

$$\delta_m = \int_o^\delta \frac{U}{U^*}(1 - \frac{U}{U^*})\, dy \qquad (F.2)$$

### F.2.1.2 Von Kaſmań Momentum Equation

The development of a turbulent boundary layer is governed by the so-called Von Kaſmań integral - momentum equation. It is a differential equation derived from the equation of motion or by making use of the momentum principle

$$-\delta \frac{dP}{dx}_p - \tau_o = \frac{d}{dx}_p (\int_o^\delta \rho U^2 dy) - U^* \frac{d}{dx}_p (\int_o^\delta \rho U dy) \qquad (F.3)$$

in which P is the pressure, $\tau_o$ represents the intensity of boundary shear stress, $\rho$ is the mass density of the fluid and $x_p$ denotes the distance in the direction of flow. It is known that for flows having a small pressure gradient the sharpe parameter of the velocity profile defined by

$$k = \frac{\delta_d}{\delta_m} \tag{F.4}$$

remains approximately constant. In this case, Eq. (F.3) can be simplified by using the definitions of $\delta_d$ and $\delta_m$ in the following form

$$C_f = \frac{\tau_o}{\rho U^{*2}} = \frac{d\delta_m}{dx_p} + (1+k/2)\,\frac{\delta_m}{U^{*2}}\,\frac{dU^{*2}}{dx_p} \tag{F.5}$$

in which $C_f$ is the local coefficient of boundary shear stress. However, the above relationship does not provide any details of the velocity distribution within the boundary layer.

Prandtl suggested that much of the experimental information available on turbulent flows in circular pipes could be used in the study of turbulent boundary layers on flat plates on the grounds that the boundary layers in the two cases are not significantly different. He assumed that the fully-developed flow within the pipe may be regarded as a boundary layer on a flat plate which has been wrapped round an axis at a distance $\delta$ from the plate which is equal to the radius $r$ of the pipe, and the maximum velocity (along the axis) $U_{max}$, corresponds to the velocity $U^*$ of the main stream past a flat plate. The universal velocity distribution law for smooth pipes is

$$\frac{U_y}{U_{max}} = \left(\frac{y}{r}\right)^n \tag{F.6}$$

in which $U_y$ is the velocity at a distance $y$ from the pipe wall and $n$ is an exponent. Prandtl applied the above relationship to the flat plate case and proposed the following convenient description for the velocity distribution in turbulent boundary layers acting under zero pressure gradient

$$\frac{U}{U^*} = \left(\frac{Y}{\delta}\right)^n \tag{F.7}$$

which is a straight line when plotted logarithmically. The value of $n$ is approximately $1/7$ for moderate Reynolds numbers ($R_p = U^* x_p/\nu < 10^7$ on a flat plate).

## F.2.2 Velocity Profiles in Region I

Earlier in this thesis it was explained that as the water came down from the spillway, the free surface converged steadily until it attained a minimum depth at section S-S (Fig.E.21), situated at the toe of the spillway and also became aligned parallel to the channel bed at this section. Due to the boundary layer development on the spillway, the velocity distribution at section S-S was non-uniform. Hence, the kinetic energy flux and the momentum flux of the flow atthis section had to be corrected by the coefficients of energy and momentum respectively. The calculation of the energy coefficient was also necessary for the evaluation of the Froude number.

To find the coefficients of energy $\alpha$ and momentum $\beta$ of the supercritical water flow at the toe of the spillway, the channel width along section S-S was divided into three equal parts and the calibrated pitot-static tube was used to investigate the velocity profile at the centre of each part. The velocity measurements in the three sections at the toe of the spillway were usually made at a depth interval $\Delta d$ equal to o.5mm. The observed manometer readings were found to remain constant as long as the pitot-static tube was located within the near-potential zone outside the boundary layer. Some variability in the manometer readings was observed over long time intervals when the pitot-static tube was moved to the boundary layer. The straight line portion of the logarithmic plot of the velocity profiles at the toe of the spillway in Figs. F.4,F.5, and F.6 was determined on the basis of the presence or absence of any variation in the manometer readings over long time intervals. In these figures, section 1 represents the section which was close to the channel outlet, section 2 corresponds the channel centre line section and section 3 denotes the section which was close to the side wall. It must be noted that the velocity measurements at the foot of the spillway were all made with the retaining wall at position *p1* and in all cases the toe of the forced hydraulic jump was at a good distance downstream of the measuring section.

The secondary motions(Henderson,1966)in region I affected the distribution of velocities and as a result the boundary layer thickness and the velocity profiles at the three sections 1,2 and 3 at the toe of the spillway were not equal. The velocity profiles indicated that for all runs the boundary layer occupied a fraction of the full depth of the flow at the toe of the spillway. This means that in all runs, the state of development of the fast water stream at the toe of the spillway was quasi-potential.

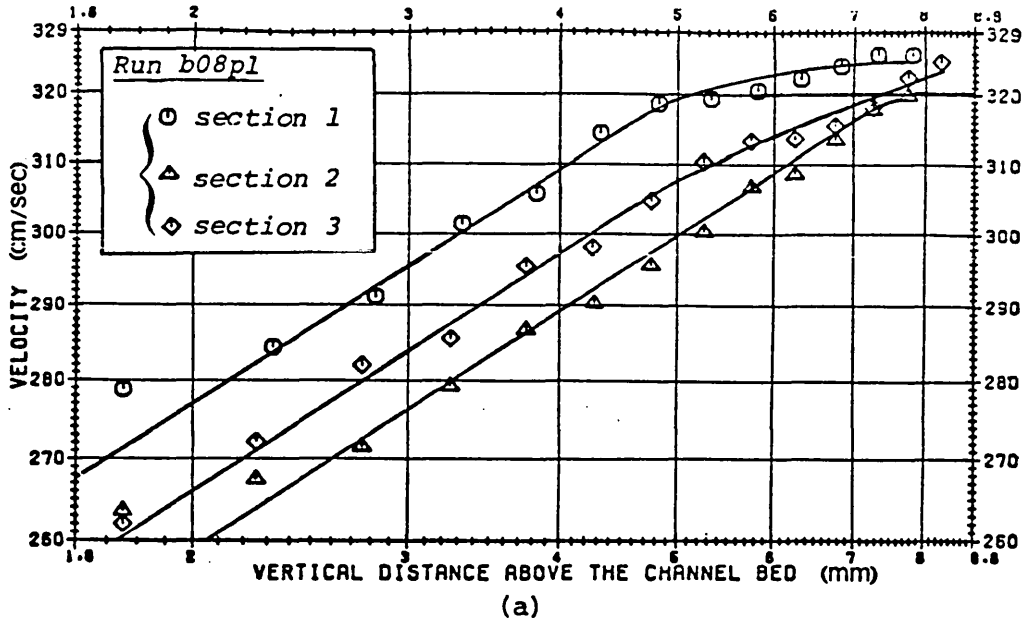


(a)

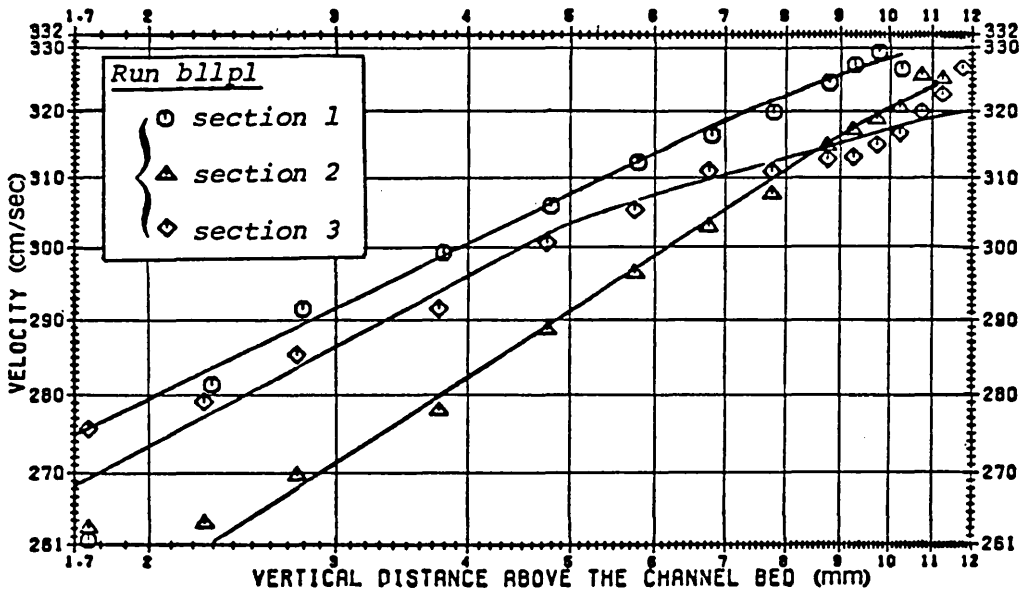


(b)

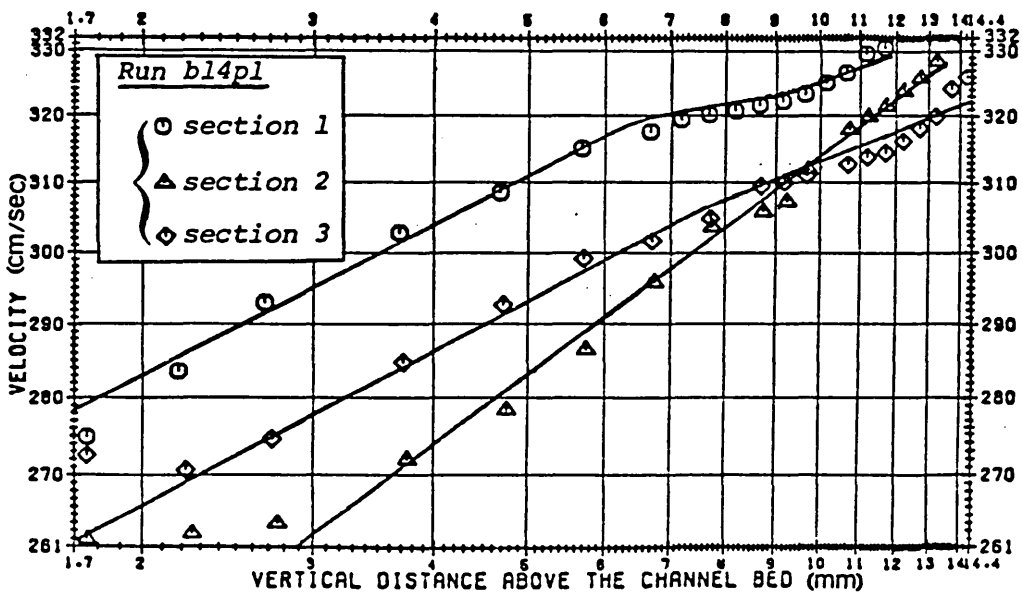


(c)

Fig. F.4 Velocity profiles at section S-S

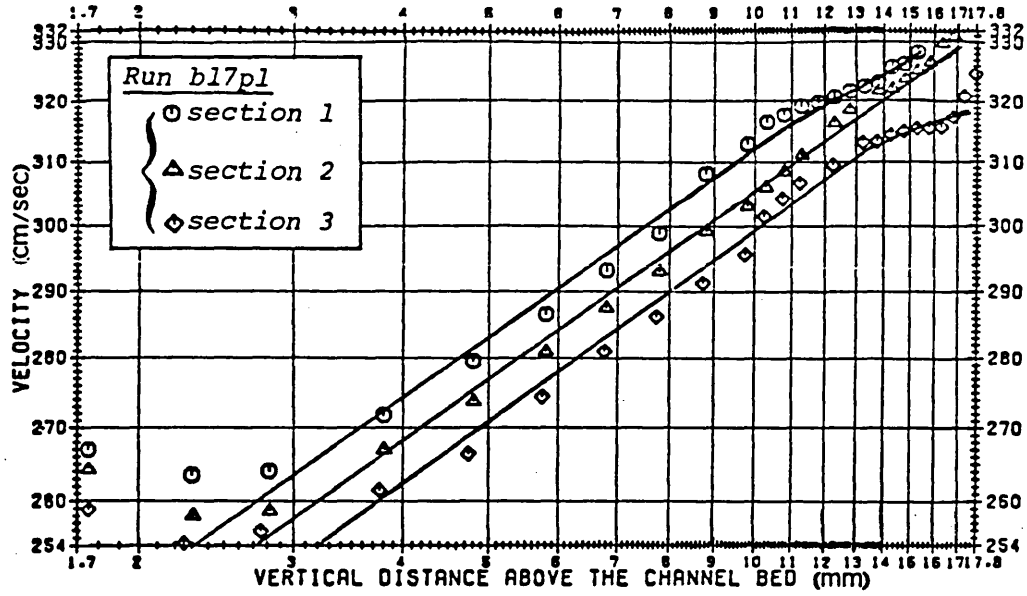


(a)

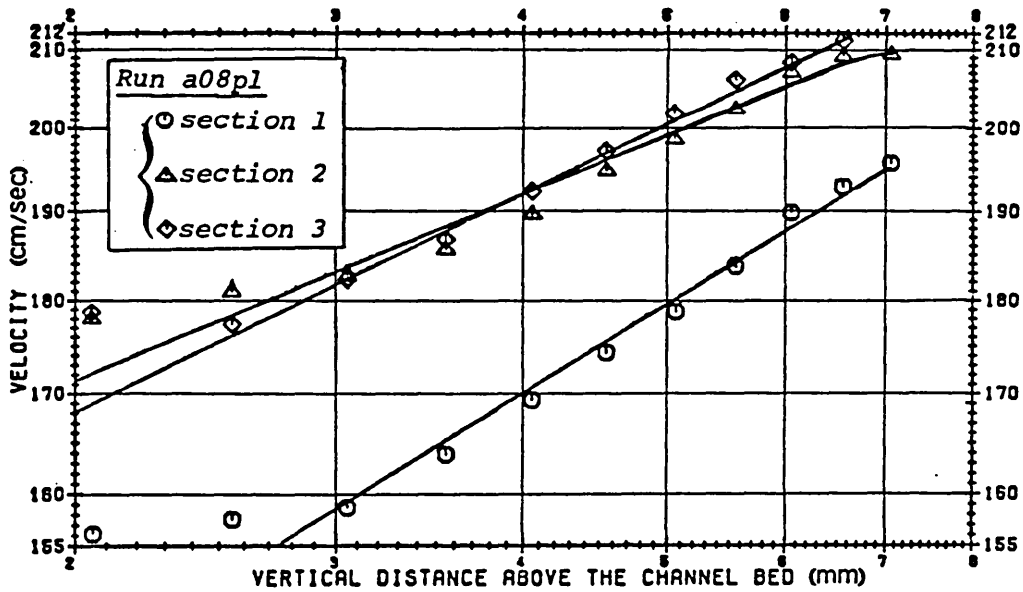


(b)

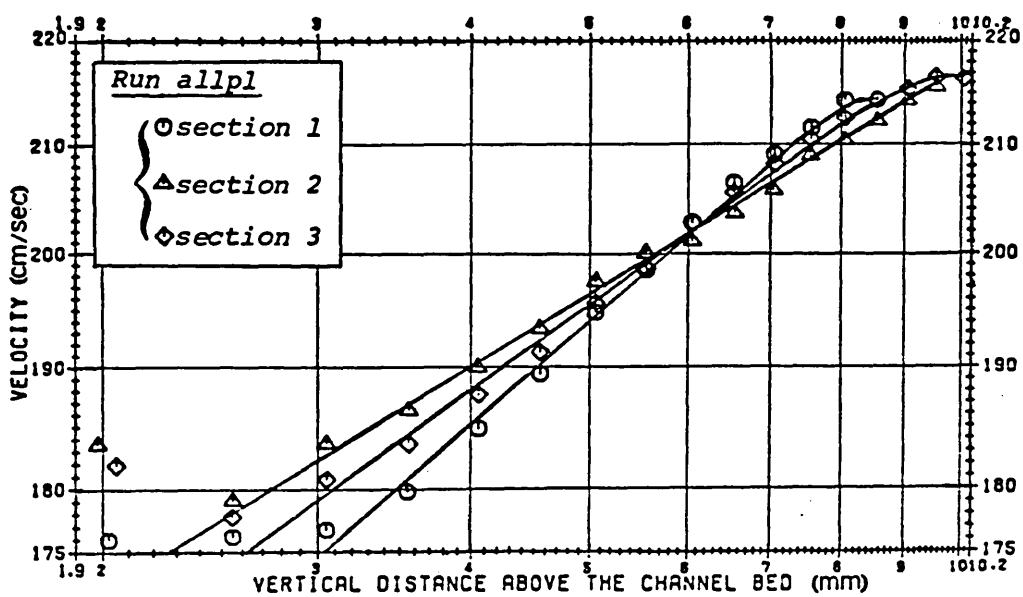


(c)

Fig. F.5 Velocity profiles at section S-S

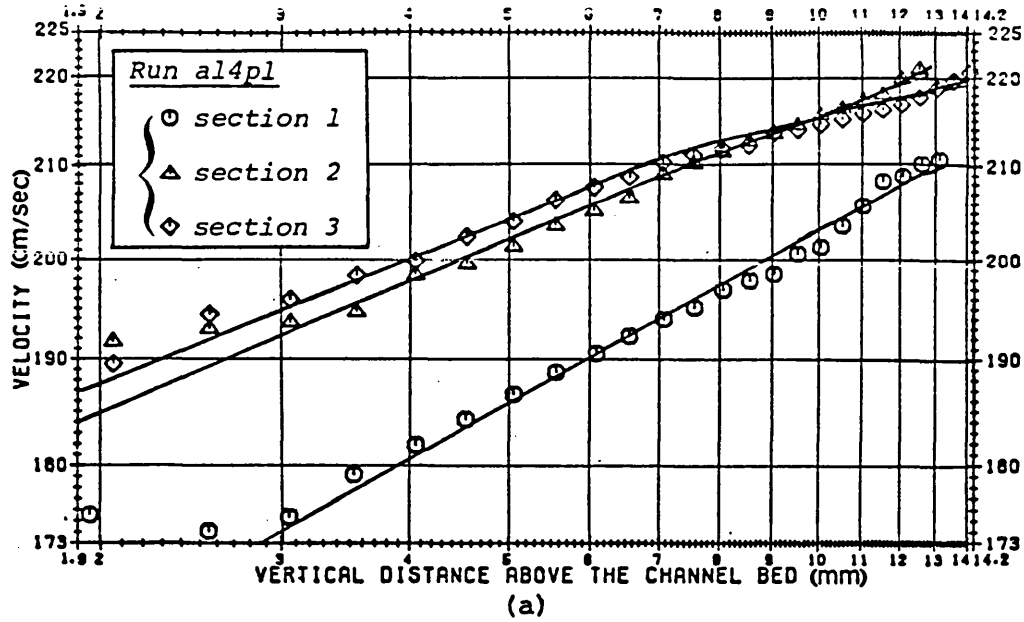


(a)

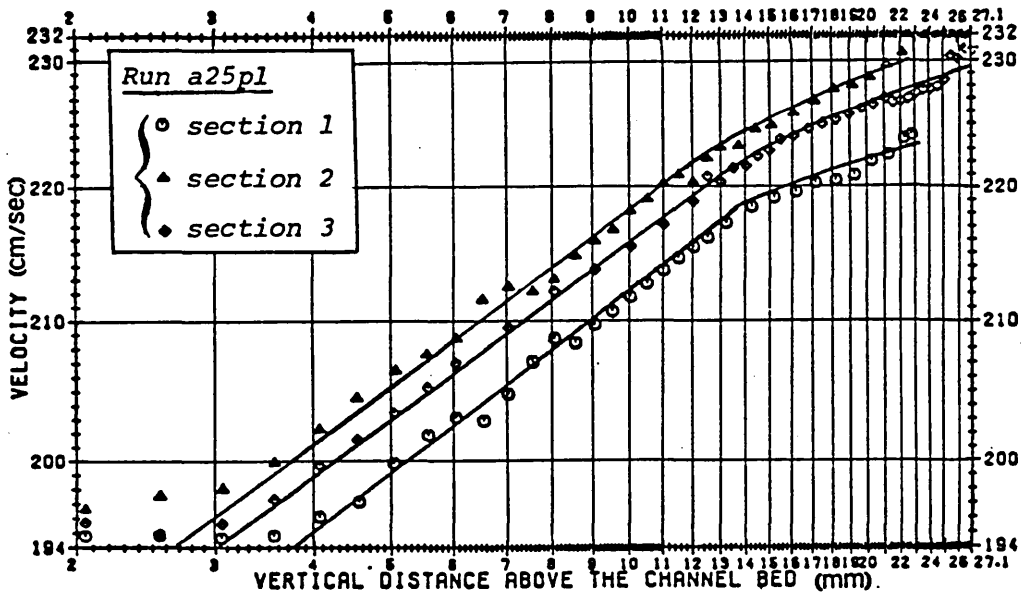


(b)

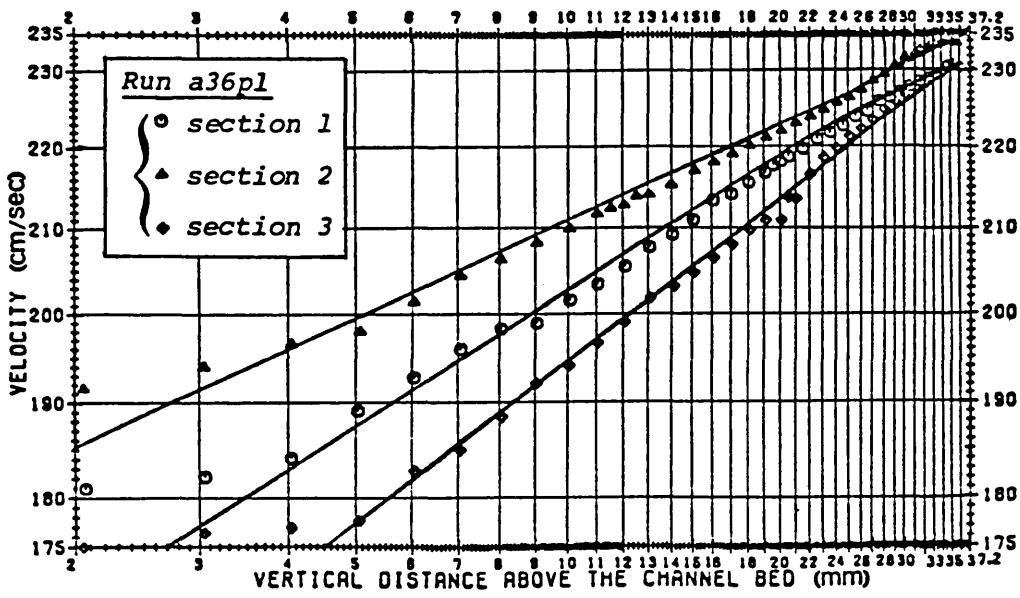


(c)

Fig. F.6 Velocity profiles at section S-S

The coefficients of energy $\alpha$ and momentum $\beta$ can be calculated from Eqs. (B.3) and (B.10). For the flow at the foot of the spillway, these equations can be written in the following form

$$\left.\begin{aligned} \beta &= \frac{\int_A U^2 dA}{U_m^2 A} = \frac{(\sum U^2 \Delta d)_1 + (\sum U^2 \Delta d)_2 + (\sum U^2 \Delta d)_3}{3 U_m^2 d_m} \quad \text{(a)} \\ \alpha &= \frac{\int_A U^3 dA}{U_m^3 A} = \frac{(\sum U^3 \Delta d)_1 + (\sum U^3 \Delta d)_2 + (\sum U^3 \Delta d)_3}{3 U_m^3 d_m} \quad \text{(b)} \end{aligned}\right\} \text{(F.8)}$$

where

$U$ = velocity of the flow at a distance y from the channel bed

$U_m$ = average velocity of the flow over full cross-section

$A$ = cross-sectional area of the flow

$d_m$ = depth of the flow on the channel centre line

$\Delta d$ = depth interval of velocity measurement which was usually 0.5 mm and occasionally 0.7 or 1 mm.

subscript 1 = represents the section which was close to the channel outlet

subscript 2 = denotes the channel centre line section

subscript 3 = represents the section which was close to the side wall

It should be noted, however, that the side walls of the spillway produced small cross waves which were superimposed on the general downstream motion. This was manifested as small pulsations of the water surface in region I. Due to this effect, velocity measurements at the points very close to the water surface in region I were not possible. However, to obtain the average water depth at each section of 1,2 and 3 at the toe of the spillway, which was necessary for the evaluation of the coefficients energy $\alpha$ and momentum $\beta$, the depth measurement at each section was repeated at least three times and the arithmetic mean of the measurements was considered as the reliable value for that section. For the calculation of $\alpha$ and $\beta$, the velocity profile of each section 1,2 and 3 at the toe of the spillway was extrapolated to the average depth of flow at that section. The values of $\alpha$ and $\beta$ associated with the supercritical water flows at the toe of the spillway are tabulated in Table F.1. In this table, it can be seen that in each group of experiments *a* and *b*, the magnitudes of the coefficients $\alpha$ and $\beta$ at the foot of the spillway decreased as the discharge increased (or alternatively the depth of the flow at the toe of the spillway increased).

| Run | a08p1 | a11p1 | a14p1 | a25p1 | a36p1 | b08p1 | b11p1 | b14p1 | b17p1 |
|---|---|---|---|---|---|---|---|---|---|
| β | 1.09 | 1.06 | 1.05 | 1.03 | 1.02 | 1.07 | 1.05 | 1.04 | 1.04 |
| α | 1.24 | 1.16 | 1.12 | 1.07 | 1.06 | 1.19 | 1.14 | 1.11 | 1.09 |

Table F.1 Coefficients of energy and momentum

F.2.2.1 Power Law Applied to the Velocity Profiles in Region I

The experimental data in Figs. F.4,F.5 and F.6 indicate that the shape of the velocity profile in the turbulent boundary layer in region I can be approximated satisfactorily by a power law of the form

$$U=cy^{n} \tag{F.9}$$

where U is the velocity at a distance y above the channel bed, $n$ is an exponent and c is a constant. However, the experimental points that occur in the proximity of the channel bed clearly show some deviation from this power law. The reasoning behind this is that the power law cannot be applied to the region immediately adjacent to the channel bed. It is especially true at the channel bed where, for example, the shear stress $\tau_o$ calculated on the basis of the power law becomes

$$\tau_o = \left(\frac{\mu \partial U}{\partial y}\right)_{y=o} = \left(\mu c n y^{n-1}\right)_{y=o} = \infty \tag{F.10}$$

where μ is coefficient of viscosity. Furthermore, immediately adjacent to the bed is the laminar sub-layer and it is usual to assume that since the laminar sub-layer is so thin, its velocity profile can be taken as linear and tangential to the power law profile at the point where the laminar sub-layer merges with the turbulent part of the boundary layer.

For a given flow depth at the toe of the spillway, the velocity profiles of the group of experiments *b* show, in most cases, lower values for $n$ than the corresponding flow depth belonging to group *a*. In most cases, $n$ decreases gradually as the Reynolds number $R_\delta$ (based on the length along the spillway) increases, varying approximately from a minimum of $\frac{1}{11}$ to a maximum of $\frac{1}{5}$. The average $n$ for the experiments is $\frac{1}{6.8}$ which indicates that the average behaviour of the boundary layer is in quite close agreement with $\frac{1}{7}$ power law.

It is difficult, however, to explain the deviation of the velocity profiles from the one-seventh power law although the pressure gradient was negligible and the Reynolds number $R_\delta$ for all runs remained less than $10^7$. The boundary layer development in region I was more complicated and in many respects was different from that of the classical flat plate in an unconfined fluid under zero pressure gradient. In the former case, first, the depth of the supercritical water flow is a finite quantity as opposed to the somewhat vague parameter assumed for the flat plate case. Secondly, there is no infinite stream above the boundary layer to maintain the motion or secondary motions to affect the distribution of velocities and the boundary layer thickness. Thirdly, due to the existence of a free surface, the gravity forces are important. Furthermore, a new condition must be satisfied, namely, that the discharge per unit width in the downstream direction along the channel centre line in region I must remain constant (the loss of discharge due to the redirection of the flow can be assumed to be negligible). The constancy of discharge may be combined with the boundary layer displacement thickness. That is

$$q = \int_0^h U\,dy = \int_0^h (U-U^*)\,dy + U^*h \qquad \text{(F.11)}$$

where $q$ is the discharge per unit width, $U$ is the velocity at a distance $y$ above the channel bed, $h$ represents the flow depth and $U^*$ denotes the velocity at the edge of the boundary layer. By virtue of the definition of the displacement thickness

$$q = U^*(h-\delta_d) \qquad \text{(a)}$$

or

$$\delta_d = h - \frac{q}{U^*} \qquad \text{(b)} \qquad \text{(F.12)}$$

This means that in region I, the displacement thickness had a larger effect on the outside flow because it acted on a finite depth of water, whereas in an infinite flow, the effect of the displacement thickness is negligible as far as the change in the potential flow pattern is concerned. It is these aspects that make the boundary layer development in region I different from that along a flat plate in an unconfined fluid under zero gradient.

As the boundary layer moves along the channel bed, the continual action of the shear stress tends to cause the thickness of the boundary layer to increase from the toe of the spillway in the downstream direction. Fig. F.7 shows the time mean veloctiy distributions along the channel centre line, at the toe of the spillway and at a section very close to the toe of the forced hydraulic jump; in addition there are some experimental velocity points at the toe of the forced hydraulic jump itself. In this figure x denotes the longitudinal distance from the retaining wall in the upstream direction. Due to the negligible pressure gradient in the downstream direction in region I, the boundary layer growth in this region is slow with the flow having an accelerative characteristic in the boundary layer. The flow outside the boundary layer introduced momentum into the layer. The velocity gradient in the outside boundary layer of the section close to the forced hydraulic jump was much more than that of the boundary layer. This could also be due to the proximity of the section to the forced hydraulic jump. At the end of the region I (toe of the forced hydraulic jump) the flow decelerated due to the existence of the adverse pressure gradient and the expansion of the fast water stream.

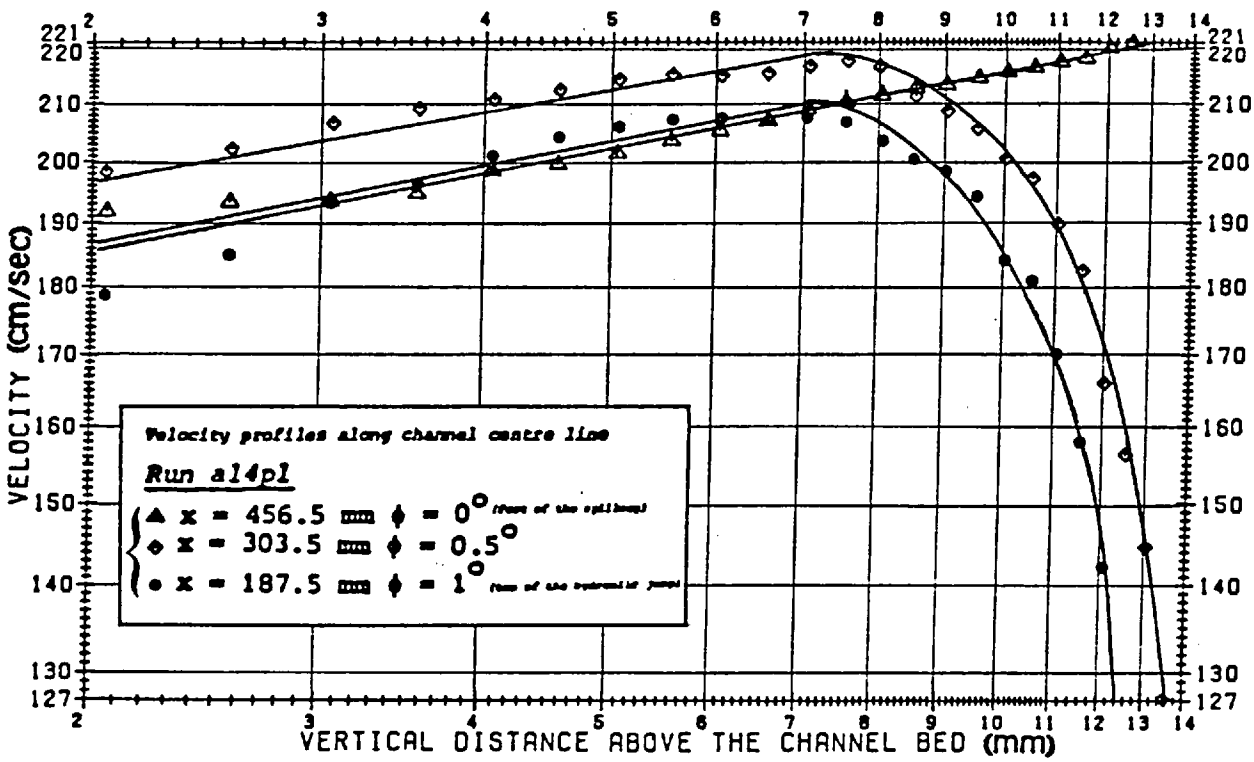


Fig. F.7 Velocity profiles in region I

F.2.3 Nominal Boundary Layer Thickness at the Toe of the Spillway

The formulae which have been developed for the computation of the boundary layer growth on the spillways are all very approximate. Application of these formulae in model studies could lead to serious error in the calculation of the boundary layer thickness as the supercritical flow depths in laboratory channels are usually small. Bauer (1954), for example, presented the following empirical formula for the variation of the boundary layer thickness on spillways

$$\frac{\delta}{x_\delta} = 0.039\ R_\delta^{-0.097} \qquad \text{(F.13)}$$

where $\delta$ is the nominal thickness of the boundary layer, $x_\delta$ is a straight line length beginning from an arbitrary point upstream from the spillway crest and $R_\delta$ represents the Reynolds number based on the length along the spillway.

However, Bauer's formula is very approximate; and this can be seen by the large scatter of the experimental points around the Bauer's curve in his published work on spillways. Moreover, Bauer's formula has been questioned by many authors (Campbell, Cox and Boyd, 1965) because of the lack of an exact definition for the origin of $x_\delta$, i.e., where the turbulent boundary layer actually starts. However, just for the sake of comparaison between the observed turbulent boundary thickness and the predicted value using Bauer's method, a detailed calculation of the nominal boundary layer thickness at the foot of the spillway for run *b14p1* is described here

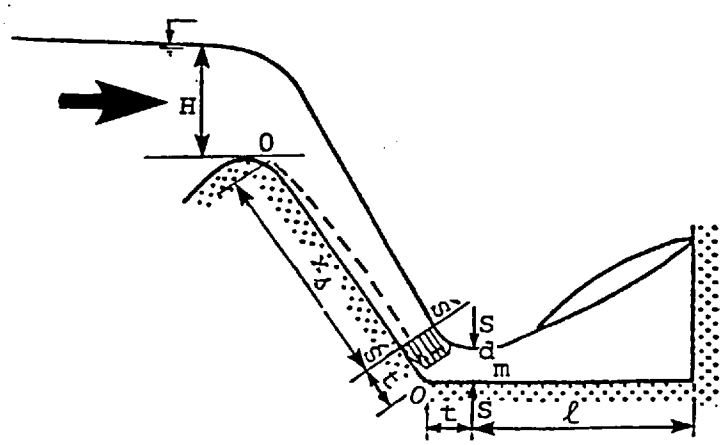


Fig. F.8 Boundary layer development on the spillway.

Fig. F.8 is the schematic representation of the boundary layer development on the spillway. As the distance from the spillway crest increased, the thickness of the boundary layer increased, while the near-potential layer was reduced in thickness. It was assumed that the origin of $x_\delta$ lies along the intersection of the spillway face with the horizontal line tangent to the spillway crest and that the turbulent boundary started from this origin. Furthermore, it was assumed that the flow depth and the boundary layer thickness at the section S-S situated at the toe of the spillway was equal to the corresponding depth and boundary layer at section $\acute{S}$-$\acute{S}$ on the spillway face, where $\acute{S}$-$\acute{S}$ and S-S were equidistant from the intersection of the channel bed and the spillway face. The main flow outside the boundary layer was governed by the Bernoulli equation

$$H+x_\delta \sin\theta = \frac{U^{*2}}{2g}+d_m\cos\theta \qquad \text{(a)}$$

or

$$U^*=\sqrt{2g(x_\delta\sin\theta+H-d_m\cos\theta)} \qquad \text{(b)} \qquad \text{(F.14)}$$

where g is the acceleration due to gravity, $d_m$ is the depth of the supercritical water flow at the toe of spillway along the channel centre line, H is the head above the spillway crest, $\theta$ is the angle between the spillway face and the horizontal, $U^*$ is the velocity in the main potential region and $x_\delta$ is the longitudinal distance along the spillway from the origin O (Fig. F.8). In run *b14p1*, the values of the parameters of Eq. (F.14b) are as follows

$$H = 76.4\text{mm} \qquad \text{(a)}$$

$$d_m = 13.9\text{mm} \qquad \text{(b)}$$

$$\theta = 62.5^\circ \qquad \text{(c)}$$

$$x_\delta = [519-(480-456)\sin 62.5]/\sin 62.5 = 561\text{mm} \qquad \text{(d)} \qquad \text{(F.15)}$$

From Eq. (F.14b), it follows that

$$U^*=334\text{cm/sec} \qquad \text{(a)}$$

Hence

$$R_\delta = U^*x_\delta/\nu = 163\ 6450 \qquad \text{(b)} \qquad \text{(F.16)}$$

and from Eq. (F.13), it is concluded that

$$\delta = 5.5\text{mm} \qquad \text{(F.17)}$$

In many cases, including the aforementioned run, the difference between the boundary layer thickness based on Bauer's method and the observed value (based on the presence or absence of any variation in manometer readings over the long time interval) was found to be approximately equal to the diameter of the pitot-static tube. It must be mentioned, however, that the boundary layer thickness was unimportant as far as the calculation of coefficients of energy and momentum was concerned.

## F.3 FLOW CHARACTERISTICS OF REGIONS II AND III

### F.3.1 Bed Pressure Field in Regions II and III

The pressure on the bed was measured by means of the piezometric tapping points provided on the channel bed. Fig.F.9 shows a typical bed pressure field in regions II and III. In this figure, section 1 corresponds to the row of the pressure taps which was close to the channel outlet, section 2 represents the row of pressure taps which was positioned along the channel centre line, section 3 denotes the row of the pressure taps which was close to the side wall and $L_j$ represents the jump length (the distance between the toe of the forced hydraulic jump and the retaining wall). Fig.F.9 clearly indicates that the pressure on the channel bed was adverse in the downstream

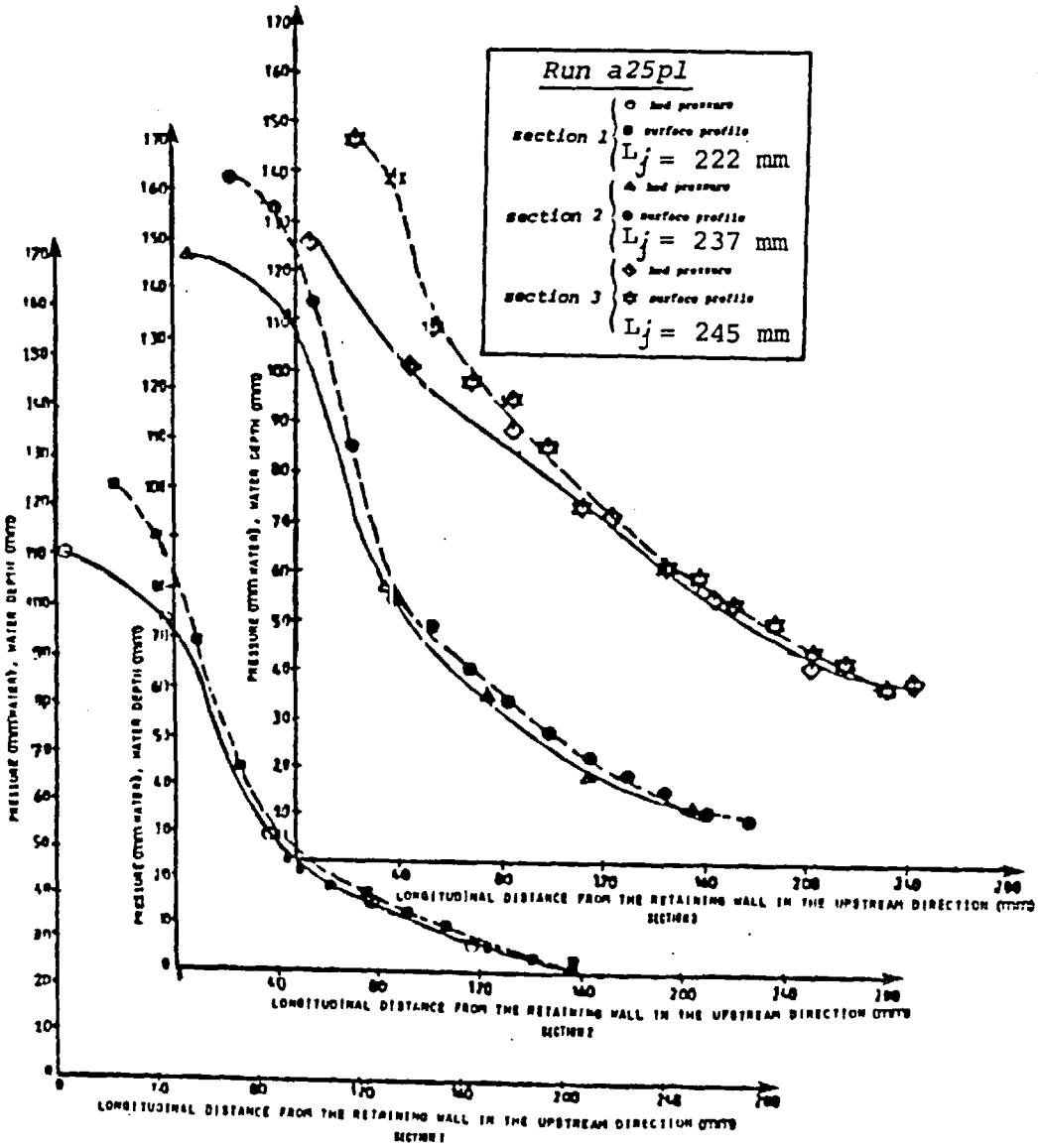


Fig. F.9 Bed pressure and surface profiles in region II and III

direction. Furthermore, apart from a region very close to the retaining wall, in a transverse cross-section (section parallel to the retaining wall), the bed pressure along section 1 was considerably lower than that along sections 2 and 3. In the impingement region, however, the bed pressure on the channel centre line was greater than those of the two other sections. This is because at the middle of the retaining wall, the forward flow along the channel centre line (which had a negligible redirection) interacted with the flow that was redirected from the area adjacent to the side wall.

The surface profiles in regions II and III along the three sections 1,2 and 3 were measured by means of the point gauge. However, because of the fluctuation of the water surface, the surface measurement at any location was repeated at least three times and the arithmetic mean of the three measurements was considered as the reliable value. It can be seen from Fig.F.9 that apart from a region close to the retaining wall, the observed surface profiles lie somewhat above the bed pressure profiles.

### F.3.2 Pressure Field

In this investigation, it was assumed that the pressure distribution in region II was hydrostatic. However, it appeared difficult to accept this assumption in view of the flow curvature and the air entrainment in the forced hydraulic jump. To resolve this doubt, a detailed study was made of the static pressure field for run *b08p1*. The pressure at various points was measured by the use of the static openings of the pitot-static tube which was used for the velocity measurements.

With regard to the pressure field measurements by the pitot-static tube, it is known that the static reading is somewhat sensitive to the angle of yaw if this angle is greater than approximately $12^{\circ}$. In region II, the angle of attack to the horizontal pitot-static tube could only be in excess of this value in a region far away from the channel bed and mainly near the top of the forward flow where the velocity vectors were considerably inclined with respect to the channel bed. Fig.F.10 shows a typical pressure field in region II. In this figure x denotes the longitudinal distance from the retaining wall in the upstream direction. However, although the measurements shown in this figure cannot be regarded as very accurate because of turbulence, they are accurate enough to indicate that the pressure distribution was not precisely hydrostatic at all points in the forced hydraulic jump. At the toe of the forced hydraulic jump, the pressure distribution was hydrostatic because the velocity vectors in region I were all parallel to the channel bed. However, the static pressure distribution in region II may be represented by a curve as shown in Fig.F.11

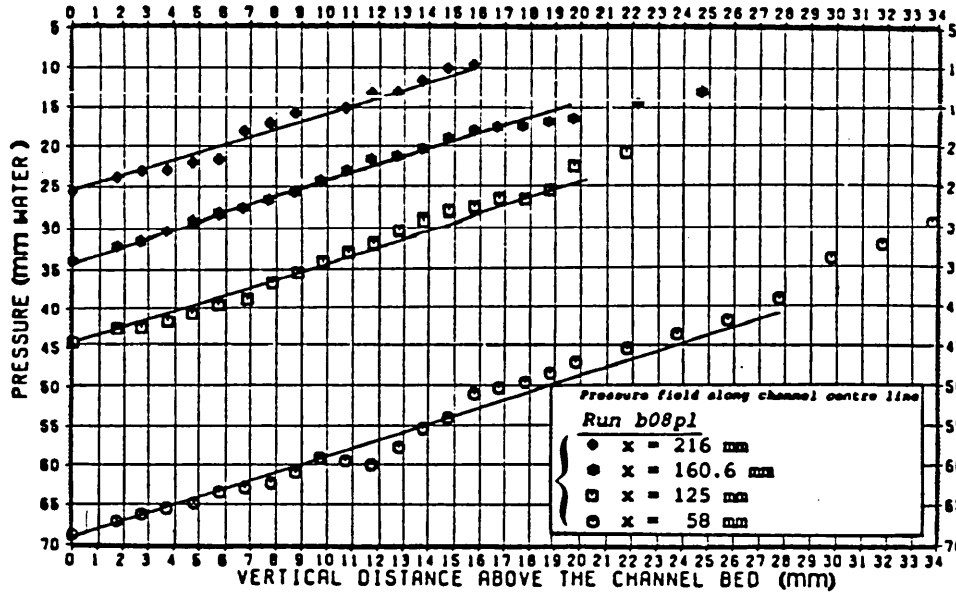


Fig. F.10 Pressure field in region II.

In this figure y is the vertical distance above the channel bed, p is the corresponding static pressure, $h$ is the water depth and p denotes the corresponding bed pressure. The lower part of the static pressure distribution is the normal hydrostatic relationship. Rouse et al. (1959), in their detailed investigation of air hydraulic jumps simulating water counterparts, concluded that the pressure distribution in the hydraulic jump could reasonably be assumed to be hydrostatic and that the quantity of air in suspension was actually insufficient to change appreciably the density. The hydrostatic pressure distribution assumption has been made by many investigators in their studies on different types of hydraulic jumps (McCorquodal and Regts,1968).

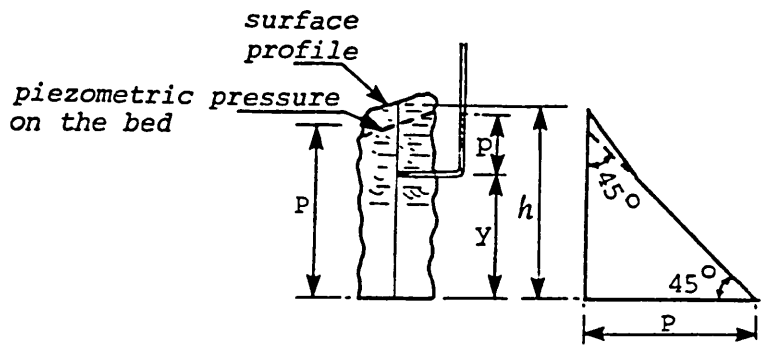


Fig.F.11 Pressure field in region II

### F.3.3 Velocity Distributions in Region II

An extensive investigation of the time mean velocity distribution in region II was performed with the aid of the calibrated pitot-static tube.* With regard to the velocity measurements by the pitot-static tube, first the pitot reading was quite insensitive to the angle of attack. The pitot-static tube gave the resultant velocity at any point and was assumed to be horizontal in this work. This assumption should only be appreciably in error in the region close to the top of the forward flow where the velocity vectors were considerably inclined with respect to the channel bed, and in the backward flow on top. In this investigation, no measurements were made in the backward flow of region II. Secondly, due to the presence of an adverse pressure gradient in region II, a pressure gradient correction, as was defined in Section E.6.5.2, had to be made to the velocity measurements. Thirdly, it was possible that air entrainment in the forced hydraulic jump might interfere with the velocity measurement. For this reason, the flushing arrangement of the pitot-static tube was used except during the time when the observations were being made. It was found that the air bubbles present in the forced hydraulic jump seldom presented difficulties.

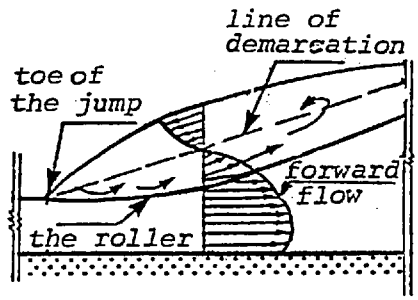


Fig.F.12 Flow in region II

Considering all these aspects, it should be noted that the measured velocities in the region of the line of demarcation (between the forward flow and backward flow Fig.F.12) should be in error because of the pronounced angularity of the flow and the high level of turbulence (average intensity of turbulence in the surface roller is greater than 15% (Resch and Leutheusser, 1971)).

* Laser Doppler Anemometry (L.D.A.) systems are the best available method for measurement of flow velocities without creating any disturbances within the flow. Unfortunately the cost of a complete system was beyond the scope of this research. Attempts at measuring the flow characteristics of a hydraulic jump by means of a hot-film anemometer have not proved to be successful, chiefly because of the presence of air bubbles which form fluid discontinuties.

Figs.F.14 and F. 15 show typical velocity profiles in region II. In these figures, x denotes the longitudinal distance from the retaining wall in the upstream direction. In region II, due to the energy loss and the presence of the adverse pressure gradient in the downstream direction, the flow had a decelerative characteristic over a major part of the forward flow. The maximum velocity of each section, which was an important characteristic of the flow in region II, experiencied the decelerative nature of this region and decreased from the toe of the forced hydraulic jump as it approached the retaining wall. The acceleration in the upper part of the velocity profile was probably due to the behaviour of the surface roller.

A careful study of the time mean velocity profiles in the forward flow of region II revealed that the magnitude of the mean velocity U increased from zero at the channel bed to a maximum velocity $U_{max}$ at $y=\delta$, where y is the vertical distance above the channel bed, it then decreased as y increased becoming zero at some large value of y (Fig.F.13). The

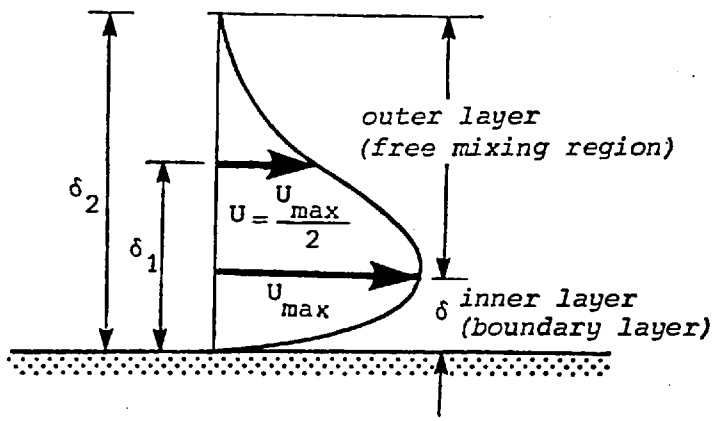


Fig.F.13 Velocity profile in the forward flow of region II.

region from the bed to the maximum velocity level can be called the inner layer or boundary layer since it appears to have a structural similarity to a boundary layer. The region above the boundary layer can be called the outer layer (free-mixing region). These two regions overlap at the point of maximum velocity.

### F.3.3.1 Universal Similarity Curves of the Velocity Distributions in the Forward Flow of Region II

The concept of similarity is of great assistance in synthesizing a large number of mean velocity measurements. For this reason, an attempt was made to discover whether the mean velocity distribution in the forward

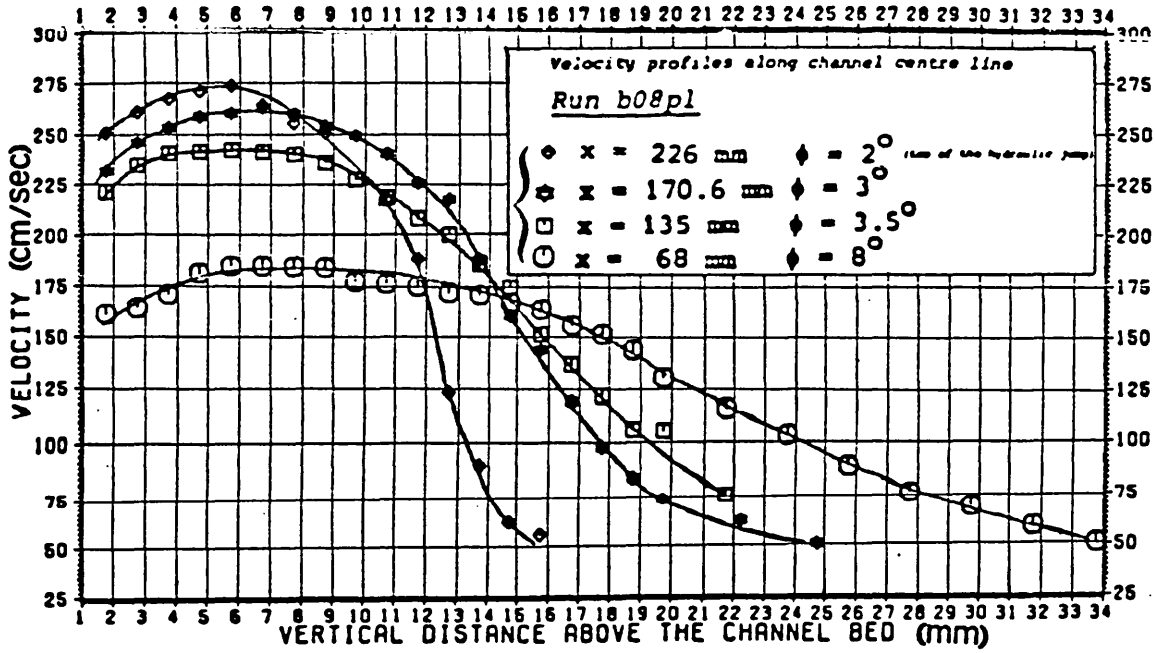


(a)

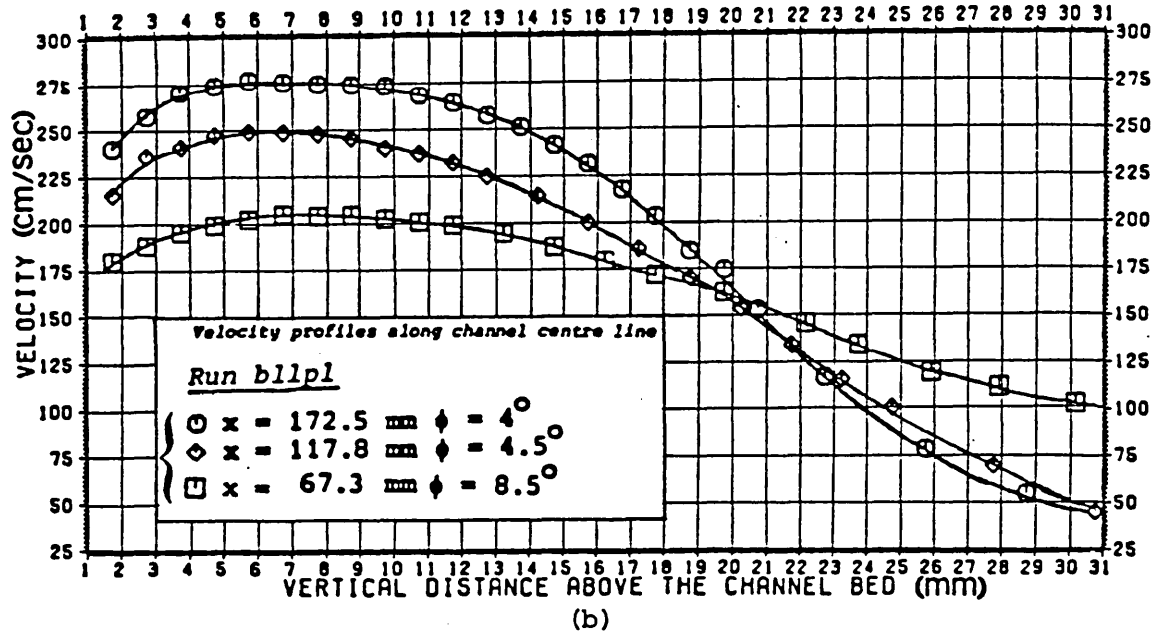


(b)

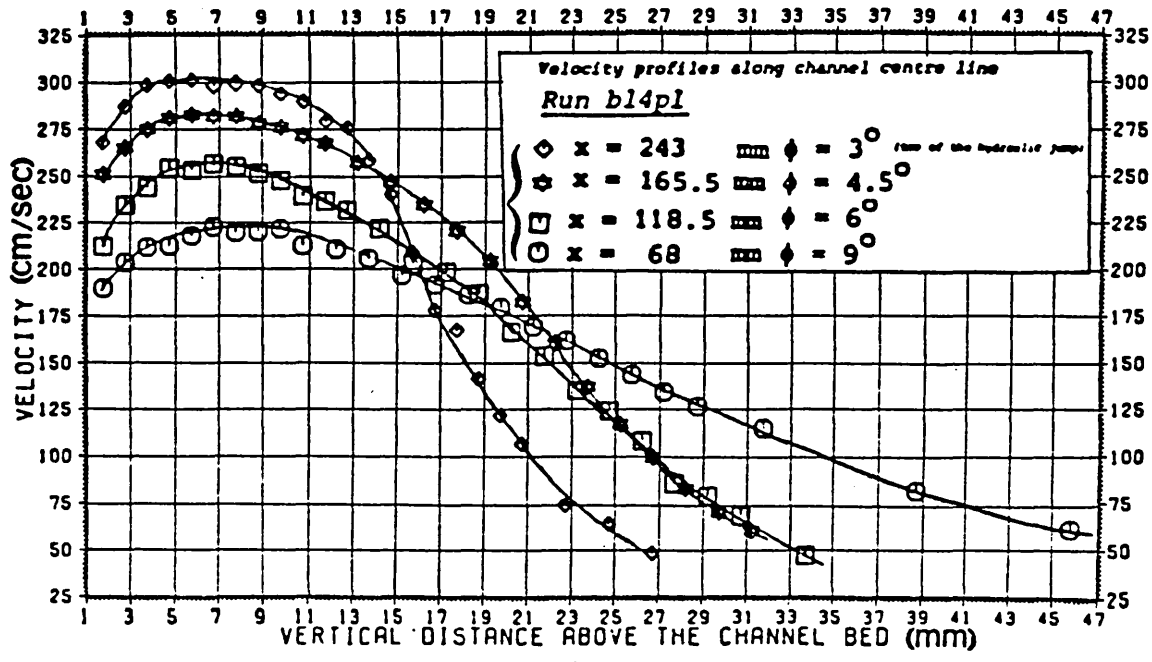


(c)

Fig. F.14 Velocity profiles in the forward flow of region II

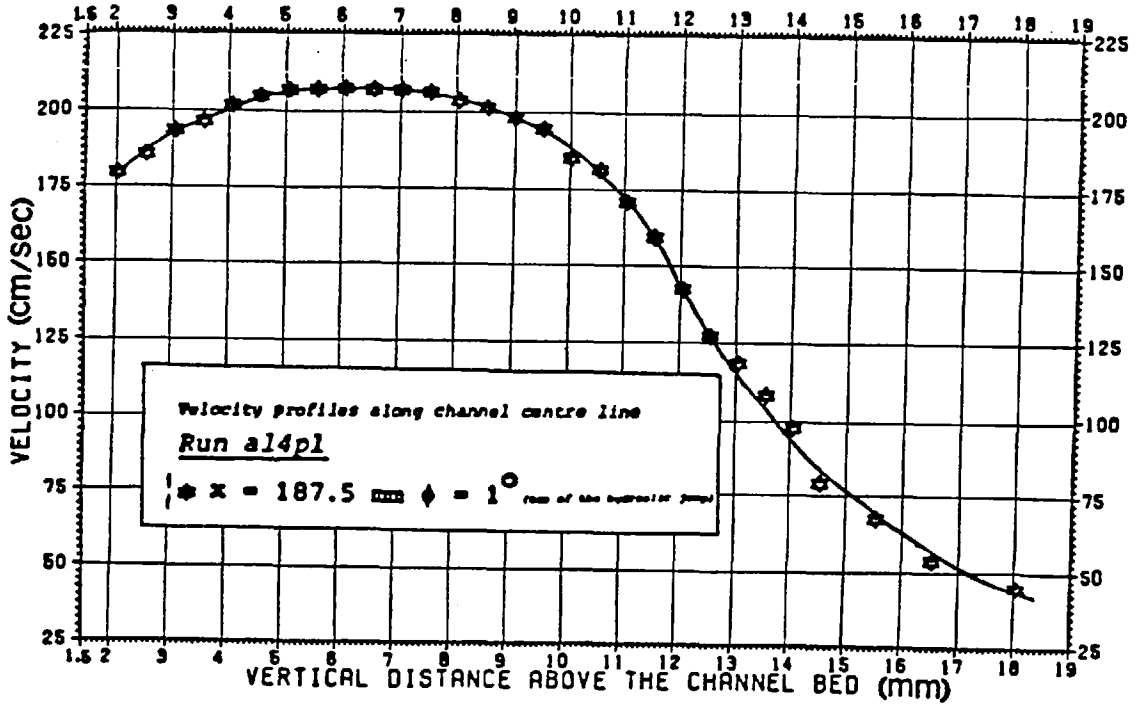


(a)

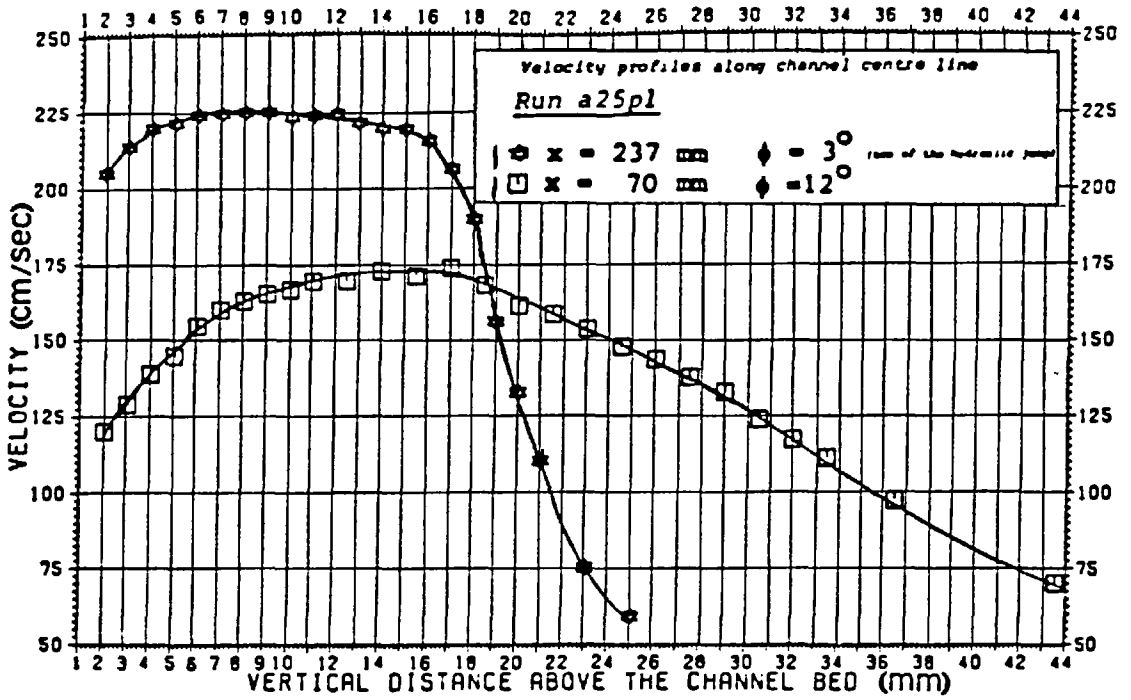


(b)

Fig. F.15 Velocity profiles in the forward flow of region II

flow of region II is self-similar. This was done by replotting the velocity distribution data in a dimensionless form with $U/U_{max}$ versus $y/\delta_1$, in which $U_{max}$ is the maximum velocity at any section; $\delta_1$ is the value of y in which $U=\frac{U_{max}}{2}$ and $\frac{\partial U}{\partial y}$ is negative (Fig.F.16). Generally, $U_{max}$ and $\delta_1$ can be named as the velocity scale and length scale respectively. It was found that the experimental points dictate a well-defined single curve. This implies that the velocity profiles in forward flow are geometrically similar despite the redirection of the forward flow, differing Froude numbers, different states of development... etc at the toe of the spillway. Mathematically, this means that a curve $f(\eta)$ defined as

$$f(\eta)=\frac{U}{U_{max}} \qquad \text{(a)}$$

where

$$\eta=\frac{y}{\delta_1} \qquad \text{(b)}$$

(F.18)

exists whose co-ordinates are constant and independent of the history of the flow. The curve of the plane turbulent wall jet issuing into the same stationary fluid of semi-infinite extent on a smooth boundary under zero pressure gradient, known as the classical wall jet, is also plotted in Fig.F.16. It can be seen that the similarity curve in region II is slightly different from that of the classical wall jet up to $\eta=1$, beyond which it falls off more quickly than the classical wall jet and lies somewhat below this curve, reducing $f(\eta)$ to zero at $\eta=1.5$.

The velocity profiles in the outer-layer region were tested for similarity by plotting $U/U_{max}$ against $\eta=\frac{y-\delta}{\delta_1-\delta}$ along with the corresponding curve of the classical wall jet (Fig.F.17). It can be seen that the mean velocity profiles in the region external to the inner layer are geometrically similar despite the redirection of the forward flow, differing Froude numbers, different states of development...etc. at the toe of the spillway and that the data agree reasonably well with the corresponding curve of the classical wall jet.

It is at first sight surprising that the universal similarity curve of the velocity profiles in the forward flow of region II showed a slight difference from the corresponding curve of the classical wall jet whereas the universal similarity curve of the outer layers showed a reasonably good agreement with that of the classical wall jet. This is probably due to the effect

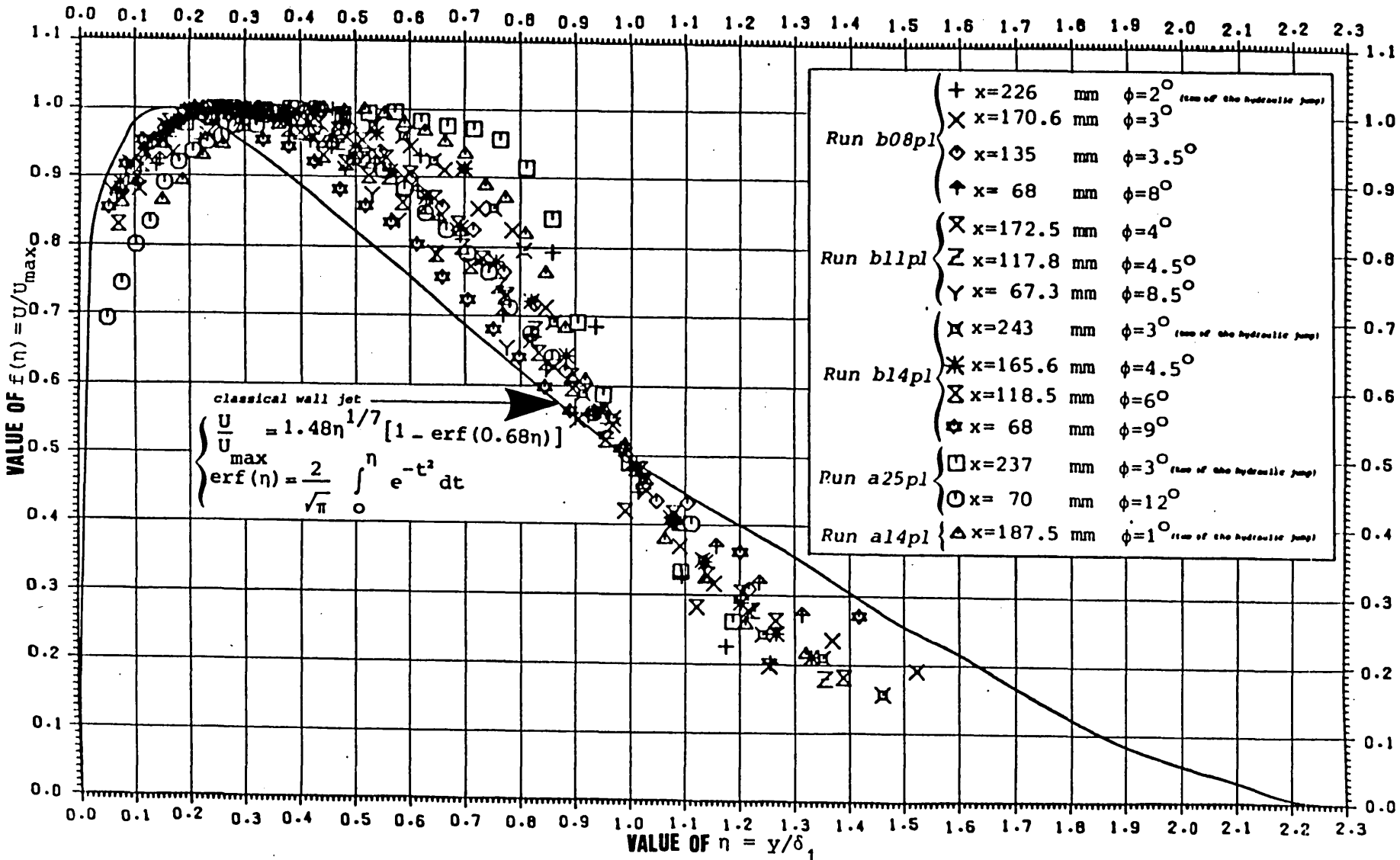


Fig. F.16 Velocity distributions in the forward flow of region II

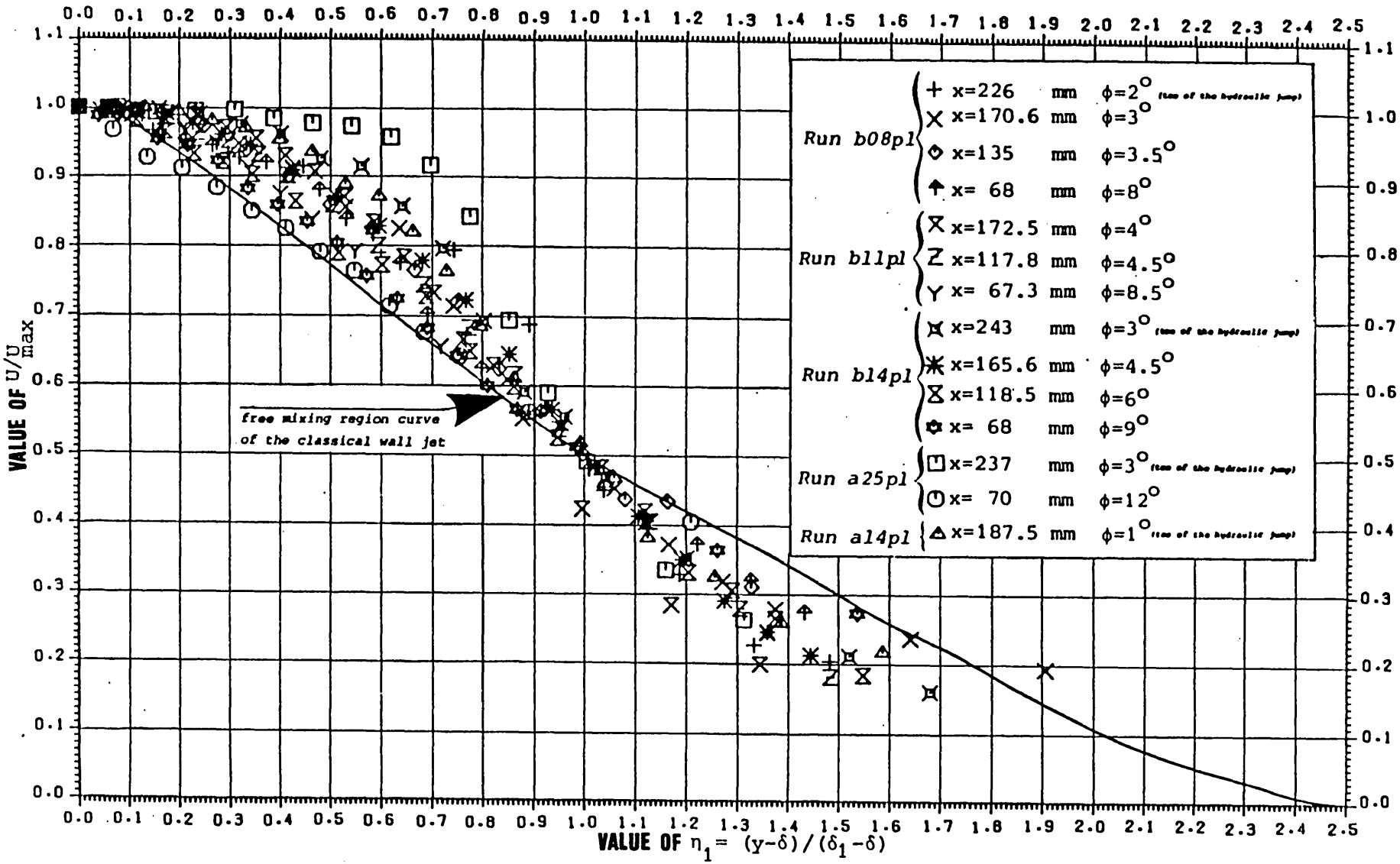


Fig. F.17 Velocity distributions in the outer layer

of the adverse pressure gradient in the downstream direction in region II. The reason is that the adverse pressure gradient decreased the momentum in the boundary layer. This means that although the pressure gradient had practically the same value through the cross section of the flow, its most significant effect was on the water flow close to the channel bed (inner layer). This is because the water flow close to the channel bed had less momentum than the water flow further out.

In the inner layer the mean velocity distribution was approximated to a functional form by Prandtl

$$\frac{U}{U_{max}} = \left(\frac{y}{\delta}\right)^{n} \qquad \text{(F.19)}$$

in which $n$ is an exponent which varies in the streamwise direction due to the pressure gradient (Narayanan, 1975). A reanalysis of the velocity distribution data of all runs in the boundary layer is shown in Fig.F.18,

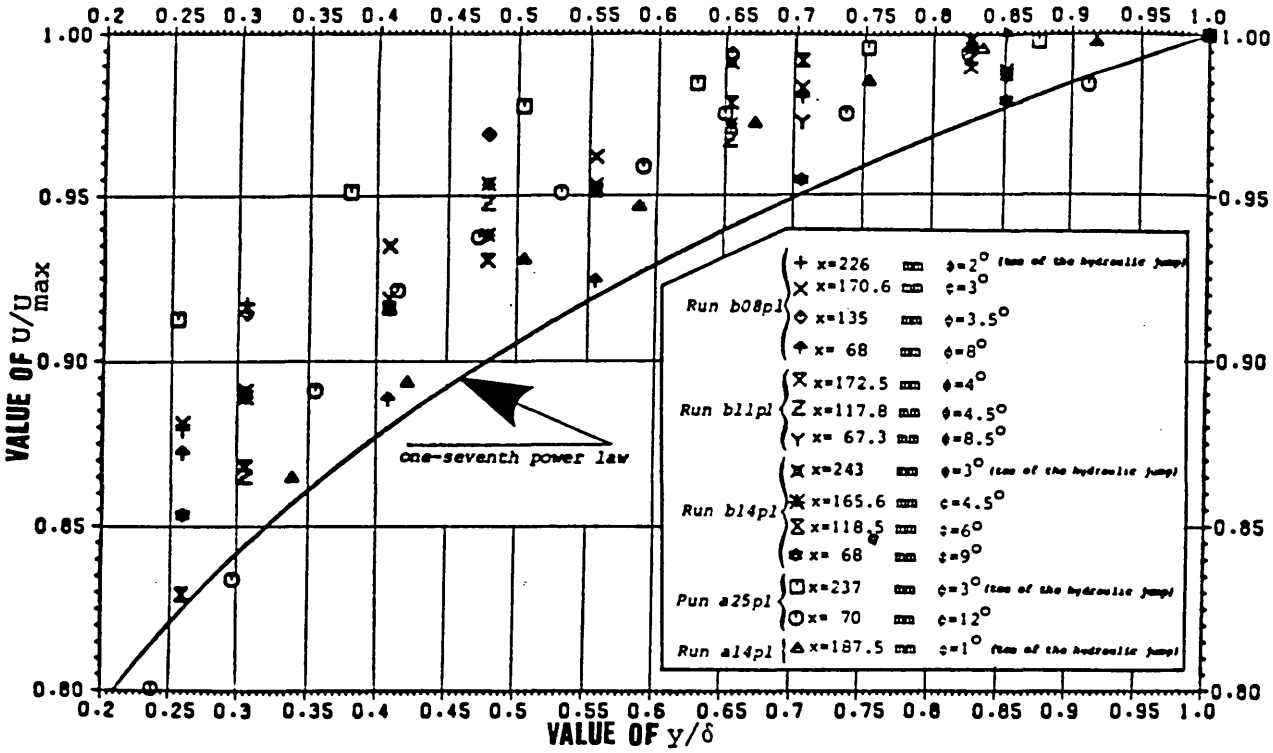


Fig. F.18 Velocity distribution in the inner layer

with $U/U_{max}$ versus $y/\delta$ in conjunction with one-seventh power law curve. It can be seen that for all runs $n$ is less than 1/7. In fact, in the inner layer, the experimental points $U/U_{max}$ versus $y/\delta$ appear to fall into a very thick band which is confined by two power law curves having the exponents equal to approximately 1/8 and 1/14 (Fig.F.19).

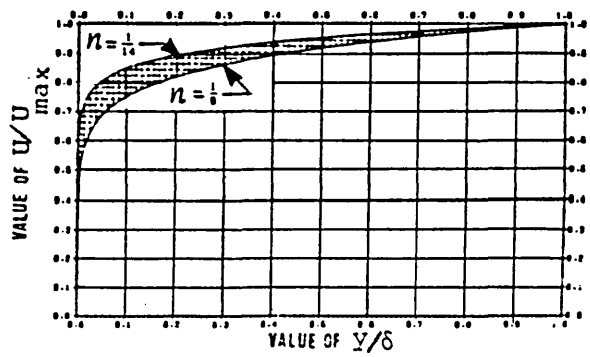


Fig. F.19 Velocity distribution in the inner layer

### F.3.3.2 Variation of the Velocity Scale and the Length Scale

Earlier in this thesis it was concluded that redirection of the forward flow along the channel centre line in region II was a minor feature of the flow. Hence, for practical purposes, it could be assumed that the forward flow per unit width along the channel centre line remained parallel to the channel centre line.

The maximum velocity $U_{max}$ at any section was an important characteristic of the flow in region II. The variation of $U_{max}/U_m$ with $x_j/d_m$ is shown in Fig. F.20, in which $U_m$ is the average velocity of supercritical water flow at the toe of the spillway, $x_j$ is the longitudinal distance from the toe of the forced hydraulic jump in a downstream direction along the channel centre line and $d_m$ is the depth of the supercritical water flow at the toe of the spillway along the channel centre line. The corresponding

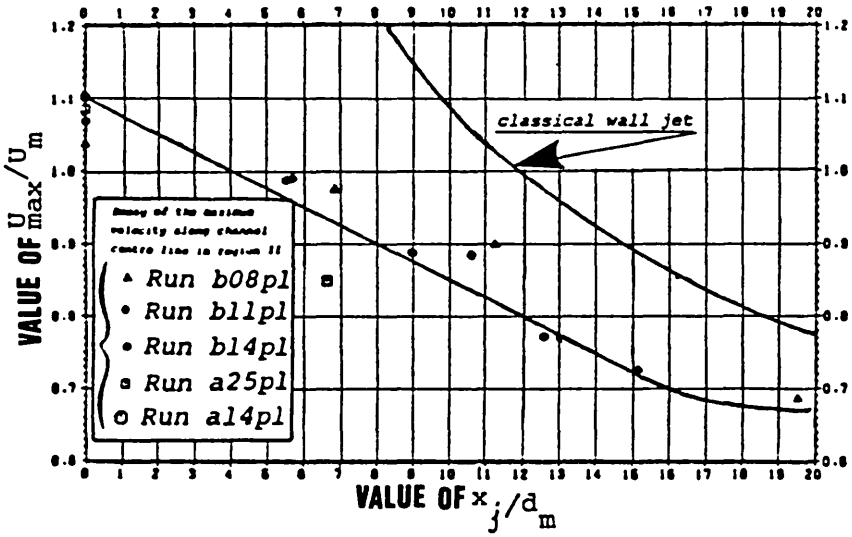


Fig. F.20 Variation of the velocity scale

curve for the classical wall jet is also plotted on this graph. It can be seen that the rate of decay of the maximum velocity in region II is faster than that of the classical wall jet. This indicates the efficiency of energy dissipation in the forced hydraulic jump.

The variation of the dimensionless length scale $\delta_1/d_m$ with $x_j/d_m$ together with the corresponding curve for the classical wall jet is shown in Fig.F.21. From this figure, it can be seen that, due to the presence of an adverse pressure gradient, $\delta_1/d_m$ increases faster than in the case of the classical wall jet. This means that the maximum velocity in region II, which already decayed at a faster rate than the corresponding rate for the classical

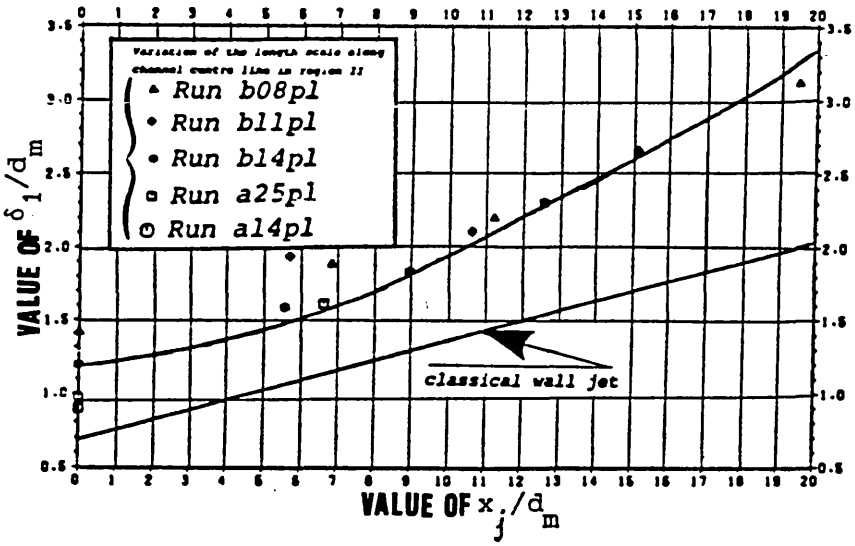


Fig. F.21 Variation of the length scale

wall jet, was also located at a height above the bed which was greater than the corresponding height for the classical wall jet. This point is of great significance in the reduction of bed scour.

### F.3.3.3 Prediction of the Surface and Energy Profiles

The procedure required to predict the surface profile and energy profile of region II along the channel centre line is based upon the following assumptions

a) the friction at the channel bed is negligible.

b) the momentum and energy associated with the backward flow of the surface roller is negligible when compared with corresponding quantities for the forward flow. This assumption has been found to be approximately true for a submerged hydraulic jump. (Lieu,1949).

c) despite the observations shown in Fig.F.11, the pressure distribution is assumed to be hydrostatic over all the forced hydraulic jump.

d) the loss of momentum and energy per unit width of the channel in the downstream direction along the channel centre line due to the redirection of the flow is negligible. This is because the redirection of the flow in region I and in the forward flow of region II along the channel centre line was negligible.

At the toe of the spillway, the pressure force plus the momentum per unit width $m_o$, and the specific energy $e_o$ can be written as

$$m_o = \tfrac{1}{2}\rho g d_m^2 + \beta \rho U_m^2 d_m \quad \text{(a)}$$

$$e_o = d_m + \alpha U_m^2 / 2g \quad \text{(b)} \qquad \text{(F.20)}$$

where $U_m$, $d_m$, $\beta$ and $\alpha$ are the average velocity, the average depth along the channel centre line, the momentum coefficient and the energy coefficient respectively of the supercritical flow at the toe of the spillway, $\rho$ denotes the mass density and g represents the acceleration due to gravity. Eq. (F.20b) can be rewritten in a simpler form

$$e_o = d_m (1+0.5 F_r^2) \qquad \text{(F.21)}$$

where Fr is the Froude number of the incoming supercritical water flow. At a section located on the channel centre line and at a distance $x_j$ from the beginning of the forced hydraulic jump in the downstream direction, the pressure force plus the momentum per unit width $m$ and the specific energy $e$ can be written as

$$m = \tfrac{1}{2}\rho g h^2 + \int_o^{\delta_2} \rho U^2 \, dy \quad \text{(a)}$$

$$e = h + \frac{1}{U_m d_m} \int_o^{\delta_2} \frac{U^3 dy}{2g} \quad \text{(b)} \qquad \text{(F.22)}$$

where $h$ is the water depth at this section, $\delta_2$ is the corresponding thickness of the forward flow and U is the magnitude of the velocity at a distance y above the channel bed at this section. Using the velocity scale $U_{max}$ and the length scale $\delta_1$, the above relationships can be rewritten in the following forms

$$m = \tfrac{1}{2}\rho g h^2 + \rho U_{max}^2 \delta_1 \int_o^{1.5} f^2(\eta) \, d\eta \quad \text{(a)}$$

$$e = h + \frac{U_{max}^3 \delta_1}{2g U_m d_m} \int_o^{1.5} f^3(\eta) \, d\eta \quad \text{(b)} \qquad \text{(F.23)}$$

The integrals in the above relationships were calculated by the use of the trapezoidal rule from the similarity curve in Fig.F.16. The magnitude of the integral of Eq. (23a) was approximately 0.71 and that of Eq. (23b) was 0.6. However based on the aforementioned assumptions, it can be written that

$$m = m_o \quad \text{(a)}$$

or

$$\tfrac{1}{2}\rho g d_m^2 + \beta \rho U_m^2 d_m = \tfrac{1}{2}\rho g h^2 + 0.71 \rho U_{max}^2 \delta_1 \quad \text{(b)} \qquad \text{(F.24)}$$

The expression for the specific energy can be written in a dimensionless form as follows

$$\frac{e}{e_o} = \frac{h + 0.6322 \frac{U_{max}^3 \delta_1}{2g U_m d_m}}{d_m(1+0.5 Fr^2)} \qquad \text{(F.25)}$$

Relationships (F.24b) and (F.25) can be reduced to the following forms

$$\left.\begin{aligned} \left(\frac{h}{d_m}\right)^2 &= 1+2\frac{Fr^2}{\alpha}\left[\beta - 0.71\left(\frac{U_{max}}{U_m}\right)^2\left(\frac{\delta_1}{d_m}\right)\right] \quad \text{(a)} \\ \frac{e}{e_o} &= \frac{\frac{h}{d_m} + 0.3\frac{Fr^2}{\alpha}\left(\frac{U_{max}}{U_m}\right)^3\frac{\delta_1}{d_m}}{1+0.5Fr^2} \quad \text{(b)} \end{aligned}\right\} \text{(F.26)}$$

The above relationships clearly indicate that the surface and energy profiles in region II along the channel centre line are functions of the Froude number. In Section F.4.1.1, a mathematical relationship (Eq.F.40) is presented to aid the prediction of the wave height in the amplitude domain at the middle of the retaining wall. The calculated surface profile at any point from Eq.(F.26a)should be less than the average wave height at the middle of the retaining wall. The above relationships were evaluated for run *a25p1* and are plotted in Figs.F.22 and F.23. The observed surface profile is also plotted in Fig.F.22. It can be seen that for values of $x_j/d_m$ up to approximately 3.5, the predicted points lie slightly above

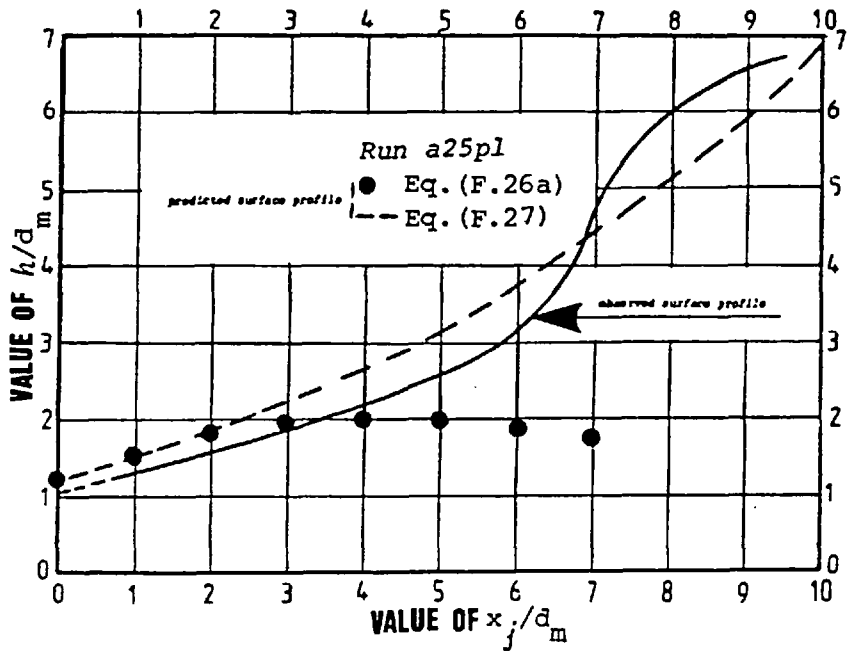


Fig. F.22 Predicted and observed surface profiles

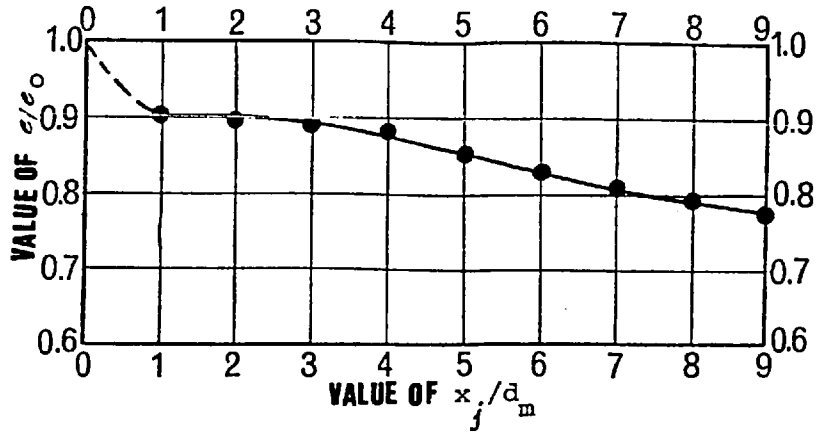


Fig. F.23 Predicted energy profile.

the observed surface profile; beyond this value of $x_j/d_m$ the calculated points occur at considerably lower positions than the corresponding observed surface profile points. The deviation of the predicted surface profile from the observed surface is due to the inherent errors in the four basic assumptions made in this procedure.

The shortcomings of the above method are; firstly, it does not allow for the effect of the changing position of the retaining wall with respect to the spillway in the prediction of the surface and energy profiles of region II, as the friction at the channel bed was assumed to be negligible. Secondly, the above procedure does not give the location of the toe of the forced hydraulic jump,i.e., where the surface profile actually starts .Furthermore, the predicted points of the surface profile close to the end of the region II occur at considerably lower positions than the corresponding observed surface profile points. For practical purposes, however, it can be assumed that the surface profile along the channel centre line from the toe of the forced hydraulic jump to the retaining wall can be approximated by the following dimensionless equation

$$\frac{h-d_m}{d_m} = A_1 \left(\frac{x_j}{d_m}\right)^2 + A_2 \left(\frac{x_j}{d_m}\right)^{\frac{1}{2}} \qquad \text{(F.27)}$$

where $A_1$ and $A_2$ are dimensionless coefficients. These coefficients can be evaluated by using the first two predicted points of the surface profile (Eq.F.26a) corresponding to $x_j/d_m = 1$ and $x_j/d_m = 2$. For run *a25p1* the coefficients of $A_1$ and $A_2$ were found to be equal to 0.043 and 0.47 respectively. Using Eq. (F.40), the average wave height at the middle of the retaining wall was found to be equal to 176mm. The value of $x_j$ from Eq. (F.27) corresponding to $h$=176mm was 256mm. The measured distance of the toe of the forced hydraulic jump from the retaining wall was $L_j$ = 237mm.

It must be mentioned that the description of the surface profile along the channel centre line from the toe of the forced hydraulic jump to the retaining wall by Eq.(F.27) was purely based on observation of the surface profiles for different test runs. Furthermore, the calculation of the energy profile by Eq.(F.26b) is only valid for region II. In region III, the flow suffers from separation and some energy is dissipated by separation.

### F.3.4 Governing Equations of Motion in the Forward Flow of Region II and the Mathematical Condition for Separation

The applicable equations for an analytical description of the forward flow per unit width in region II along the channel centre line are the steady state Reynolds equations and the corresponding continuity equation. Herein the region is considered as an essentially two-dimensional phenomenon in the $x_j$-y co-ordinate system where $x_j$ is the longitudinal distance from the toe of the forced hydraulic jump in a downstream direction along the channel centre line and y is the vertical distance above the channel bed. If U and V are the turbulent time mean velocities in the $x_j$ and y direction respectively, and u and v are the corresponding fluctuations, then the Reynolds equations can be written as

$$\left.\begin{aligned} U\frac{\partial U}{\partial x_j} + V\frac{\partial U}{\partial y} &= -\frac{1}{\rho}\frac{\partial P}{\partial x_j} + \nu\left(\frac{\partial^2 U}{\partial x_j^2} + \frac{\partial^2 U}{\partial y^2}\right) - \left(\frac{\partial \overline{u^2}}{\partial x_j} + \frac{\partial \overline{uv}}{\partial y}\right) \quad \text{(a)} \\ U\frac{\partial V}{\partial x_j} + V\frac{\partial V}{\partial y} &= -\frac{1}{\rho}\frac{\partial P}{\partial y} + \nu\left(\frac{\partial^2 V}{\partial x_j^2} + \frac{\partial^2 V}{\partial y^2}\right) - \left(\frac{\partial \overline{uv}}{\partial x_j} + \frac{\partial \overline{v^2}}{\partial y}\right) \quad \text{(b)} \end{aligned}\right\} \text{(F.28)}$$

in which $\nu$ is the kinematic viscosity and p is the mean pressure at any point. The time-averaged continuity equation is

$$\frac{\partial U}{\partial x_j} + \frac{\partial V}{\partial y} = 0 \qquad \text{(F.29)}$$

With regard to the nature of the forward flow in region II, it can be assumed that, firstly, over a major portion of the forward flow $U >> V$. Secondly, the gradients of the quantities in the y direction are generally much larger than the gradients of the corresponding quantities in the $x_j$ direction, for example $\frac{\partial U}{\partial y} >> \frac{\partial U}{\partial x_j}$. Furthermore, it is assumed that the pressure distribution is hydrostatic over all the forced hydraulic jump.

Using these assumptions, the equations of the motion can be reduced to the form

$$\left.\begin{aligned} U\frac{\partial U}{\partial x_j} + V\frac{\partial U}{\partial y} &= -\frac{1}{\rho}\frac{\partial P}{\partial x_j} + \nu\frac{\partial^2 U}{\partial y^2} - \frac{\partial \overline{uv}}{\partial y} - \frac{\partial \overline{u^2}}{\partial x_j} \quad \text{(a)} \\ 0 &= -\frac{1}{\rho}\frac{\partial P}{\partial y} - \frac{\partial \overline{v^2}}{\partial y} \quad \text{(b)} \end{aligned}\right\} \text{(F.30)}$$

By combining the above equations

$$U\frac{\partial U}{\partial x_j} + V\frac{\partial U}{\partial y} = -\frac{1}{\rho}\frac{dP}{dx_j} + \nu\frac{\partial^2 U}{\partial y^2} - \frac{\partial \overline{uv}}{\partial y} - \frac{\partial}{\partial x_j}(\overline{u^2} - \overline{v^2}) \qquad \text{(F.31)}$$

The last term in the above equation is smaller than the other terms and could be neglected. The fifth term of Eq.(F.31) can be rewritten as

$$-\frac{\partial \overline{uv}}{\partial y} = \frac{1}{\rho}\frac{\partial}{\partial y}(-\rho\overline{uv}) = \frac{1}{\rho}\frac{\partial \tau_t}{\partial y} \qquad \text{(F.32)}$$

where $\tau_t$ stands for the turbulent shear stress. With hydrostatic pressure distribution assumption, the equations of motion reduce to the following form

$$\left.\begin{aligned} U\frac{\partial U}{\partial x_j} + V\frac{\partial U}{\partial y} &= -g\frac{dh}{dx_j} + \nu\frac{\partial^2 U}{\partial y^2} + \frac{\partial \tau_t}{\partial y} \quad \text{(a)} \\ \frac{\partial U}{\partial x_j} + \frac{\partial V}{\partial y} &= 0 \quad \text{(b)} \end{aligned}\right\} \text{(F.33)}$$

where $h$ is the flow depth.

### F.3.4.1 Mathematical Condition for Separation

The adverse pressure gradient in region II decreased the momentum in the boundary layer. The low-velocity water close to the channel bed in the boundary layer had less momentum than that farther away. Towards the end of region II (near the retaining wall), the development of the boundary layer produced a thicker layer due to the steep adverse pressure gradient. Consequently, in this region, there was more low-velocity water close to the channel bed. This was more sensitive to the opposing pressure force and so when its momentum was reduced still more by the net pressure force, the water near the channel bed was soon brought to a standstill. The water was no longer able to follow the channel bed and therefore broke away from it. This breakway which is usually termed separation first occurred at the

point where the variation of the velocity in the direction perpendicular to the channel bed was zero. This condition can be expressed mathematically by

$$\left(\frac{\partial U}{\partial y}\right)_{y=0} = 0 \qquad \text{(F.34)}$$

At the separation point on the channel bed, U=V=0, and the equation of motion (F.33a) will be reduced to the following form

$$\frac{dh}{dx_j} = \frac{\nu}{g}\left(\frac{\partial^2 U}{\partial y^2}\right)_{y=0} \qquad \text{(F.35)}$$

The above relationship represents the mathematical condition for the separation of the forward flow from the bed. It can be infered from Eq. (F.35) that the curvature of the velocity profile at the onset of separation on the channel bed must be positive (since $\frac{dh}{dx_j} > 0$). However, from the channel bed towards the boundary layer edge, $\frac{\partial U}{\partial y}$ decreases at a continuously lesser rate. This means that $\frac{\partial^2 U}{\partial y^2} < 0$ near the edge of the inner layer. Hence, at

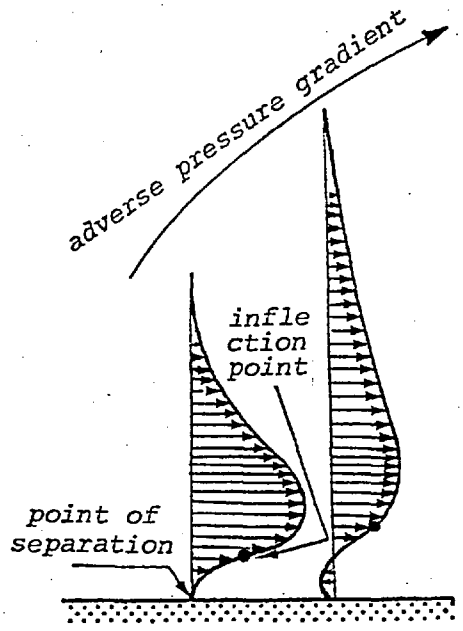


Fig. F.24 Point of separation

the onset of separation, there must be an inflection point on the velocity profile in the boundary layer.

The boundary layer separation of the forward flow of region II occurred very close to the retaining wall. As a result of the reversed flow in the separated zone, large irregular eddies were formed in which a great deal of energy was dissipated. The separated boundary layer tended to curl up in the reversed flow. Finally, the flow impinged violently on the retaining wall and became parallel to it; resulting in a complex flow pattern at the wall.

### F.3.5 Pressure Distribution on the Retaining Wall

The mean retaining wall pressure was measured by means of the pressure tapping points provided on the retaining wall. Figs.F.25,F.26 and F.27 show the pressure distribution on the retaining wall for several test runs. It must be noted that the pressures measured by the tapping points which were subjected to the fluctuating waves at the retaining wall are appreciably in error. This is because the pressure fluctuations in this region were as large as the mean. This fact is probably responsible for the increase in the pressures indicated by the upper tapping points.

Due to the complex behaviour of the flow in the impingement region, the interpretation of the pressure distribution on the retaining wall is difficult. However, Figs. F.25, F.26 and F.27 indicate that the maximum pressure on the retaining wall was concentrated around the middle of the retaining wall. This is because of the interaction of the forward flow along the channel centre line (which had a negligible redirection) with the flow that was redirected from the area adjacent to the side wall. It can be seen from these figures that the pressures near the outlet drop considerably. This is due to the considerable redirection of the flow near the channel outlet. Furthermore it can be seen that with a constant discharge of incoming flow, the maximum pressure on the retaining wall was not changed appreciably by changing the position of the retaining wall with respect to the spillway (although the pressure distribution on the retaining wall was changed).

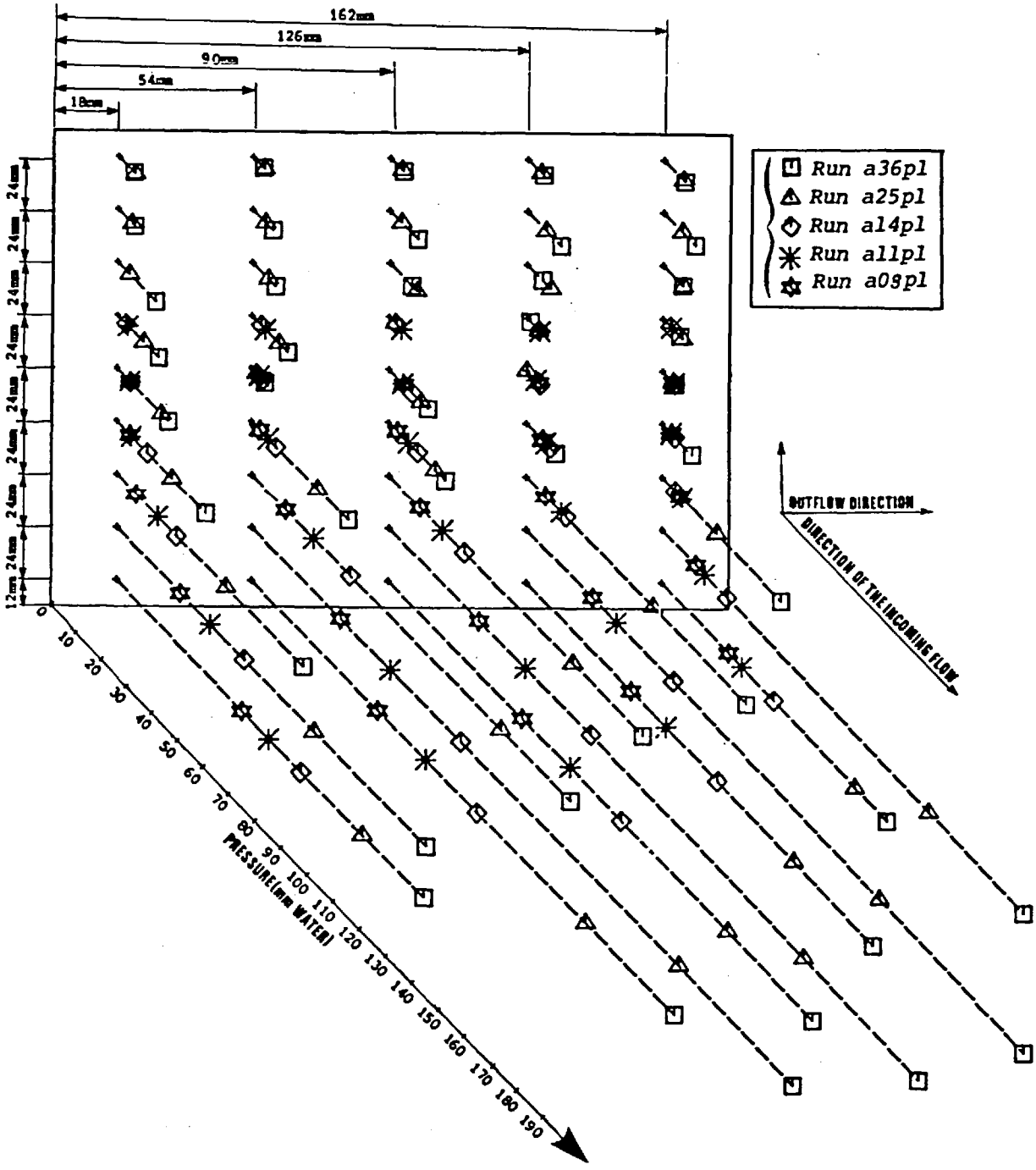


Fig. F.25 Pressure distribution on the retaining wall

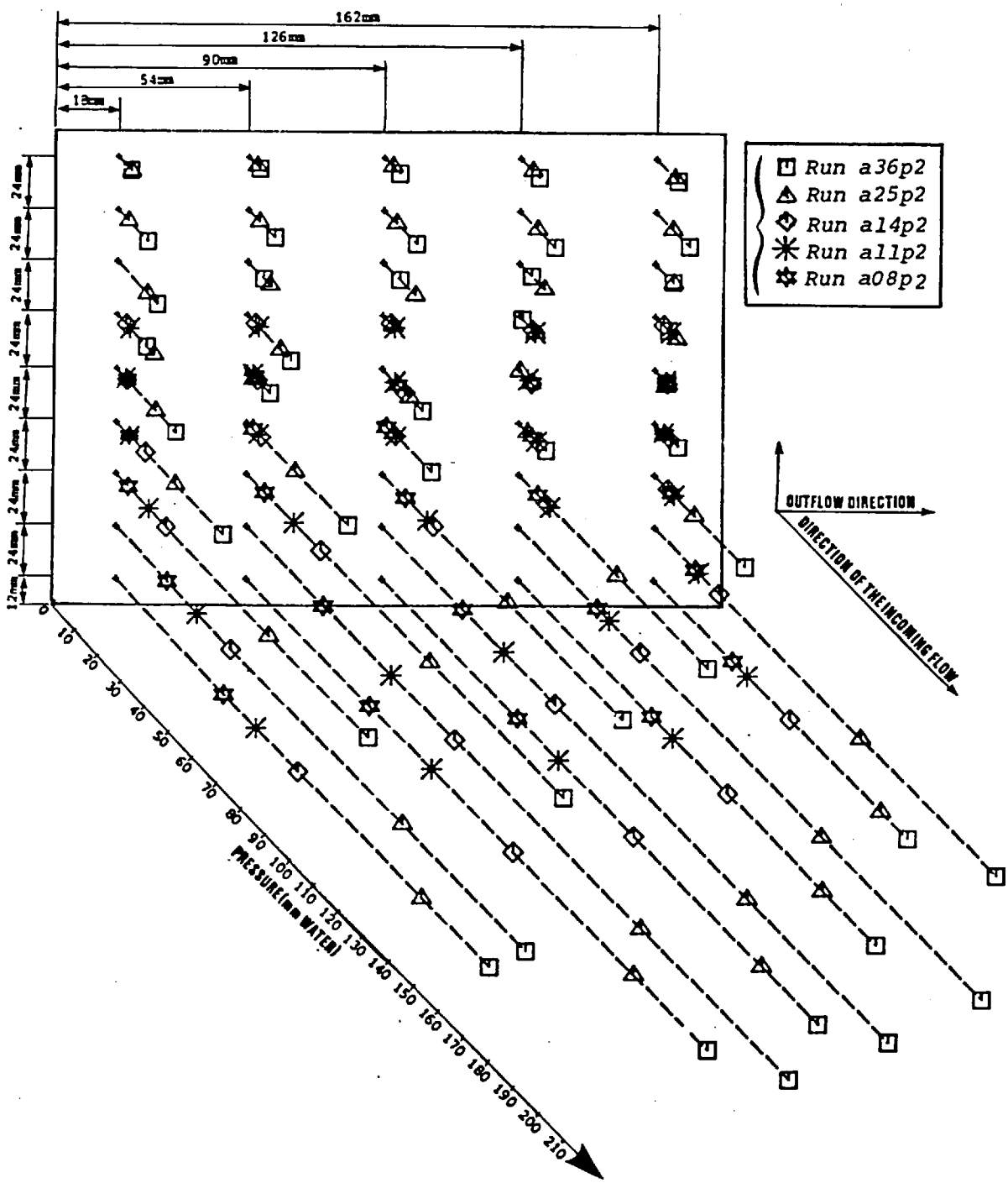


Fig. F.26 Pressure distribution on the retaining wall

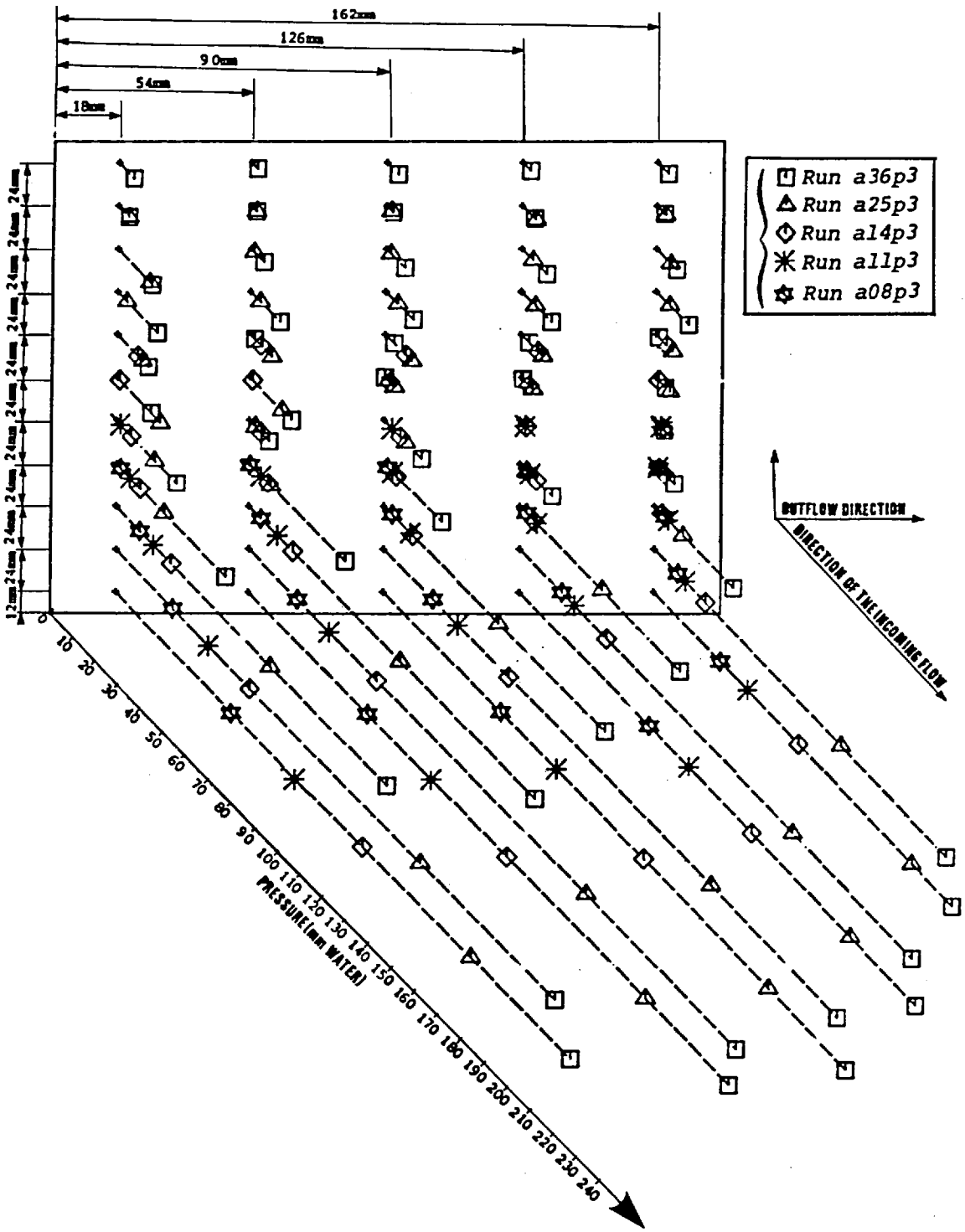


Fig. F.27 Pressure distribution on the retaining wall

## F.4 WAVES AT THE RETAINING WALL

During the initial stages of this investigation, several wave height records, measured with respect to the channel bed, were taken at a fixed location along the retaining wall and under identical flow conditions which yielded different water level records. The process had a random element in its structure and could therefore be described as a stochastic process. At a fixed location along the retaining wall and at any time t, a number of different values of the water level y(t) above the channel bed were possible. This indicated that a wave height record obtained at a point along the retaining wall was basically one example of an infinitely large number of water level records which might have occurred. The variation of the wave height records at a given point along the retaining wall could have been described by a random process $\{y(t)\}$, where $\{\ \}$ denotes an ensemble of sample functions and of which y(t) was one possible realisation. Mathematically the stochastic process could have been defined as a collection of random variables $\{y(t), t \in T\}$, where T is the time over which the process was defined.

The study of a stochastic process is not a study of a simple realisation but of the collection of realisations in the form of the random variable $\{y(t)\}$. In this investigation, it was assumed that the wave height at a given point along the retaining wall was ergodic. This means that the sample means and autocorrelations were equal for all possible realisations, the samples being taken in time. In this case, the statistical properties could be derived from only one realisation of the process, y(t). Plates XIII, XIV and XV show some typical simultaneous continuous records of fluctuating wave heights at three different locations along the retaining wall made by the ultra-violet recorder on photographic paper. In these plates, as was described in Chapter E, wave recording probe 1 corresponds to the probe which was close to the channel outlet, wave recording probe 2 represents the probe which was positioned in the middle of the retaining wall and wave recording probe 3 denotes the probe which was close to the side wall.

The wave height records made in this investigation were continuous traces of water level. To study their characteristics, the records were digitised in the same manner as was detailed in Chapter E, i.e. by reading off the values of the traces at each discrete time interval $\Delta t$.

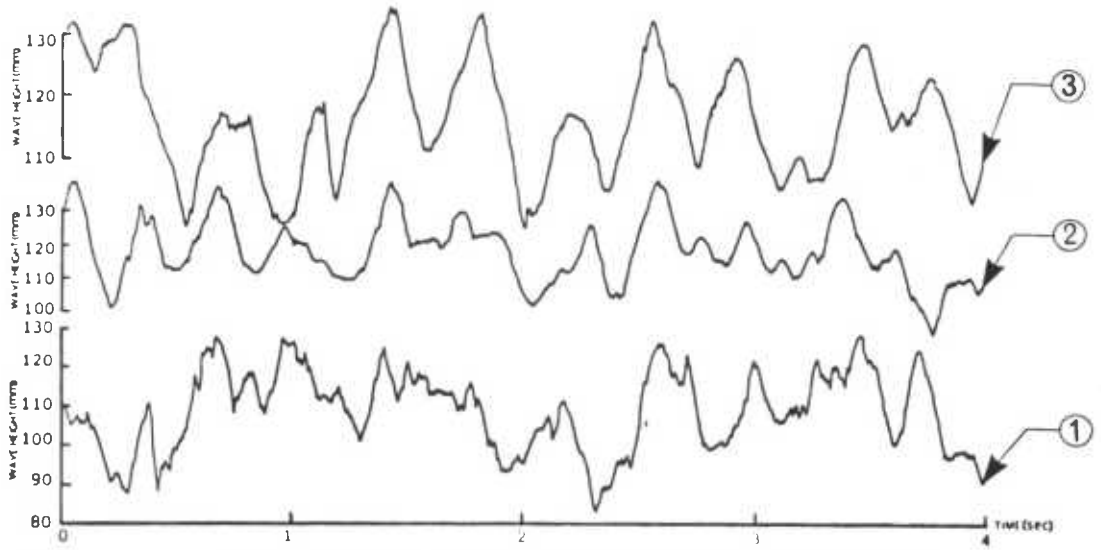


(c) *Run a14p3 : Simultaneous records of fluctuating wave heights at three locations along the retaining wall*

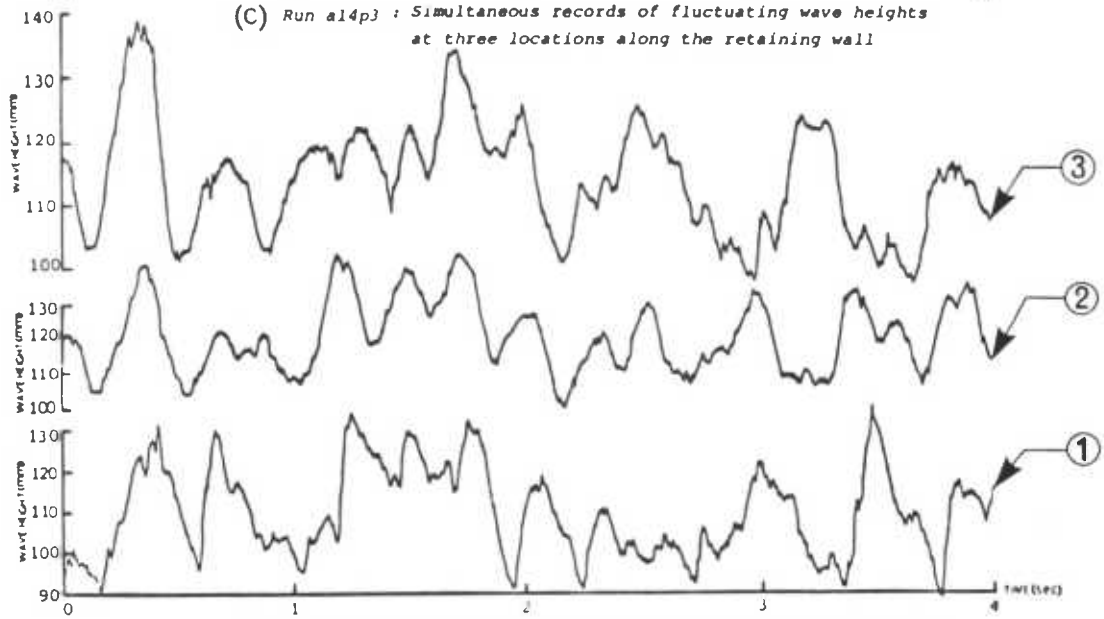


(b) *Run a14p2 : Simultaneous records of fluctuating wave heights at three locations along the retaining wall*

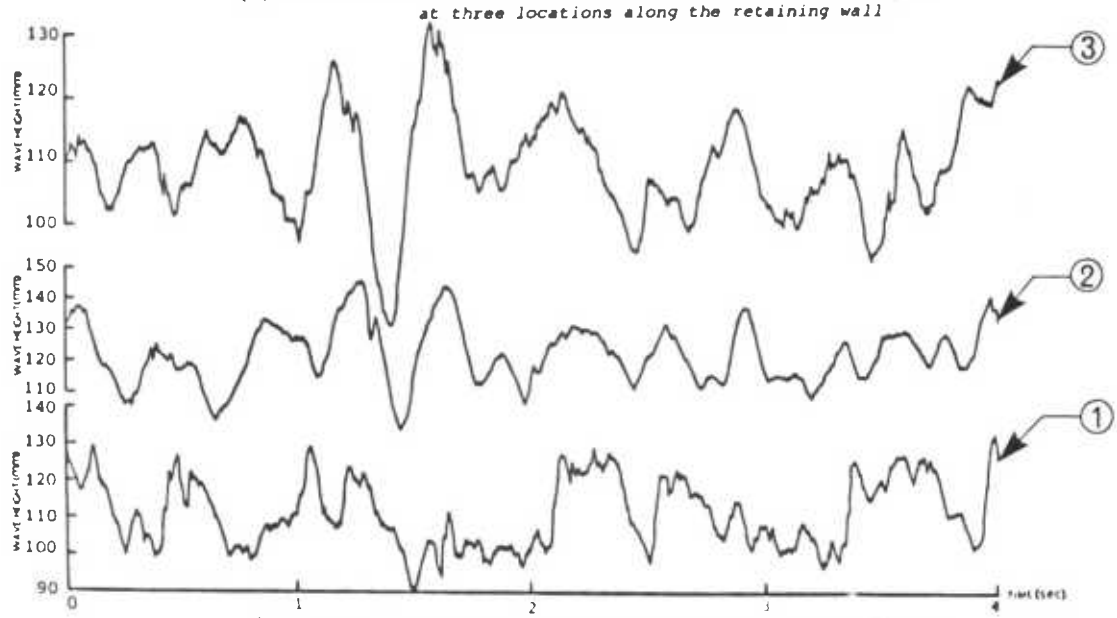


(a) *Run a14p1 : Simultaneous records of fluctuating wave heights at three locations along the retaining wall*

PLATE XIII WAVE HEIGHT RECORDS

(1) *Trace from wave recording probe 1*

(2) *Trace from wave recording probe 2*

(3) *Trace from wave recording probe 3*

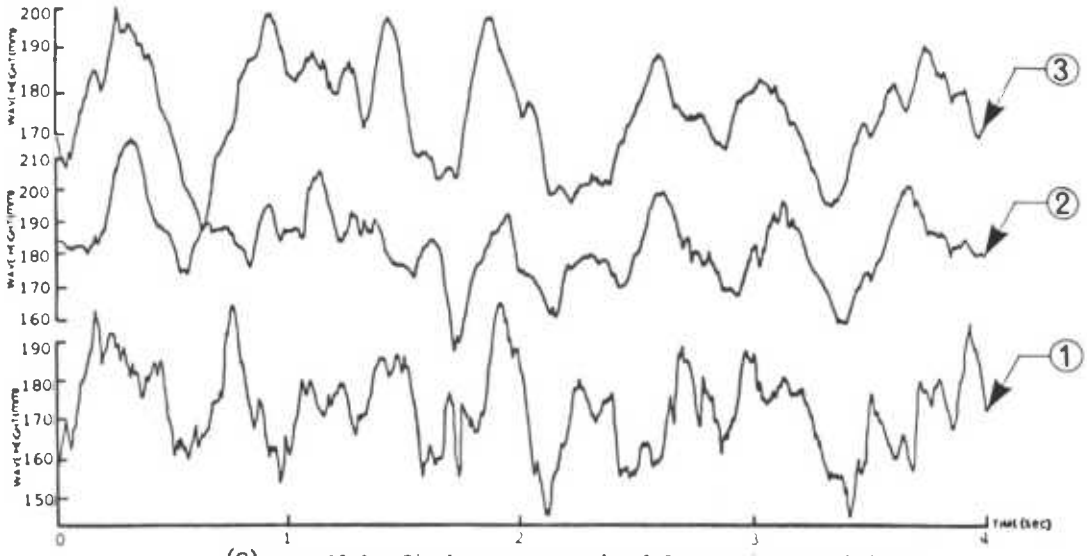


(c) *Run a25p3 : Simultaneous records of fluctuating wave heights at three locations along the retaining wall*

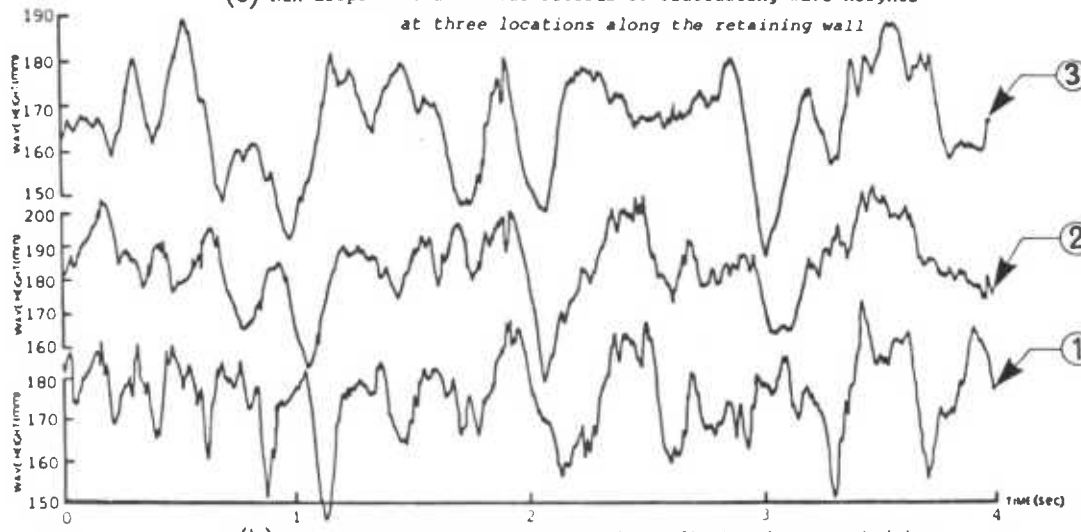


(b) *Run a25p2 : Simultaneous records of fluctuating wave heights at three locations along the retaining wall*

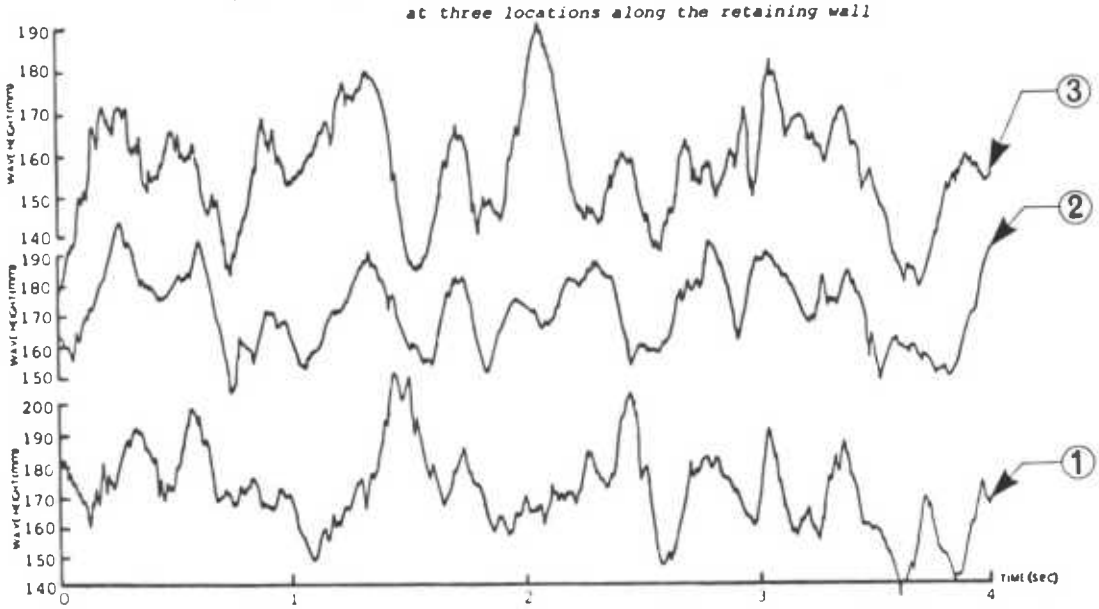


(a) *Run a25p1 : Simultaneous records of fluctuating wave heights at three locations along the retaining wall*

PLATE XIV WAVE HEIGHT RECORDS

(1) *Trace from wave recording probe 1*

(2) *Trace from wave recording probe 2*

(3) *Trace from wave recording probe 3*

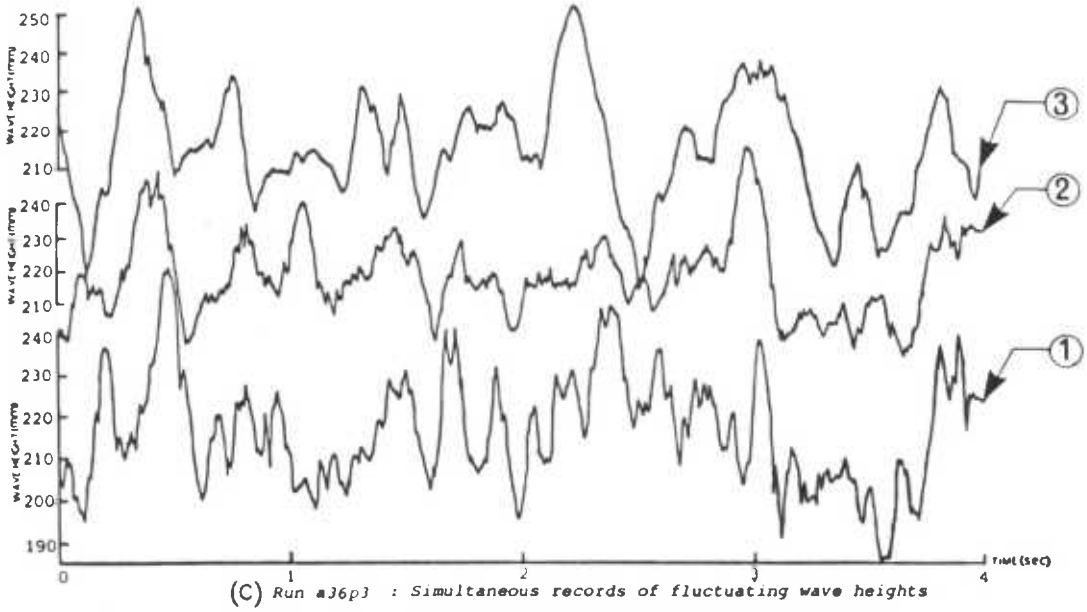


(c) *Run a36p3 : Simultaneous records of fluctuating wave heights at three locations along the retaining wall*

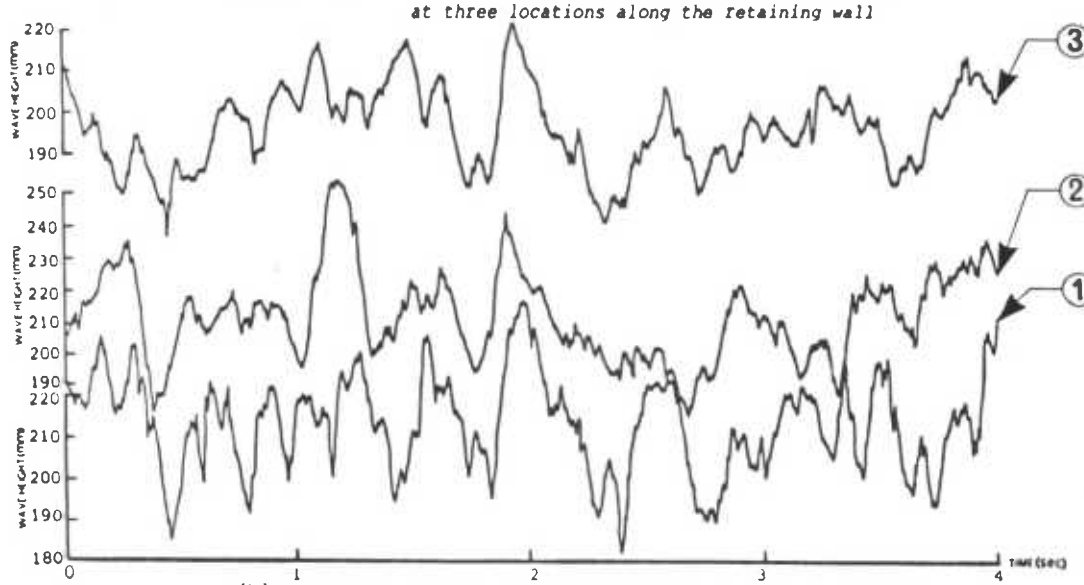


(b) *Run a36p2 : Simultaneous records of fluctuating wave heights at three locations along the retaining wall*

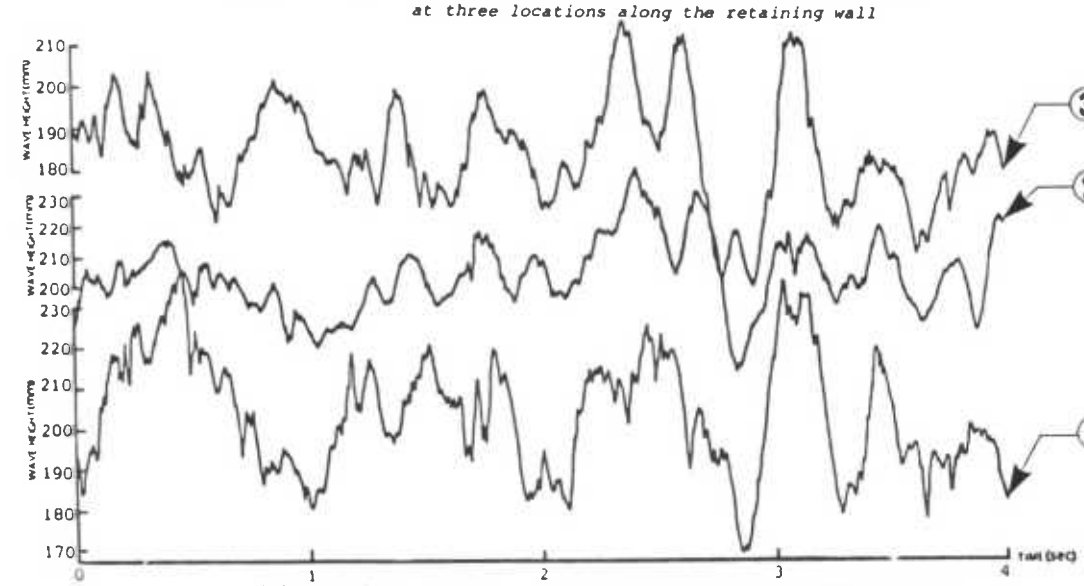


(a) *Run a36p1 : Simultaneous records of fluctuating wave heights at three locations along the retaining wall*

PLATE XV WAVE HEIGHT RECORDS

(1) *Trace from wave recording probe 1*

(2) *Trace from wave recording probe 2*

(3) *Trace from wave recording probe 3*

## F.4.1 Analysis of the Waves in Amplitude Domain

For a digitised wave height record $y_i$ of size N, the expected proportion of population values greater than $y_i$ is equal to the ratio of the descending ranked order of $y_i$ divided by one more than the total number of data points, no matter what form of the continuous probability density function in the population. The sample size N for all wave height records was 1024 with the sampling interval $\Delta t$=0.025 sec. The percentage P of wave heights with elevations greater than or equal to a specified value, was calculated and then plotted as an ordinate with the retaining wall height $w_h$ (the wave heights) as the abscissa. Figs. F.28, F.29, F.30, F.31, F.32, and F.33 show the statistical variation of the wave heights in the amplitude domain with each curve having its own distinct S-shape. The probability of exceedance of the wave height above the retaining wall associated with the maximum wall height was $\frac{1}{1025}$ = 0.0976% and with the minimum wall height was $\frac{1024}{1025}$ =99.9%. It must be noted, however, that due to the sampling error, the uncertainty of the experimental points at the upper and lower ends of the S- curves (maximum and minimum wall height) was greater than the other points of the S- curves.

A number of conclusions can be made by examining the statistical variation of the wave heights in the amplitude domain for different test runs. In the first instance, the fluctuating water level at the middle of the retaining wall was generally higher than at other locations along the retaining wall. As was concluded earlier, this is because at the middle of the retaining wall, the forward flow along the channel centre line (which had a negligible redirection) interacted with the flow that was redirected from the area adjacent to the side wall. Secondly, with the retaining wall at a fixed position with respect to the spillway, an increase in the discharge of the incoming flow caused the wave heights at the retaining wall to increase (Fig.F.28(a)). Thirdly, with a constant discharge of incoming flow, when the retaining wall was fixed in a position closer to the spillway, the wave heights at the retaining wall increased due to the friction to the flow being less. However, this increase in the wave heights was found to be quite small. For example, Fig.F32(a) reveals that by reducing the impingement length by 28% and 55%, the wave heights in the middle of the retaining wall increased, on average, only by 4% and 7% respectively.

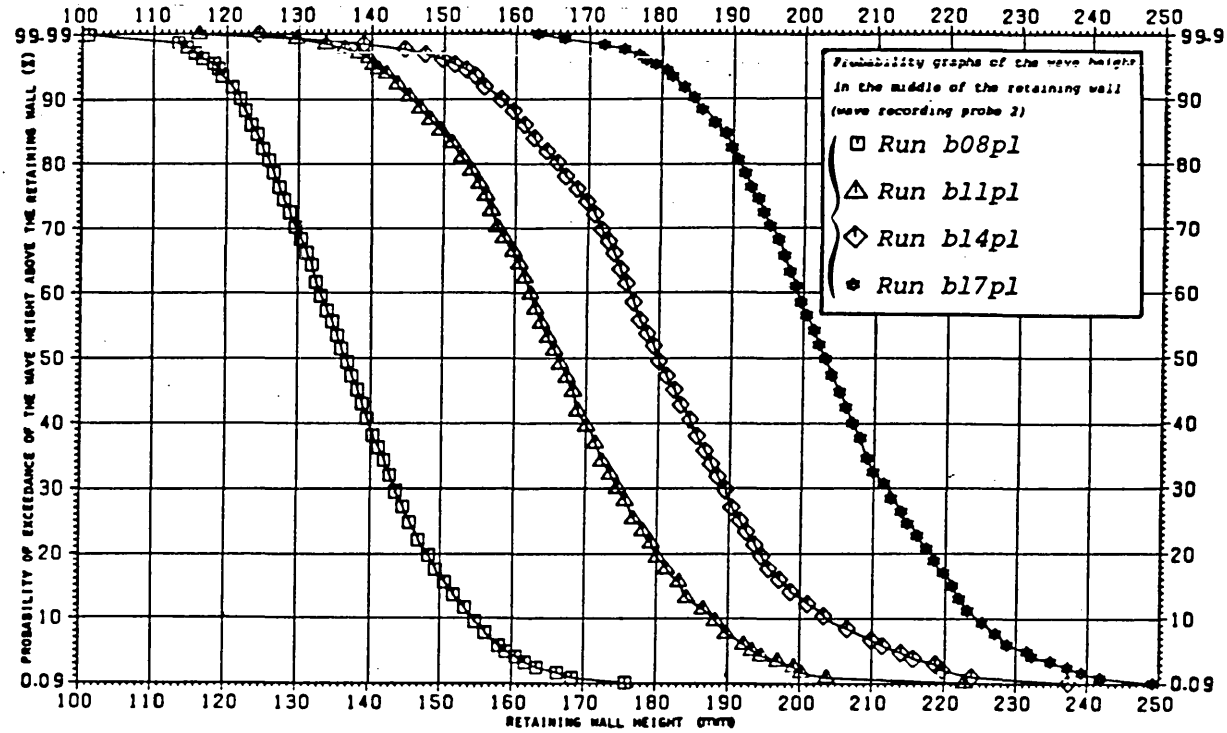


(a)

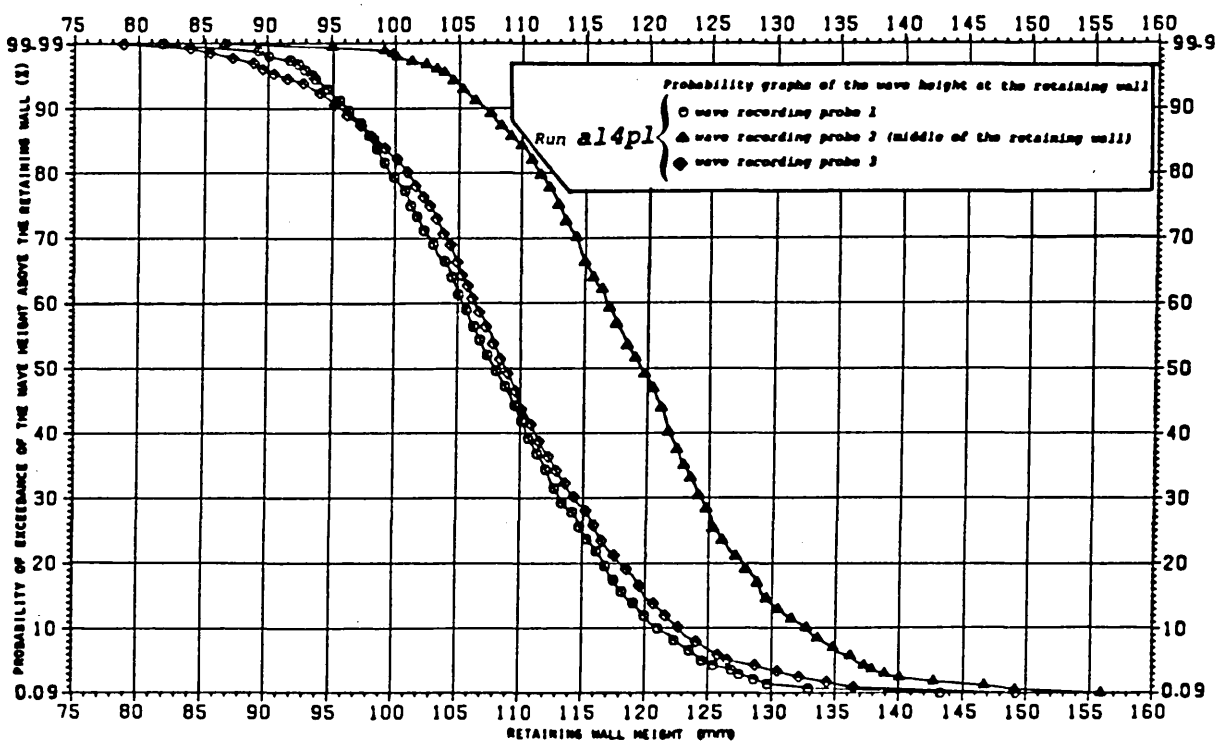


(b)

Fig. F.28 Wave heights distribution in the amplitude domain.

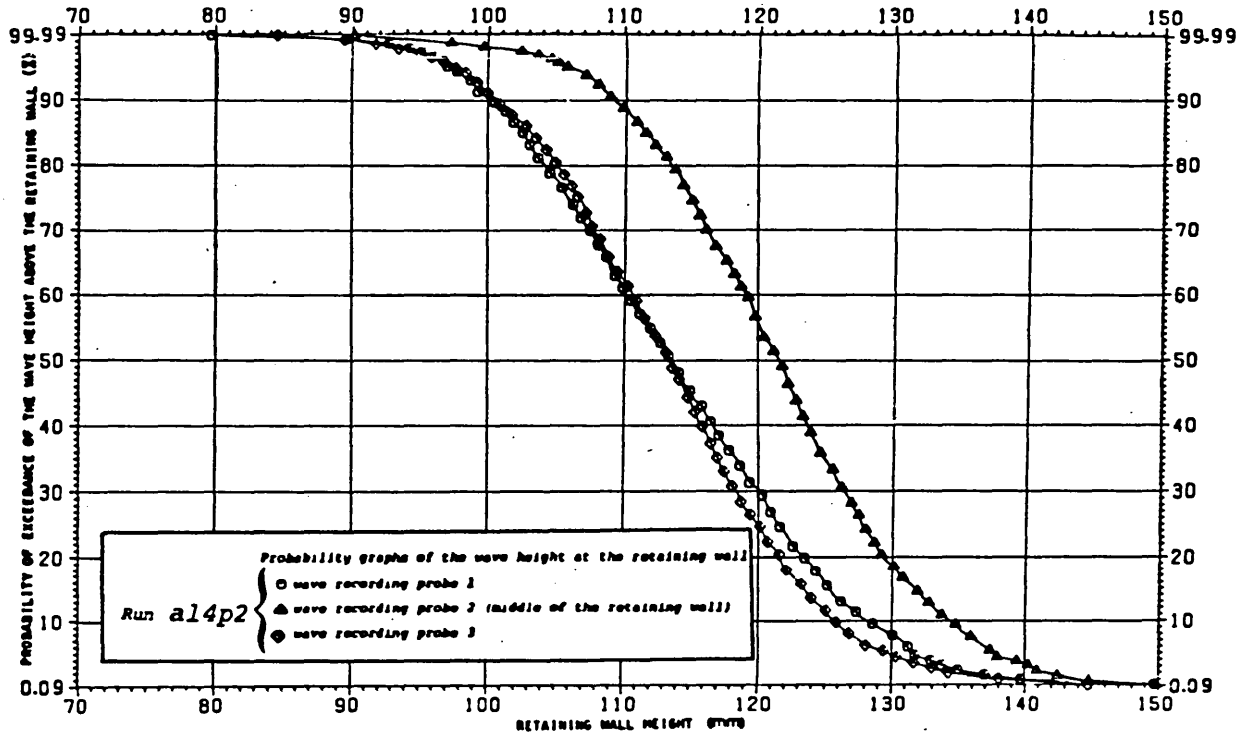


(a)

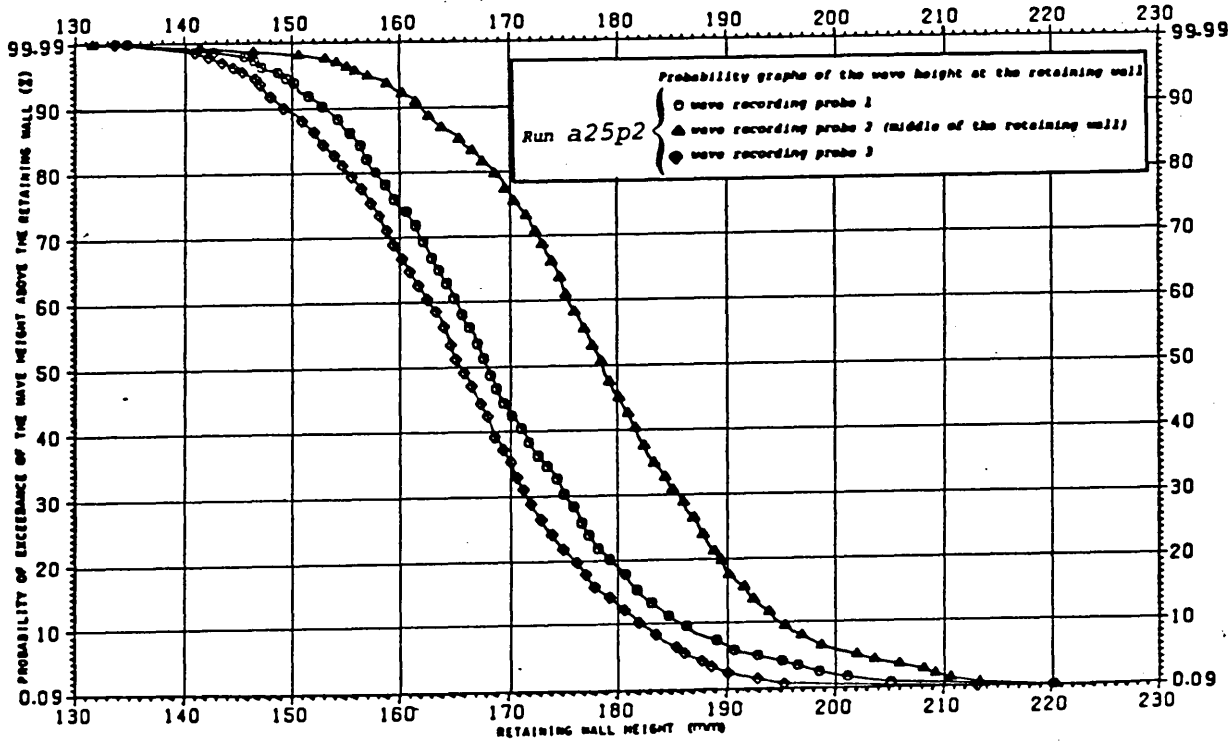


(b)

Fig. F.29 Wave heights distribution in the amplitude domain.

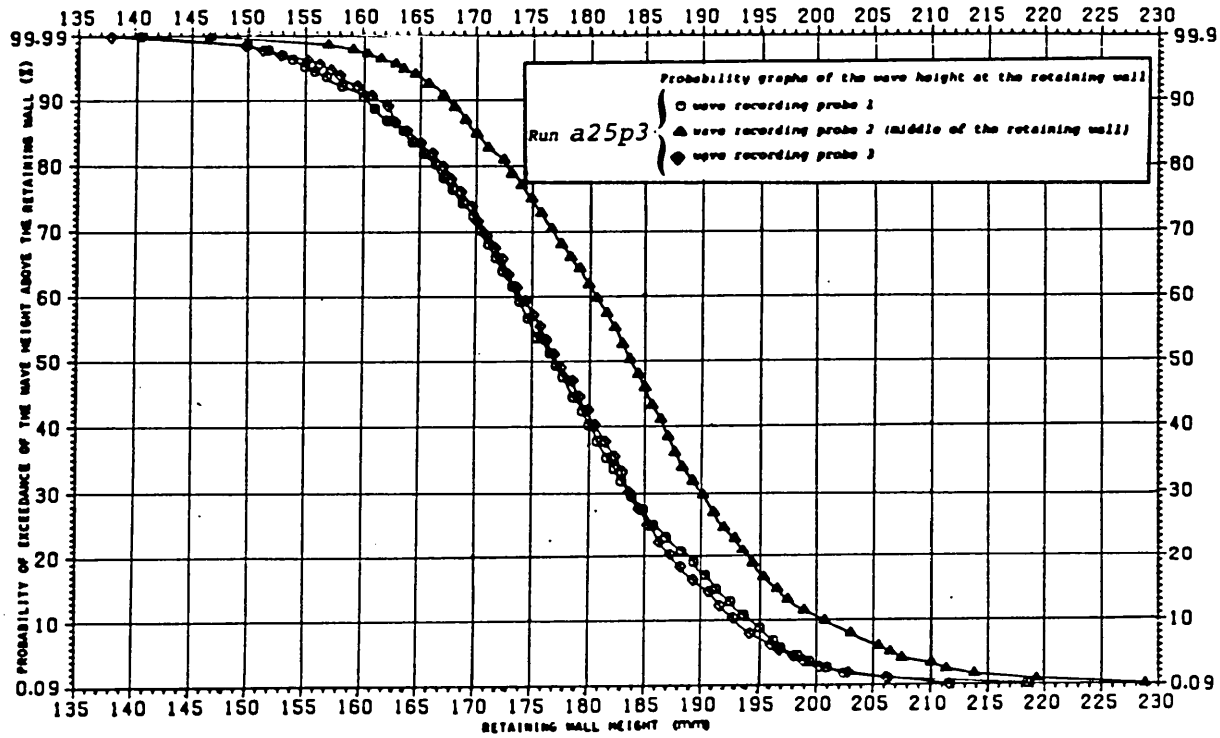


(a)

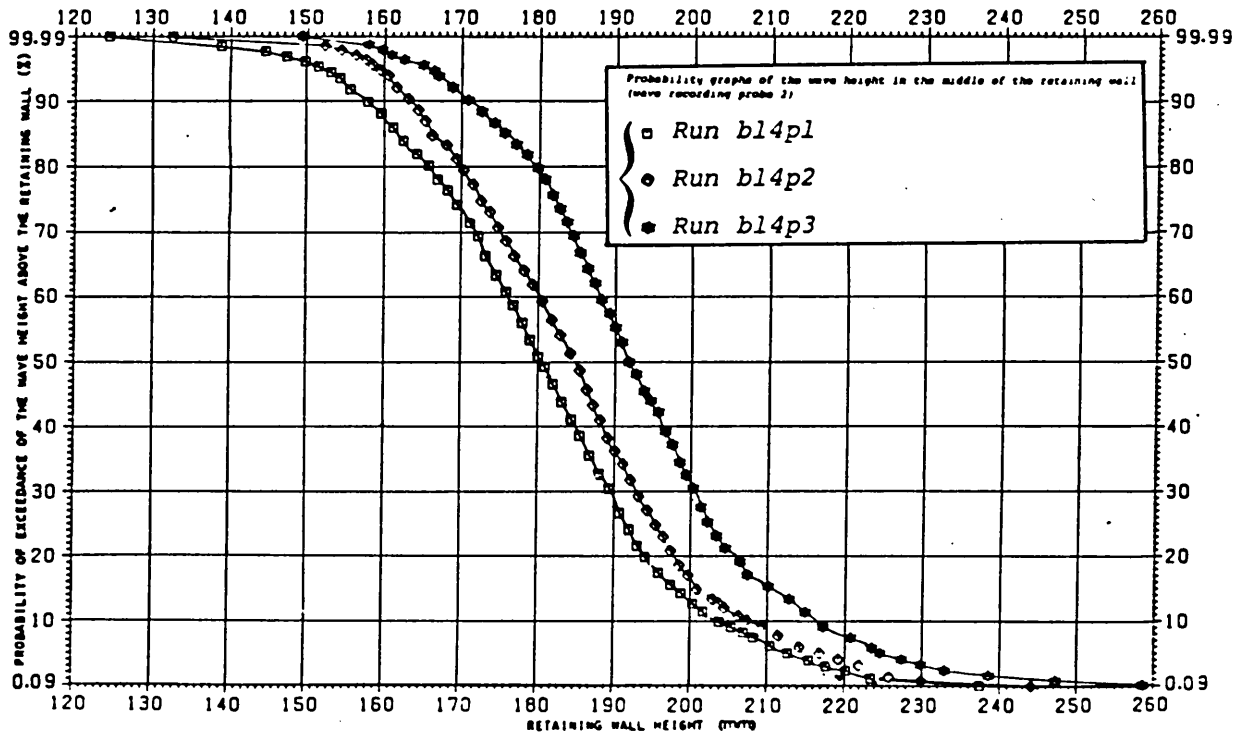


(b)

Fig. F.30 Wave heights distribution in the amplitude domain

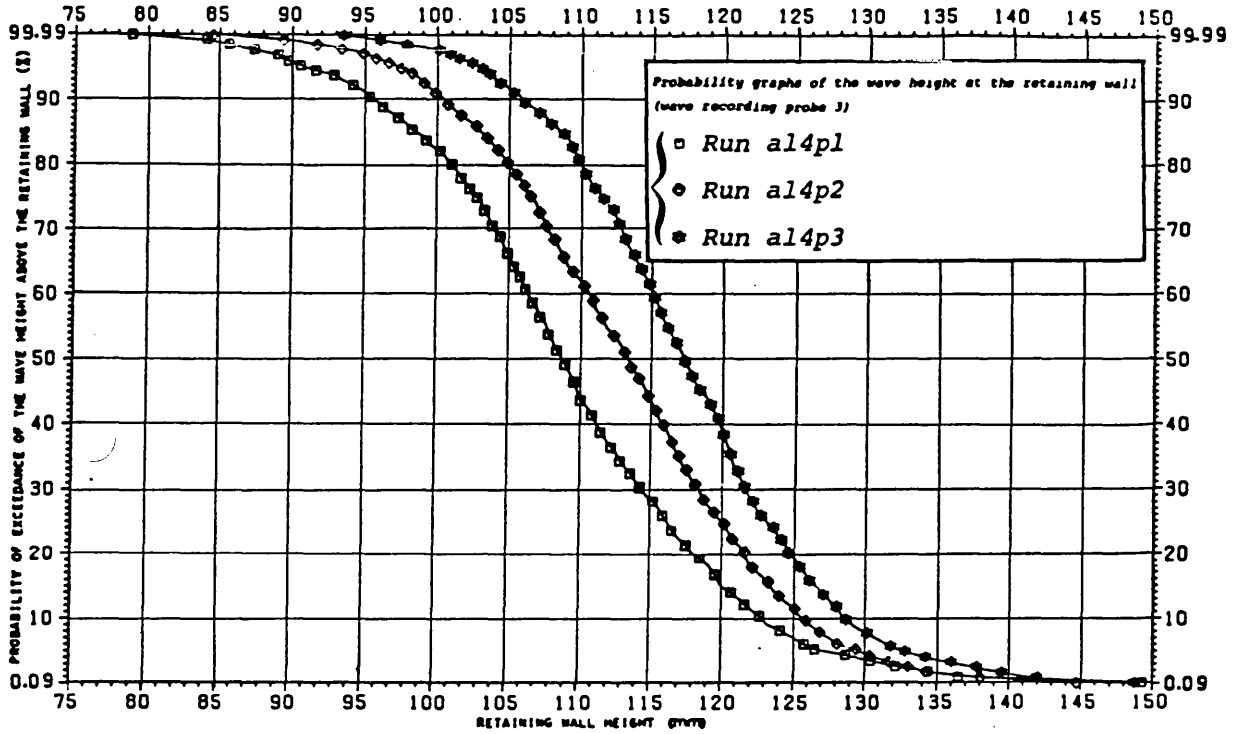


(a)

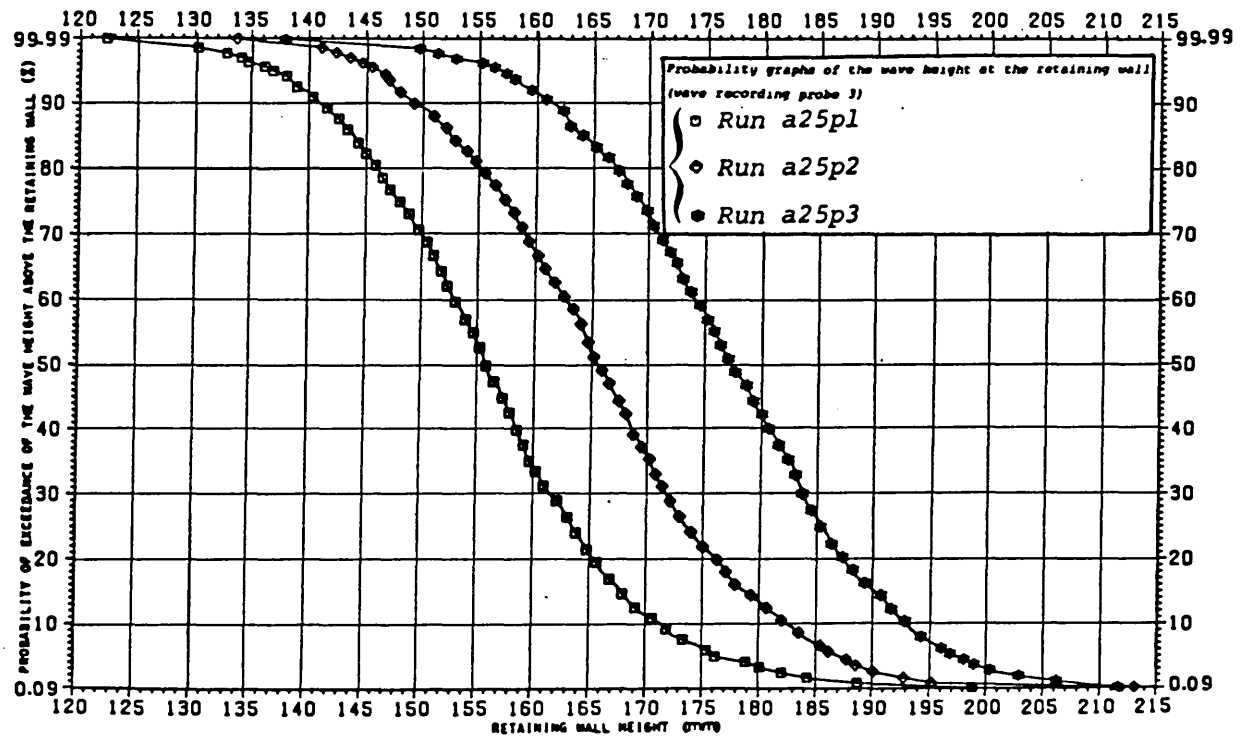


(b)

Fig. F.31 Wave heights distribution in the amplitude domain

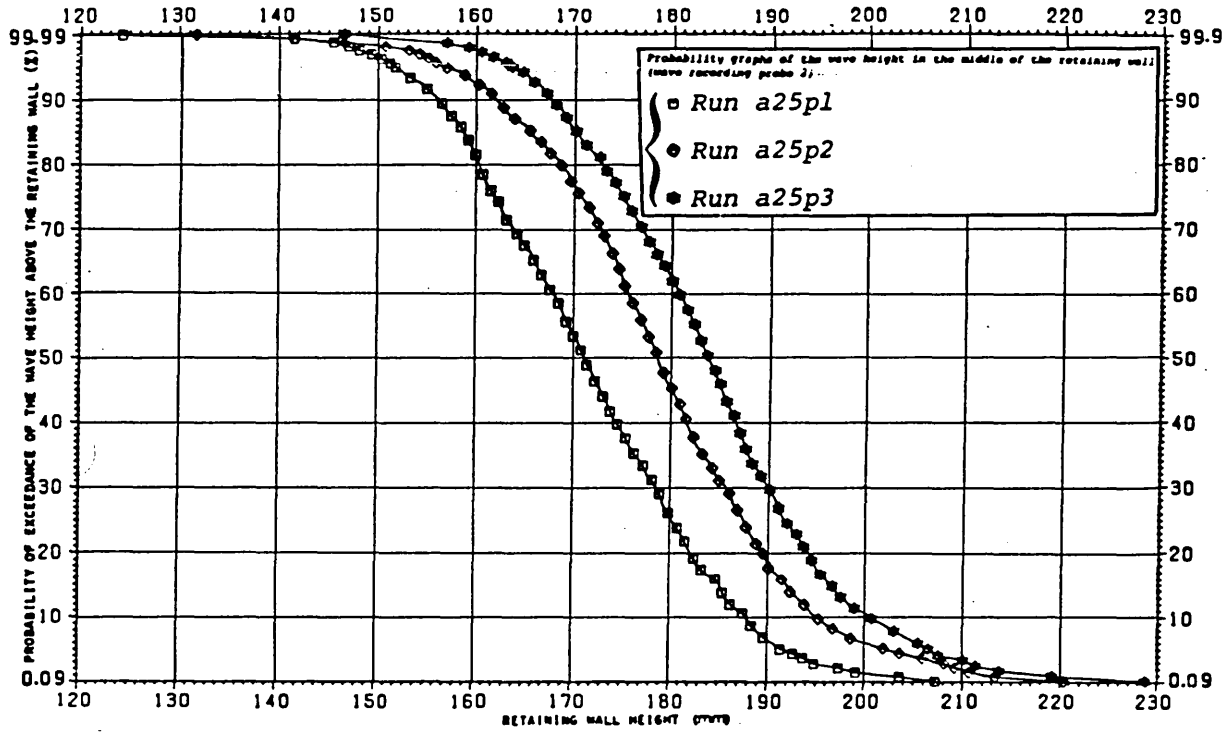


(a)

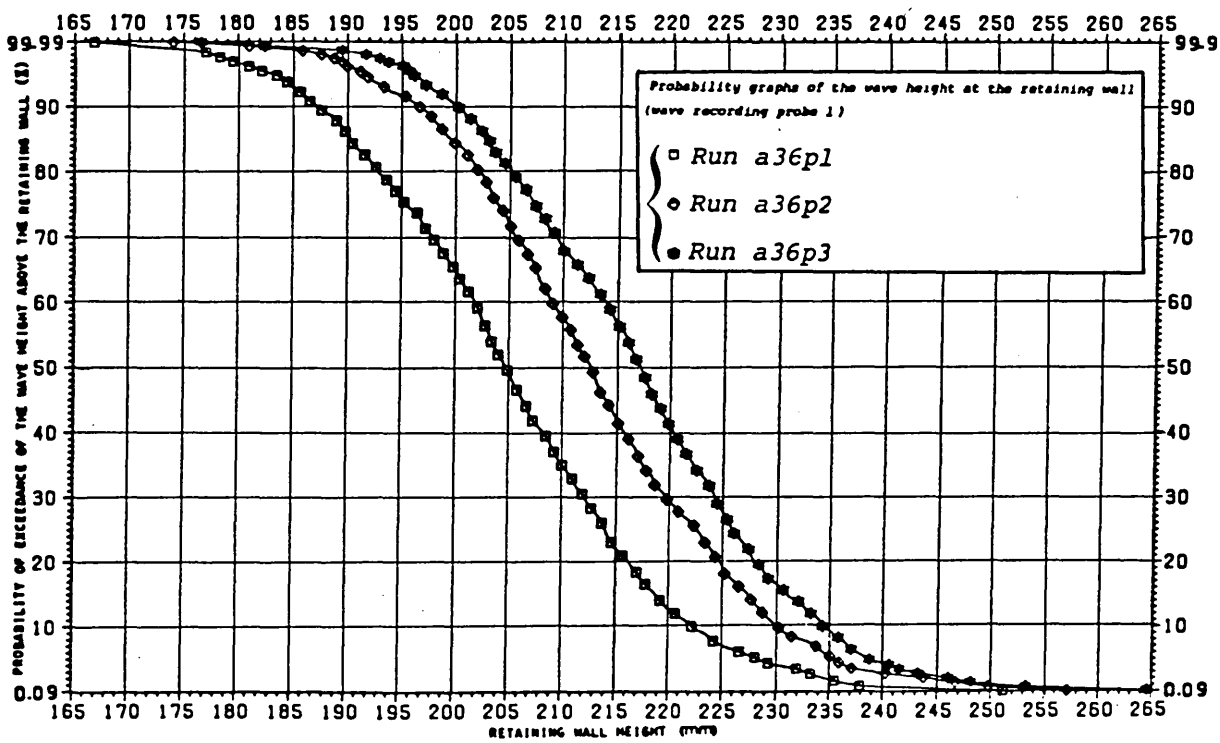


(b)

Fig. F.32 Wave heights distribution in the amplitude domain

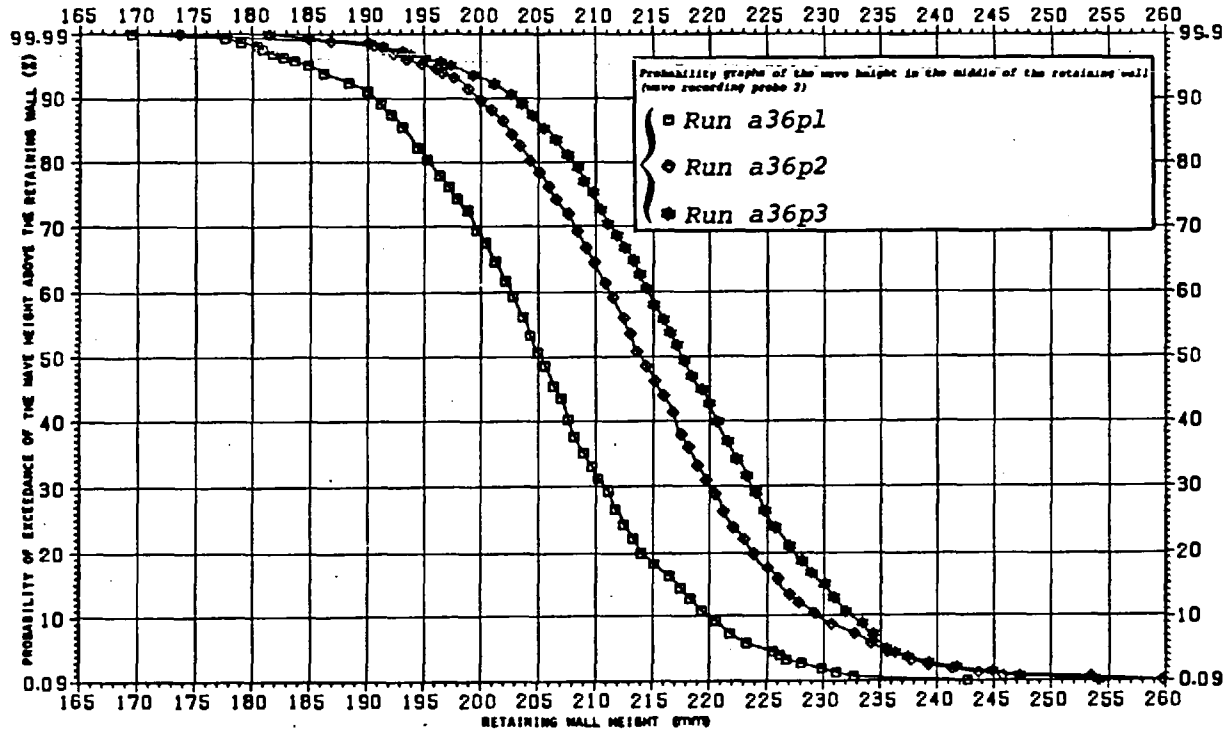


(a)

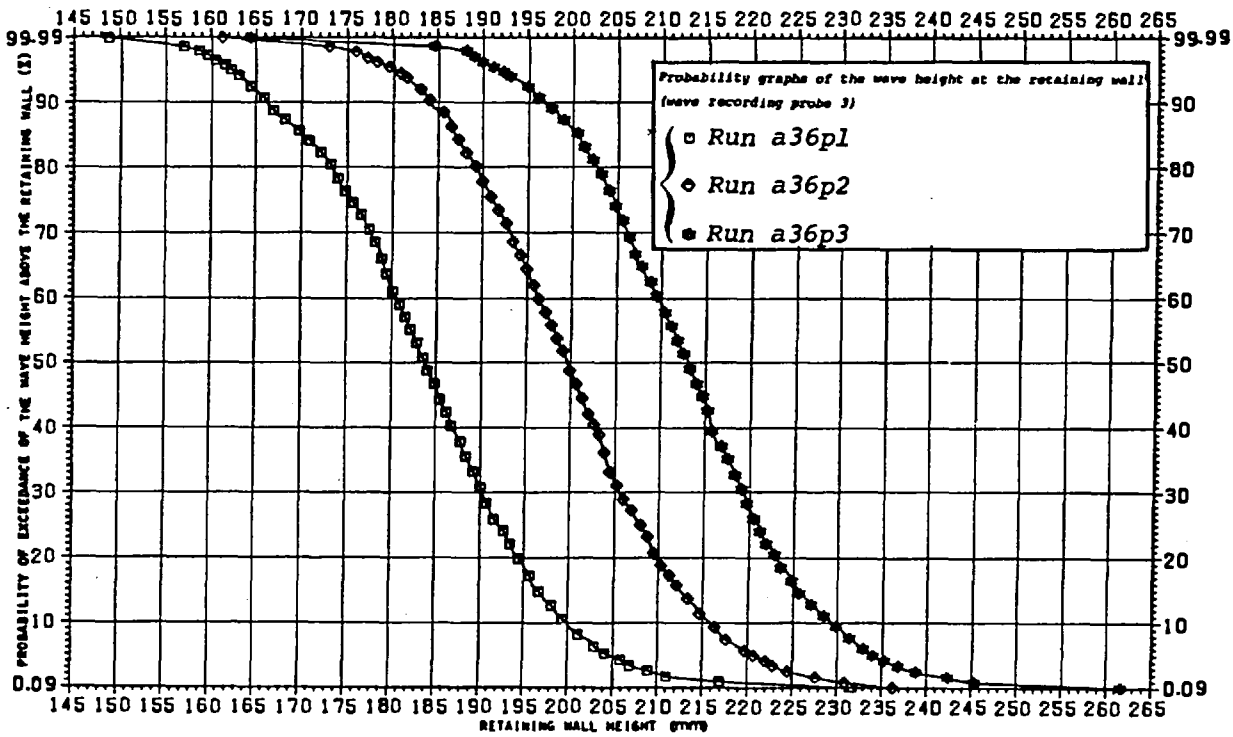


(b)

Fig. F.33 Wave heights distribution in the amplitude domain

### F.4.1.1 Universal Similarity Curve for the Distribution of the Wave Height at the Middle of the Retaining Wall

The significant variables influencing the behaviour of a plane turbulent water jet of finite dimensions deflected by a transverse wall are

$d_m$, the depth of the supercritical water flow at the toe of the spillway along the channel centre line.

$U_m$, the average velocity of the supercritical water flow at the toe of the spillway,

$\ell$ , the impingement length,

$b$ , the impingement width,

$\rho$ , the mass density of water,

$g$ , the acceleration due to gravity,

$\nu$ , the kinematic viscosity of water,

$\beta$ and $\alpha$, the momentum and energy coefficients respectively of the incoming supercritical water flow at the toe of the spillway.

According to Buckingham $\pi$ theorem, the aforementioned variables can be replaced by six dimensionless groups, namely, the Froude number, the Reynolds number, the coefficients of energy and momentum(all pertaining to the incoming supercritical water flow) and two geometrical ratios as follows

$$Fr = \frac{U_m}{\sqrt{gd_m/\alpha}} , R_j = \frac{U_m d_m}{\nu} , \alpha, \beta, \frac{b}{d_m} , \frac{\ell}{d_m} \qquad (F.36)$$

where $\frac{b}{d_m}$ is the aspect ratio of the water jet and $\frac{\ell}{d_m}$ is the dimensionless impingement length. The Reynolds number $R_j$ in all test runs was greater than $10^4$ and hence its effect on the characteristics of the flow could be assumed to be negligible (Delleur,1954). Hence, the governing flow parameters can be replaced by five dimensionless groups as follows

$$Fr = \frac{U_m}{\sqrt{gd_m/\alpha}} , \alpha , \beta, \frac{b}{d_m} , \frac{\ell}{d_m} \qquad (F.37)$$

An attempt was made to discover whether the probability graphs in the middle of the retaining wall were similar. This was achieved by replotting the probability graphs data in a dimensionless form with the

probability of exceedance of the wave height above the retaining wall P, against $\mathcal{G}$, where $\mathcal{G}$ is defined as

$$\mathcal{G} = \frac{w_h}{d_w}\left(\frac{\ell}{d_m}\right)^{\frac{1}{11.5}}\left(\frac{d_m}{b}\right)^{0.15} \qquad \text{(F.38)}$$

In the above relationship, $w_h$ is the retaining wall height and $d_w$ is the 'mean momentum depth' associated with the water jet at the toe of the spillway which was calculated from the following relationship

$$m_o = \tfrac{1}{2}\rho g d_m^2 + \rho\beta U_m^2 d_m = \tfrac{1}{2}\rho g d_w^2 \qquad \text{(a)}$$

or

$$d_w = d_m\sqrt{1+2\beta/\alpha\ Fr^2} \qquad \text{(b)} \qquad \text{(F.39)}$$

The left hand side of the relationship (F.39a) is basically the pressure force plus the momentum per unit width of the water jet at the toe of the spillway. As was mentioned earlier, the loss of momentum per unit width in the downstream direction along the channel centre line in regions I and II due to the redirection of the flow was negligible. This is because the redirection of the flow along the channel centre line was a negligible feature of the flow. Furthermore, with a constant discharge from the spillway, the magnitude of the mean momentum depth associated with the water jet at the toe of the spillway remained approximately the same when changing the retaining wall position with respect to the spillway. Fig.F.34 shows that all the experimental data condensed into a single curve described mathematically by

$$P = e^{-(0.888\mathcal{G})^{14.975}} \qquad \text{(F.40)}$$

in which P is expressed as a percentage. From Fig.F.34, it can be seen that the lower end of the above curve approaches the P=0 axis asymptotically. This means that for a condition in which the wave heights never overtop the retaining wall, the magnitude of the retaining wall height must be $w_h = \infty$. Also, for P = 100%, Eq.(F.40) yields $w_h = 0$ (mathematically, no retaining wall). The average wave height at the retaining wall corresponds to P = 50%.

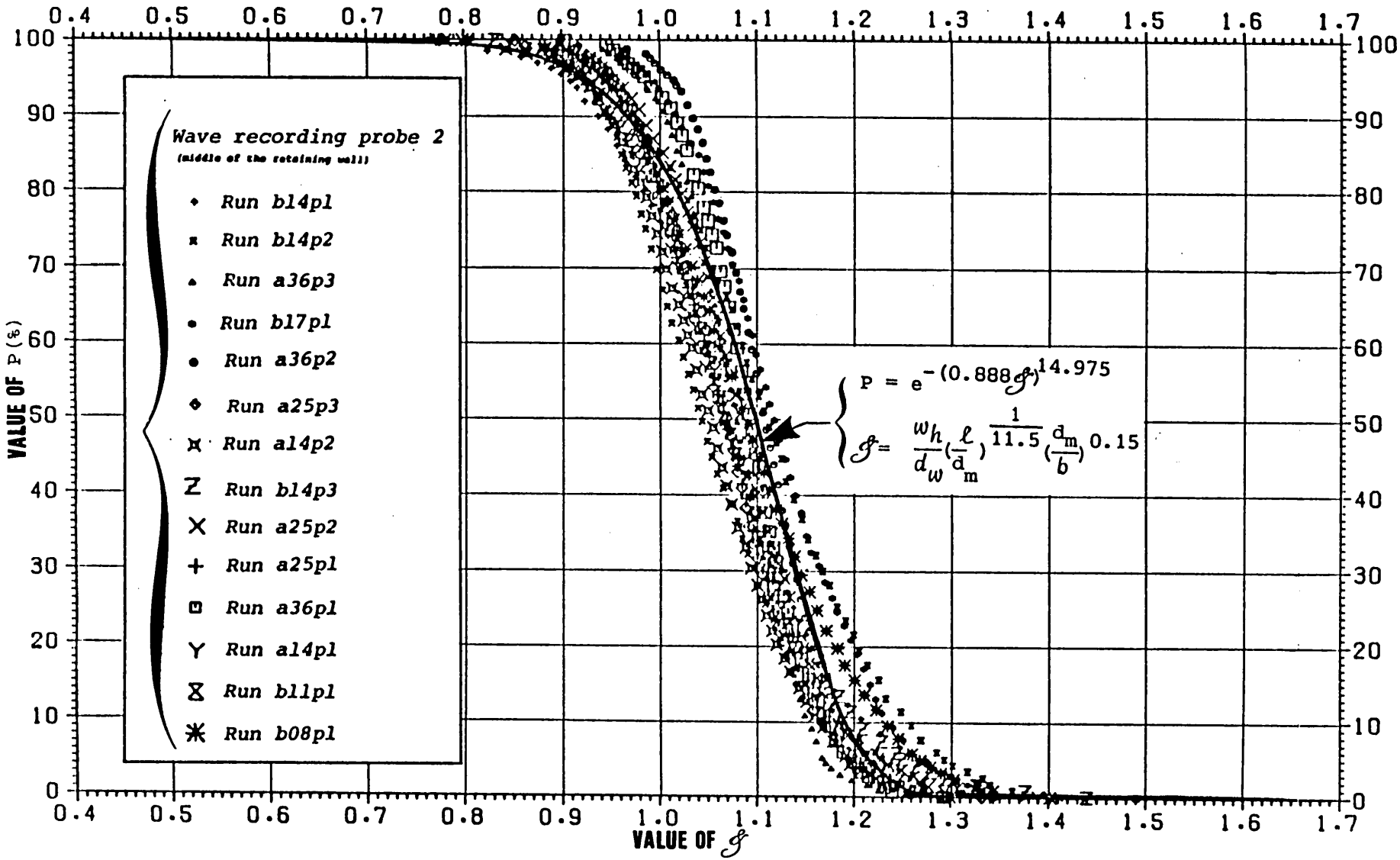


Fig. F.34 Wave height distribution at the middle of the retaining wall

### F.4.1.2 Coefficients of Dispersion of the Wave Heights

The coefficient of dispersion associated with a digitised wave height record $y_i$ of size N and mean $\bar{y}$ may be written as

$$C_d = \frac{\{[\sum_{i=1}^{N} (y_i - \bar{y})^2]/(N-1)\}^{\frac{1}{2}}}{\bar{y}} \qquad (F.41)$$

It can be seen from the above relationship that the coefficient of dispersion of a wave height record indicates the average wave height measured with respect to the mean water level divided by the mean water level; the mean water level $\bar{y}$ and $y_i$ being measured with respect to the channel bed. Table F.2 shows that the coefficients of dispersion of the wave heights at the retaining wall varied between 5.6% and 10.7%.

| *Run* | *Wave Recording Probe 1* | *Wave Recording Probe 2* | *Wave Recording Probe 3* |
|---|---|---|---|
| *a14p1* | 0.088 | 0.083 | 0.099 |
| *a25p1* | 0.076 | 0.073 | 0.077 |
| *a36p1* | 0.066 | 0.056 | 0.070 |
| *a14p2* | 0.094 | 0.080 | 0.087 |
| *a25p2* | 0.078 | 0.075 | 0.074 |
| *a36p2* | 0.063 | 0.056 | 0.061 |
| *a14p3* | 0.095 | 0.077 | 0.077 |
| *a25p3* | 0.072 | 0.0702 | 0.069 |
| *a36p3* | 0.062 | 0.054 | 0.060 |
| *b08p1* | 0.091 | 0.092 | 0.101 |
| *b11p1* | 0.091 | 0.096 | 0.107 |
| *b14p1* | 0.089 | 0.1 | 0.092 |
| *b17p1* | 0.091 | 0.076 | 0.095 |
| *b14p2* | 0.097 | 0.09 | 0.094 |
| *b14p3* | 0.084 | 0.092 | 0.091 |

Table F.2 Coefficients of Dispersion of the wave heights.

## F.4.2 Analysis of the Wave Heights in Time Domain

The correlogram was the most useful tool to provide information concerning the properties of the wave height records in time domain. For a wave height record, the actual times $t_i$ associated with the observations were unimportant; only the difference $t_i - t_j$ known as the lag was significant. The coefficient of correlation $r_\tau$ associated with the lag $\tau$ of a digitised wave height record $y_i$ of size N and mean $\bar{y}$ was calculated according to the Eq. (C.50) as

$$r_\tau = \frac{\frac{1}{N-\tau} \sum_{i=1}^{N-\tau} (y_i - \bar{y})\ (y_{i+\tau} - \bar{y})}{\frac{1}{N} \sum_{i=1}^{N} (y_i - \bar{y})^2} \qquad \text{(F.42)}$$

Figs.F.35, F.36, and F.37 show the correlograms of the wave height records of size N=1024 at three different positions along the retaining wall for several test runs. In these figures, the autocorrelation coefficient $r_\tau$ was plotted as the ordinate and the lag $\tau$ as the abscissa. As was explained earlier, each of the three simultaneous records of fluctuating wave heights measured at three different locations along the retaining wall may be considered to be a sample from a population time series consisting of an infinite number of observations. Therefore $r_\tau$ was an estimate of $\rho_\tau$, the population $\tau$th order serial correlation. The estimated correlograms were all subject to sampling errors, particularly for the estimated values of $r_\tau$ where the lag $\tau$ was large. This means that for a fixed value of N (during this investigation, N was always equal to 1024), the variance of $r_\tau$ increased as $\tau$ increased, since the number of pairs of observations used to determine $r_\tau$ decreased. The value of $r_\tau$ for $\tau > \frac{N}{10}$ = 102 time intervals (each time interval was equal to 0.025sec) were not determined. The 103 correlogram ordinates were calculated for each wave height record and the adjacent points were connected by straight lines.

A close study of the shapes of the correlograms of the wave heights measured at three different points along the retaining wall shows that the correlogram ordinate for the lag zero was equal to one for all test runs. This is because the correlation of a set of observations with itself was unity. However, this property holds true for any time series. The values of $r_\tau$ for

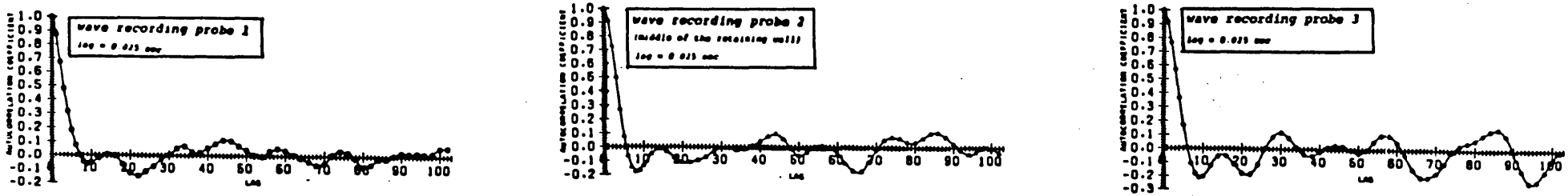


(a) *Run a25p1: Correlograms of the wave height records at three different positions along the retaining wall*

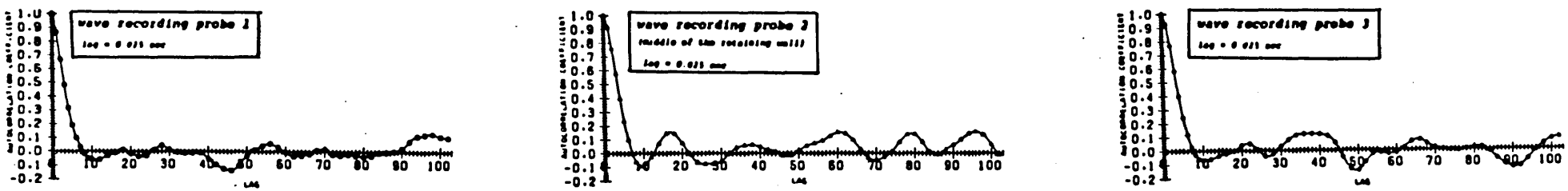


(b) *Run a25p2 ; Correlograms of the wave height records at three different positions along the retaining wall*

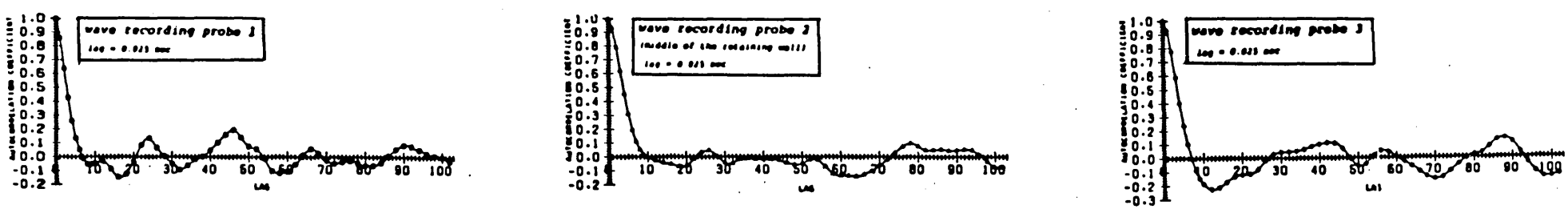


(c) *Run a25p3: Correlograms of the wave height records at three different positions along the retaining wall*

Fig. F.35

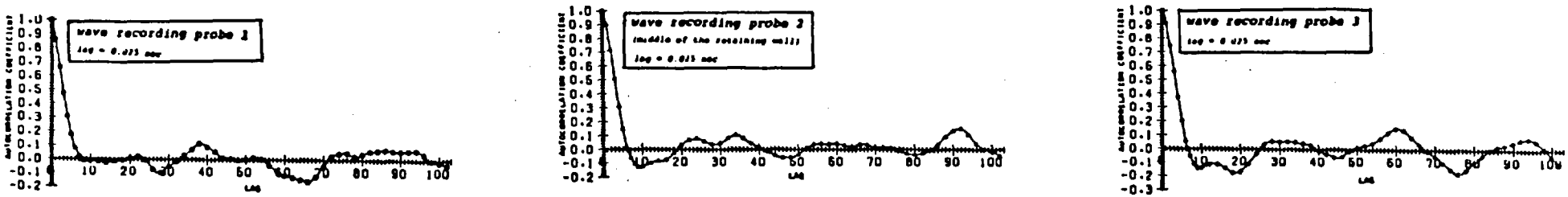


(a) *Run a36p1 : Correlograms of the wave height records at three different positions along the retaining wall*

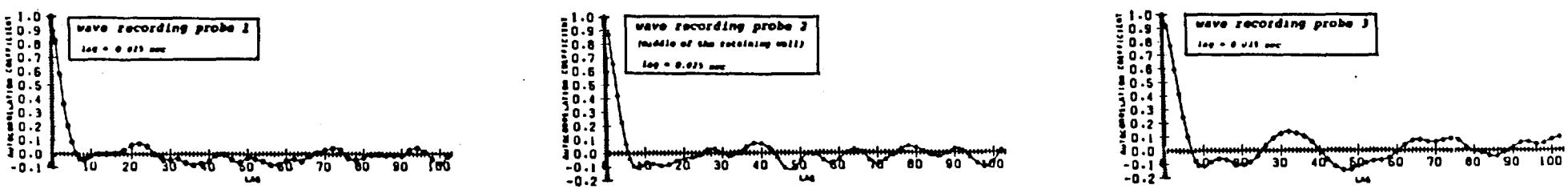


(b) *Run a36p2 ; Correlograms of the wave height records at three different positions along the retaining wall*

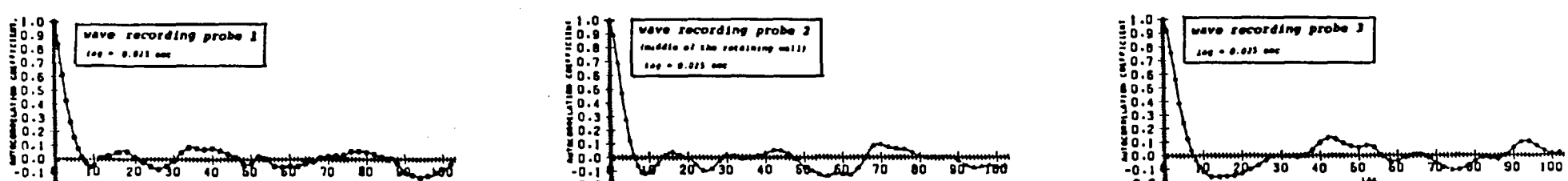


(c) *Run a36p3 : Correlograms of the wave height records at three different positions along the retaining wall*

Fig. F.36

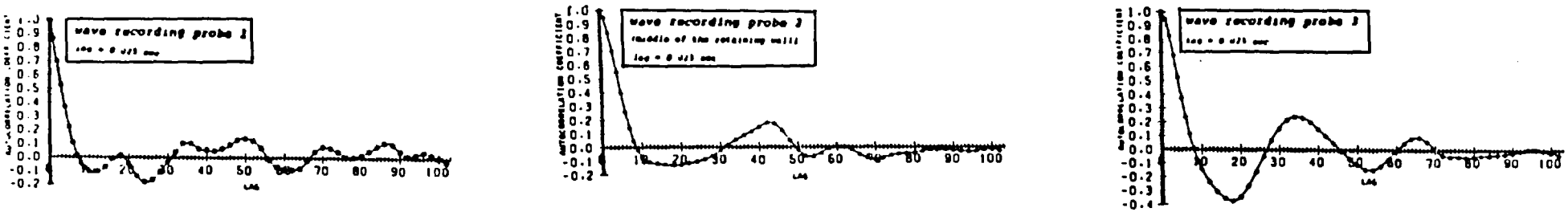


(a) *Run b14p1 : Correlograms of the wave height records at three different positions along the retaining wall*

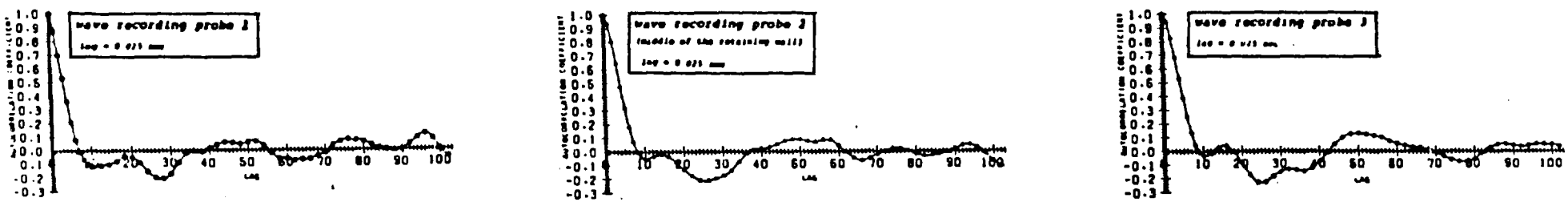


(b) *Run b14p2 ; Correlograms of the wave height records at three different positions along the retaining wall*

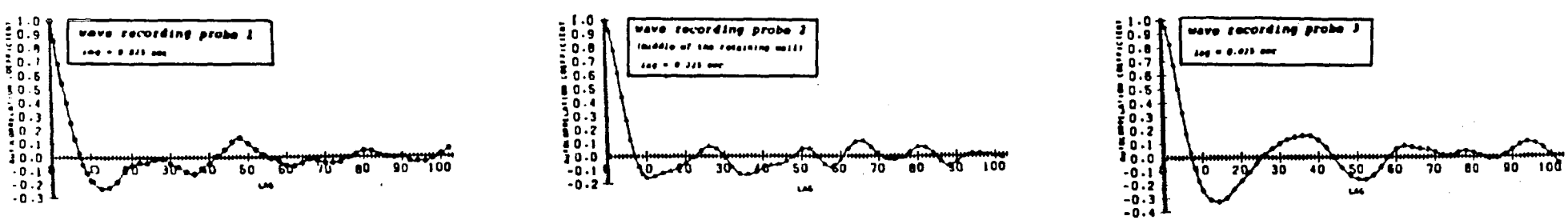


(c) *Run b17p1 : Correlograms of the wave height records at three different positions along the retaining wall*

Fig. F.37

$\tau \neq 0$ reflect to some extent the structure of the wave heights. All the correlograms show a rapid decay of the autocorrelation coefficient from $r_{\tau=0}=1$ after only a few time steps. Such a trend is characteristic of stationary random wave heights having a wide band of frequencies. The regularity of peaks and troughs in the correlograms reflects the pseudo-periodic behaviour of the wave heights. The correlograms approach their first zero value around the $\tau=8$ time interval. They remain negative for a considerable duration of the lag time. This implies that macropulsations of strong intensity were present in the wave heights at the retaining wall.

### F.4.3 Analysis of the Wave Heights in Frequency Domain

Power spectral density function was the best available method for considering the frequency properties of wave height records. In this investigation the spectrum was used essentially to detect non-random components in a wave height record. A property of a power spectrum, as was described in Chapter C, is that if there are periodicities in the water level record y(t), they appear as spikes in the spectrum. The amplitude of each spike is proportional to the contribution of the periodic component to the variance of the wave height record. A peak in the spectrum signifies the presence of a cyclic component. The underlying theoretical background for the calculation of power spectral density functions was discussed in Chapter C. In summary, for each wave height record, first, a Hanning window was applied to the first and the last 12.5% of the digitised wave height record. Secondly, since the sample size of all wave height records was $N=1024=2^{10}$, the Fast Fourier Transform could be applied to the tapered wave height record to achieve the raw periodogram ordinates. Thirdly, the raw periodogram was smoothed using the weights $^1/_4$, $^1/_2$, $^1/_4$ (3 point smoothing procedure) to estimate the power spectral density function $\hat{G}(f)$ of the wave height record. Each power spectral density function was then normalized by dividing its ordinates by the variance of the digitised wave height record.

The Nyquist frequency for all wave height records was equal to $f_N = \frac{1}{2\Delta t} = 20.3 H_z$ . An examination of all the power spectra made in this investigation in the range f=0 to f=20.3Hz showed that the ordinates of the power spectra beyond the frequency approximately equal to f=6Hz were very small. This means that the ordinates of power spectra near the Nyquist frequency contributed very little or nothing to the total variance and aliasing never occurred.

Figs. F.38, F.39, and F.40 show the normal power spectral density functions of the wave height records of size N=1024 at three different locations along the retaining wall for several test runs. In these figures $\hat{G}(f)/s^2$ was plotted as ordinate and the frequency f as abscissa, where $s^2$ is the variance of the wave height record. There was one feature which dominated all normal spectral density functions of the wave height records at the retaining wall, namely, they all had many peaks and troughs in a wide band of frequencies (less than 6Hz). The ordinates of all the power spectra between the frequency f=6Hz and $f=f_N$ were very small. All these aspects implied that the waves associated with the impingement of the flow on the retaining wall were not entirely random. In each spectrum, significant ordinates were spread over a range of frequencies; the variance was thus not concentrated at a single frequency as would be expected for a truly periodic process. A pseudo-periodic behaviour of the wave heights was detected in their correlograms. This was in fact observed in the water level records itself (see Plates XIII, XIV and XV) and was verified by their power spectra. However, in all spectra, a large proportion of the variance was accounted for by frequencies f less than approximately 3Hz.

The estimate of the spectrum from a sample size record equal to 1024 was merely one from an infinite numbers of possible samples of the same or of different sizes. However, because each estimated spectrum was one of many possible estimates, there was a certain amount of sampling error associated with the estimate. In the initial stage of the investigation, some tests were made to examine the variability of the power spectra at the retaining wall. A wave height record of size 1024 was divided into two equal parts of 512 points and the power spectra of the smaller records were compared with that of size 1024. It was observed that while all three spectra showed the same range of significant frequencies, there was a good deal of variation in the magnitude and location of the peaks. This test was repeated and confirmed for some other wave height records at the retaining wall. The conjecture as to whether these differences were inherent entirely in the waves themselves (eg. caused by an unstable process) or are a result of sampling error could only be ascertained by analysing spectra from larger samples. It is emphasized, however, that although the number and magnitude of the peaks of a power spectrum were affected by sampling error, the range of significant frequencies was bounded by fairly definite limits, which could be estimated quite accurately using a sample of 512 points or more.

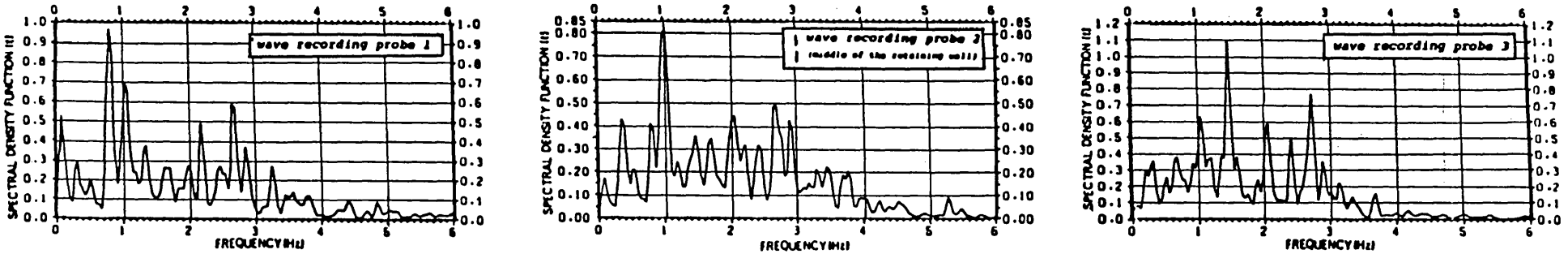


(a) *Run a25p1: Normal spectral density functions of the wave height records at three different poisitions along the retaining wall*

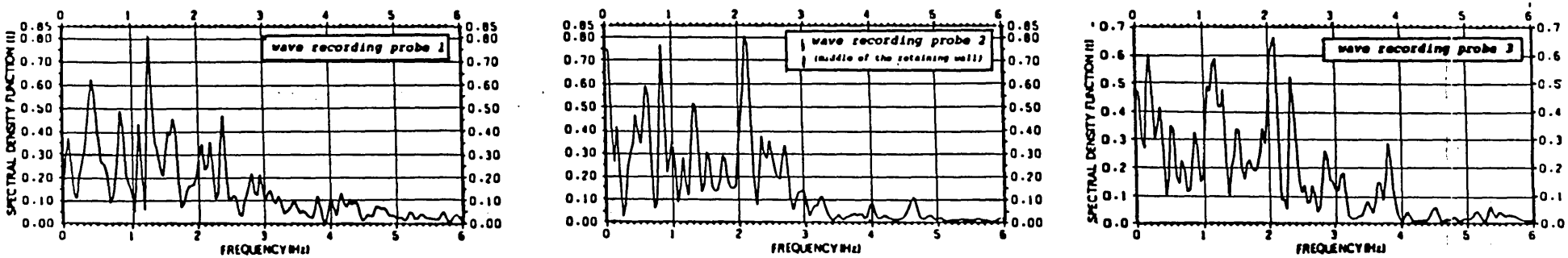


(b) *Run a25p2: Normal spectral density functions of the wave height records at three different poisitions along the retaining wall*

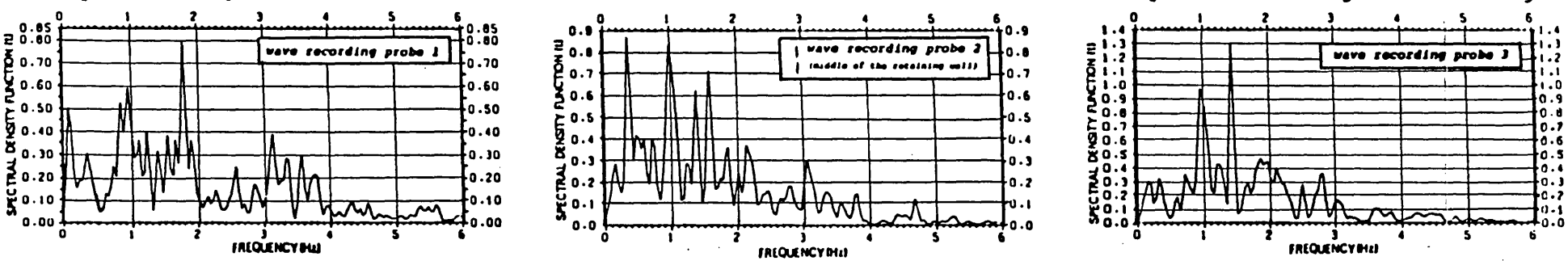


(c) *Run a25p3: Normal spectral density functions of the wave height records at three different poisitions along the retaining wall*

Fig. F.38

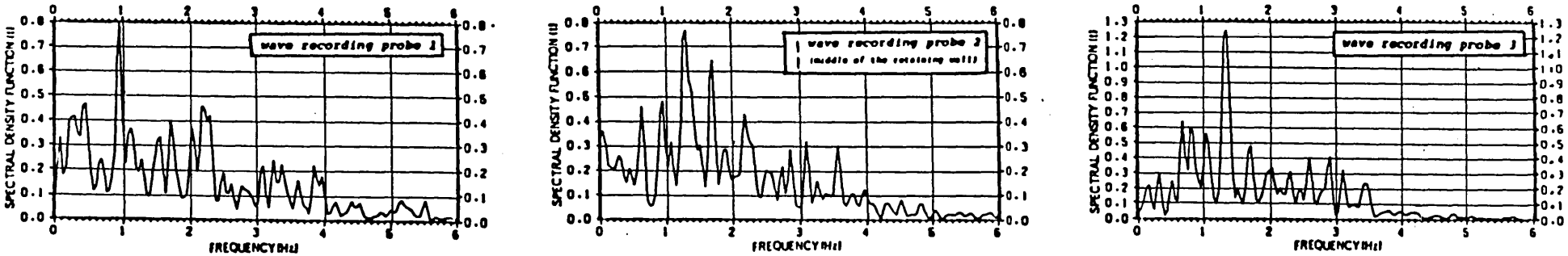


(a) *Run a36p1: Normal spectral density functions of the wave height records at three different poisitions along the retaining wall*

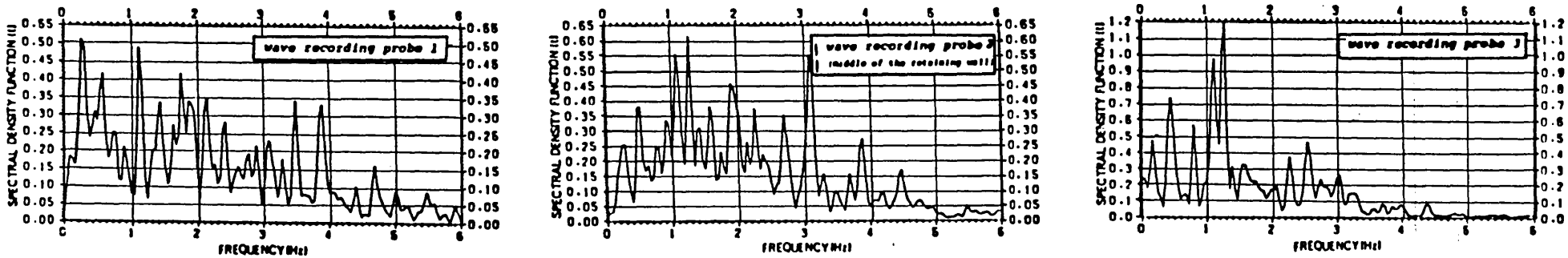


(b) *Run a36p2: Normal spectral density functions of the wave height records at three different poisitions along the retaining wall*

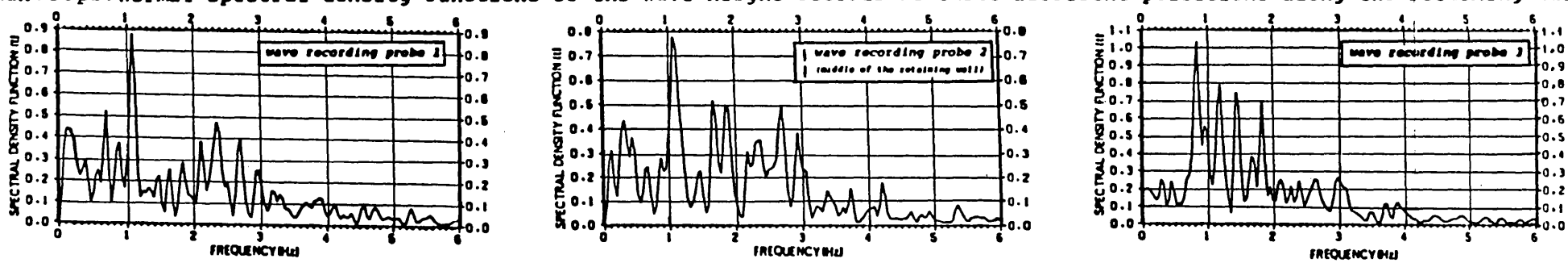


(c) *Run a36p3: Normal spectral density functions of the wave height records at three different poisitions along the retaining wall*

Fig. F.39

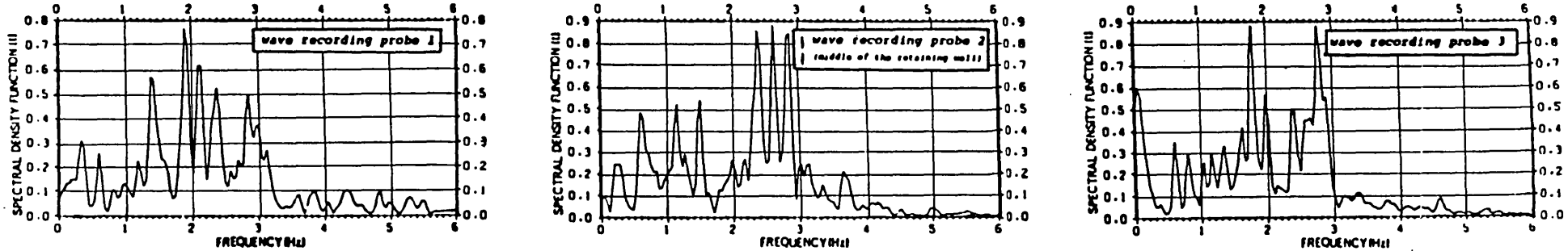


(a) *Run b08p1: Normal spectral density functions of the wave height records at three different poisitions along the retaining wall*

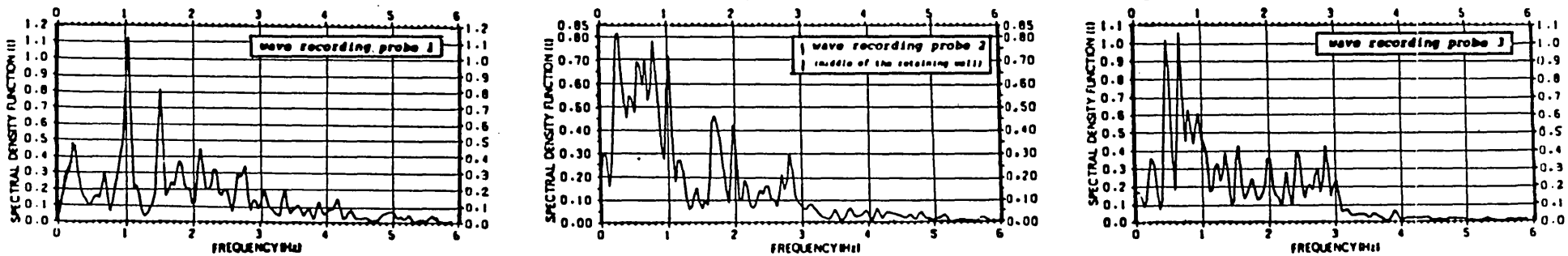


(b) *Run b14p3: Normal spectral density functions of the wave height records at three different poisitions along the retaining wall*

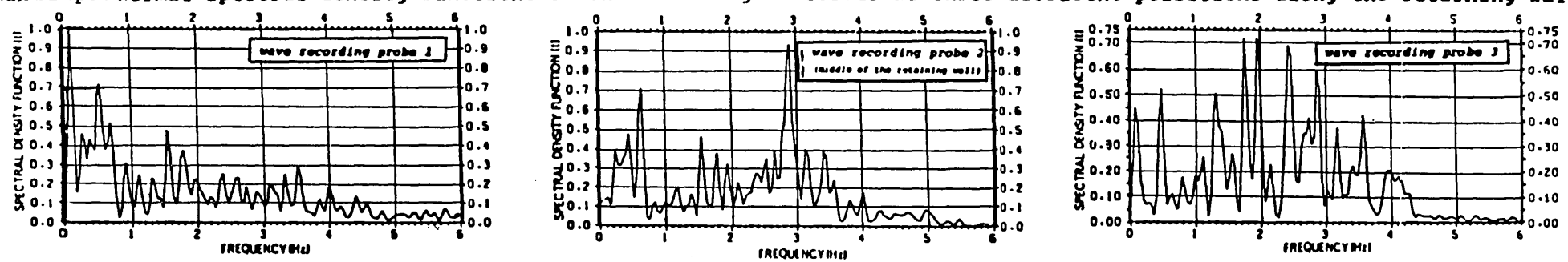


(c) *Run a14p1: Normal spectral density functions of the wave height records at three different poisitions along the retaining wall*

Fig. F.40

## F.5 SUMMARY OF CONCLUSIONS AND SUGGESTIONS FOR FURTHER RESEARCH

### F.5.1 Summary of Conclusions

The phenomena associated with a water jet of finite dimensions issuing from an overflow spillway when it is deflected by a smooth vertical transverse wall which is perpendicular to the initial flow direction was investigated both experimentally and analytically. The entire flow was divided into three different regions. In region I, which began at the toe of the spillway, the water depth remained approximately constant apart from a region adjacent to the outlet where a degree of lateral discharge was observed. The state of development of the supercritical water flow at the toe of the spillway was quasi-potential in all tests. In region II a forced hydraulic jump with a lateral discharge was observed. In region III the flow impinged violently on the retaining wall and became entirely parallel to it, resulting in a complex wave pattern at the wall. There was a surface and bed pressure gradient in a transverse cross-section (in a plane parallel to the retaining wall) in both regions II and III. In region II, near the channel outlet, the bed pressure and the surface profile fell considerably.

In region I and in the forward flow of region II, the flow remained two-dimensional with the velocity plane perpendicular to the channel bed and at an angle to the channel centre line. The redirection of the flow along the channel centre line in both regions I and II was found to be small enough such that for practical purposes it could be assumed that the flow per unit width along the channel centre line in region I and in the forward flow portion of region II remained parallel to the channel centre line. The secondary motions in region I affected the distribution of velocites and as a result the boundary layer thickness and the velocity profiles were not indentical at any one cross-section. The velocity profiles in the turbulent boundary layer in region I could be approximated by a power law, where the power varied approximately from a minimum of $\frac{1}{11}$ to a maximum of $\frac{1}{5}$ . The average power $n$ for the experiments was $\frac{1}{6.8}$ which indicated that the average behaviour of the boundary layer was in quite close agreement with $\frac{1}{7}$ power law.

The mean velocity characteristics in the forward portion of region II along the channel centre was investigated in a form relevant to a two-dimensional plane turbulent wall jet. The mean velocity in the forward flow was found to be self-similar when a velocity scale and a length scale were used. The similarity curve showed some deviation from the corresponding curve of the classical wall jet. With increasing distance from the toe of the forced

hydraulic jump in a downstream direction along the channel centre line, the length scale increased, while the maximum velocity decayed. The stream wise development of these scales showed some departures from those observed in classical wall jets. The mean velocity profiles in the outer layers were found to be self-similar and the similarity curve agreed reasonably well with the corresponding curve of the classical wall jet. In the inner layers, the velocity distributions were approximated by a power law and it was found that the power varied between approximately $\frac{1}{8}$ and $\frac{1}{14}$ . In conclusion, it can be said that the mean motion of the forward flow in region II behaved in a manner that was a typical of a plane turbulent wall jet. A procedure was developed to predict the surface profile along the channel centre line. Finally, the forward flow of region II became separated from the bed and impinged violently on the retaining wall. A mathematical condition for the separation of the forward flow was developed. The maximum pressure on the retaining wall was concentrated around the middle of the retaining wall. However, the pressure near the outlet dropped considerably.

The impingement of jet on the retaining wall produced a continuous disturbed periodic change in water level at the retaining wall with the frequency remaining less than approximately 3Hz. The fluctuating water level at the middle of the retaining wall was generally higher than that at other locations along the retaining wall. Using the governing dimensionless parameters, a mathematical relationship was developed to predict the wave distribution in amplitude domain at the middle of the retaining wall by a probabilistic approach. The ratio of the average wave height measured in respect of the mean water level to the mean water level at the retaining wall varied between 5.6% and 10.7. Some variability was observed in the magnitude and location of the peaks in the normal power spectral density functions of the wave height records at the retaining wall. In fact, the power spectra obtained were only approximations to the true power spectra. However, while the range of significant frequencies existing in the wave height at a given location along the retaining wall and for given flow parameters could easily be obtained from a sample spectrum, the details of the spectrum, beyond the relative variance contributions, were subject to a considerable sampling error. Increasingly accurate estimates of the power spectra could be made by increasingly large samples of data.

## F.5.2 Recommendations for Further Research

There is still a need for investigation into the general problem of a supercritical water flow deflected by a transverse wall. Suggestions for further research which was not possible in the present investigation are

a) The generality of the results presented could be checked in a similar investigation but under different geometry and scale conditions, and extended to encompass a wider range of Froude numbers, aspect ratios and the ratios of impingement length to impingement width. It would be especially interesting to extend the present investigation to a short or a square impingement where the impingement length is less or equal to the impingement width.

b) The pressure fluctuations on the channel bed in the impingement region may cause severe loading conditions on the channel bed resulting in damage through the mechanism of fatigue or structural resonance etc. The stochastic character of the pressure field on the channel bed in the impingement region could also be studied. It would be instructive to compare the power spectra of the fluctuating pressures with those of the wave heights at the retaining wall.

c) The pressure on the retaining wall was of a fluctuating nature. A detailed study of the stochastic behaviour of the pressure field on the retaining wall might improve its design. A spectral analysis of the various fluctuating pressures on the retaining wall subjected to the impinging jet flow together with an exploration of the fluctuating pressure field on the portion of the side wall which is adjacent to the retaining wall may give a further insight into the complex behaviour of the flow in the impingement region.

d) An exploration of the mean velocity characteristics in the forward flow of region II in a transverse direction (parallel to the retaining wall) has still to be attempted. It would be especially interesting to check the generality of the results obtained along the channel centre line in region II for the section close to the channel outlet.

e) The internal structure of the flow can become clearer by measurements of the quantities such as Reynolds stresses, boundary shear stresses, turbulent intensities etc, especially in the impingement region. Sophisticated instrumentation such as a Laser-Doppler Anemometer system would be required to obtain accurate and reliable measurements of these quantities.

# APPENDICES

## APPENDIX I

## THE DIRAC DELTA FUNCTION

Given the function shown in Fig. I.1, which consists of a suddenly applied excitation of constant magnitude acting for a certain period of time which then suddenly ceases, the product of duration and magnitude being unity. If $\varepsilon$, the period of application, is small, the magnitude of the excitation $1/\varepsilon$ is very great. It is sometimes convenient to pursue this idea to the limit and imagine a forcing function of arbitrarily large magnitude acting for an infinitesimal time, the product of duration and intensity remaining unity as $\varepsilon \to 0$. The resulting

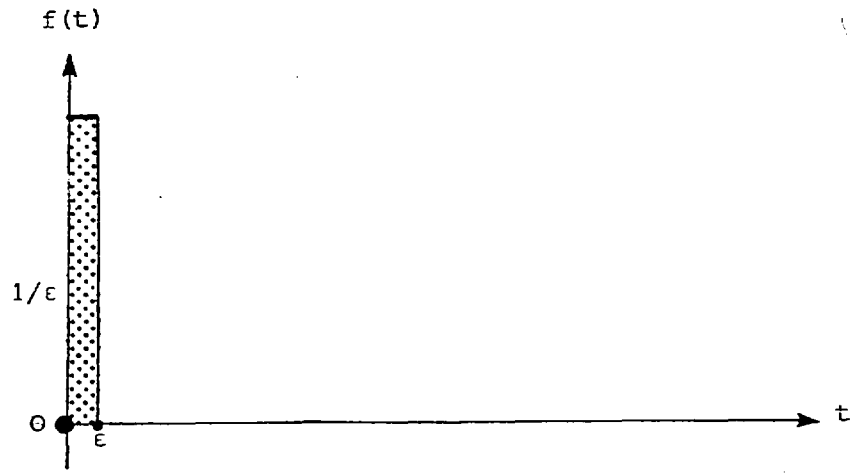


Fig. I.1 Plot suggesting the nature of a unit impulse

'funtion' is usually referred to as the *unit impulse,* the *delta function* $\delta(t)$ or *Dirac delta function.*

In somewhat different terms, the $\delta$ function $\delta(t-t_o)$ may be described by the following definition

$$\delta(t-t_o) = \begin{cases} 0, & t \neq t_o \quad \text{(a)} \\ \infty, & t = t_o \quad \text{(b)} \end{cases} \qquad \text{(I.1)}$$

such that

$$\int_{-\infty}^{+\infty} \delta(t-t_o)\,dt = 1 \qquad \text{(c)}$$

But while this definition is intuitively helpful, it is mathematically meaningless.

One interesting and important property of the Dirac function is its ability to isolate or reproduce a particular value of a function $f(t)$ (continuous at $t = t_o$) according to the following formula

$$\int_{-\infty}^{+\infty} f(t)\delta(t-t_o)dt = f(t_o) \tag{I.2}$$

Because of this property, it is sometimes called the *spotting* function since it picks out one particular value of $f(t)$. In a similar manner, it is possible to define the mth derivative of a delta function, namely $\delta^{(m)}(t)$. This can be used to select the mth derivative of a function at a given point. This leads to a generalization of Eq. (I.2), namely

$$\int_{-\infty}^{+\infty} \delta^{(m)}(t-t_o)f(t)dt = (-1)^m f^{(m)}(t_o) \tag{I.3}$$

Using Eq. (I.3), the first moment of $\delta'(t)$ is

$$\int_{-\infty}^{+\infty} \delta'(t)t\,dt = -1 \tag{I.4}$$

It is important to realize that $\delta(t-t_o)$ is *not* a function, rather it is a generalized function, or distribution, which maps a function into the real line. It can be handled as if it were an ordinary function with particular interest in the values of integrals involving $\delta(t-t_o)$ rather than the value of $\delta(t-t_o)$ by itself.

The delta function has the following Fourier Transform pair

$$\left.\begin{aligned} &\int_{-\infty}^{+\infty} \delta(f)e^{2\pi ift}df = 1 \qquad (a)\\ &\int_{-\infty}^{+\infty} e^{-2\pi ift}dt = \delta(f) \qquad (b)\end{aligned}\right\} \tag{I.5}$$

## APPENDIX II

## THE CHI-SQUARED DISTRIBUTION

Becuase the *chi-squared* distribution occupies a central position in the approximation to the distribution of smoothed estimators of the energy density function, an outline of this distribution is given below.

A random variable $\chi^2$ ($\chi^2$ is used rather than just $\chi$ to emphasize that the statistic cannot be negative) having probability density function given by

$$f(\chi^2) = \frac{1}{2^{\nu/2}\,\Gamma(\nu/2)}\,\chi^{(\nu-2)}\,e^{-\chi^2/2} \qquad \text{(II.1)}$$

where $\Gamma(\nu/2) = \int_0^\infty e^{-t} t^{(\nu/2)-1} dt$ for $\nu > 0$ is the *Gamma function* with argument $\nu/2$, is said to be a chi-squared or $\chi^2_\nu$ distribution with $\nu$ degrees of freedom. The distribution is always skewed to the right and has a mean value equal to the number of degrees of freedom i.e.

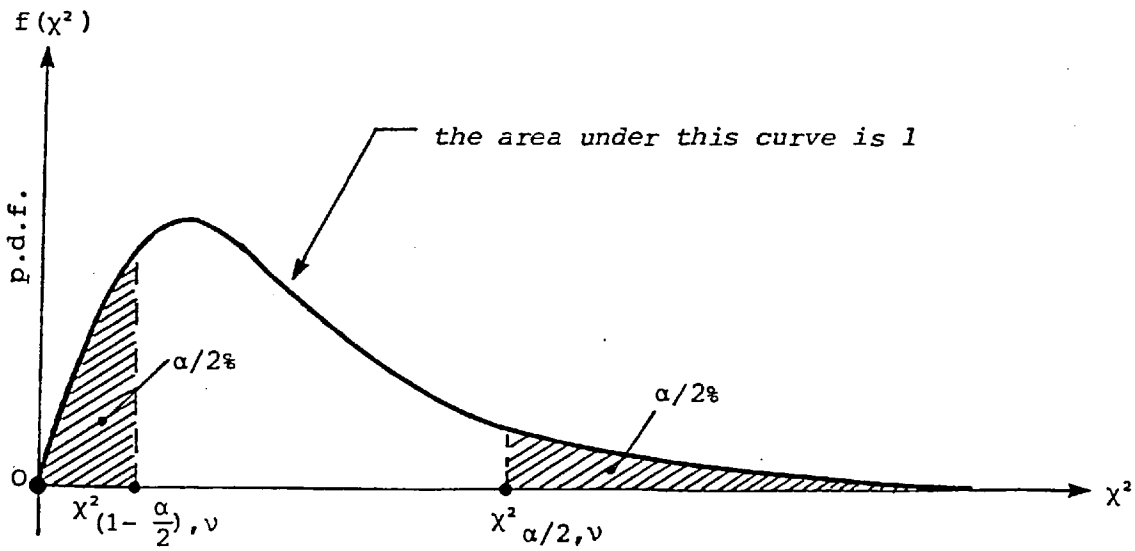


Fig. II.1 Chi-squared probability density function

$$E[\chi^2_\nu] = \nu \qquad \text{(a)}$$

and

$$\mathrm{Var}[\chi^2_\nu] = 2\nu \qquad \text{(b)} \qquad \text{(II.2)}$$

so coefficient of dispersion $= \sqrt{2/\nu}$

For large values of $\nu$, the distribution tends towards the *normal distribution*. An example of a $\chi^2_\nu$ distribution is shown in Fig. II.1. The percentage point $\chi^2_{\beta,\nu}$ is chosen so that the proportion of the distribution, with $\nu$ degrees of freedom, which lies above it, is equal to $\beta$.

# APPENDIX III

## THE LINEAR REGRESSIONS

It is often possible to see, by inspection of the scatter diagram, that a smooth curve can be fitted to the data. In particular, if a straight line can be fitted to, n (n>2), pairs of measurements, $(x_1,y_1)$ ... ... $(x_n,y_n)$, where $y_i$ is the dependent variable and $x_i$ is the independent variable, then it can be said that a *linear* relationship exists between the two variables and that a *regression* analysis will fit the *best line* through the points. Regression analyses, in general, are based on the following assumptions:

(a) There is no uncertainty in the indepednent variable x

(b) For a given x, the y values *normally* distributed with a variance $s_e^2$

(c) The variance $s_e^2$ is the same for all values of x.

Two cases are separately described here.

### III.1 The Linear Regression with Constant

The regression analysis fits a straight line of the form $y = bx+a$ to the data points, where b is the *regression coefficient* and a is the *regression constant*. The quantities normally calculated are summarized as follows:

(a) Means

$$\left.\begin{aligned} \bar{x} &= \Big(\sum_{i=1}^{n} x_i\Big)/n \quad \text{(a)} \\ \bar{y} &= \Big(\sum_{i=1}^{n} y_i\Big)/n \quad \text{(b)} \end{aligned}\right\} \text{(III.1)}$$

(b) Standard deviations

$$\left.\begin{aligned} s_x &= \Big[\sum_{i=1}^{n} (x_i-\bar{x})^2/(n-1)\Big]^{\frac{1}{2}} \quad \text{(a)} \\ s_y &= \Big[\sum_{i=1}^{n} (y_i-\bar{y})^2/(n-1)\Big]^{\frac{1}{2}} \quad \text{(b)} \end{aligned}\right\} \text{(III.2)}$$

(c) The Pearson product-moment correlation coefficient

$$r = \Big[\sum_{i=1}^{n} (x_i-\bar{x})(y_i-\bar{y})\Big]/\Big[\sum_{i=1}^{n} (x_i-\bar{x})^2 \sum_{i=1}^{n} (y_i-\bar{y})^2\Big]^{\frac{1}{2}} \qquad \text{(III.3)}$$

(d) The regression coefficient, b, and the regression constant, a

$$b = \left[\sum_{i=1}^{n} (x_i-\bar{x})(y_i-\bar{y})\right] / \sum_{i=1}^{n} (x_i-\bar{x})^2 \quad \text{(a)}$$

$$a = \bar{y} - b\bar{x} \quad \text{(b)} \qquad \text{(III.4)}$$

(e) The sum of squares attributable to the regression, s.s.r., the sum of squares of deviations about the regression, s.s.d., and the total sum of squares, s.s.t are

$$\text{s.s.t.} = \sum_{i=1}^{n} (y_i-\bar{y})^2 \quad \text{(a)}$$

$$\text{s.s.d.} = \sum_{i=1}^{n} (y_i-a-bx_i)^2 \quad \text{(b)} \qquad \text{(III.5)}$$

$$\text{s.s.r.} = \text{s.s.t.} - \text{s.s.d.} \quad \text{(c)}$$

(f) The degrees of freedom attributable to the regression, d.f.r., the degrees of freedom of deviations about the regression, d.f.d, and the total degrees of freedom, d.f.t., are

$$\text{d.f.t.} = n-1 \quad \text{(a)}$$

$$\text{d.f.d.} = n-2 \quad \text{(b)} \qquad \text{(III.6)}$$

$$\text{d.f.r.} = 1 \quad \text{(c)}$$

(g) The mean square attributable to the regression, m.s.r., and the mean square of deviations about the regression, m.s.d.

$$\text{m.s.r.} = (\text{s.s.r.})/(\text{d.f.r.}) \quad \text{(a)}$$

$$\text{m.s.d.} = s_e^2 = (\text{s.s.d.})/(\text{d.f.d.}) \quad \text{(b)} \qquad \text{(III.7)}$$

(h) The standard error of the regression coefficient, s.e.(b), the standard error of the regression constant, s.e.(a), the standard error of the predicted value for a given x, s.e.($y_p$), and 100(1-$\alpha$) confidence interval for $y_p$,

$$\text{s.e.(b)} = [(\text{m.s.d.})/\sum_{i=1}^{n}(x_i-\bar{x})^2]^{\frac{1}{2}} \quad \text{(a)}$$

$$\text{s.e.(a)} = \{(\text{m.s.d})[\frac{1}{n} + \bar{x}^2/\sum_{i=1}^{n}(x_i-\bar{x})^2]\}^{\frac{1}{2}} \quad \text{(b)}$$

$$\text{s.e.}(y_p) = \{\text{m.s.d.}[1 + \frac{1}{n} + \frac{(x-\bar{x})^2}{\sum_{i=1}^{n}(x-\bar{x})^2}]\}^{\frac{1}{2}} \quad \text{(c)}$$

(III.8)

$$\text{uncertainty for } y_p = t_{\alpha/2,(n-2)}\{\text{m.s.d.}[1 + \frac{1}{n} + \frac{(x_o-\bar{x})^2}{\sum_{i=1}^{n}(x_i-\bar{x})^2}]\}^{\frac{1}{2}} \quad \text{(d)}$$

where $t$ is the value of the mathematical function known as Student $t$.

## III.2 The Linear Regression with no Constant

The regression analysis fits a straight line of the form $y = bx$ to the data points, where b is again called the regression coefficient. The quantities normally calculated are summarized below

(a) Means

$$\bar{x} = (\sum_{i=1}^{n} x_i)/n \quad \text{(a)}$$

$$\bar{y} = (\sum_{i=1}^{n} y_i)/n \quad \text{(b)}$$

(III.9)

(b) Standard deviations

$$s_x = [\sum_{i=1}^{n}(x_i-\bar{x})^2/(n-1)]^{\frac{1}{2}} \quad \text{(a)}$$

$$s_y = [\sum_{i=1}^{n}(y_i-\bar{y})^2/(n-1)]^{\frac{1}{2}} \quad \text{(b)}$$

(III.10)

(c) The Pearson product-moment correlation coefficient

$$r = [\sum_{i=1}^{n}(x_i-\bar{x})(y_i-\bar{y})]/[\sum_{i=1}^{n}(x_i-\bar{x})^2 \sum_{i=1}^{n}(y_i-\bar{y})^2]^{\frac{1}{2}} \quad \text{(III.11)}$$

(d) The regression coefficient, b, and the regression constant, a

$$b = [\sum_{i=1}^{n} (x_i y_i)]/[\sum_{i=1}^{n} x_i^2] \qquad \text{(III.12)}$$

(e) The sum of squares attributable to the regression, s.s.r., the sum of squares of deviations about the regression, s.s.d, and the total sum of squares, s.s.t.

$$\left.\begin{aligned} \text{s.s.t.} &= \sum_{i=1}^{n} y_i^2 && \text{(a)} \\ \text{s.s.d.} &= \sum_{i=1}^{n} (y_i - bx_i)^2 && \text{(b)} \\ \text{s.s.r.} &= \text{s.s.t.} - \text{s.s.d.} && \text{(c)} \end{aligned}\right\} \text{(III.13)}$$

(f) The degrees of freedom attributable to the regression, d.f.r., the degrees of freedom of deviations about the regression, d.f.d, and the total degrees of freedom, d.f.t., are

$$\left.\begin{aligned} \text{d.f.t.} &= n && \text{(a)} \\ \text{d.f.d.} &= n-1 && \text{(b)} \\ \text{d.f.r.} &= 1 && \text{(c)} \end{aligned}\right\} \text{(III.14)}$$

(g) The mean square attributable to the regression, m.s.r., and the mean square of deviations about the regression, m.s.d.

$$\left.\begin{aligned} \text{m.s.r.} &= (\text{s.s.r.})/(\text{d.f.r.}) && \text{(a)} \\ \text{m.s.d.} &= s_e^2 = (\text{s.s.d.})/(\text{d.f.d}) && \text{(b)} \end{aligned}\right\} \text{(III.15)}$$

(h) The standard error of the regression coefficient, s.e.(b)

$$\text{s.e.(b)} = [(\text{m.s.d.})/\sum_{i=i}^{n} x_i^2]^{\frac{1}{2}} \qquad \text{(III.16)}$$

# REFERENCES

ABDUL KHADER, M.H. and ELANGO,K. (1974), "Turbulent pressure field beneath a hydraulic jump". J.Hyd.Res.,12,4,469-489.

ABRAMOVICH, G.N. (1963), "The theory of turbulent jets". MIT Press, Cambridge, Massachusetts.

ARBHABHIRAMA, A. and ABELLA, A.U. (1971), "Hydraulic jump within gradually expanding channel". J.Hyd.Div.Am.Soc.Civ.Engrs., 97,HY1,31-42.

BAUER, W.J. (1954), "Turbulent boundary layer on steep slopes". Trans. Am.Soc.Civ.Engrs.,119,1212-1232.

BÉLANGER, J.B. (1828), "Essai sur la solution numérique de quelques problemes relatifs au mouvement permanent des eaux courantes". Carikan-Goeury,Paris.

BENDAT, J.S. and PIERSOL, A.G. (1971), "Measurement and analysis of random data". 2nd edn. John Wiley and Sons, New York.

BERGLAND, G.D. (1969), "A guided tour of the Fast Fourier Transform". IEEE Spectrum,41-52.

BINGHAM, C.,GODFREY, M.D. and TUKEY, J.W. (1967), "Modern techniques of power spectrum estimation". IEEE Trans.on Audio and Electroacoustics, AU-15,2,56-66.

BLACKMAN, R.B. and TUKEY, J.W. (1958), "The measurement of power spectra". Dover Publications Inc. New York.

BLENCH, T. (1969), "Dimensional analysis and dynamical similarity for hydraulic engineers". Univ. of Alberta Press, Edmonton, Alberta, Canada.

BOWERS, C.E. and TSAI, F.Y. (1969), "Fluctuating pressures in spillway stilling basins". J.Hyd.Div.Am.Soc.Civ.Engrs.,95,HY6, 2071-2079.

BRACEWELL, R. (1965), "The Fourier Transform and its application". McGraw-Hill, New York.

BRADLEY, J.N. and PETERKA, A.J. (1957), "The hydraulic design of stilling basin". J.Hyd.Div.Am.Soc.Civ.Engrs.,83,HY5,1-24.

BRADSHAW, P. and GEE, M.T. (1962), "Turbulent wall jets with and without an external stream". Rep.Memor.Aero.Res.Coun.,No.3252, London.

BRADSHAW, P., GOODMAN, M.P. and DOROTHY, G.(1968),"The effect of turbulence on static pressure tubes". Rep.Memor.Aero.Res.Coun., No.3257,London.

BRITISH STANDARDS INSTITUTION (1975), "Glossary of terms used in metrology". British Standard 5233, London.

BRUNDRETT, E. and BAINES, W.D. (1964), "The production and diffusion of vorticity in duct flow". J.Fl.Mech., 19,375-394.

BRYER,D.W. and PANKHURST, R.C. (1971), "Pressure-probe methods for determining wind speed and flow direction". N.P.L., HMSO.

CAMPBELL, F.B., COX, R.G. and BOYD, M.B. (1965), "Boundary layer development and spillway energy losses". J.Hyd.Div.Am.Soc. Civ.Engrs.,91,HY3,149-163.

CHATFIELD, C. (1975a), "Statistics for technology". Chapman and Hall, London.

CHATFIELD, C. (1975b), "The analysis of time series: Theory and practice". Chapman and Hall, London.

CHIARI, F. (1976), "The height of the retaining wall for side-channels and pools". M.Sc.Thesis, Univ. of London.

CHIU, C.L., HSIUNG, D.E. and Lin, H.C. (1978), "Three-dimensional open channel flow". J.Hyd.Div.Am.Soc.Civ.Engrs., 104,HY8, 1119-1136.

CHOW, V.T. (1959), "Open-channel hydraulics". McGraw-Hill, New York.

COOLEY, J.W. LEWIS, P.A.W. and WELCH, P.D. (1969), "Historical notes on the Fast Fourier Transform". IEEE Trans. On Audio and Electroacoustics, AU-17,2,77-85.

COOLEY, J.W. and TUKEY, J.W. (1965), "An algorithm for the machine calculation of complex Fourier series". Math.Computation, 19,297-301.

DELLEUR, J.W. (1957), "The boundary layer development in open channels". Proc.Am.Soc.Civ.Engrs., 83,EM1,1-24.

DRAPER, L. (1963), "Derivation of design wave from instrumental records of sea waves". Proc. I.C.E.,26,291-304.

DWIGHT, H.B. (1961), "Tables of integrals and other mathematical data". 4th edn., Macmillan, New York.

EICHELBRENNER, E.A. and DUMARGUE, P. (1962), "Le problem du jet pariétal plan en régime turbulent pour un écoulement extérieur de vitesse $U_e$ constante". J.Mécanique,1,1,109-134 and 1,2,123-152.

ELEVATORSKI, E.A. (1959), "Hydraulic energy dissipators". McGraw-Hill, New York.

ESKINAZI, S. and YEH, H. (1956), "An investigation on fully developed turbulent flows in a curved channel". J.Aero.Sci., 23,23.

ETTE, V. (1973), "Statistical properties of ocean waves". Intern. Courses in Hydraulic and Sanitary Engineering,Delft, The Netherlands

FLÔRES, J.O. (1954), "Le ressaut". La Houille Blanche, 10,811-822.

FÖRTHMANN, E. (1936), "Turbulent jet expansion". Technical Memorandum No. 789, Natl.Advisory Committee on Aeronautics, Washington, D.C.

FORSTER, J.W. and SKRINDE, R.A. (1950), "Control of the hydraulic jump by sills". Trans.Am.Soc.Civ.Engrs.,115,973-1022.

FUNKE, E.R. (1960), "Correlation function and power spectral density analysis". A paper presented at the Boston Meeting of Am.Soc.Civ.Engrs.

FUNKE, E.R., STOCK, F.T. and GROVES, L. (1968), "A digital programme for on-line correlation and power spectral density analysis". N. Res. Coun., Rep.DME MK-23,Ottawa.

GANGADARIAH, T., LAKSHMANA RAO, N.S. and SEETHARAMIAH, K. (1970), "Inception and entrainment in self-aerated flow". J.Hyd.Div.Am. Soc.Civ.Engrs., 96,HY7,1171-1184.

GARG, S.P. and SHARMA, H.R. (1971), "Efficiency of hydraulic jump". J. Hyd.Div.Am.Soc.Civ.Engrs., 97,HY3,409-420.

GARTSHORE, I.S. and NEWMAN, B.G. (1969), "The turbulent wall jet in an arbitrary pressure gradient". Aero.Quart., 20,25-65.

GERARD,R. (1978), "Secondary flow in non-circular conduit". J.Hyd.Div. Am.Soc.Civ.Engrs., 104,HY5,733-755.

GLAUERT, M.B. (1956), "The wall jet". J.Fl.Mech.,1,625-643.

GOLDSTEIN, S. (1936), "A note on the measurement of total head and static pressure in a turbulent stream". Proc.Roy.Soc.,A155,570

GÖRTLER, H. (1942), "Berechnung von aufgaben der frein turbulenz auf grund eines neuen Näherungsansatzes". ZAMM22,244-254.

GREGORIUS, B.H. (1976), "The spectral analysis of waves generated in a hydraulic jump". M.Sc.Thesis, Univ.of London.

HARLEMAN,D.R.F. (1955), "Effect of baffle piers on stilling basin performance". J.Boston Soc.Civ.Engrs.,42,84-99.

HARRISON, A.J.M. (1965), "Some problems concerning flow measurement in steep rivers". J.Instn.Wtr.Engrs.,19,469-474.

HARRISON,A.J.M., WHITE,W.R.,PERKINS,J.A. and ACKERS,P.(1978), "Weirs and flumes for flow measurement". A Wiley-interscience Publication, John Wiley and Sons, New York.

HARTUNG, F.and CSALLNER, K. (1967), "The scouring energy of the macroturbulent flow downstream of a hydraulic jump". Proc.12th Cong.Intern. Ass.Hyd.Res.,(Fort Collins), 3,97-102.

HAYWARD, A.T. (1977), "Repeatability and accuracy". Mechanical Engineering Publication LTD, London and New York.

HENDERSON, F.M. (1966), "Open channel flow". Macmillan, London.

HENRY, H.R. (1950), "A study of flow from a submerged sluice gate". M.Sc.Thesis, State Univ. of Iowa.

HERBRAND, K. (1973), "The spatial hydraulic jump". J.Hyd.Res.,11,3, 205-218.

JENKINS, G.M. and WATTS, D.G. (1968), "Spectral analysis and its applications". Holden-Day.

JOHANSEN, F.C. and OWER, E. (1932), "On a determination of the pitot-static tube factor at low Reynolds numbers with special reference to the measurement of low air speeds". Proc. Roy.Soc.,A136,153.

KAMPHUIS, J.W. (1969), "Introduction to wave spectrum analysis". C.E. Res., Rep. No.64, Civ.Engng.Dept., Queen's Univ. at Kingston, Ontario, Canada.

KAO, T.Y. (1971), "Hydraulic jump assisted by a cross jet". J.Hyd.Div. Am.Soc.Civ.Engrs., 97,HY12,2037-2050.

KARKI, K.S. (1976), "Supercritical flow over sills". J.Hyd.Div.Am.Soc. Civ.Engrs.,102,HY10,1449-1459.

KAWALL, J.G. and KEFFER, J.R. (1971), "Digital analysis of turbulent signals". Rep.UTMETP7104, Mech.Engng.Dept., Univ. of Toronto, Canada.

KELLER, R.J. LAI, K.K. and WOOD, I.R. (1974), "Developing region in self-aerated flows". J. Hyd.Div.Am.Soc.Civ.Engrs.,100,HY4, 553-568.

KENDALL, M.G. and STUART, A. (1968), "The advanced theory of statistics". 3,2nd edn., Griffin & Co.

KINSMAN, B. (1965), "Wind waves". Englewood Cliffs, Prentice-Hall, Inc.

KLINE, S.J. and McLINTOCK, F.A. (1953), "Describing uncertainties in single-sample experiments". Mech.Engng.,75,3-8.

KOHAN, S.M. (1969), "Some studies of the intermittent region and wall region of a two-dimensional plane wall jet". Ph.D. Thesis, Chem.Engng.Dept. Stanford Univ.

KOOPMANS, L.H. (1974), "The Spectral analysis of time series". Academic Press, New York and London.

LARSON, H.J. (1975), "Statistics: An inroduction". John Wiley and Sons, New York.

LEUTHEUSSER, H.J. and KARTHA, V.C. (1972), "Effects of inflow condition on hydraulic jump". J.Hyd.Div.Am.Soc.Civ.Engrs., 98,HY8,1367-1385.

LIGHTHILL, M.J. (1961), "Introduction to Fourier Analysis and Generalized Functions". Cambridge, Univ. Press.

LIU, H.K. (1949), "Diffusion of flow from a submerged sluice gate". M.Sc. Thesis, State Univ. of Iowa.

LONGUET-HIGGINS, M.S. (1952), "On the statistical distribution of heights of sea waves". J. Marine Res.,X,3,245.

MASSEY, B.S. (1968), "Mechanics of fluid". Van Nostrand Company, New York.

MATALAS, N.C. (1967), "Time series analysis". Water Resour.Res.,3,817-829.

MATHIEU, J. (1959), "Evolution d'un jet plan frappant sous une incidence de $7^{o}$ une plaque plan lisse". Comptes Rendus, Acad. Sci.,248,2713.

MATHIEU, J. and TAILLAND, A. (1963), "Étude d'un jet plan dirigé tangentiellement à une paroi". Comptes Rendus, Acad. Sci.,Paris,257,44-47.

McCORQUODALE, J.A. and REGTS, E.H. (1968), "A theory for the forced hydraulic jump". Trans.Engng.Instn.Canada, 11,C-1.

MOORE, W.L. and MORGAN, C.W. (1959), "Hydraulic jump at an abrupt drop". Trans.Am.Soc.Civ.Engrs.,124,507-524.

MUNK,W.H. and SVERDRUP, H.V. (1947), "Wind, sea and swell theory of relations for forecasting". U.S. Hydrogr.Office, Publ.601.

MYERS, G.E., SCHAUER, J.J. and EUSTIS, R.H. (1963), "Plane turbulent wall jet flow development and friction factor". J. Bas.Engng., Trans.Am.Soc.Mech.Engrs.,85,47-54.

NAAS, S.L. (1972), "The characteristics of the hydraulic jump over a rock susage basin". M.Sc.Thesis, Univ. of Colorado.

NARASIMHA, R., NARAYAN, K.Y. and PARTHASARATHY, S.P. (1973), "Parametric analysis of turbulent wall jets in still air". Aero. J.,77,355-359.

NARAYANAN, R. (1975), "Wall jet analogy to hydraulic jump". J.Hyd.Div.Am. Soc.Civ.Engrs.,101,HY3,347-358.

OTNES,R.K. and ENOCHSON, L. (1972), "Digital time series analysis". John Wiley and Sons, New York.

OWER, E. and PANKHURST, R.C. (1966), "The measurement of air flow". 4th edn.,Chapman and Hall,London.

POWELL, R.W. and POSEY, C.J. (1959), "Resistance experiments in a triangular channel". J. Hyd.Div.Am.Soc.Civ.Engrs., 85,HY5,31-59.

PRANDTL, L. (1904), "Über flüssigkeiten bei sehr kleiner reibung". 3rd. Intern. Mathematics Cong., Heidelberg.

PRESTON, J.H. (1972), "Measurement of low velocities". Physics.E,Sci, Instrum.,5,277.

RAJARATNAM, N. (1964), "The forced hydraulic jump". Water Power,14-19 and 61-65.

RAJARATNAM, N. (1965a), "The hydraulic jump as a wall jet". J.Hyd.Div. Am.Soc.Civ.Engrs.,91,HY5,107-132.

RAJARATNAM, N. (1965b), "Submerged hydraulic jump". J. Hyd,Div.Am.Soc.Civ. Engrs.,91,HY4,71-96.

RAJARATNAM, N. (1967), "Advances in hydroscience - Hydraulic jumps". 4, edn.Ven Te Chow, Academic Press,New York.

RAJARATNAM, N. (1976), "Turbulent jets". Elsevier Scientific Publishing Co., Amsterdam, The Netherlands.

RAJARATNAM, N. and MURAHARI, V. (1971), "A contribution to forced hydraulic jumps". J.Hyd.Res.,9,2,217-239.

RAJARATNAM, N. and ORTIZ, N.V. (1977), "Hydraulic jumps and waves at abrupt drops". J.Hyd.Div.Am.Soc.Civ.Engrs.,103,HY4, 381-394.

RAJARATNAM, N. and RAO, N.S.G. (1963), "The submerged hydraulic jump". J.Hyd.Div.Am.Soc.Civ.Engrs.,89,HY1,139-162.

RAJARATNAM, N. and SUBRAMANYA, K. (1967), "Diffusion of rectangular wall jets in wider channels". J.Hyd.Res.,5,2,281-294.

RAJARATNAM, N. and SUBRAMANYA, K. (1968), "Hydraulic jump below abrupt symmetrical expansions". J. Hyd.Div.Am.Soc.Civ.Engrs., 94,HY2,481-503.

RAND, W. (1965), "Flow over a vertical sill in an open channel". J.Hyd. Div.Am.Soc.Civ.Engrs.,91,HY4,97-121.

RAY, A.K. (1956), "On the effect of orifice size on static-pressure reading at different Reynolds numbers". Ingènieur-Archiv.,24.

RESCH, F.J. and LEUTHEUSSER (1971), "Mesures de turbulence dans le ressaut hydraulique". La Houille Blanche,1,17-31.

RESCH, F.J. and LEUTHEUSSER, H.J. (1972), "Étude de la structure cinématique et dynamique du ressaut hydraulique". J.Hyd.Res.,8,3, 293-318.

REYNOLDS, A.J. (1974), "Turbulent flows in engineering". A Wiley-Interscience Publication, John Wiley and Sons, London - New York.

ROUSE, H. (1959), "Advanced mechanics of fluids". John Wiley and Sons, New York.

ROUSE, H., BHOOTA, B.V. and HSU, E.Y. (1951), "Design of channel expansions". Trans.Am.Soc.Civ.Engrs.,116,347-363.

ROUSE, H. and INCE, S. (1957), "History of hydraulics". Iowa Inst. of Hyd.Res., State Univ. of Iowa.

ROUSE, H., SIAO, T.T. and NAGARATNAM, S. (1959), "Turbulence characteristics of the hydraulic jump". Trans.Am.Soc.Civ.Engrs.,124, 926-966.

SARMA, K.V.N. and NEWNHAM, D.A. (1973), "Surface profiles of hydraulic jump for Froude numbers less than four". Water Power, 139-142.

SCHLICHTING, H. (1960), "Boundary layer theory". Translated from German by KESTIN, J.,4th edn., McGraw-Hill, New York.

SCHUËLLER, G.I. (1976), "On the reliability of the spectral method for the design of offshore structures". J.Hyd.Res.,14,3,229-239.

SCHWARZ, W.H. and COSART, W.P. (1961), "The two dimensional turbulent wall jet". J.Fl.Mech.,10,481-495.

SELIN, H.J. (1969), "Flow in channels". Macmillan Engineering Hydraulic series, Macmillan, St. Martin's Press.

SIGALLA, A. (1958), "Measurements of skin friction in a plane turbulent wall jet". J.Roy.Aero.Soc.,62,873-877.

SINGLETON, R.C. (1969), "An algorithm for computing the mixed radix Fast Fourier Transform". IEEE Trans.on Audio and Electro_ acoustics, Au-17,93-103.

STEPANOV, P.M. (1958), "The submerged hydraulic jump". English Translation by Israel Programme for Scientific Translations.

THOM, A.and APELT, C.J. (1958), "The pressure in a two-dimensional static hole at low Reynolds numbers". Rep.Memor.Aero.Res.Coun. No.3090 London.

THOMPSON, D.M. and GILBERD, G. (1971), "The Fast Fourier Transform". INT 100, Hyd.Res.Station Wallingford.

THOMSON, J. (1876), "On the origin and winding of rivers in alluvial plains, with remarks on the flow around bends in pipes". Proc. Roy.Soc.,25,5-8.

THOMSON, P.W. and VOGEL, H.D. (1933), "Flow in river bends ". Civ.Engng., 3,5,266-268.

TOLLMIEN, W. (1933), "Die von kármánsche ähnlichkeitshypothese in der turbulenz - theorie und das ebene windschattenproblem". Ing. - Arch. 4,1-15.

TOWNSEND, A.A. (1956), "The structure of turbulent shear flow". Cambridge Univ.Press.

TUCKER, M.J. (1957), "The analysis of finite length records fluctuating signals". Brit.J.App.Phys.8.

TUCKER, M.J. (1963), "Analysis of records of sea waves". Proc. I.C.E., 26,305-316.

TYAGI, D.M., PANDE, P.K. and MITTAL, M.K. (1978), "Drag on baffle walls in hydraulic jump". J. Hyd.Div.Am.Soc.Civ.Engrs.,104,HY4, 515-524.

UNNY, T.E. (1961), "The spatial hydraulic jump". Proc. 9th Cong. Intern. Ass.Hyd.Res., Dubrovnik,Yugoslavia, 32-42.

VERHOFF, A. (1963), "The two-dimensional turbulent wall jet with and without an external stream". Rep.No.626,Princeton Univ.

VIPARELLI, M. (1953), "The flow in a flume with 1:1 slope". Proc.Intern. Ass. Hyd. Res., Minneapolis, Minnesota,415-425.

WEAVER, R.W. (1950), "Discussion on control of the hydraulic jump by sills". Trans.,Am.Soc.Civ.Engrs.,115,1003-1006.

WIEGEL, R.L. (1964), "Oceanographical engineering". Englewood Cliffs, Prentice-Hall, Inc.

WILSON, E.H. (1965), "The hydraulic jump in rectangular channels". M.Sc. Thesis, Univ. of London.

WILSON, E.H. (1967), "Location of the hydraulic jump in open rectangular channels". The Engineers, 145-149.

WILSON, E.H. and TURNER, A.A. (1972), "Boundary layer effects on hydraulic jump location". J. Hyd.Div.Am.Soc.Civ.Engrs., 98,HY7, 1127-1142.

WINTERNITZ, F.A.L. (1956), "Probe measurements in three-dimensional flow". Aircr., Engng., 28,273.

WYLIE, C.R. (1966), "Advanced engineering mathematics". 3rd edn., McGraw-Hill, New York.

YEVDJEVICH, V.M. (1966), "Diffusion of slot jets with finite orifice length-width ratios". Hydraulics Papaer 2, Colorado State Univ. Fort Collins, Colorado.

ZERBE, J. and SELNA, J. (1946), "An experimental equation for the coefficient of heat transfer to a flat surface from a plan heated air jet directed tangentially to the surface". NACA, TN, 1070.